Development of a Modular Cavity Design for Mass Production of Superconducting CH Cavities for the Superconducting Heavy Ion Accelerator HELIAC at GSI

Dissertation

zur Erlangung des Doktorgrades der Naturwissenschaften

vorgelegt beim Fachbereich Physik der Goethe-Universität in Frankfurt am Main

von

Thorsten Conrad

aus Hanau

Frankfurt am Main 13.09.2022

D 30

vom Fachbereich Physik der Goethe-Universität als Dissertation angenommen.

Dekan: Prof. Dr. Roger Erb
Erstgutachter: Prof. Dr. Holger Podlech
Zweitgutachter: Prof. Dr. Ulrich Ratzinger
Datum der Disputation: 03.02.2023

Zusammenfassung

In dieser Arbeit wird die Entwicklung und das Prinzip einer neuartigen Designmethode für supraleitende CH-Kavitäten beschrieben, welche auf einem modularen Kavitätendesign basiert. Bei dieser Methode für das Design von Kavitäten werden dabei zahlreiche Komponenten der einzelnen CH-Kavitäten eines supraleitenden Linearbeschleunigers trotz der sich ändernden Spaltmittenabstände und den damit einhergehenden sich ändernden Radien der Kavitäten mit denselben geometrischen Dimensionen designt und gefertigt und nachträglich an die jeweiligen geometrischen Randbedingungen der zu betrachtenden CH-Kavität angepasst. Dieser Ansatz dient dabei dazu die ansonsten für einen gesamten Linearbeschleuniger zeitaufwendige und kostenintensive Designphase und Fertigung deutlich zu vereinfachen und somit sowohl Kosten als auch Zeit zu sparen, da CH-Kavitäten, die auf diesem modularen Kavitätendesign basieren, in Massenproduktion gefertigt werden können. Als Ausgangspunkt für die Entwicklung dieser Designmethode dienten die supraleitenden, 216,816 MHz CH-Kavitäten CH3 bis CH11 des Helmholtz Linear Accelerator (kurz HELIAC), welcher sich an dem GSI Helmholtzzentrum für Schwerionenforschung in Darmstadt aktuell im Aufbau befindet. Dieser neuartige Beschleuniger soll dabei Schwerionen mit einem Masse-zu-Ladung Verhältnis von bis zu 6 bei einem sehr hohen Tastverhältnis bis zum CW-Betrieb beschleunigen. Dabei wird er durch den Hochladungsinjektor (HLI) mit einer Eingangsenergie von 1,4 MeV/u gespeist und beschleunigt den Teilchenstrahl auf eine variable Ausgangsenergie von 3,5 MeV/u bis 7,3 MeV/u. Der Hauptfokus der Experimente, die durch den HELIAC mit Ionen versorgt werden, liegt dabei auf der Synthese neuer, superschwerer Elemente (SHE). Für die Entwicklung des modularen Kavitätendesigns wurde das bereits erfolgreich umgesetzte und gefertigte Design der beiden baugleichen supraleitenden CH-Kavitäten des HELIAC CH1 und CH2 analysiert und nach Rücksprache mit dem Hersteller dieser beiden Kavitäten die modularen Komponenten ausgewählt. So wurde entschieden aus diesem erfolgreichen Design die Deckel, die Spokes, die Flansche, die Heliumtanks, sowie die statischen Tuner als auch die dynamischen Balgtuner zu entnehmen und sie mit einem Einheitsdesign zu entwerfen. Die Auslegung dieser Komponenten unterlief dabei unterschiedliche Designprozesse. Zunächst wurde begonnen die Kavität mit dem geringsten Spaltmittenabstand, CH3, zu entwerfen. Hierbei wurde besondere Aufmerksamkeit der Optimierung hinsichtlich der Drucksensitivität der Kavität gewidmet und sowohl die Spokes als auch die Deckel so ausgelegt, dass die Kavität möglichst stabil gegenüber äußeren Druckschwankungen ist. So wurde an den Spokes sowohl die Dimension des Spokefußes als auch die des geraden Spokestückes nahe der Strahlachse angepasst und bei den Deckeln der Radius der konischen Vertiefung. Dabei wurden diese Bauteile direkt so entworfen, dass sie zu Beginn der Auslegung der Kavität eine deutlich größere Dimension aufweisen, als benötigt, um sie auf die im Radius wachsenden, späteren Kavitäten anpassen zu können. Auf die Deckel wurden dann die sich bei CH1 und CH2 nützlich erwiesenen Spülflansche für die HPR (high pressure rinsing zu deutsch Hochdruckspülung)

abseits der Strahlachse und die Ablaufflansche für die BCP (Buffered Chemical Polishing) angebracht. Dabei sind jeweils zwei Spülflansche pro Deckel vorhanden, so dass zusätzlich zur Strahlachse alle vier Quadranten der Kavität gespült werden können.
Das Design der dynamischen Balgtuner, welches als Teil des modularen Kavitätendesign entworfen wurde, wurde im Vergleich zu dem Design der dynamischen Balgtuner in CH1 und CH2 stark angepasst. So wurde der Radius des Balgtuners soweit vergößert, dass ein Auslagern nach außen hin der Balglamellen nicht mehr nötig ist. Dies ist durch den vergrößerten Spaltmittenabstand und somit den größeren Abstand zwischen den Spokes möglich. Der Radius der Lamellen und damit des Tuners wurde dabei so gewählt, dass eine Auslenkung von $\pm 1\,\mathrm{mm}$ bei drei Lamellen durch eine wirkende Kraft von circa $\pm 300\,\mathrm{N}$ bewirkt wird. Dabei darf der innere von Mises Stress $\sigma_{\mathrm{v,\ von\ Mises}}$ den kritischen Wert von Niob im kalten Zustand, aus dem die gesamte Kavität gefertigt wird, von $\sigma_{\mathrm{v,\ von\ Mises,\ yield,\ Nb\ cold}} = 0{,}49\,\mathrm{GPa}$ nicht überschreiten. Das im Rahmen dieser Arbeit entworfene dynamische Balgtunerdesign des modularen Kavitätendesigns erfüllt diese Randbedingungen bei einem inneren Stress von $\sigma_{\mathrm{v,\ von\ Mises}} \approx 0{,}24\,\mathrm{GPa}$, sodass es für den späteren Betrieb geeignet ist. Zudem wurde die Rundung des Tunerkopfes weiter vergrößert, um die die Supraleitung limitierenden, elektrischen Spitzenfelder am Tunerkopf weiter zu reduzieren und somit die Performanz der Kavität zu steigern. In Abb. I ist stellvertretend für alle Kavitäten CH4 in einem Dreiviertelschnitt gezeigt.

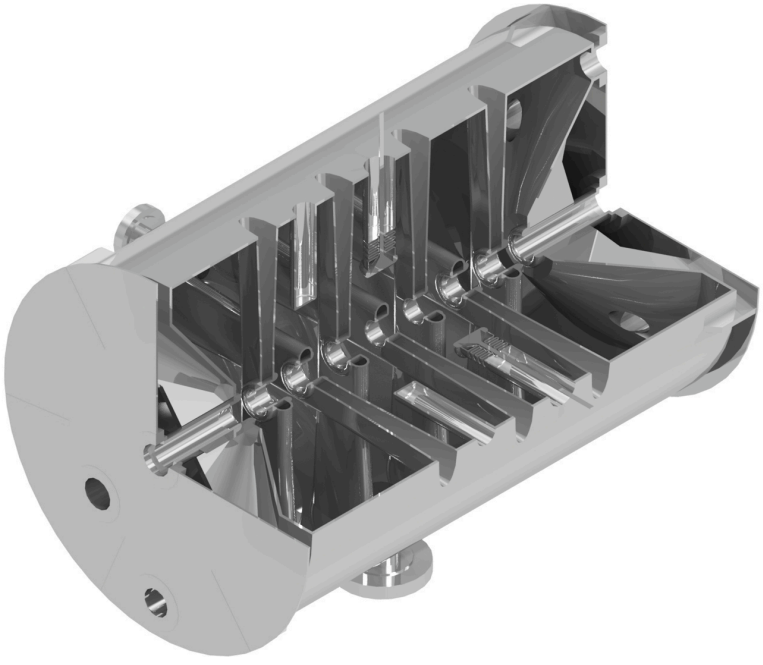

Abb. I Stellvertretend für alle Kavitäten: CH4 des HELIAC ohne angebrachten Heliumtank. Zu sehen sind die konischen Deckel, die geraden Spokes und sowohl die dynamischen Balgtuner als auch die statischen Tuner.

Zuletzt wurden verschiedene Möglichkeiten betrachtet den die Kavität umgebenden Heliumtank modular für alle Kavität zu entwerfen. Die auftretende Problematik dabei ist, dass durch den wachsenden Spaltmittenabstand der Kavitäten auch der Radius anwächst, um die Zielresonanzfrequenz des HELIAC zu erreichen, wodurch bei einem wachsenden Kavitätenradius aber konstant bleibendem Heliumtankradius die Menge an flüssigem Helium als Kühlmittel der Kavitäten, um die Supraleitung aufrecht zu erhalten, signifikant abnimmt. Zudem begrenzt der Radius der bereits vorhanden Kryostaten den maximalen Radius der Heliumtanks. Nach Absprache mit den späteren Operatoren des HELIAC wurde beschlossen, den durch die Kryosta-ten begrenzten maximal möglichen Radius der Heliumtanks auf 320 mm zu setzen und die Flansche in ihm zu versenken. Dies ergibt für die größte Kavität CH11 ein Heliumreservoir von circa 80 l, was nach der Aussage der Operatoren ausreichend sein sollte. Nachdem alle benötigten Bauteile des modularen Kavitätendesigns fertig entworfen waren, wurde die benötigten Dimensionen wie die Spaltmittenabstände und die Spaltenanzahl aus der vorliegenden Strahldynamik entnommen und die Kavitäten modular aufgebaut.
Nachdem alle neun Kavitäten modular entworfen worden waren, wurden sie auf ihre Tauglichkeit untersucht. So waren die Anforderungen des HELIAC Projekts an die neuen Kavitäten, dass sie ausreichend stabil gegenüber mechanischer Verformung durch Druckschwankungen und Evakuieren des Innenraumes sind, ein Frequenztuningbereich durch die dynamischen Balgtuner von circa 150 kHz abgedeckt ist und nach einer Oberflächenbehandlung (BCP) von 200 μm ein Puffer bis zur eigentlichen Zielfrequenz von ungefähr 250 kHz bestehen bleibt. So wurde zunächst die Drucksensitivtät aller neun Kavitäten durch Simulationen mit CST Studio Suite untersucht und festgestellt, dass mit einer maximalen Drucksensitivität von $\Delta f/\Delta p$ = 10,8 Hz/mbar trotz des modularen Aufbaus die Kavitäten ausreichend stabil gegenüber Druckänderung sind. Zudem konnten die Kavitäten so ausgelegt werden, dass alle Kavitäten nach der gewünschten Behandlung mit BCP den Puffer von ungefähr 250 kHz zur Zielfrequenz von 216,816 MHz erreichen. Dies bestätigt die Tauglichkeit sowohl aller neun Kavitäten für den späteren Bau und Betrieb als auch das modulare Kavitätendesign an sich als eine geeignete Designmethode für supraleitende CH-Kavitäten für die Massenproduktion eines gesamten supraleitenden Linearbeschleunigers.
Der letzte Schritt in der Designphase der Kavitäten war die Optimierung jeder einzelnen Kavität hinsichtlich der Reduzierung der elektrischen und magnetischen Spitzenfelder. Da durch den modularen Aufbau eine individuelle Optimierung der Deckel und der Spokes nicht möglich war, beschränkte sich die Optimierung auf die Driftröhrengeometrie und auf den Radius der Kavität. Dabei wurde zunächst der in CST Studio Suite integrierte Optimizer, basierend auf der Nelder-Mean-Methode, auf die Kavitäten angewendet und anschließend die Parameter händisch angepasst. Dabei konnten die Spitzenfelder so weit optimiert werden, dass im Vergleich zu den beiden Vorgängerkavitäten CH1 und CH2 eine deutliche Verbesserung hinsichtlich der elektrischen Spitzenfelder bei allen Kavitäten und hinsichtlich der magnetischen

Spitzenfelder eine Verbesserung bei den Kavitäten CH3 bis CH8 erzielt werden konnte. Diese Verbesserung wird ersichtlich, wenn das Verhältnis der Spitzenfelder E_{peak} und B_{peak} zu dem Beschleunigungsfeld E_{a} betrachtet wird (siehe Abb. II). Diese Verhältnisse $E_{\text{peak}}/E_{\text{a}}$ und $B_{\text{peak}}/E_{\text{a}}$ geben an, wie viel Leistung in eine supraleitende Kavität eingespeist werden kann, bevor die resultierenden Spitzenfelder die Supraleitung zusammenbrechen lassen. Je niedriger diese Verhätlnisse sind, umso besser performt eine supraleitende Kavität. Dabei konnte die Performanz hinsichtlich der Reduktion der elektrischen Felder um 15 % und hinsichtlich der magnetischen Felder um 4 % im Vergleich zu CH1 und CH2 gesteigert werden. Somit wurde nicht nur die Tauglichkeit der Kavitäten sowie des modularen Kavitätendesigns gezeigt, sondern es konnte auch die Performanz der aus dem modularen Kavitätendesign hervorgegangenen Kavitäten im Vergleich zu den Vorgänger deutlich verbessert werden, sodass die im Rahmen dieser Arbeit entwickelte Methode angewendet und die damit entworfenen Kavitäten gebaut werden können, um später in den HELIAC der GSI zum Einsatz zu kommen.

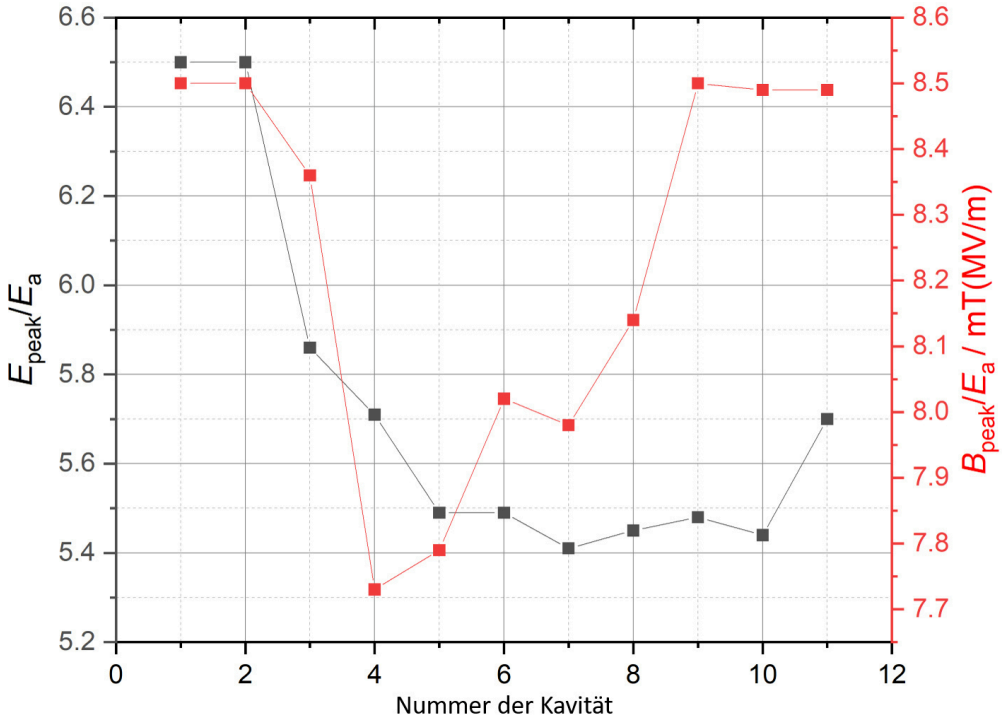

Abb. II Die Ergebnisse der Optimierung der Kavitäten CH3 bis CH11 in Form der Verhältnisse $E_{\text{peak}}/E_{\text{a}}$ (schwarz) und $B_{\text{peak}}/E_{\text{a}}$ (rot).

Neben der Entwicklung des modularen Kavitätendesigns sowie dem Design der Kavitäten CH3 bis CH11 des HELIAC werden in dieser Arbeit die Ergebnisse eines aufgeschobenen Kalttests der Kavität CH2 vorgestellt. Dieser Kalttest wurde zuvor bereits einmal angesetzt, musste jedoch auf Grund eines auftretenden Kaltlecks vorzeitig abgebrochen werden. Im Rahmen dieses Kalttests wurde die Kavität

im vertikalen Kryostaten des IAP Frankfurt der Goethe Universität Frankfurt am Main auf 4 K Betriebstemperatur herunter gekühlt und anschießend vermessen. Diese Messungen beinhalteten die Drucksensitivitätsmessung, bei der mit einem Wert von $\Delta f/\Delta p = -9{,}6\,\mathrm{Hz/mbar}$ die beim vorherigen abgebrochenen Kalttest aufgenomme Drucksensitivität bestätigt werden konnte. Zudem wurde während des erneuten Aufwärmens der Kavität auf Raumtemperatur die durch die thermische Kontraktion/ Expansion auftretende Frequenzänderung auf $\Delta f_{\mathrm{thermisch}} = 0{,}405\,\mathrm{MHz}$ zwi-schen Raumtemperatur und 4 K bestimmt. Dabei liegt eine Abweichung von $\Delta f_{\mathrm{Theorie}} \approx 0{,}095\,\mathrm{MHz}$ vor. Dieser Unterschied lässt sich so erklären, dass die Aufhängung, in der die Kavität in den vertikalen Kryostat gelassen wird, aus Aluminium besteht und somit einen unterschiedlichen thermischen Ausdehnungskoeffizienten als die aus Niob bestehende Kavität aufweist und sich dadurch unterschiedlich stark verformt, was eine Abweichung der Kontraktion und der Frequenz verursacht. Während des Kalttests wurde mehrfach versucht zu bestätigen, dass die Kavität CH2 den vom HELIAC geforderten Beschleunigungsgradienten von $E_{\mathrm{a}} = 5{,}5\,\mathrm{MV/m}$ bei einer Güte von $Q_0 = 3 \cdot 10^8$ erreicht. Auf Grund eines seltsamen Verhaltens, dessen Ursprung im Rahmen dieser Arbeit aus zeitlichen und infrastrukturellen Gründen nicht näher untersucht werden konnte, konnte dieses Ziel insgesamt nur bei den ersten beiden Messungen erreicht werden. In allen darauffolgenden Messungen konnte dies nicht reproduziert werden. Daraufhin wurde der Kalttest erneut abgebrochen und die Kavität zum Hersteller zurückgeschickt. Dort wurde sie erneut gespült und der Heliumtank angeschweißt.

Im letzten Abschnitt dieser Arbeit wird das entwickelte Prinzip eines im Rahmen dieser Arbeit designeten Balgtunerteststands genauer erläutert. Während der ersten Charakterisierung der Kavität CH1, die im Rahmen der Doktorarbeit von Markus Basten [1] durchgeführt wurde, wurde der dynamische Balgtuner versehentlich einer größeren Kraft als der maximalen Belastungskraft ausgesetzt, was eine dauerhafte Verformung des Balgs nach sich zog. Dieser Umstand warf die Frage auf, wie langlebig diese Art von dynamischen Tunern ist. Anders als bei normalleitenden Tunern, welche bei Beschädigung einfach ausgetauscht werden können, sind die dynamischen Balgtuner der supraleitenden CH-Kavitäten fest mit der Kavität verschweißt, was ein einfaches Austauschen unmöglich macht und somit eine Beschädigung des Balgtuners eine Beschädigung der gesamten Kavität bedeutet was lange und kostenintensive Reparaturen nach sich ziehen würde. Dieser Umstand bedeutet zusätzlich, dass die Lebenszeit des Balgtuners gleichzusetzen ist mit der Lebenszeit der Kavität. Deshalb wurde beschlossen einerseits sowohl die Lebenszeit eines Balgtuners als auch die maximale Belastungsgrenze experimentell zu bestimmen. Dabei wird für die Untersuchung der Lebenszeit der Balgtuner mehrfach über seine gesamte Auslenkungsstrecke von $\pm 1\,\mathrm{mm}$ ausgelenkt und überprüft, ab welcher Anzahl von Auslenkungen eine dauerhafte Verformung des Balgs durch Materialermüdung auftritt. Bei der Bestimmung der maximalen Belastungsgrenze wird die Kraft auf die Tunerstange so lange erhöht, bis ein Bruch im Material auftritt. Für

die Realisierung dieses Balgtunerteststandes wurde beschlossen, die sich bereits am IAP Frankfurt befindliche Pillbox-Kavität so zu modifizieren, dass sie für den Balgtunerteststand geeignet ist (siehe Abb. III).

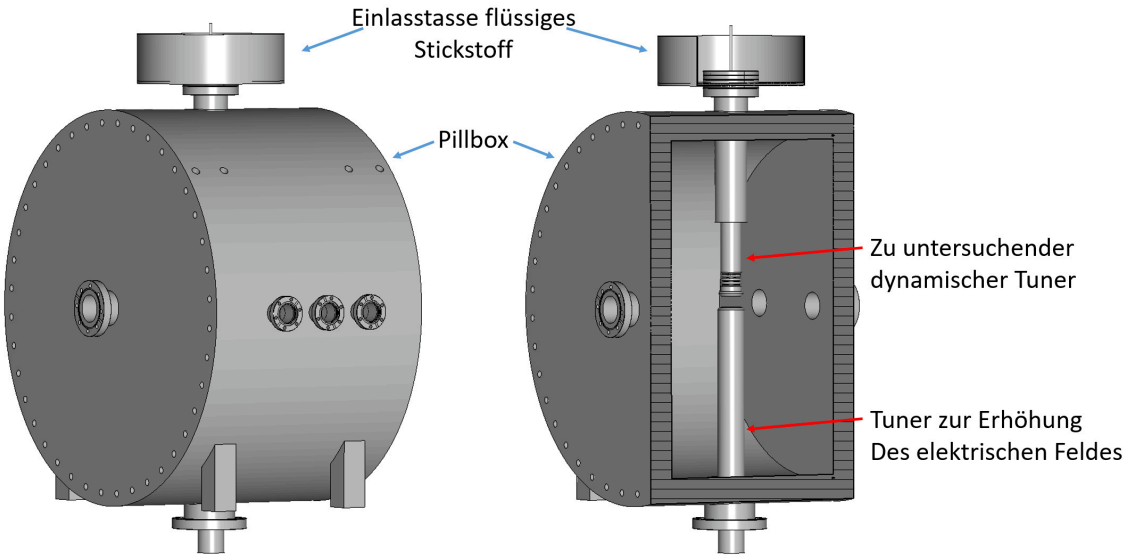

Abb. III Auf der bereits am IAP Frankfurt befindlichen Pillbox-Kavität basierender Tunerteststand. Zu sehen sind die erweiterte Einlasstasse für den flüssigen Stickstoff, der statische Tuner zur Felderhöhung und der zu untersuchende dynamische Balgtuner.

Diese Modifikation der Pillbox beinhalten dabei vor allem Maßnahmen zur Gewährleistung der Arbeitssicherheit während des Betriebs. So wurde eine Stickstofftasse und eine Einfülllanze für die sichere Befüllung des Balgtuners mit flüssigem Stickstoff während der Tests entworfen. Das Prinzip des Balgtunterteststandes ist dabei, dass der Balgtuner permanent durch flüssiges Stickstoff auf 77 K herunter gekühlt wird, da Niob im kalten Zustand andere mechanische Eigenschaften als im warmen aufweist. Während der mehrfachen Auslenkung des Tuners wird permanent die Resonanzfrequenz der Pillbox durch einen Netzwerkanalysator aufgezeichnet. Durch Vergleich der Resonanzfrequenz während des Nulldurchgangs des Tuners kann auf Verformungen im μm-Bereich zurückgeschlossen werden, welche mit einer Längenmessung nicht aufzulösen wären. Zudem kann durch den Vergleich der Frequenzänderungen, die durch den Tuner bewirkt werden, darauf zurückgeschlossen werden, ob das Material des Tuners durch die vermehrte Auslenkung weicher oder härter wird. Das Innere der Pillbox wird dabei durch Turbopumpen abgepumpt und der innere Druck durch Druckmessköpfe gemessen. Sollte ein Bruch des Tuners während einem der Tests auftreten, so würde der Druck in der Pillbox auf Grund des in die Pillbox strömenden Stickstoffs rasant steigen, was durch die Druckmessköpfe eindeutig gemessen werden könnte. Da die Pillbox einen deutlich größeren Radius als die Späteren Kavitäten des HELIAC aufweisen, musste der zu untersuchende Tuner an die gegebenen Randbedingungen angepasst wer-

den. Hierfür wurde er so verlängert, dass der Tunerkopf bis zur Mitte der Kavität reicht, da dort die Messung durch die Frequenzänderung die beste Auflösung garantiert. Um zusätzliche Freiheitsgrade durch den verlängerten Tuner zu unterdrücken, wurde das Tunerrohr bis zum eigentlich Balg verlängert. Um Kosten zu sparen, werden die für die Untersuchung unwichtigen Teile des Tuners aus Titan gefertigt, da es einen ähnlichen thermischen Ausdehnungskoeffizienten wie Niob aufweist. Lediglich der Balg und der Tunerkopf werden aus Niob gefertigt. Es konnte durch unterschiedliche Simulationen bestätigt werden, dass die Anpassungen des zu untersuchenden Tuners keinerlei Einfluss auf die Übertragbarkeit der Messung von dem Balgtunerteststand auf die späteren Tuner aufweisen, da die Verformung lediglich im Balg auftreten. Zudem konnten Simulationen eine mögliche Auflösung der Verformung des Tuners auf $\pm 1\,\mu$m bestätigen. Das im Rahmen dieser Arbeit entwickelte und vorgestellte Prinzip des Balgtunerteststand ist somit für die Untersuchung und Charakterisierung der dynamischen Balgtuner supraleitender CH-Kavitäten geeignet.

Table of Contents

1 Introduction

1.1 Synthesis of Superheavy Elements

The first version of the periodic table of the elements, in which all elements known until then were ordered according to their properties and grouped together, was published independently of each other in 1869 by several chemists, including Dimitri Mendeleev[1] and Julius Lothar Meyer[2] [2]. This arrangement of elements made it possible to make predictions about so far undiscovered elements as well as their properties. This search for new elements, which began with the definition of the first periodic table, is still today an attempt to answer questions of fundamental nature [3].
After the discovery of naturally occurring elements, attention was devoted to the synthesis of new elements. The foundation for these syntheses was laid in 1934 by Irène Joliot-Curie[3] and Frédéric Joliot[4]. By bombarding chemical elements with alpha particles[5] they were able to convert light nuclei into other elements. This discovery, of the transformation of elements by bombardment of an accelerated particle, enabled the Italian physicist Enrico Fermi[6] to produce artificial radioactivity in 1934 by bombarding atomic nuclei with neutrons [4]. In addition, he discovered that neutrons can enter the atomic nucleus freely because they are not subjected to the Coulomb repulsion. The neutron now in the nucleus decays by β^-decay into a proton emitting an electron and an electron antineutrino. Thus, an atomic nucleus with the same atomic mass A as the previously excited nucleus is formed but with the atomic number Z increased by one. This process is called neutron capture.
By neutron capture and bombardment with other particles, the first 6 transuranics[7] were synthesized in a time period from 1940 to 1950 by colliding Uranium or one of the previously produced transuranics with accelerated neutrons, protons, or alpha particles. As a result, the elements Neptunium ($_{93}$Np), Plutonium ($_{94}$Pu), Americium ($_{95}$Am), and Curium ($_{96}$Cm) could be synthesized for the first time at Ohio State University, Columbus, Ohio [5] and shortly after the elements Berkelium ($_{97}$Be) [6] and Californium ($_{98}$Cf) [7] were synthesized at the University of California, Berkley, California. The following elements, Einsteinium ($_{99}$Es) and Fermium ($_{100}$Fm), were accidentally detected in the fallout[8] in the United States in 1952 after a test explosion of the first American hydrogen bomb, 'Ivy Mike'. Fermium is the

[1] ⋆27 January 1834 in Tobolsk, Russian Empire; †20 January 1907 in Saint Petersburg, Russian Empire
[2] ⋆19 August 1830 in Varel, Germany; †11 April 1895 in Tübingen, Germany
[3] ⋆12 September 1897 in Paris, France; †17 March 1956 in Paris, France
[4] ⋆19 March 1900 in Paris, France; †14 August 1958 in Paris, France
[5] Alpha particles, or α particles, are equivalent to a Helium-4 atomic nucleus consisting of 2 protons and 2 neutrons.
[6] ⋆29 September 1901 in Rome, Italy; †28 November 1954 in Chicago, USA
[7] elements with an atomic number Z greater than $Z = 92$
[8] radioactive fallout produced after a nuclear weapon explosion or nuclear reactor accident

heaviest element that can be produced in this way. Neutron capture in Fermium followed by β^-decay produces isotopes which, because of their short half-lives, decay either into fission products or into lighter nuclei via α-decay.
Heavier elements or SHE[9] greater than the atomic number $Z = 100$ can only be produced by fusion reactions. For this purpose, ions, so-called projectiles, are accelerated by means of a particle accelerator so that their kinetic energy is sufficiently large to overcome the Coulomb repulsion. When these projectiles collide with the heavy nuclei of the so-called target, the strong nuclear interaction takes effect and a compound nucleus is created, which is in an excited state. By emitting one or more neutrons, the compound nucleus falls back from an excited to the ground state and forms a new element. In this reaction, also called 'hot fusion', a thin foil of the size of $1\,\mathrm{mg/cm^2}$ is used as target, because a thicker target would cause a higher energy loss of the projectiles, so that the energy distribution would be too broad for the production of fusion nuclei [3].
The 'hot fusion' made it possible to synthesize for the first time the elements $Z = 101$ up to and including $Z = 106$[10] at the JINR[11], at the LBNL[12] and at LLNL[13].

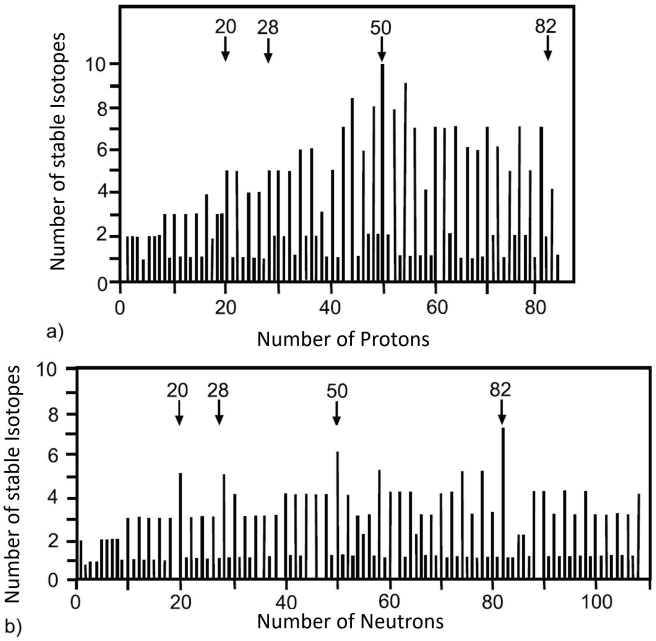

Fig. 1 Number of stable isotopes against the number of nuclides. It is seen that at the magic numbers for protons (a) and neutrons (b) there are more stable isotopes [8].

[9] **S**uper **H**eavy **E**lements
[10] Mendelevium ($_{101}$Md) LBNL, Nobelium ($_{102}$No) LBNL, Lawrencium ($_{103}$Lr), Rutherfordium ($_{104}$Rf) JINR, Dubnium ($_{105}$Db) JINR, Seaborgium ($_{106}$Sg) LLNL
[11] **J**oint **I**nstitute for **N**uclear **R**esearch in Dubna, Russia
[12] **L**awrence **B**erkeley **N**ational **L**aboratory in Berkley, USA
[13] **L**awrende **L**ivermore **N**ational **L**aboraory, Livermore, USA

The stability of the generated nuclei depends on the number of protons and neutrons in the nucleus. Similar to the shell model for the stability of atoms, the nuclear shell model describes the stability of atomic nuclei [8]. It shows that in the case of closed shells for protons and neutrons, the binding energy of the nuclides is particularly high and the nuclei thus form more stable isotopes than the neighbouring nuclei (see figure 1).
These closed shells are also called 'magic' and 'double magic' numbers, if both the proton and the neutron shell are closed. Experimentally, the magic numbers $Z = 2$, 8, 20, 28, 50, 82 and $N = 2$, 8, 20, 28, 50, 82, 126 have been confirmed so far. Other magic numbers predicted so far by theory but not experimentally confirmed are $Z =$ 114 or 120 – 126 and $N = 184 – 196$ [3]. The shell model theory therefore predicts additional stable nuclei, which are not yet discovered. These stable elements are suspected to exist around the presumably double magic isotope Flerovium $^{298}_{114}$Fl or $^{310}_{114}$Fl [9] (see figure 2), whose synthesis has not yet been successful.

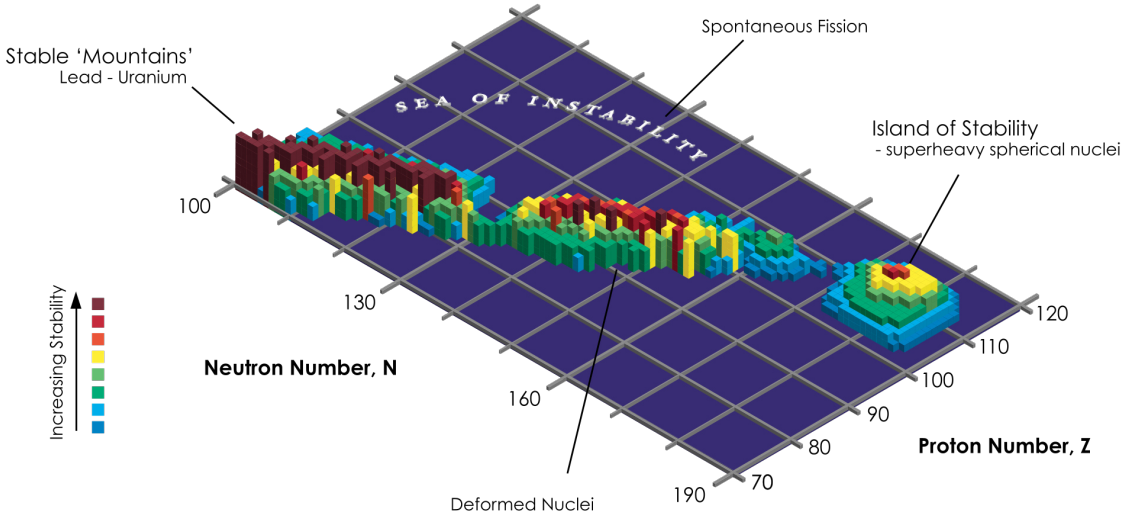

Fig. 2 Island of stability around the double magic nuclid $^{298}_{114}$Fl or $^{310}_{114}$Fl [10].

The disadvantage of 'hot fusion' is the high excitation energy of the compound nucleus, which entails a high probability of spontaneous fission. For this reason, the approach of so-called 'cold fusion' is being pursued at the GSI[14]. This involves bombarding naturally occurring, moderately heavy elements such as Lead ($_{82}$Pb) and Bismuth ($_{83}$Bi) with comparatively heavy projectiles such as Argon ($_{18}$Ar). The excitation energy of the compound nucleus is several times lower than in 'hot fusion'. Using the 'cold fusion' method, it was possible at GSI to synthesize the elements

[14]GSI Helmholtz Centre for Heavy Ion Research in Darmstadt, Germany (founded in 1969 as **G**esellschaft für **S**chwer**I**onenforschung)

with the atomic number $Z = 107$ to $Z = 112$[15] [3] [11]. Finally, in 1999 at JINR, the element ${}_{114}\mathrm{Fl}$ was successfully synthesized by 'cold fusion' by bombarding a target of the heavy isotope ${}^{242}_{94}\mathrm{Pu}$ of the element Plutonium with a beam of Calcium (${}^{48}_{20}\mathrm{Ca}$) [12]. It exhibits a significantly longer half-life than the neighbouring elements, which seems to confirm the atomic number $Z = 114$ as a magic number. The confirmation of the double magic isotope like that of the island of stability as a whole is still pending.

1.2 The sc cw-LINAC HELIAC at GSI

At GSI, the linear accelerator UNILAC[16] [13] and the high charge injector HLI [14] were crucial for the production of SHE by 'cold fusion'. With the HLI and the high current injector HSI, the UNILAC can be fed from a total of six different ion sources. The HSI is thereby fed by a total of five ion sources (PIG[17], MUCIS[18], CHORDIS[19], MEVVA[20] and VARIS[21]), which are supplied by two high-voltage terminals (South and North terminal), and the HLI by a 14.5 GHz ECRIS[22]. The ions of the HSI are accelerated in a 36 MHz RFQ[23] and two IH[24] cavities at a mass-to-charge ratio A/q $\leq$ 65 to a final energy of up to 1.4 MeV/u and their charge state is increased in a subsequent gas stripper (for example from U^{4+} to U^{28+}) [15].
The HLI runs parallel to the UNLIAC, as shown in figure 3. The ions are here also accelerated in a 108 MHz RFQ and an IH cavity to 1.4 MeV/u and injected directly into the poststripper [16]. The poststripper, which can be supplied with a total of three different ion species from both injectors, consists of five 108 MHz Alvarez DTLs[25] and accelerates the ions to an energy of up to 11.4 MeV/u. At the end of this there is a sequence of single-gap resonators that can be used to vary the output energy between 3.6 and 12.4 MeV/u [15].

[15] Bohrium (${}_{107}\mathrm{Bh}$), Hassium (${}_{108}\mathrm{Hs}$), Meitnerium (${}_{109}\mathrm{Mt}$), Darmstadtium (${}_{110}\mathrm{Ds}$), Roentgenium (${}_{111}\mathrm{Rg}$), Copernicum (${}_{112}\mathrm{Cp}$)
[16] **UNI**versal **L**inear **AC**celerator
[17] **P**enning **I**onization **G**auge ion source
[18] **MU**lti **C**usp **I**on **S**ource
[19] **C**old or **H**ot **R**eflex **D**ischarge **I**on **S**ource
[20] **M**etal **V**apor **V**acuum **A**rc ion source
[21] **V**acuum **A**rc **I**on **S**ource
[22] **E**lectron **C**yclotron **R**esonance **I**on **S**oure
[23] **R**adio **F**requency **Q**uadropole
[24] **I**nterdigital **H**-mode
[25] **D**rift **T**ube **L**inac

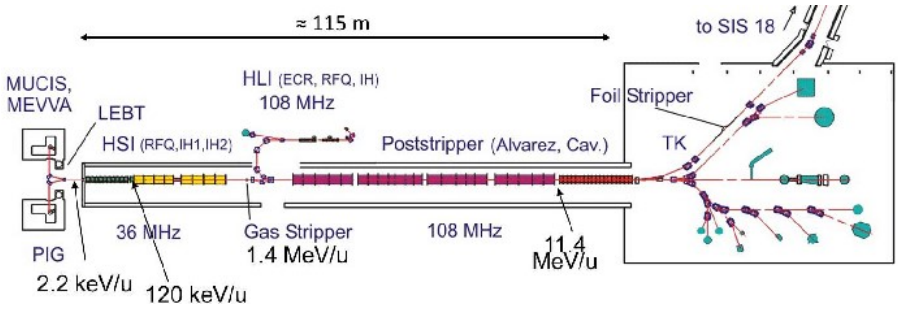

Fig. 3 Representation of the current structure of the UNILAC [17].

As part of the upgrade of GSI to the FAIR[26]-project, which was conceptualized in 2001 [18] and approved by the BMBF[27] in 2003, UNILAC together with the normal conducting synchrotron SIS18[28] will be used as injector for the superconducting SIS100[29] synchrotron currently under construction (see figure 4) [19].

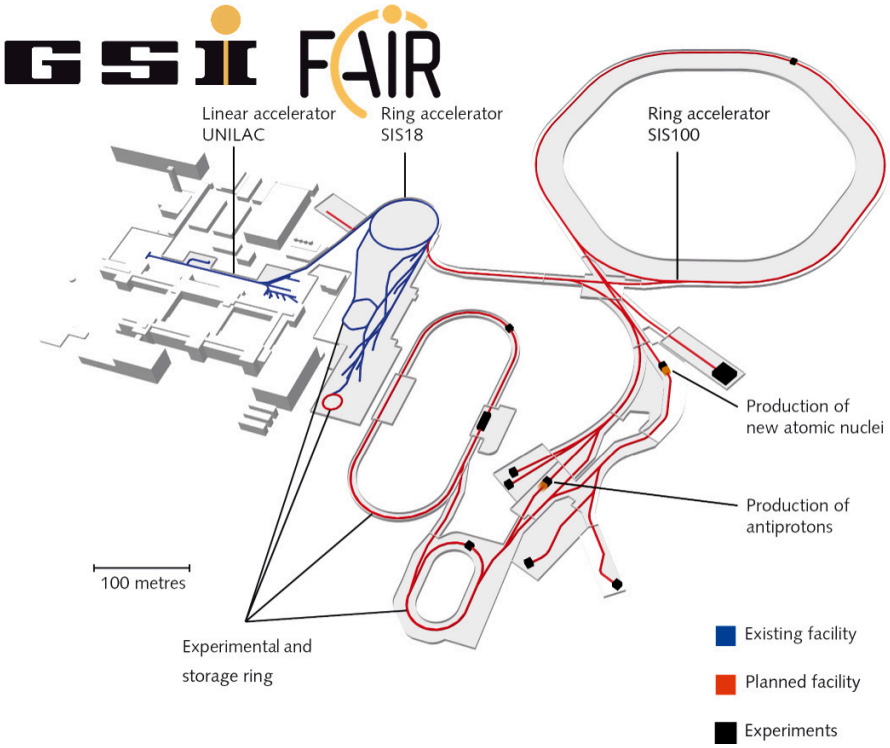

Fig. 4 Existing accelerator facility at GSI (blue) and the planned expansion within the FAIR project (red) [20].

[26]**F**acility for **A**ntiproton and **I**on **R**esearch
[27]**B**undes**M**inesterium für **B**ildung und **F**orschung
[28]**S**chwer **I**on **S**ynchrotron (heavy ion synchrotron) with a magnetic rigidity of 18 mT
[29]**S**chwer **I**onen **S**ynchrotron (heavy ion synchrotron) currently under construction, with a magnetic rigidity of 100 mT and a circumference of 1084 m

Due to a new distribution of tasks for UNILAC, it was decided to establish a new linear accelerator at GSI for the synthesis of SHE. A continuous-wave (cw), superconducting (sc) linear accelerator consisting of compact CH[30] cavities was chosen, as this ensures efficient acceleration over a short distance [21]. Another reason why a sc cw linac was targeted is that the effective cross section of the generation of SHE decreases significantly with increasing nuclear charge number. To compensate for this, a higher beam intensity or repetition rate is needed [22]. Furthermore, the reduction in cost due to the lower power requirement and the higher production rate of the SHE in this case outweighs the higher investment cost compared to a normal conducting linear accelerator. As a result, the superconducting HELIAC could synthesize SHE up to a factor of 20 faster compared to the existing UNILAC, so that the production of one atom of element $Z = 120$ could be expected in about four days [23]. In order to realize HELIAC at the GSI as the first sc CH linac, a collaboration between GSI, the IAP[31] and the HIM[32] was established.

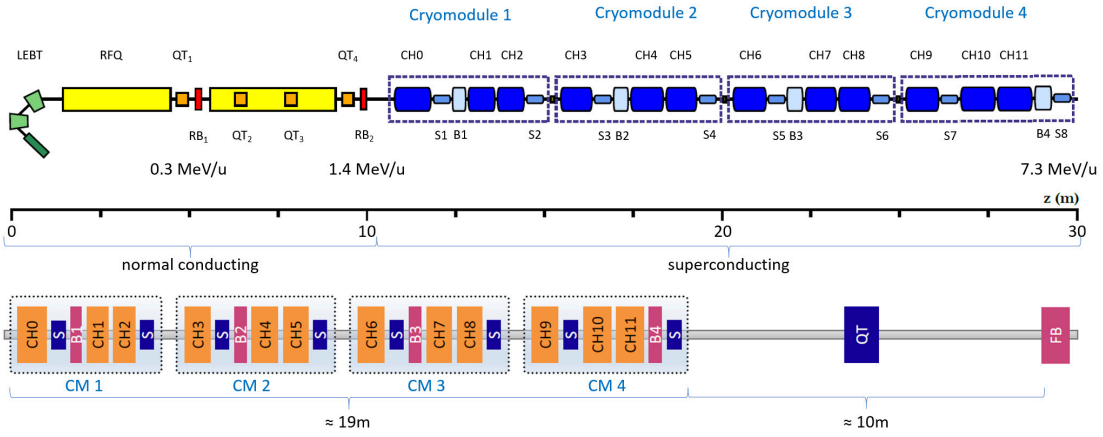

Fig. 5 Schematic diagram of the heavy ion linear accelerator HELIAC. Top: Entire accelerator from source to last cryomodule [24]. Bottom: Superconducting part with subsequent drift and the final buncher [25].

The HELIAC will be filled from a new 28 GHz ECR[33] source and then preaccelerate the ions to 0.3 MeV/u in a normal-conducting cw-capable RFQ, analogous to the HLI [22] (see figure 5). After focusing by a quadrupole magnet and bunching of the beam by a rebuncher cavity, the ions are accelerated to 1.4 MeV/u in a normal conducting IH cavity. Further acceleration takes place in a total of twelve CH cavities, which accelerate the ions at a frequency of 216.816 MHz, which is twice the frequency of the HLI, and a gradient of about 5 – 7.1 MV/m [21] [24].

[30] **C**rossbar **H**-mode
[31] **I**nstitute of **A**pplied **P**hysics, Goethe University Frankfurt
[32] **H**elmholtz-**I**nstitute **M**ainz
[33] **E**lectron **C**yclotron **R**esonance

At a mass-to-charge ratio $A/q \leq 6$, the ions are accelerated from the input energy 1.4 MeV/u to the output energy of 7.3 MeV/u. Thereby, a variable final energy of 3.5 – 7.3 MeV/u should be able to be set at a beam current of 1 mA with an energy width of $< \pm$ 3 keV/u [22]. In the normal-conducting segment of the accelerator, the beam is focused in the transverse planes by a total of four quadropole magnets (QT_1 to QT_4) and in the superconducting segment by eight sc solenoids. The particle bunches are focused in the longitudinal direction by a total of six buncher cavities, with two rebuncher cavities (RB_1, RB_2) in the normal conducting segment and four sc bunchers (B1 to B4) in the superconducting segment. The total length of the accelerator is 30 m, with the superconducting part being about 19 m long. The accelerator is followed by an approximately 10 m normal conducting transport section with a subsequent final buncher (FB). The superconducting section here consists of a total of four cryomodules, in each of which two solenoids, one buncher and three CH cavities (starting at CH0) are cooled with liquid Helium [24].
The first superconducting CH cavity [26] CH0 was created as part of the above-mentioned collaboration in 2009 in the course of the so-called demonstrator project. The cavity consists of 15 acceleration cells. The drift tubes are located in hollow spokes, which are mounted on a so-called girder [27]. In 2017, as part of the demonstrator project, CH0 was tested in a horizontal, variably operational cryostat with two superconducting solenoids, each with 9.5 T, under realistic conditions and was able to successfully accelerate ions [28]. The design of the CH1 and CH2 cavities was further adapted compared to the CH0 design (figure 6). The CH cavities were shortened to a maximum of eight accelerator cells per cavity, and the geometry was also simplified by, among other things, removing the girders, which on the one hand direct the generated magnetic fields better around the spokes but on the other hand reduce the mechanical stability because of a break of the cylindrical symmetry. The simplified geometry of CH1 and CH2 thus increase the mechanical stability of the cavities and should reduce the manufacturing time and possible manufacturing errors [1].

The angular end spokes have also been eliminated, which also increases mechanical stability and makes it possible to use a consistent spoke geometry. The end caps of the cavities have also been changed from a rounded geometry to a conical geometry. As a result, a similar amount of electric as well as magnetic field is displaced when the cavity is evacuated, so the resonant frequency is less affected than with CH0, which has the effect of significantly reducing the pressure sensitivity [1].
In this thesis, a concept for simplifying the design and manufacturing process of superconducting CH cavities is presented, in which the cavities CH3 to CH11 following CH1 and CH2 can be mass produced and thus both the production time and the production costs can be reduced. For this purpose, based on the successfully realized cavities CH1 and CH2, certain components such as the spokes, the lids, the Helium vessels, the dynamic bellow tuner, the static tuner and the flanges were standardized on a unit geometry. The individual cavities were then built modularly

with these standardized components. This novel modular cavity design is thereby different from the classical design process of CH cavities, where each component is customized to the specific cavity. By optimizing the drift tube geometry of each individual cavity, it was possible to optimize performance in terms of reducing peak electric and magnetic fields. In addition, the design of the dynamic bellow tuner was further improved. Finally, a concept for the experimental investigation and characterization of the dynamic bellow tuner with respect to their mechanical properties is presented.

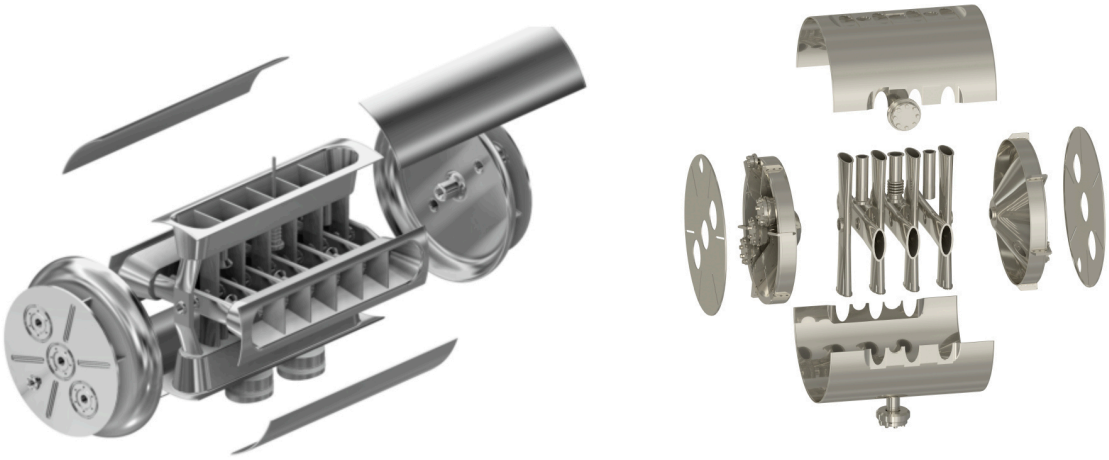

Fig. 6 Exploded view of CH0 (left) [27] compared to CH1/CH2 (right) [1].

2 Theoretical Fundamentals of Superconductivity

At the beginning of the 19th century, it was still controversial how the electrical resistance of metals behaves at low temperatures. Although a dependence of resistance on temperature was already known, three theories were still under discussion for low temperatures. According to the theory of Heinrich Friedrich Ludwig Matthiesen[34], the electrical resistance at decreasing temperatures runs towards a fixed limit. William Lord Kelvin[35], on the other hand, believed that electrical resistance would pass through a minimum at low temperatures and then approach infinity for very low temperatures. The last theory, put forward by Sir James Dewar[36], stated that electrical resistance would go continuously towards zero with decreasing temperature [29].

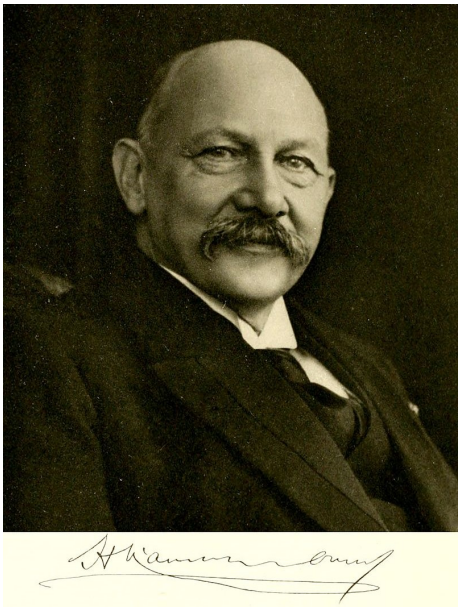

Fig. 7 Heike Kamerlingh Onnes (before 1926) with signature, Nobel laureate in Physics 1913 [30].

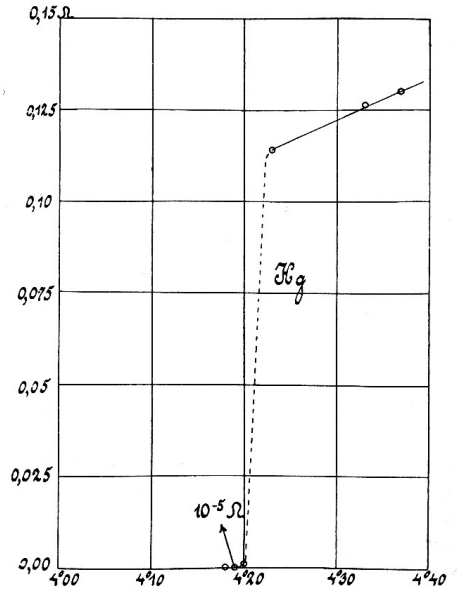

Fig. 8 Historical plot of the disappearing electrical resistance of Mercury (Hg) at low temperatures from 1911 [31].

The Dutch physicist Heike Kamerlingh Onnes[37] (figure 7) presented a talk in which he described how the electrical resistance of a sample of Mercury (Hg) in an experiment in which the sample had been cooled to low temperatures with previ-

[34] ⋆22 September 1830 in Fissau, Germany; †14 November 1906 in Rostock, Germany
[35] ⋆26 June 1824 in Belfast, United Kingdom; †17 December 1907 in Largs, Scotland
[36] ⋆20 September 1842 in Kincardine, Scotland; †27 March 1923 in London, England
[37] ⋆21 September 1853 in Groningen, Netherlands; †21 February 1926 in Leiden, Netherlands

ously liquefied Helium (He) was measured and became immeasurably small below a temperature of 4.2 K. However, contrary to Sir James Dewar's prediction, the resistance did not fall steadily with temperature but abruptly (see figure 8). Onnes himself called this condition superconductivity [29].
Superconductivity, discovered by Onnes in 1911, has a wide variety of applications in modern times, including high-frequency accelerator physics. When designing an accelerator, for example, the fundamental question arises as to whether normal-conducting or superconducting components should be chosen. Probably the clearest advantage of superconducting components over normal conducting ones is the orders of magnitude lower surface resistance and the associated lower power dissipation during operation. However, superconducting components require a tremendous amount of energy to maintain the superconducting state, which offsets the previously mentioned efficiency. Therefore, a generalized decision for superconducting cavities is not recommended. The decision to use one type of structure or another must take into account the particular boundary conditions of the project. These boundary conditions are the desired particle energy, the desired beam power and the necessary duty cycle (see figure 9).

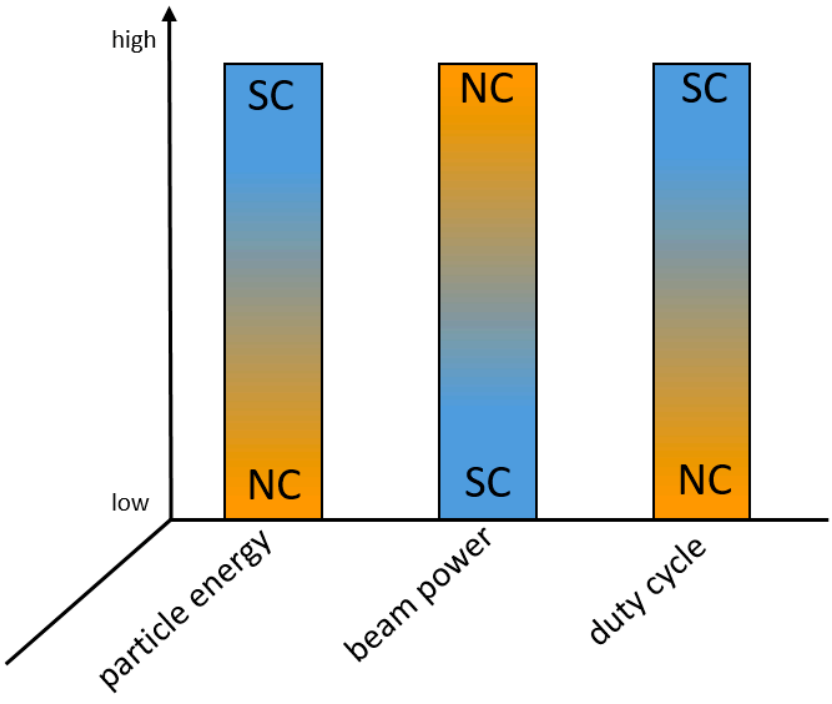

Fig. 9 Schematic representation of the selection criteria whether an accelerator should be planned normal or superconducting. The decisive criteria particle energy, beam power and duty cycle as well as the preferred choice depending on the magnitude are shown.

If particle energy and duty cycle are high and beam power is low, it is advisable to use superconducting components, in the opposite case normal conducting

ones. In large projects, however, the question is often not whether superconducting structures should be used, but at what energy. In the following chapter, superconductivity will be explained in more detail. To this end, the basic properties of superconductivity and the classification into Type I and Type II superconductors will first be explained. A brief theoretical description of superconductivity as well as of the BCS theory[38] is also given. A comprehensive description of superconductivity is beyond the scope of this thesis, for a more detailed and comprehensive description, literature can be consulted [29] [32] [33].

2.1 The Characteristics of Superconductivity

The properties of superconductivity include some magnetic properties in addition to the disappearance of surface resistance above a critical low temperature T_C discovered by Kamerlingh Onnes. The two physicists Fritz Walther Meissner[39] and Robert Ochsenfeld[40] discovered that external magnetic fields are displaced from the interior of the superconductor upon entering the superconducting state at temperatures below T_C [34]. This displacement of the external magnetic field is called the Meissner-Ochsenfeld effect and describes the superconductor as an ideal diamagnet ($\mu_r = 0$). Since, according to this effect, an arbitrarily large magnetic field cannot be displaced from the superconductor, the magnetic field is a limiting quantity of superconductivity in addition to the temperature, so that there exists a critical magnetic field strength H_C in addition to the critical temperature T_C. Whether this is an external magnetic field or a magnetic field generated by a current flowing through the superconductor is irrelevant. The following relationship exists between T_C and H_C: [32]

$$H_C \approx H_C(0) \left[1 - \left(\frac{T}{T_C} \right)^2 \right]. \tag{1}$$

The limiting critical magnetic field generated in the superconductor leads directly to a third limiting parameter, the maximum current within the superconductor and thus to the critical current density j_C. If the three limiting parameters are represented graphically, they span a critical area within which the material under consideration is in superconducting state (figure 10).

[38] named after John **B**ardeen, Leon Neil **C**ooper and John Robert **S**chrieffer; they recieved the Nobel Prize in Physics for their theory in 1972

[39] ⋆16 December 1882 in Berlin, Germany; †15 November 1974 in Munich, Germany

[40] ⋆18 May 1901 in Helberhausen, Germany; †5 December 1993 in Helberhausen, Germany

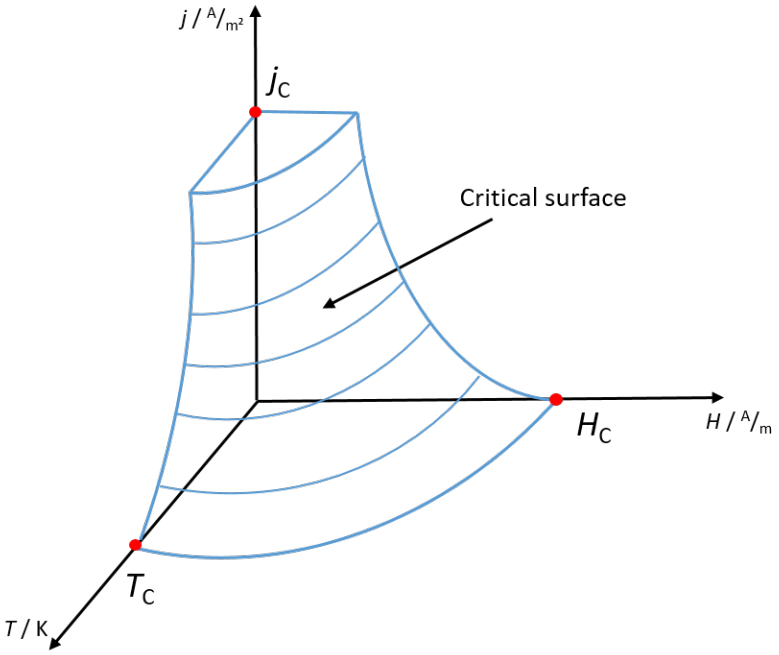

Fig. 10 Graphical representation of the critical surface and the parameters critical temperature T_C, critical magnetic field H_C and critical current density j_C.

A closer look, however, reveals that the displacement does not take place completely, since this would result in an infinitely high current density at the surface of the superconductor. The brothers Fritz Wolfgang London[41] and Heinz London[42] described the Meissner-Ochsenfeld effect theoretically in 1935 [35]. With the London equations named after them [29]

$$\frac{\partial}{\partial t}\vec{j}_s = \frac{n_s e^2}{m_e}\vec{E}; \quad \vec{\nabla} \times \vec{j}_s = -\frac{n_s e^2}{m_e}\vec{B} \tag{2}$$

and the Maxwell's equations

$$\vec{\nabla} \cdot \vec{E} = \frac{\vec{\rho}}{\epsilon_0} \tag{3}$$

$$\vec{\nabla} \cdot \vec{B} = 0 \tag{4}$$

$$\vec{\nabla} \times \vec{E} = -\frac{\partial \vec{B}}{\partial t} \tag{5}$$

$$\vec{\nabla} \times \vec{B} = \mu_0 \vec{j} + \mu_0 \epsilon_0 \frac{\partial \vec{E}}{\partial t} \tag{6}$$

results

$$\vec{\nabla}^2 \vec{B} = \mu_0 \epsilon_0 \frac{\partial \vec{B}^2}{\partial t^2} + \frac{n_s \mu_0 e^2}{m_e}\vec{B}. \tag{7}$$

[41] ⋆7 March 1900 in Breslau, Germany; †30 March 1954 in Durham, USA
[42] ⋆7 November 1907 in Bonn, Germany; †3 August 1970 in Oxford, United Kingdom

Since in good conductors $\mu_0\epsilon_0 << n_s\mu_0 e^2/m_e$ holds, (7) can be further simplified to

$$\vec{\nabla}^2\vec{B} = \frac{n_s\mu_0 e^2}{m_e}\vec{B} = \frac{1}{\lambda_L^2}\vec{B}. \tag{8}$$

The first solution of this differential equation would be a constant magnetic field, but this can be discounted by the Meissner-Ochsenfeld effect. The second solution of this equation indicates that an external magnetic field inside a superconductor decays exponentially. The quantity describing the depth from which the magnetic field has decayed to the e-th part is called London's penetration depth λ_L [35]
.

$$\lambda_L = \sqrt{\frac{m_e}{n_s\mu_0 e^2}}. \tag{9}$$

Where here m_e corresponds to the mass of the electron pairs, e to the elementary charge and n_s to the density of the superconducting charge carriers. The magnitude of λ_L is typically a few 10 nm. This definition of λ_L from (9) is valid only for temperatures close to 0 K. For higher temperatures up to the critical temperature T_C applies: [32]

$$\lambda_L(T) \approx \frac{\lambda_L(0)}{\sqrt{1-\left(\frac{T}{T_C}\right)^4}} \quad \forall T \text{ in } (0 < T \leq T_C). \tag{10}$$

Where here $\lambda_L(0)$ is the London penetration depth at 0 K. Tab. 2 gives examples for some superconducting elements critical temperature T_C, critical magnetic flux density B_C, London penetration depth λ_L and Ginzburg-Landau coherence length ξ_{GL} (see section 2.3).
The phenomenon of superconductors occurs in a variety of elements of the periodic table, with Niobium having the highest critical temperature of 9.2 K among all elements. In addition, the critical magnetic field strength of Niobium is quite high at 0.195 T, due to the fact that Niobium is a so-called Type II superconductor. The classification into Type I and Type II superconductors and their differences will be discussed in more detail in the following section. These two quite high critical limits, as well as the property that Niobium is well formable and thus its processability is high, make Niobium so suitable for the fabrication of accelerator components. To optimally enhance the performance of accelerator components fabricated from Niobium, it is advisable to use the purest Niobium possible. One measure of the purity of superconducting materials is the residual resistance ratio (RRR). This value sets the resistance of the material at room temperature[43] $R_{300\,K}$ in relation to the resistance of the material in the normal conducting state immediately above the critical temperature T_C (R_{T_C})

[43] Temperature of 300 K. This corresponds to a temperature of 26.85 °C

Tab. 1 A selection of different superconducting elements used in engineering. Listed are the critical temperature T_C, the critical magnetic field B_C, the London penetration depth λ_L and the superconducting coherence length ξ_{GL} [29].

Element	T_C in K	B_C in T	λ_L in nm	ξ_{GL} in nm
Aluminium (Al)	1.18	0.01	50	1600
Mercury (Hg)	4.15	0.04		55
Niobium (Nb)	9.2	0.195	32-44	39-40
Lead (Pb)	7.2	0.08	32-39	51-83
Tantalum (Ta)	4.4	0.08	35	93
Tungsten (W)	0.01	$1.24{\cdot}10^{-4}$		

$$RRR = \frac{R_{300\,\mathrm{K}}}{R_{T_C}} \tag{11}$$

Starting at a RRR of about 300, one can already speak of high-purity Niobium, with the theoretical achievable maximum being $RRR = 35000$ [36].

2.2 The Classification in Type I and II

The classification of superconductors into Type I and Type II is based on the behavior of the material with respect to the magnetization M in an external magnetic field H_e. A superconductor of Type I completely displaces the field from its interior ($H_i = 0$) below the critical magnetic strength H_C according to the Meissner-Ochsenfeld effect as described above, except for a thin boundary layer. This regime is also described as the Meissner-phase. If H_e increases, the current generated in the surface of the superconductor also increases and thus M, so that the interior of the superconductor remains field-free. If H_e exceeds the critical value H_C the material is no longer magnetizable and H_i jumps to the value of H_e (see figure 11). The superconductor becomes normal conducting [32].

In contrast to a Type I superconductor, a Type II superconductor has two critical magnetic field strengths H_{C1} and H_{C2}. The behavior is analogous to that of the Type I superconductor up to H_{C1}. M increases until H_e reaches the value of H_{C1} and causes the interior to be field-free (Meissner-phase). Once H_{C1} is exceeded, the magnetic field penetrates the superconductor so that the internal magnetic field H_i increases while M decreases. This phase, where $H_{C1}<H_e<H_{C2}$, is called the mixed phase or Shubnikov-phase. Once H_{C2} has been exceeded, the material is no longer

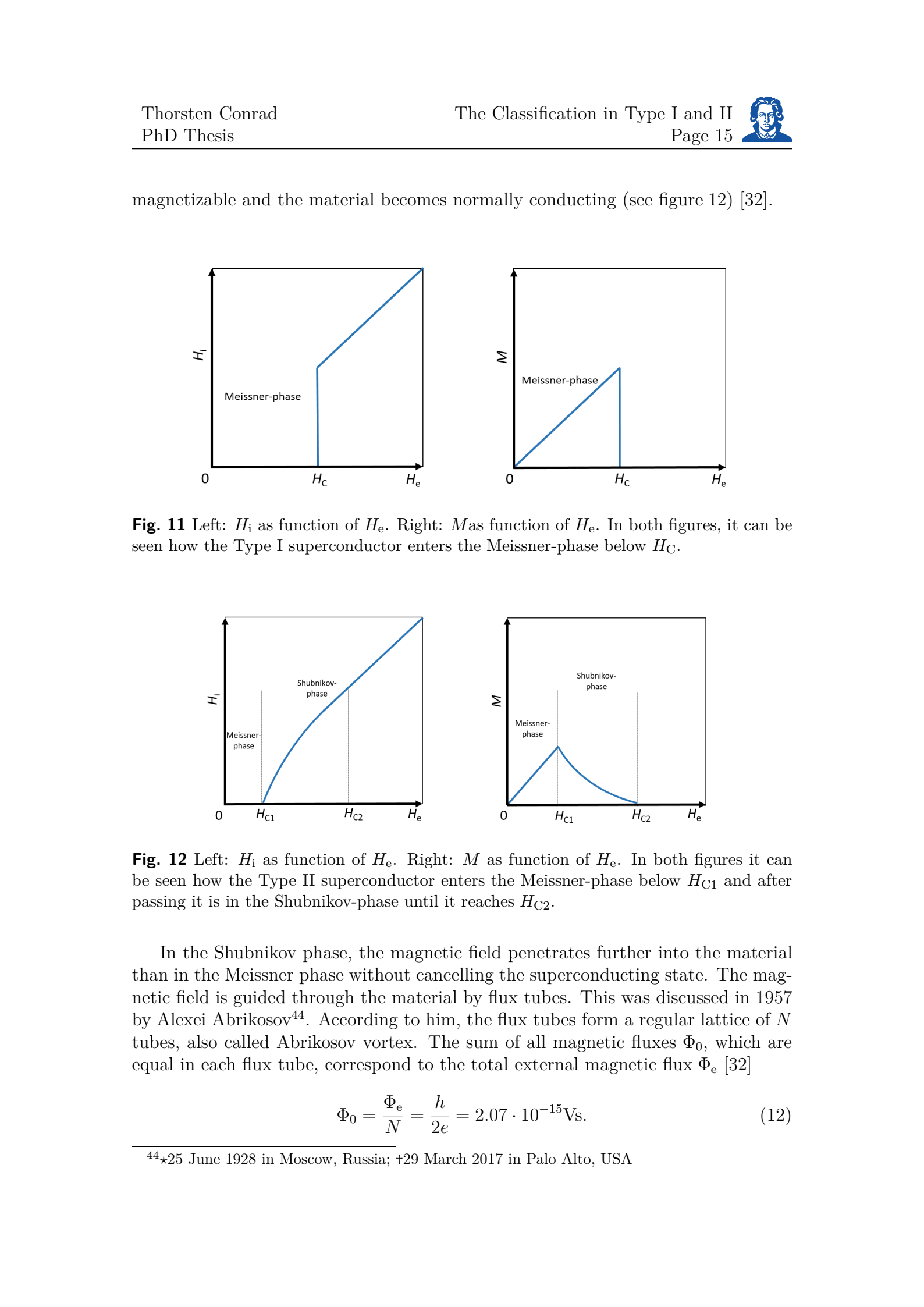

magnetizable and the material becomes normally conducting (see figure 12) [32].

Fig. 11 Left: H_i as function of H_e. Right: Mas function of H_e. In both figures, it can be seen how the Type I superconductor enters the Meissner-phase below H_C.

Fig. 12 Left: H_i as function of H_e. Right: M as function of H_e. In both figures it can be seen how the Type II superconductor enters the Meissner-phase below H_{C1} and after passing it is in the Shubnikov-phase until it reaches H_{C2}.

In the Shubnikov phase, the magnetic field penetrates further into the material than in the Meissner phase without cancelling the superconducting state. The magnetic field is guided through the material by flux tubes. This was discussed in 1957 by Alexei Abrikosov[44]. According to him, the flux tubes form a regular lattice of N tubes, also called Abrikosov vortex. The sum of all magnetic fluxes Φ_0, which are equal in each flux tube, correspond to the total external magnetic flux Φ_e [32]

$$\Phi_0 = \frac{\Phi_\mathrm{e}}{N} = \frac{h}{2e} = 2.07 \cdot 10^{-15}\mathrm{Vs}. \tag{12}$$

[44]⋆25 June 1928 in Moscow, Russia; †29 March 2017 in Palo Alto, USA

The interior of the flux tubes is normal conducting, while the remaining material is superconducting. The magnetic flux enclosed by the flux tubes decreases along a length the magnitude of the coherence length ξ_0. If H_e increases, the density of the flux tubes also increases, until at $H_e = H_{C2}$ the entire material is interspersed with flux tubes and superconductivity has collapsed.

In summary, figure 13 shows how a superconductor behaves in a magnetic field. Far left is the normal conducting state shown, when the material is completely penetrated by the magnetic field. Second picture from the left shows the Meissner-phase which exists in both Type I and Type II superconductors. The magnetic field is displaced into a small layer on the surface. The third picture displays the Shubnikov-phase. It only occurs in Type II superconductors. The magnetic field can penetrate the material through so-called Abrikosov vortexes. On the far right the magnetic field is above H_{C2}, both Type I and Type II superconductors are completely penetrated by the magnetic field and the superconductivity collapses [32].

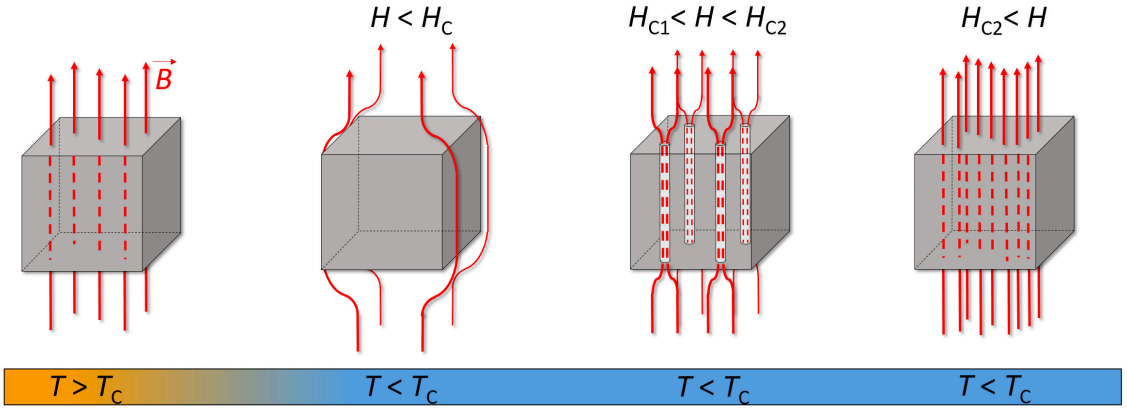

Fig. 13 Schematic representation of a superconductor penetrated by a magnetic field once in the normal state ($T > T_C$) and in the superconducting state ($T < T_C$).

The value of H_{C2} limiting Type II superconductors can be significantly larger than H_C for Type I superconductors, which is what makes Type II superconductors, like Niobium, so interesting for building accelerator components. A parameter describing the classification between Type I and Type II superconductors is the Ginzburg-Landau parameter κ, which relates the coherence length ξ_0 (see section 2.3) and the London penetration depth λ_L [37]. The classification is as followed:

$$\text{Type I: } \kappa = \frac{\lambda_L}{\xi_0} < \frac{1}{\sqrt{2}} \qquad \text{Type II: } \kappa = \frac{\lambda_L}{\xi_0} > \frac{1}{\sqrt{2}} \tag{13}$$

2.3 The Bardeen Cooper Schrieffer Theory

A theoretical description of superconductivity was established in 1957 by John Bardeen[45], Leon Neil Cooper[46] and John Robert Schrieffer[47], who were also awarded the Nobel Prize in Physics in 1972 [38]. This theory is based on the observation made experimentally in the 1950s that there is a dependence

$$T_{\mathrm{C}} \propto \frac{1}{\sqrt{M}} \tag{14}$$

between the transition temperature T_{C} and the atomic mass M of the metal isotope. From this dependence it was concluded that there must exist a connection between superconductivity and the mass-dependent lattice oscillations[48]. For simplification, one can imagine a lattice of the atomic nuclei in the material, which initially do not move but are not completely stiffly bound to their position. If there is an electron between the positively charged atomic nuclei, it attracts them, causing them to move slightly out of their original position, so that the lattice is polarized at this deformed point by the accumulation of the atomic nuclei. A second electron is affected by this deformation. There is an attraction of the second electron by the first electron via the lattice polarization. The energy transfer of the first electron to the lattice is equal to the energy transfer of the lattice to the second electron and must be larger than the Coulomb repulsion between them. To realize this condition, both the electrons and the atomic nuclei must move sufficiently slowly, which is true at low temperatures below T_{C} [29].

If one now extends the model by an electron moving through the lattice of the atomic nuclei, a track of polarization within the lattice is created. Due to the inertia of the atomic nuclei, this deformation within the track of the lattice persists for a certain time of

$$\tau \approx \frac{2\pi}{\omega_{\mathrm{D}}} \approx 10^{-13} s. \tag{15}$$

Here ω_{D} is the so-called Debye frequency, which indicates the oscillation frequency of the atomic lattice. Also, the distance between the electrons must not be arbitrarily large, otherwise the effect of the lattice polarization would decrease too much. The largest possible distance between the electrons is called the coherence length ξ_0 [32].

$$\xi_0 = \frac{\hbar v_{\mathrm{F}}}{k_{\mathrm{B}} T_{\mathrm{C}}} \tag{16}$$

Where $\hbar$ is the Planck constant, v_{F} is the Fermi velocity, and k_{B} is the Boltzmann constant. The order of magnitude of the coherence length is a few 100 to 1000 nm.

[45] ⋆23 May 1908 in Madison, USA; †30 January 1991 in Boston, USA
[46] ⋆28 February 1930 in New York City, USA
[47] ⋆31 May 1931 in Oak Parks, USA; †27 July 2019 in Tallahassee, USA
[48] If a lattice oscillation is considered quantized, it is also referred to as a phonon

Compared to the average spatial distance between two conduction electrons, which is a few 0.1 nm, the coherence length is much larger, so that the pairs of electrons overlap strongly. In the region of a pair lie 10^6 to 10^7 of unbound electrons. New pairs of electrons are constantly forming and existing ones are breaking up, so that the formation of pairs of electrons represents a dynamical system [29].
In the case of moving electrons there are two possibilities. First, both electrons could move with the same momentum $\vec{p}$, so that both form a so-called electron pair, whose momentum is exactly equal to the double of the momentum of each electron ($\vec{p_1} = \vec{p_2}$). In the second case, both electrons move with exactly opposite momentum, so that $\vec{p_1} = -\vec{p_2}$ applies. Such a pair has therefore the total momentum of 0 and is called Cooper pair (see figure 14), since Cooper could prove that such a coupling of the electrons leads to a lowering of the total energy [29].

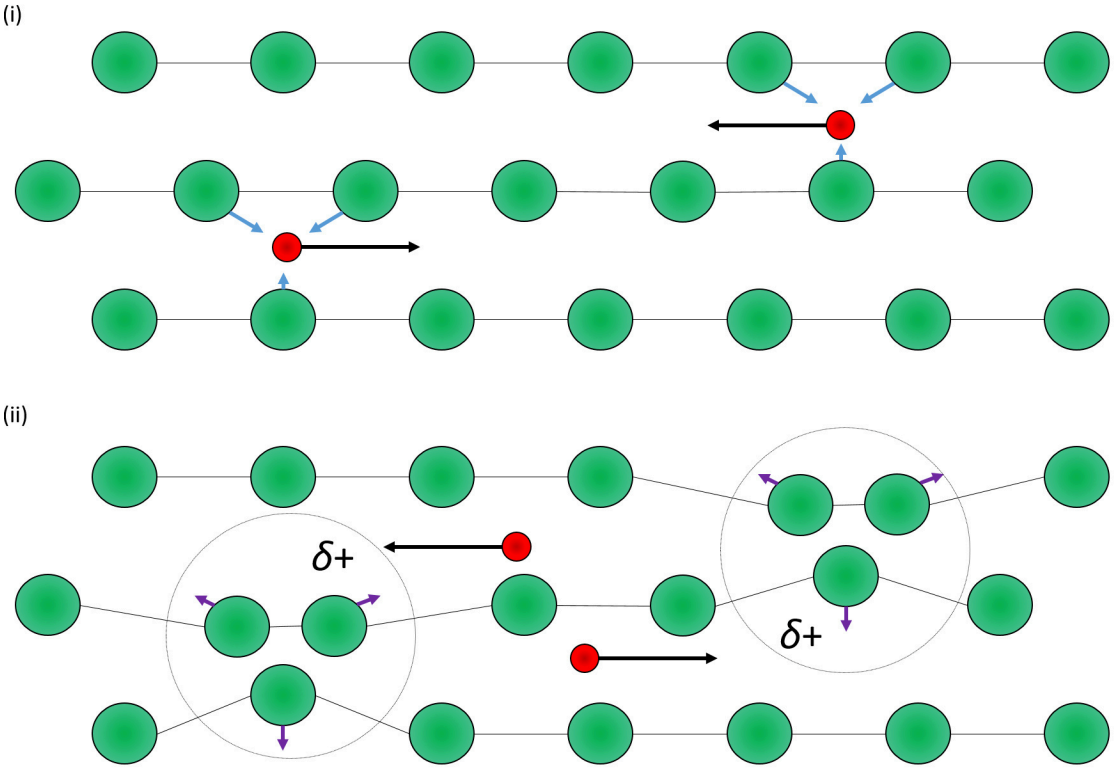

Fig. 14 Schematic representation of the formation of a Cooper pair. The positive atomic nuclei are shown in green, the electrons in red, the impulses of the electrons in black, the blue arrows represent the coulomb attraction and the purple arrows the coulomb repulsion.

Taking further into account the intrinsic angular momentum, also called spin, a Cooper pair consists of two electrons that have equal momentum in opposite directions and opposite spin.

$$\{\vec{p}\uparrow, -\vec{p}\downarrow\} \tag{17}$$

The total spin of the Cooper pair is therefore integer, which means that it belongs to the bosons and is therefore no longer subject to the Pauli principle and can occupy the quantum mechanical ground state. On the one hand, the correlation of the Cooper pair is energetically more favourable than that of the electron pair with respect to the polarization of the positive lattice [29]. On the other hand, a Cooper pair is thereby subject to the Bose-Einstein wave function for interaction-free particles. A Cooper pair therefore no longer interacts with the phonons of the atomic lattice and can move unhindered through the metal, which causes resistance-free charge transport and thus explains the characteristic of vanishing electrical resistance in superconductors [33].

Only at a temperature of $T = 0$ all electrons are coupled in Cooper pairs. At a temperature $T > 0$, the number of unpaired electrons increases with temperature according to $\exp(\frac{\Delta}{k_\mathrm{B}T})$ [32]. Here Δ corresponds to the energy gap between the Cooper pairs and the unpaired electrons. If a DC voltage is applied to the superconductor, the charge transport within the superconductor takes place exclusively through the Cooper pairs. In the case of an AC voltage, however, the increased inertia of the Cooper pairs due to their increased mass ($2m_\mathrm{e}$) causes a delay between the electric field and the motion of the Cooper pairs, so that the unpaired electrons are not fully shielded and contribute to the charge transport. From this follows the surface resistance R_s of the superconductor according to BCS theory, which depends on the number of unpaired electrons:

$$R_\mathrm{s,BCS} = A\omega^2 e^{(\frac{\Delta}{k_\mathrm{B}T})} \tag{18}$$

Where ω corresponds to the frequency of the AC voltage and A to the material constant of the material used. Usually values for $R_\mathrm{s,BCS}$ are in the range of some 10^{-8} to 10^{-9} Ω [32].

3 Physical Principles of RF CH Cavities

In the following section, the physical principle of a CH cavity will be explained in more detail. For this purpose, a classical cylindrical cavity resonator is first assumed, since the CH cavity is based on a cylindrical tank with integrated components. These components include spokes and drift tubes as well as static and dynamic tuner, which will be discussed in more detail later in this thesis (see section 8). The spokes in the cavity are arranged alternately rotated by 90° (crossed), which is also the reason for the C of the acronym in CH, which stands for crossbar. The H stands for H-mode, which indicates the direction of propagation of the magnetic field. Thus, the CH belongs to the resonators in which the H-mode (or TE[49]-mode) is used as operating mode, to be more precise the H_{211}-mode (see section 3.1). The CH cavity was developed at the IAP of the Goethe University Frankfurt in 1998 [39]. Another representative of the H-mode resonators is the IH-cavity, which was developed before. The spokes of the IH cavity run alternately on the upper and lower side of the cavity. The CH is a further development of the IH. Figure 15 shows the geometric differences between these two structures.

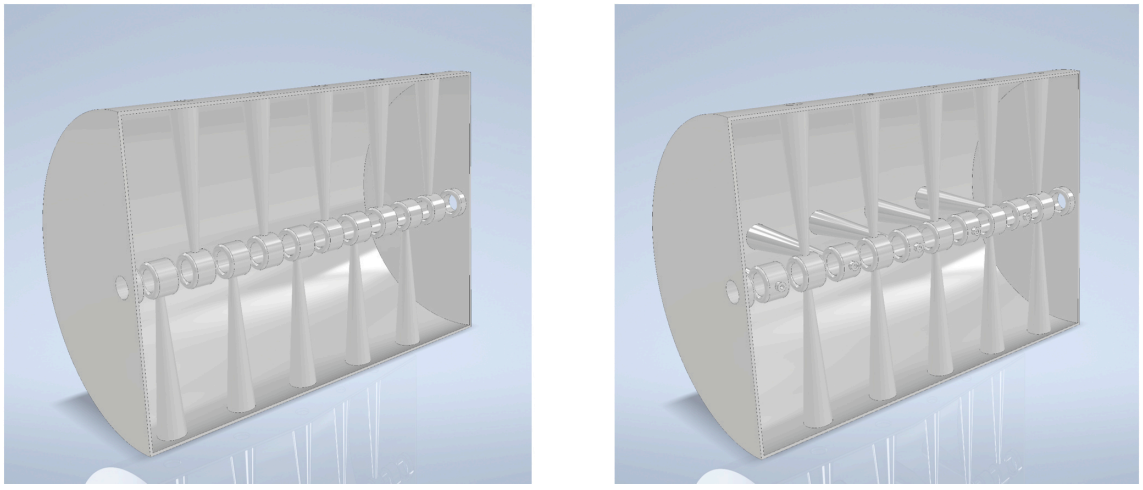

Fig. 15 Two simple examples of an IH cavity (left) and a CH cavity (right) designed with CST Studio Suite and rendered in Autodesk Inventor 2020. It can be seen that the difference is in the spoke geometry and the rotated arrangement.

Due to this modified spoke geometry, the CH cavity has a few key advantages over the IH cavity in the context of superconducting accelerator technology. For one, cooling the spokes and drift tubes is easier in a CH cavity because the liquid Helium can flow completely through the spokes, whereas in an IH cavity it must flow both in and out through the same spoke foot, which can cause turbulence. On the other hand, a CH cavity is mechanically more stable due to the continuous and

[49] **T**ransversal **E**lectric

alternately rotated spokes, which helps to reduce frequency fluctuations due to external influences in superconducting cavities, which are often very thin-walled (the wall thickness is only a few mm).

3.1 Field distribution within a CH Cavity

The field distribution inside a cavity resonator, which includes both IH and CH cavities, can be derived using Maxwell's equations [(3), (4), (5), (6)]. However, to simplify the next calculation steps, they are considered in vacuum and in a charge-free space[50]. This leads to the four Maxwell equations in form of

$$\vec{\nabla} \cdot \vec{E} = 0 \tag{19}$$

$$\vec{\nabla} \cdot \vec{B} = 0 \tag{20}$$

$$\vec{\nabla} \times \vec{E} = -\frac{\partial \vec{B}}{\partial t} \tag{21}$$

$$\vec{\nabla} \times \vec{B} = \mu_0 \epsilon_0 \frac{\partial \vec{E}}{\partial t}. \tag{22}$$

By rotating (21) and (22), the wave equations for the electric (23) and magnetic (24) fields in vacuum follow. Here applies for the electric field

$$\vec{\nabla}^2 \vec{E} - \frac{1}{c^2} \frac{\partial^2 \vec{E}}{\partial t^2} = 0 \tag{23}$$

and for the magnetic field

$$\vec{\nabla}^2 \vec{B} - \frac{1}{c^2} \frac{\partial^2 \vec{B}}{\partial t^2} = 0. \tag{24}$$

These two equations are homogeneous, linear partial differential equations of the 2nd order. However, they can only be solved for simple special cases and are therefore unsuitable for a realistic consideration of a CH cavity. Numerical programs such as CST Microwave Studio [40], though, can simulate a real cavity in an approximated way. For simple structures such as rectangular or circular wave guides and rectangular or circular cylindrical cavity resonators, the wave equation can be solved analytically. A circular cylindrical cavity resonator with radius R_C and length L is first considered to approximately derive the field distribution of a CH cavity, since these two structures have the most in common. Due to the cylindrical symmetry of the cavity resonator, a consideration in cylindrical coordinates (ρ, ϕ, z) is appropriate. For the examination the boundary conditions

[50] $\rho(x) = 0 \; \forall \vec{x}$, $\vec{j}(x) = 0 \; \forall \vec{x}$

$$E_\phi = E_z = 0\Big|_{\rho=R_C} \tag{25}$$

$$E_\phi = E_\rho = 0\Big|_{z=0,z=L} \tag{26}$$

$$B_\rho = \frac{\partial B_z}{\partial z}\Big|_{\rho=R_C} \tag{27}$$

$$B_z = 0\Big|_{z=0,z=L} \tag{28}$$

are considered. These boundary conditions represent the conducting walls of the resonator at the locations $\rho = R_C$, $z = 0$ and $z = L$. A distinction is made between solutions which have only transverse magnetic field components ($B_z = 0$), also called TM or electric E-modes, and solutions which inversely have only transverse electric field components ($E_z = 0$), also called TE or magnetic H-modes. Considering the field distribution within the circular-cylindrical cavity resonator in cylindrical coordinates, transverse (ρ, ϕ) and longitudinal (z) field components are obtained. The transverse field strengths $(E_\rho, E_\phi, B_\rho, B_\phi)$ can be fully expressed by the longitudinal field strengths (E_z, B_z).

$$E_\rho = \frac{1}{\frac{\omega^2}{c^2} - k_z^2} \cdot \left[\frac{\partial^2 \vec{E_z}^2}{\partial\rho\partial z} - \frac{i\omega}{\rho} \frac{\partial \vec{B_z}}{\partial\phi} \right] \tag{29}$$

$$B_\rho = \frac{1}{\frac{\omega^2}{c^2} - k_z^2} \cdot \left[\frac{\partial^2 \vec{B_z}^2}{\partial\rho\partial z} - \frac{i\omega}{\rho c^2} \frac{\partial \vec{E_z}}{\partial\phi} \right] \tag{31}$$

$$E_\phi = \frac{1}{\frac{\omega^2}{c^2} - k_z^2} \cdot \left[\frac{1}{\rho} \frac{\partial^2 \vec{E_z}^2}{\partial\phi\partial z} - i\omega \frac{\partial \vec{B_z}}{\partial\rho} \right] \tag{30}$$

$$B_\phi = \frac{1}{\frac{\omega^2}{c^2} - k_z^2} \cdot \left[\frac{1}{\rho} \frac{\partial^2 \vec{B_z}^2}{\partial\phi\partial z} - \frac{i\omega}{c^2} \frac{\partial \vec{E_z}}{\partial\rho} \right] \tag{32}$$

It can be seen that a determination of the longitudinal components of (23) and (24) is sufficient. The propagation direction of the standing wave is in z-direction due to the choice of the cylindrical coordinates. With the solution approaches

$$\vec{E}(\rho, \phi, z, t) = \vec{E}(\rho, \phi) e^{\pm i k_z z} e^{i\omega t} \tag{33}$$

for the electric and

$$\vec{B}(\rho, \phi, z, t) = \vec{B}(\rho, \phi) e^{\pm i k_z z} e^{i\omega t}, \tag{34}$$

for the magnetic field, the wave equations (23) and (24) and the boundary conditions (25) to (28), E_z and B_z and hence E_ρ, E_ϕ, B_ρ, and B_ϕ can be calculated with (29) to (32). The analytical solutions for the TM and E-modes, respectively, where $B_z = 0$ hold are:

$$\vec{E}_z(\rho,\phi,z,t) = E_0 J_m\left(\frac{x_{mn}}{R_\mathrm{C}}\rho\right) cos(m\phi) cos\left(\frac{p\pi}{L}z\right) e^{i\omega t} \tag{35}$$

$$\vec{E}_\rho(\rho,\phi,z,t) = -\frac{p\pi R_\mathrm{C}}{L x_{mn}} E_0 J'_m\left(\frac{x_{mn}}{R_\mathrm{C}}\rho\right) cos(m\phi) sin\left(\frac{p\pi}{L}z\right) e^{i\omega t} \tag{36}$$

$$\vec{E}_\phi(\rho,\phi,z,t) = \frac{p\pi m R_\mathrm{C}^2}{L\rho x_{mn}^2} E_0 J_m\left(\frac{x_{mn}}{R_\mathrm{C}}\rho\right) sin(m\phi) sin\left(\frac{p\pi}{L}z\right) e^{i\omega t} \tag{37}$$

$$\vec{B}_z(\rho,\phi,z,t) = 0 \tag{38}$$

$$\vec{B}_\rho(\rho,\phi,z,t) = -\frac{i\omega R_\mathrm{C}^2}{x_{mn}^2 c^2 \rho} E_0 J_m\left(\frac{x_{mn}}{R_\mathrm{C}}\rho\right) sin(m\phi) cos\left(\frac{p\pi}{L}z\right) e^{i\omega t} \tag{39}$$

$$\vec{B}_\phi(\rho,\phi,z,t) = \frac{i\omega R_\mathrm{C}}{x_{mn} c^2} E_0 J'_m\left(\frac{x_{mn}}{R_\mathrm{C}}\rho\right) cos(m\phi) cos\left(\frac{p\pi}{L}z\right) e^{i\omega t} \tag{40}$$

Here E_0 represents the amplitude of the electric field, J_m the Bessel function of the first type and m-th order, x_{mn} the n-th zero of the Bessel function as well as J'_m the derivative of the Bessel function and x'_{mn} its n-th zero [41]. The respective modes are named after the corresponding indices m, n and p. These give the number of nodes and antinodes of the field component E_z along a given coordinate. The resonant frequency of the TM mode is calculated by

$$f_0^\mathrm{TM} = c\sqrt{\left(\frac{x_{mn}}{2\pi R_\mathrm{C}}\right)^2 + \left(\frac{p}{2L}\right)^2}. \tag{41}$$

3.1.1 The CH cavity operation mode

The operating mode of CH, H_{211}, is a TE or H-mode, where $E_z = 0$ holds. The analytical solutions for this case are:

$$\vec{B}_z(\rho,\phi,z,t) = B_0^* J_m\left(\frac{x'_{mn}}{R_\mathrm{C}}\rho\right) cos(m\phi) sin\left(\frac{p\pi}{L}z\right) e^{i\omega t} \tag{42}$$

$$\vec{B}_\rho(\rho,\phi,z,t) = \frac{p\pi R_\mathrm{C}}{L x'_{mn}} B_0^* J'_m\left(\frac{x'_{mn}}{R_\mathrm{C}}\rho\right) cos(m\phi) cos\left(\frac{p\pi}{L}z\right) e^{i\omega t} \tag{43}$$

$$\vec{B}_\phi(\rho,\phi,z,t) = -\frac{p\pi m R_\mathrm{C}^2}{L\rho x'^2_{mn}} B_0^* J_m\left(\frac{x'_{mn}}{R_\mathrm{C}}\rho\right) sin(m\phi) cos\left(\frac{p\pi}{L}z\right) e^{i\omega t} \tag{44}$$

$$\vec{E}_z(\rho,\phi,z,t) = 0 \tag{45}$$

$$\vec{E}_\rho(\rho,\phi,z,t) = -\frac{i\omega m R_\mathrm{C}^2}{x'^2_{mn}\rho} B_0^* J_m\left(\frac{x'_{mn}}{R_\mathrm{C}}\rho\right) sin(m\phi) sin\left(\frac{p\pi}{L}z\right) e^{i\omega t} \tag{46}$$

$$\vec{E}_\phi(\rho,\phi,z,t) = \frac{i\omega R_\mathrm{C}}{x'_{mn}} B_0^* J'_m\left(\frac{x'_{mn}}{R_\mathrm{C}}\rho\right) cos(m\phi) sin\left(\frac{p\pi}{L}z\right) e^{i\omega t} \tag{47}$$

Here B_0^* is a quantity proportional to the amplitude of the magnetic field and J_m, x_{mn}, J'_m, x'_{mn} are analogous to the TM mode solutions, the Bessel function, its zeros,

the derivative of the Bessel function and its zeros [41]. However, here the indices m, n and p, after which the modes are named, describe the number of nodes and antinodes, respectively, of the field component B_z. The frequency of a TE mode is calculated from

$$f_0^{\mathrm{TE}} = c\sqrt{\left(\frac{x'_{mn}}{2\pi R_{\mathrm{C}}}\right)^2 + \left(\frac{p}{2L}\right)^2}. \tag{48}$$

As can be seen in (45), the operating mode of the CH cavity has no electric field component in the z-direction, which is, however, necessary for the acceleration of charged particles inside the cavity. For this reason, spokes with enclosed drift tubes are installed in the cavity to generate an electric field component in the z-direction. As a result, the time-dependent, longitudinal magnetic field induces a potential difference in the tank quarters between two neighbouring spokes.

$$U_{\mathrm{ind}} = -\frac{d\Phi}{dt} = -\int_A \frac{dB}{dt} dA \tag{49}$$

Between the drift tubes embedded in the spokes, an electric field is formed whose polarity changes. The drift tubes serve to focus the electric field on the beam axis (see figure 16).

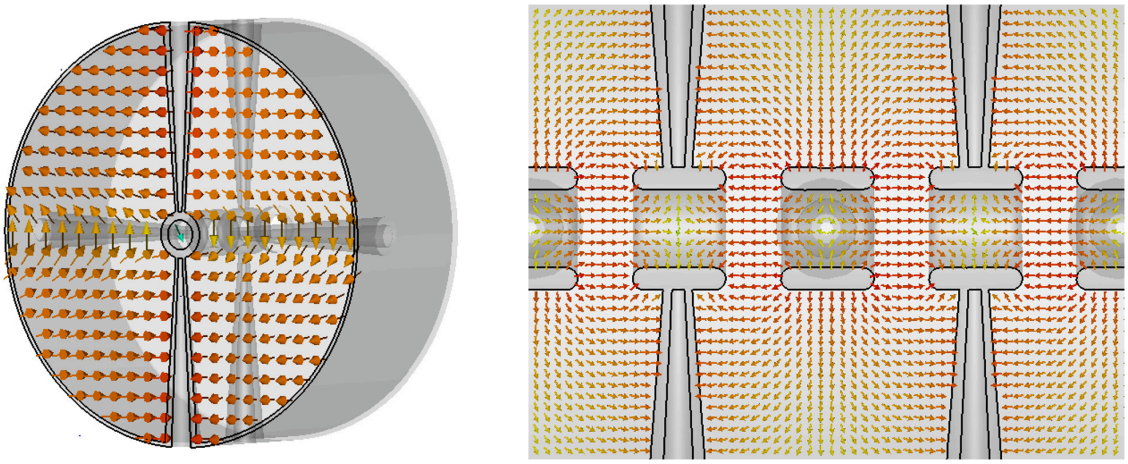

Fig. 16 Simulated magnetic (left) and electric (right) field of the H_{211}-mode of a CH cavity.

Since after (28) the magnetic field component B_z must vanish completely, no real zero mode H_{mn0} can exist. However, since a homogeneous E_z component would be preferable for the acceleration of charged particles, a pseudo-zero mode $H_{21(0)}$ is generated by adjusting the lengths of the drift tubes and tank caps in such a way that a homogeneous field distribution is achieved by the capacitive loading.

3.1.2 The Slater Perturbation Theorem

The resonant frequency of the cavity f_0 can still be influenced during operation by changing the cavity geometry. For this purpose, for example, dynamic tuners are moved into or out of the cavity, or external forces slightly deform the cavity walls, as in the case of elliptical Tesla cavities. Consequently, a change in the internal volume V of the resonator body causes a frequency change Δf_0. To be able to explain this circumstance, the classical harmonic oscillator is considered first. This is invariant to adiabatic change, which in this case does not correspond to the thermodynamic description of a time rapid change of state, but to the fact that the frequency change occurring due to the volume change is several orders of magnitude smaller than the resonance frequency itself. The constant energy, which is stored in a classical oscillator is given by [41]

$$H(p,q) = W = \frac{p^2}{2m} + \frac{m\omega_0^2 q^2}{2}. \tag{50}$$

Here p corresponds to the momentum, m to the mass and q to the displacement. The energy within the system is preserved, so that q and p span an ellipse, whose area is constant and the semi-axes are q_0 and p_0. These semiaxes are calculated from [41]

$$q_0 = \sqrt{\frac{2W}{m\omega_0}} \quad \text{and} \quad p_0 = \sqrt{2mW}. \tag{51}$$

This gives the constant area of the ellipse A to

$$A = \pi \cdot p_0 \cdot q_0 = \pi \cdot \sqrt{\frac{4mW^4}{m \cdot (2\pi f_0)^2}} = \frac{W}{f_0} \quad \text{with} \quad \omega_0 = 2\pi f_0. \tag{52}$$

A change of the stored energy ΔW thus causes a change of the frequency Δf_0 for a constant area A.

$$\Delta W = A \cdot \Delta f_0 = \frac{W \cdot \Delta f_0}{f_0} \;\Rightarrow\; \frac{\Delta W}{W} = \frac{\Delta f_0}{f_0}. \tag{53}$$

This is called the Boltzmann-Ehrenfest theorem[51] and applies to both mechanical oscillators and electromagnetic resonators [41]. In an electromagnetic resonator, such as a CH cavity, the stored energy W is equally distributed on time average between the stored, electric energy W_e and the stored, magnetic energy W_m (see section 3.2.3). The stored energy thus oscillates between the electric and magnetic fields. If, for example, a dynamic tuner is moved into or out of the resonator, it causes a change of the resonator volume by ΔV. Depending on the position of the tuner, either W_e or W_m is changed more strongly, and in each case there is a change

[51] named after Ludwig Eduard Boltzmann (⋆20 February 1844 in Vienna, Austria; †5 September 1906 in Duino, Italy) and Paul Ehrenfest (⋆18 January 1880 in Vienna, Austria; †25 September 1933 in Amsterdam, Netherlands)

in the resonant frequency Δf_0 until the equilibrium between the two stored energies has been restored. Depending on whether the electric field or the magnetic field has been influenced in several parts, a distinction is made between capacitive and inductive frequency influence. This relation is also called the Slater perturbation theorem [42] [41].

$$\frac{\Delta f_0}{f_0} = \frac{\Delta W_\mathrm{m} - \Delta W_\mathrm{e}}{W_\mathrm{m} + W_\mathrm{e}} \tag{54}$$

3.2 Fundamental Characteristics

In the following section some important parameters are presented, which are used for the description and comparison of different cavity resonators. The following section will only concentrate on parameters which are also important for this thesis. For a larger selection and a more detailed description of the parameters, please refer to the literature ([32], [39], [41]. [43], [44]).

3.2.1 Acceleration Field E_a

For cavities that are to be used to accelerate charged particles, one of the most meaningful quantities is the acceleration gradient E_a. This is a measure of the voltage difference experienced by the charged particles as they pass through the accelerator. The voltage that builds up between the drift tubes is calculated by

$$U_0 = \int_{-Z_L/2}^{Z_L/2} E_z(z)dz. \tag{55}$$

Here Z_L is the cell length of the accelerating cell, which is defined from drift tube center to drift tube center. Since the electric field and thus the voltage changes in time, a particle passing the cell does not experience the maximum voltage during its entire flight through the cell, but (assuming an ideal time of injection, i.e. passing the center of the drift tube while the field changes sign) the maximum electric field only in the center of the cell. The voltage which the particle finally experiences effectively is called U_eff and includes the build-up of the electric field at the entrance into the cell and the decay of the electric field at the exit of the particle from the cell (see figure 17). This results in U_eff:

$$U_\mathrm{eff} = \int_{-Z_L/2}^{Z_L/2} E_z(z) cos\left(\frac{\omega z}{\beta c}\right) dz \tag{56}$$

The ratio between the effective and the maximum voltage is called the time transit factor T [41].

$$T = \frac{U_\mathrm{eff}}{U_0} = \frac{\int_{-Z_L/2}^{Z_L/2} E_Z(z) cos\left(\frac{\omega z}{\beta c}\right) dz}{\int_{-Z_L/2}^{Z_L/2} E_Z(z) dz} \tag{57}$$

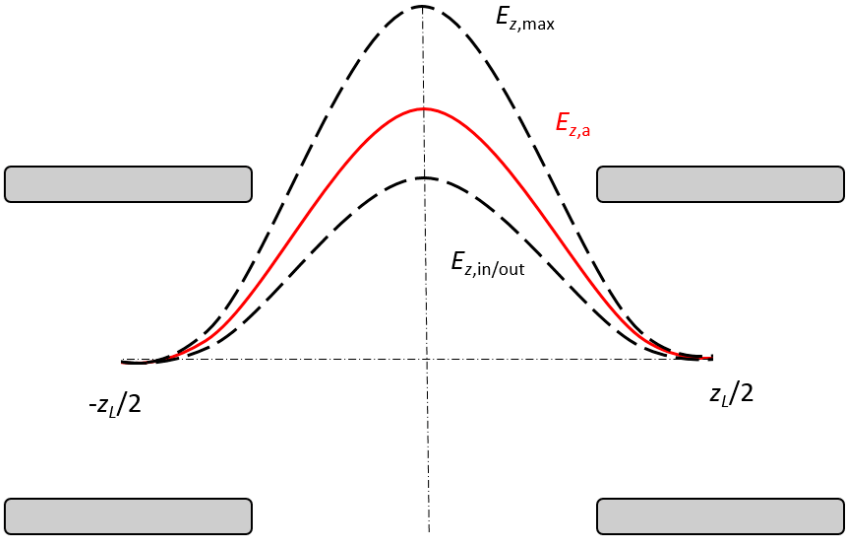

Fig. 17 Schematic representation of the time-dependent field curve in an accelerator cell. The maximum field $E_{z,\max}$, the field when entering or leaving the cell $E_{z,\text{in/out}}$ and the effective field $E_{z,\text{a}}$ are shown.

Thereby T can be solved analytically only for quite simple structures, for more complex structures like a CH, for example, the running time factor must be determined numerically. Since U_{eff} is always smaller than U_0, it is always $T < 1$. Typical values for T are between 0.7 and 0.9. If there are several accelerator cells within a resonator, as it is the case in a CH, the total electric field on the beam axis is calculated by the quotient of the sum of all single gap voltages and the effective total length L_{eff} [39].

$$E_{\text{a}} = \frac{1}{L_{\text{eff}}} \int_0^{L_{\text{eff}}} |E_z(z) cos(\omega t)| dz \tag{58}$$

E_{a} is the effective acceleration gradient and is given in MV/m. The total effective length L_{eff} is defined differently. In this thesis, the definition range of L_{eff} is set to take into account that the electric field still extends into the first and last drift tubes, so the sum of the individual cell lengths is used for definition (also called $\beta\lambda/2$-definition) [44]:

$$L_{\text{eff}} = n \cdot \frac{\beta\lambda}{2} \tag{59}$$

Here n represents the number of acceleration cells within the resonator.

3.2.2 Impedance R_{A}

A quantity that can be used to estimate the efficiency of resonators is the so-called impedance R_{A}. It indicates how well the resonator is able to transfer the within

stored power P_c into the accelerator voltage U_{eff}.

$$R_A = \frac{U_{eff}^2}{P_c} \tag{60}$$

The greater the impedance is, the greater is the acceleration voltage at constant injected power.

3.2.3 Stored Energy W

In order to generate an acceleration field in a resonator, power must be injected into the cavity. A certain part of the injected energy is stored within the cavity. This stored energy can be calculated from both the magnetic and the electric field within the resonator volume, since the energy content of both fields is the same on average over time. This results in the following for the stored energy W

$$W = \frac{1}{2}\mu_0 \int_V |H_0|^2 dV = \frac{1}{2}\epsilon_0 \int_V |E_0|^2 dV. \tag{61}$$

3.2.4 Power Dissipation P_C

The magnetic fields induced inside the resonator in turn induce surface currents on the inner wall surface of the resonator S, which generate Ohm losses. The dissipated power P_C is calculated from:

$$P_C = \frac{1}{2}R_s \int_S |H|^2 dS \tag{62}$$

Where R_s here represents the surface resistance.

3.2.5 Quality Factor Q

The Q-factor is another important parameter used to characterize resonators. It is a measure of how much of the stored energy W is dissipated per oscillation period. Different types of Q-factor are defined, such as the intrinsic quality or quality factor Q_0, the external quality Q_e and the loaded quality Q_L. The intrinsic quality is calculated from

$$Q_0 = \frac{\omega_0 W}{P_C}. \tag{63}$$

The higher the quality, the lower the losses of the oscillating system. However, the intrinsic quality Q_0 only considers the losses within the cavity. In real cavities losses also occur at both the input and the output couplers. These losses are referred to as $P_{e,l}$[52] and $P_{t,l}$[53], and together with P_C give the total power loss P_{tot} [32].

$$P_{tot} = P_C + P_{e,l} + P_{t,l} \tag{64}$$

[52]Loss by emitted
[53]Loss by transmitted

The definition of the loaded quality Q_L is analogous to the definition of Q_0, except that the total power dissipation P_tot is considered [32].

$$Q_\mathrm{L} = \frac{\omega W_0}{P_\mathrm{tot}} \tag{65}$$

The determination of the influences of the coupler or the pick-up for realistic conditions is only possible under special circumstances, which makes the determination of Q_0 only possible to a limited extent. For this reason, the loaded quality Q_L is usually determined and Q_0 is derived from it. Dividing (64) by ωW_0 gives

$$\frac{P_\mathrm{tot}}{\omega W_0} = \frac{P_\mathrm{C} + P_\mathrm{e,l} + P_\mathrm{t,l}}{\omega W_0} = \frac{P_\mathrm{C}}{\omega W_0} + \frac{P_\mathrm{e,l}}{\omega W_0} + \frac{P_\mathrm{t,l}}{\omega W_0}. \tag{66}$$

The subexpressions from (66) correspond to the reciprocal of the definition of the quality, so that one can assign a quality of its own to the cavity (Q_0), the coupler (Q_e), and the pick-up(Q_t).

$$\frac{1}{Q_\mathrm{L}} = \frac{1}{Q_0} + \frac{1}{Q_\mathrm{e}} + \frac{1}{Q_\mathrm{t}} \tag{67}$$

When the injected RF power is turned off, the stored energy within the cavity decreases, with the rate of decrease corresponding to the power dissipation P_tot [32]

$$\frac{dW}{dt} = -P_\mathrm{tot} = -\frac{\omega_0 W}{Q_\mathrm{L}} \tag{68}$$

The solution of this equation is an exponential function with the time constant τ.

$$W(t) = W_0 \cdot e^{\left(-\frac{t}{\tau_\mathrm{L}}\right)} = W_0 \cdot e^{\left(-\frac{\omega_0 t}{Q_\mathrm{L}}\right)} \quad \text{with} \quad \tau = \frac{Q_\mathrm{L}}{\omega} \tag{69}$$

This measurable τ can now be used to determine Q_L, but this is only the case if the injected RF signal is pulsed. To determine the Q-factor for a continuous RF signal, the so-called 3dB method is used. For this, the resonance curve $A(\omega)$ must first be determined. To determine the resonance curve, the fields inside the cavity are considered, which also decay with $1/\tau$. The time dependence of the field amplitude is

$$A(t) = A_0 e^{\left(-\frac{\omega_0 t}{2Q_\mathrm{L}}\right)} e^{(i\omega_0 t)}. \tag{70}$$

To express the field amplitude $A(t)$ as a frequency ω dependent function $A(\omega)$, it has to be Fourier transformed. This results in the frequency dependent field amplitude

$$|A(\omega)| = \frac{1}{\sqrt{2\pi}} \frac{|A_0|}{\sqrt{\left(\frac{\omega_0}{2Q_\mathrm{L}}\right)^2 + (\omega - \omega_0)^2}}. \tag{71}$$

The maximum of this function is at ω_0 and is calculated from

$$A(\omega_0) = \frac{2Q_L |A_0|}{\sqrt{2\pi}\omega_0} \tag{72}$$

In order to determine Q_L using the 3dB method, the so-called half-width of the resonance curve is calculated first. Figure 18 represented this method graphically.

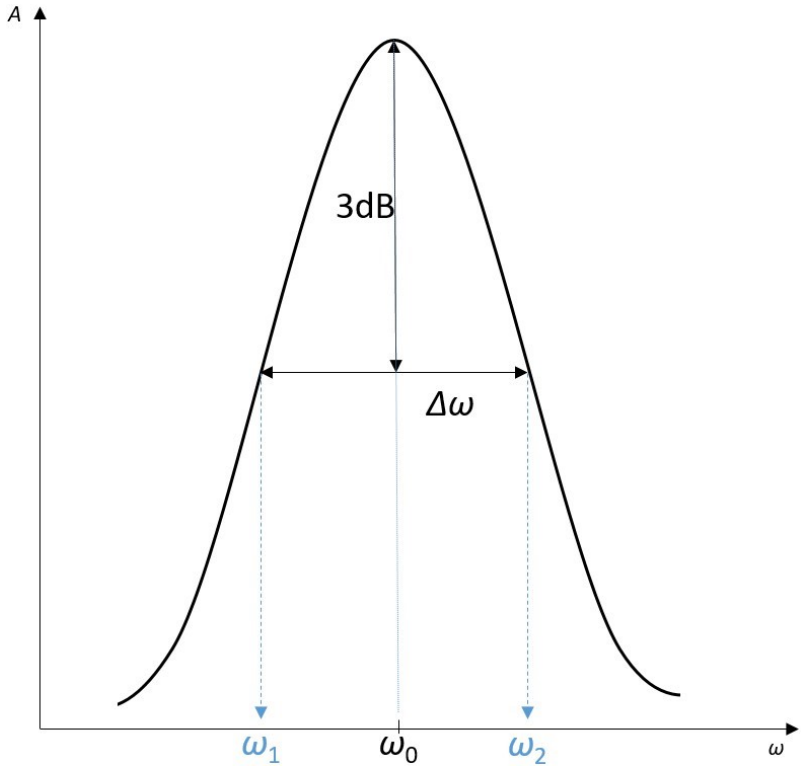

Fig. 18 Graphical representation of the concept of the 3dB method.

The half-width indicates the width of the resonance curve $\Delta\omega = \omega_2 - \omega_1$ at the point where the decay of the resonance curve corresponds to 3dB, hence

$$A(\omega) = \frac{A_{\omega_0}}{\sqrt{2}}. \tag{73}$$

Putting this into (71) gives:

$$\begin{aligned} \frac{A_{\omega_0}}{\sqrt{2}} = \frac{2Q_\mathrm{L}|A_0|}{\sqrt{2\pi}\omega_0\sqrt{2}} = \frac{1}{\sqrt{2\pi}} \frac{|A_0|}{\sqrt{\left(\frac{\omega_0}{2Q_\mathrm{L}}\right)^2 + (\omega-\omega_0)^2}} \\ \Rightarrow \omega_{1,2} = \omega_0 \pm \frac{\omega}{2Q_\mathrm{L}}. \end{aligned} \tag{74}$$

This allows to directly determine the width of the resonance curve and thus the loaded quality Q_L to

$$\begin{aligned} \Delta\omega = \omega_2 - \omega_1 = \frac{\omega_0}{Q_\mathrm{L}} \\ \Rightarrow Q_\mathrm{L} = \frac{\omega_0}{\omega_2 - \omega_1} \end{aligned} \tag{75}$$

3.2.6 Coupling Factor β

A quantity that is directly related to the quality and can be used to determine the quality factor is the so-called coupling factor β. The individual qualities can each be assigned their own coupling factor. Thus, the coupling factor of the coupler is β_e and that of the pick-up is β_t. These indicate in each case how strongly the associated coupler influences the resonator field. They are defined by the associated qualities to [32]:

$$\beta_e = \frac{Q_0}{Q_e} \qquad (76) \qquad\qquad \beta_t = \frac{Q_0}{Q_t} \qquad (77)$$

From these definitions and from (67) results

$$\frac{1}{Q_L} = \frac{1}{Q_0}(1 + \beta_e + \beta_t) \;\Rightarrow\; Q_0 = Q_L(1 + \beta_e + \beta_t). \qquad (78)$$

Thus, the quality factor Q_0 can be determined from the loaded quality Q_L and the two coupling factors β_e and β_t. In practice, the pick-up is usually designed in such a way that it has very little influence on the fields, so that $\beta_t \approx 0$ applies. Q_0 thus depends only on Q_L and β_e. The strength of the coupling is thereby divided into three different cases, the distinction of which is defined by the value of β_e. Thus, the coupling is considered weak or undercoupled if $0 < \beta_e < 1$. If $\beta_e = 1$ then the coupling is said to be critical. In this case, the qualities of the resonator and the coupler are equal and Q_0 is twice the loaded Q_L. In the last case $\beta_e > 1$, which is called strong coupling or overcoupling.

To determine the coupling factors, a square-wave pulse from the signal generator is applied to the resonator and the reflection and transmission behavior of the signal is observed when the high frequency is switched on or off. At switch-on, all power is initially reflected (P_f[54] $= P_r$[55]) because the excitation of the resonator requires a settling time and is thus delayed. After this settling time, the reflected power decreases, until it reaches an equilibrium state. Since the output coupler was chosen to couple as weakly as possible ($\beta_t \approx 0$), almost all the injected energy of the resonator flows back through the coupler at the end of the square pulse ($P_r \approx P_e$). Figure 19 shows the plots of P_f, P_t[56] and P_r for different couplings [32].

For critical coupling ($\beta_e = 1$) it can be seen that P_r almost completely disappears after the settling time and thus P_f can be injected into the resonator almost without loss. For weak coupling ($\beta_e < 1$), P_r does not drop that far, and for strong coupling ($\beta_e > 1$), P_r initially drops almost to 0 after the settling time, but then rises again. In practice, these curves can be read directly from an oscilloscope and from the two maxima of P_r β_e can be derived [32].

[54] forward power
[55] reflected power
[56] transmitted power

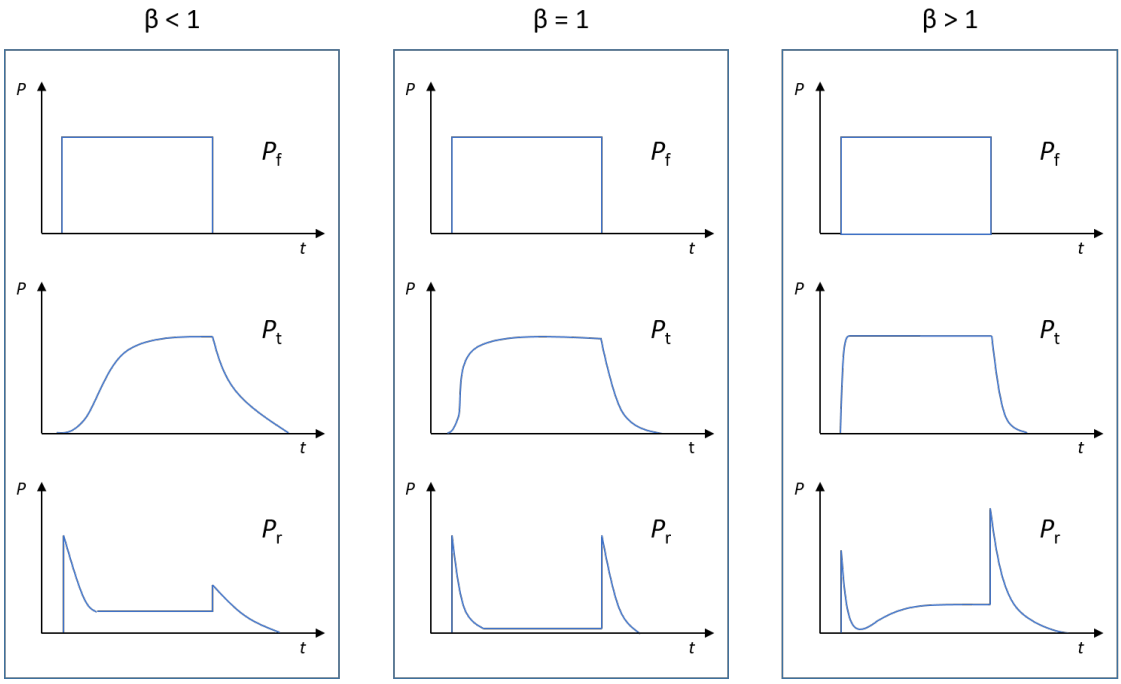

Fig. 19 Schematic representation of the reflected (P_r) and the transmitted (P_t) signal for a coupled square pulse (P_f) for a total of three different coupling factors (β).

$$\beta_e = \frac{1}{2 \cdot \sqrt{\frac{P_f}{P_r}} - 1} \tag{79}$$

When determining β_e with this method, care must be taken that the pulse length used is sufficiently large so that the resonator is in the equilibrium state. However, it is not necessary to know how strongly the coupler couples. With constant applied RF power, β_e can be calculated via [32]

$$\beta_e = \frac{1 \pm \sqrt{\frac{P_r}{P_f}}}{1 \mp \sqrt{\frac{P_r}{P_f}}}. \tag{80}$$

The upper sign in (80) is used when overcoupling and the lower sign when undercoupling.

3.2.7 Surface Resistance normal state $R_{s,n}$

In addition to the surface resistance of a superconductor in the superconducting state according to BCS theory given in (18), a superconductor also has a surface resistance in the normal conducting state. This is needed for measurements in the

normal conducting state. To derive it, Maxwell's equations are used again, but this time not in a current- and charge-free space. This time, Maxwell's equations are used in a sourceless space[57] to derive the so-called telegrapher's equation:

$$\vec{\nabla} \cdot \vec{E} = 0 \qquad (81)$$

$$\vec{\nabla} \cdot \vec{B} = 0 \qquad (82)$$

$$\vec{\nabla} \times \vec{E} = -\frac{\partial \vec{B}}{\partial t} \qquad (83)$$

$$\vec{\nabla} \times \vec{B} = \mu_0 \vec{j} + \mu_0 \epsilon_0 \frac{\partial \vec{E}}{\partial t}. \qquad (84)$$

The derivation of the telegrapher's equation is analogous to the derivation of the wave equation, but here additionally the electric conductivity σ, which is defined as a constant of proportionality between the current density $\vec{j}$ and the electric field strength $\vec{E}$

$$\vec{j} = \sigma \vec{E} \qquad (85)$$

is used. This results in the so-called telegrapher's equation

$$\vec{\nabla}^2 \vec{E} = \mu_0 \sigma \frac{\partial \vec{E}}{\partial t} + \mu_0 \epsilon_0 \frac{\partial \vec{E}^2}{\partial t^2}. \qquad (86)$$

The telegrapher's equation for the magnetic field is derived analogously

$$\vec{\nabla}^2 \vec{B} = \mu_0 \sigma \frac{\partial \vec{B}}{\partial t} + \mu_0 \epsilon_0 \frac{\partial \vec{B}^2}{\partial t^2}. \qquad (87)$$

In good conductors $\mu_0 \epsilon_0 \ll \mu_0 \sigma$ is valid, so that (86) can be simplified to

$$\vec{\nabla}^2 \vec{E} = \mu_0 \sigma \frac{\partial \vec{E}}{\partial t} \quad \text{for} \quad \mu_0 \epsilon_0 << \mu_0 \sigma. \qquad (88)$$

For a time-dependent electric field[58], (88) results in

$$\vec{\nabla}^2 \vec{E} = i\omega_0 \mu_0 \sigma \vec{E} = \alpha^2 \vec{E} \quad \text{with} \quad \alpha^2 = i\omega_0 \mu_0 \sigma. \qquad (89)$$

The surface can be assumed to be a conductive half-space $x > 0$ whose electrical conductivity is between $0 < \sigma < \infty$. A harmonic time-dependent field is now generated at this surface. A further assumption is that the field is constant in y- and in z-direction and thus independent of y and z. Therefore, the solution of (89) for the field components is

$$E_y(x) = E_z(x) = E_0 e^{-\alpha x}. \qquad (90)$$

Since $\vec{j} = \sigma \vec{E}$ is valid, it becomes obvious that not only the transverse electric field components within the conductor decrease exponentially, but also the respective

[57] $\vec{\rho} = 0 \ \forall \vec{x}$
[58] $E \propto e^{i\omega_0 t}$

current densities. Thus, current does not flow homogeneously in an electric conductor when a high-frequency alternating field is applied to its surface, but only in a thin layer immediately below the surface. In this case, it penetrates only a certain depth. The electric field and thus the current decrease exponentially from the outside to the inside of the conductor. The penetration depth at which E_0 has decreased to $1/e$ is called the skin depth δ and the entire effect of the decrease is called skin effect [32]

.

$$\delta = \sqrt{\frac{1}{\sigma \pi f_0 \mu_0 \mu_r}} = \sqrt{\frac{\rho}{\pi f_0 \mu_0 \mu_r}} \tag{91}$$

Where ρ is the resistivity of the conductor and μ_r the permeability of the conductor. As a simplification, it is now assumed that the current within the conductor does not decrease exponentially, but that a constant current I flows within a layer of depth δ. In addition, it is assumed that no current flows outside this layer. This current can be calculated by integration of the current density:

$$I_y = I_z = \int_0^\infty j_z(x)dx = \frac{j_0}{\alpha} \tag{92}$$

The surface impedance Z_s is now given by the field E at the surface and the current I inside the layer.

$$Z_\mathrm{s} = \frac{E_0}{I} = \frac{E_0 \alpha}{j_0} = \frac{E_0 \alpha}{\sigma E_0} = \frac{\alpha}{\sigma} = R_\mathrm{s} + iX_\mathrm{s} \tag{93}$$

The real part of this surface impedance Z_s is now called the surface resistance R_s.

$$R_\mathrm{s,n} = \sqrt{\frac{\pi f_0 \mu_r \mu_0}{\sigma}} = \frac{1}{\sigma \delta} \tag{94}$$

It can be seen that $R_\mathrm{s,n}$ increases as the skin depth δ decreases, this seems logical as there is less room for the current to flow. Also noticeable is that $R_\mathrm{s,n}$ increases proportionally to $\sqrt{f_0}$, while the surface resistance in the cold state $R_\mathrm{s,BCS}$ depends quadratically on the frequency (see (18)).

4 Phenomena limiting Superconductivity

In chapter 2 of this thesis, the theoretical basis of superconductivity was explained and it was mentioned that there are limiting phenomena that limit superconductivity, such as a critical temperature T_C, a critical current density j_C or a critical magnetic field H_C. In addition to these limiting variables, superconducting resonators have other constraints that can occur during operation. These technical limitations, which can also occur during the fabrication of the cavity or during the preparation of the Niobium used, will be discussed in more detail in the following section. A more detailed description of these issues can be found, as in chapter 2, in the respective literature [29] [32] [44].

4.1 Electric and Magnetic Peak Fields $E_{\mathbf{peak}}$ & $B_{\mathbf{peak}}$

As already explained, a too strong magnetic field B_C exceeding a certain critical value leads to the breakdown of the superconductivity. Since superconducting resonators are designed to excite strong electric and magnetic fields inside to oscillate, it is interesting to know the strength of both the electric and magnetic peak fields (E_{peak} and B_{peak}) generated inside the cavity. While a too strong magnetic field will directly lead to superconductivity breakdown, a too strong electric field could cause field emission (see section 4.5), which would severely limit the performance of the resonator or could even lead to superconductivity breakdown. Since these peak fields depend on the injected power and the cavity structure, it is interesting to consider them in relation to the maximum achievable field gradient E_a.

$$2 \leq \frac{E_{\text{peak}}}{E_a} \leq 10 \tag{95}$$

The smaller this ratio, the lower the probability of field emission for a given gradient. This ratio is already minimized during the design of the cavity by optimally adjusting the drift tubes within the cavity and simulating the electric field distribution and the peak fields. Values for E_{peak}/E_a are between 2, for example for superconducting elliptical Tesla cavities, and 10 [44]. The sc CH cavities are in the middle range with an E_{peak}/E_a of about 6 [1].

In practice, it is shown that the superconductivity of superconducting resonators can already break down at magnetic field strengths well below the critical magnetic field strength of Niobium B_{C2} (see Tab. 1). This is caused by so-called defects within the material, which form a normal conducting region. Within this region, a temperature rise occurs which is sufficiently large to cause superconductivity breakdown, also known as quenching. For this reason, the ratio between peak magnetic fields and field gradients must also be minimized as much as possible from the beginning. Typical values for B_{peak}/E_a are between [44]:

$$3\,\frac{\mathrm{mT}}{\mathrm{MV/m}} \leq \frac{B_{\mathrm{peak}}}{E_{\mathrm{a}}} \leq 20\,\frac{\mathrm{mT}}{\mathrm{MV/m}} \tag{96}$$

Minimization of these two ratios can only be achieved for complex structures such as the CH cavity using numerical software such as CST Microwave Studio [40]. In chapter 8 the way of this minimization will be discussed in more detail.

4.2 Residual Resistance

In reality, the resistance of a superconductor reaches a value above the theoretical $R_{\mathrm{s,BCS}}$ calculated in (18) when cooling down to low temperatures. Thus, the actual resistance R_{s} is composed of the sum of the temperature-dependent resistance $R_{\mathrm{s,BCS}}$ and a temperature-independent residual resistance R_0 [32].

$$R_{\mathrm{s}} = R_{\mathrm{s,BCS}}(T) + R_0 \tag{97}$$

The causes for R_0 can vary and range from welds and contamination of foreign atom inclusions. The value of R_0 is typically in the order of a few 10 nΩ, although 1-2 nΩ has also been achieved. Furthermore, R_0 can be divided into two components, a material-dependent resistance R_{mat} and a magnetic field-dependent resistance R_{mag}. As explained in section 2.2, a magnetic field applied to the superconductor from the outside can penetrate the superconductor as long as it is a Type II superconductor, such as Niobium for example. Thus, if the external magnetic field strength H_{e} is between the two critical magnetic field strengths $H_{\mathrm{C1}}<H_{\mathrm{e}}<H_{\mathrm{C2}}$, the magnetic field penetrates the superconductor within flux tubes whose centers are normal conducting and are surrounded by induced circular currents. These flux tubes can move within the superconductor by a force generated by the superposition of the induced circular currents and the currents flowing through the superconductor, creating an electrical resistance and increasing R_{s}. For this reason, it is necessary to shield Type II superconductors from external magnetic fields such that $H_{\mathrm{e}}<H_{\mathrm{C1}}$, which corresponds to a complete displacement of the magnetic field by the Meissner effect. For the shielding, μ-metal[59] is used. The magnetic component of the residual resistance R_{mag} can be calculated from [32]

$$R_{\mathrm{mag}} = \frac{H_{\mathrm{e}}}{2H_{\mathrm{C2}}} R_{\mathrm{s,n}}. \tag{98}$$

Using for $H_{\mathrm{C2}} = 2400\,\mathrm{Oe}$ and the normal conducting surface resistance for Niobium with a $RRR = 300$, $R_{\mathrm{s,n}} \approx 1.5\,\mathrm{m\Omega}$ at 1 GHz this gives (98) to [32]

.

$$R_{\mathrm{mag}} = 0.3\,(\mathrm{n\Omega}) H_{\mathrm{e}}(\mathrm{mOe}) \sqrt{f(\mathrm{GHz})}. \tag{99}$$

[59] μ-metals belong to the group of soft magnetic nickel-iron alloys, which have a high magnetic permeability of $\mu_r = 10^5 - 10^6$.

A permanent, external magnetic field is the magnetic field of the earth ($H_{\text{earth}} = 500\,\text{mOe}$). If this was not shielded, the residual resistance would be of the order of 100 nΩ, which is significantly higher than $R_{\text{s,BCS}}$ and thus strongly dominate the surface resistance.

4.3 Multipacting

The term multipacting describes the creation of an electron avalanche within a cavity by repeated emission and impact of electrons on the resonator walls. This is a resonant process. Initially, an electron is emitted from the wall of the resonator by, for example, cosmic rays, photoemission, radioactive decay, or field emission, and then accelerated in the electric field $E_0\sin(\omega t)$ [32]. If the kinetic energy of the electron is sufficiently large and it hits a wall, it is able to release secondary electrons, which again can be accelerated in the field and hit a wall (see figure 20). If these release electrons again, an exponential increase in the number of electrons can occur. If the number of emitted electrons is larger than the number of incoming electrons, an electron avalanche occurs and it is called multipacting [32].

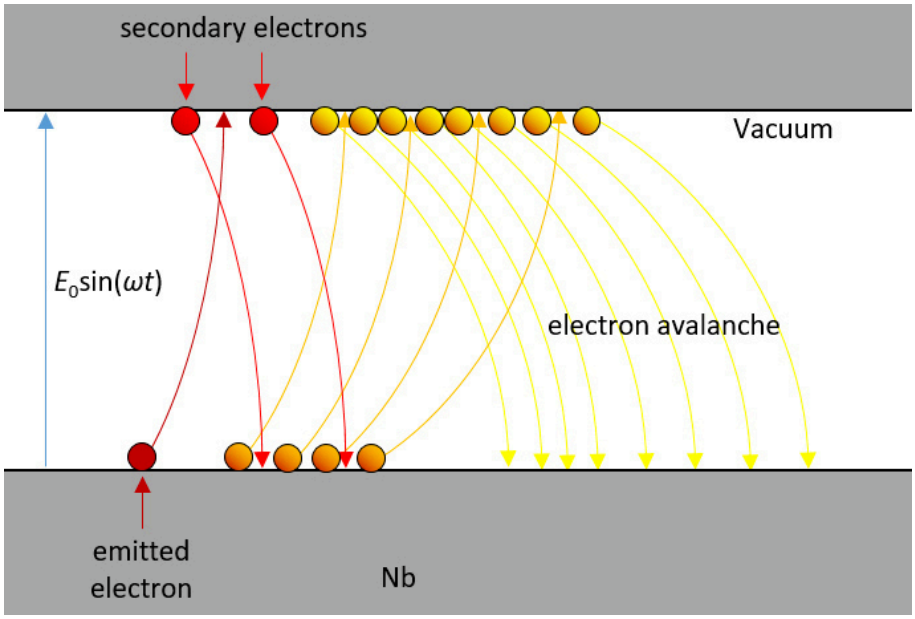

Fig. 20 Sketch of the development of an electron avalanche inside a cavity by multipacting.

The electron avalanche triggered in the cavity compensates to a certain extent for the power injected into the cavity, since a large part of it is used to accelerate the emitted electrons. The absence of the power, which is no longer included in the accelerating voltage U_{eff}, can be observed directly from the curve of the transmitted power P_{t}. Once an electron avalanche has been initiated, P_{t} cannot increase any

further and enters a plateau. In figure 21 this plateau is shown for a measurement with the network analyser or with an RF pulse. After the field energy inside the cavity has flattened out sufficiently to not provide the necessary energy to release secondary electrons, the course of the transmitted power normalizes [44].

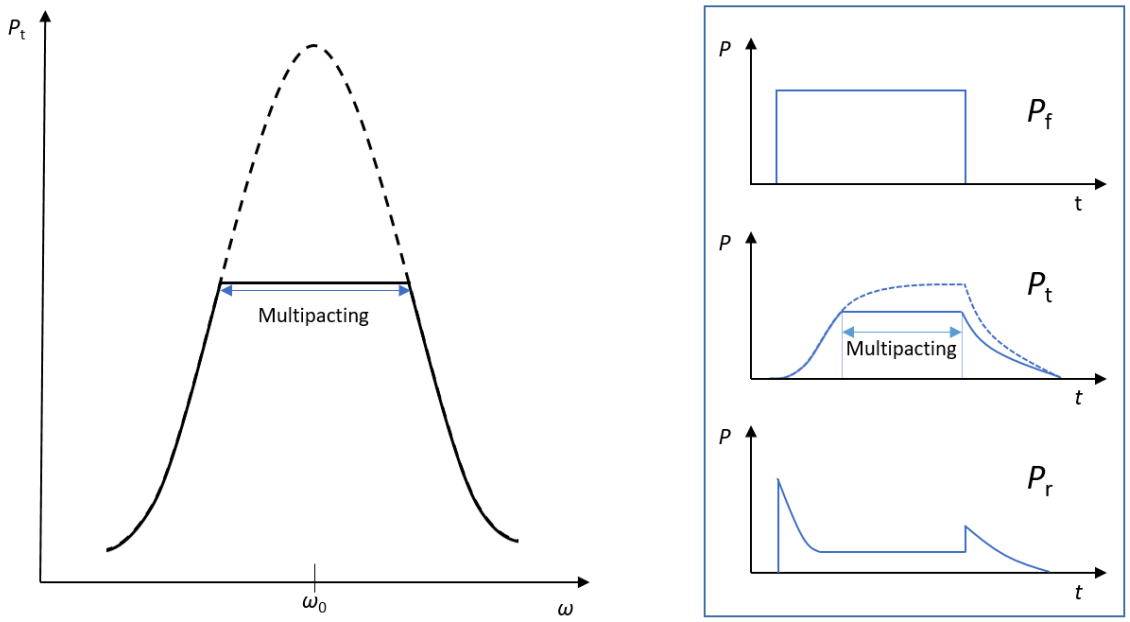

Fig. 21 Schematic representation of transmission signals when multipacting occurs. Left: The transmission signal as it would be displayed on a network analyser. Right center: The transmission signal during an RF pulse, while the forward and reflected signals remain invariant.

Besides the sufficiently large field energy, another condition for multipacting is the trajectory of the electrons. A distinction is made between one-point multipacting, in which the electrons strike at the same point of their emission, and two-point multipacting, in which the electrons strike at a new location. The transit time of the electrons in one-point multipacting is an integer multiple of the radio frequency period. In this process, the emitted electrons are accelerated by the electric field component perpendicular to the resonator walls, while the magnetic field components deflect them along quasi-circular paths so that they strike again at their origin (see figure 22). The number of high frequency periods between emission and impact are called 1st, 2nd and 3rd order [32].

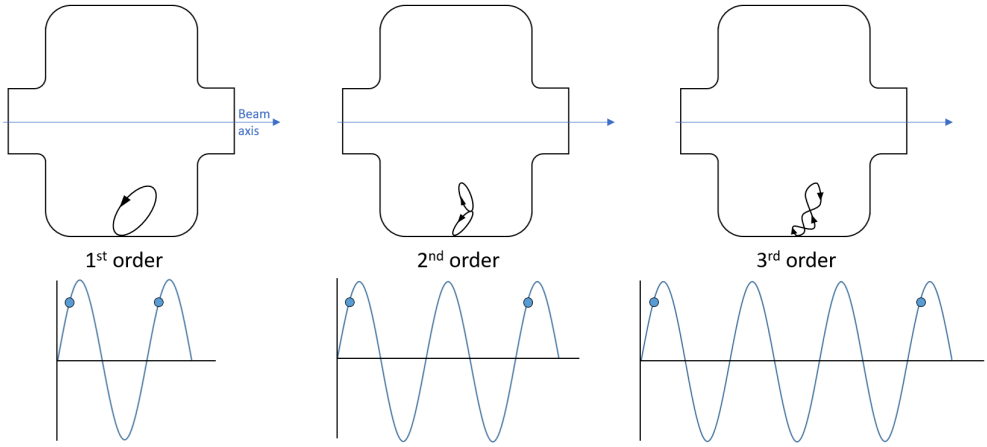

Fig. 22 Schematic representation of 1-point multipacting for modes 1, 2, and 3.

The number of generated electrons N_e is composed of the originally emitted electrons N_0 and the material specific SEC[60] $\delta(K)$ [32].

$$N_e = N_0 \prod_{m=1}^{k} \delta K_m \tag{100}$$

Here K_m is the kinetic energy after the m-th impact and k the number of impacts. As described above, a condition for multipacting is that N_e goes to infinity when k goes to infinity, which is satisfied by (100) when $\delta>1$ [32]. δ varies from material to material and can be affected by different surface preparations, so that later conditioning is simplified (see figure 23).

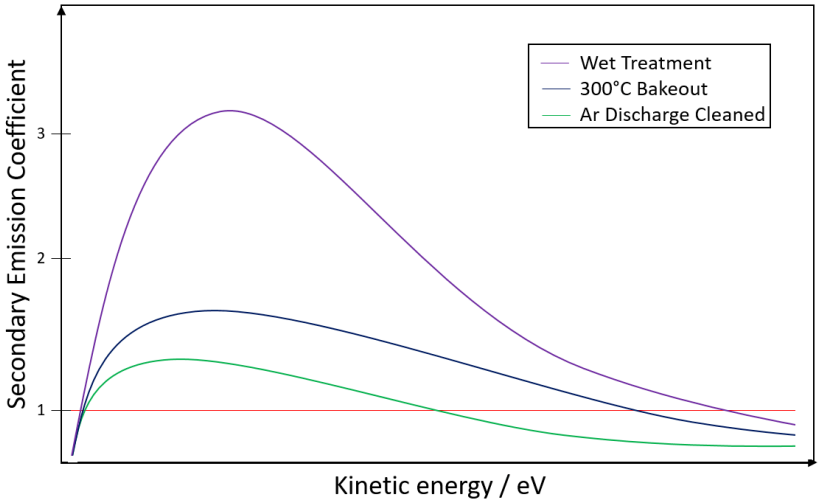

Fig. 23 Schematic profile of the secondary electron emission coefficient of Niobium as a function of the kinetic impact energy of the electrons for different surface preparations.

[60] **S**econdary **E**lectron emission **C**oefficent

At low field levels, the kinetic energy of the emitted electrons is not sufficient to trigger secondary electrons (δ<1). If the energy increases, it is sufficiently large so that the emitted electrons can trigger secondary electrons when they hit the resonator wall (δ>1). If the energy is too high, the emitted electrons penetrate the surface of the material to such an extent that the secondary electrons cannot escape from the material, causing δ to drop again until it is δ<1 again [32].

When the desired acceleration gradient E_a is first set within a resonator, so-called multipacting barriers typically appear. A distinction is made between 'soft' and 'hard' barriers. Soft barriers are usually residues on the surface of the resonator, which can be removed by the impact of the electrons. So, at constant power P_f, intended multipacting is triggered to remove these residues. At a constant applied vacuum, the stripped residues are extracted and the soft barriers are eliminated. This process of removing residues by intentionally triggering multipacting for a certain time is called conditioning. A hard barrier, however, often occurs due to geometric boundary conditions and cannot be removed by conditioning. If a hard barrier affects the maximum achievable acceleration gradient E_a excessively, it may be necessary to redesign the resonator. Barriers can be recognized by the decrease of the unloaded Q-factor Q_0 in the Q_0 versus E_a curve (see figure 24) [32].

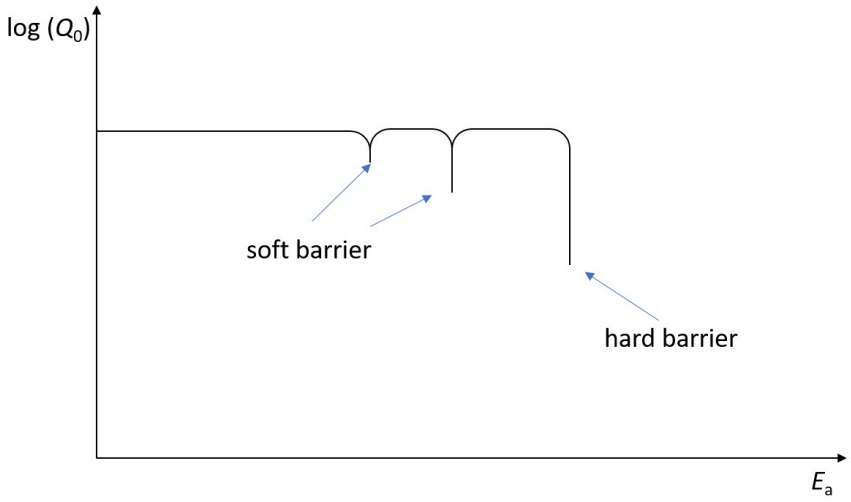

Fig. 24 Typical Q_0 versus E_a curve of a superconducting cavity in case of multipacting.

Another limitation is that in superconducting structures, the impact of electrons into the resonator walls can cause local heating of the material. With a large number of electrons up to an electron avalanche, these impact areas can be heated to such an extent that local normal conduction spots or even quenching can occur.

4.4 Thermal Breakdown

The thermal breakdown of superconductivity is also called quench, as described above. The reason for a thermal breakdown is due to defects in the surface of the superconductor and are caused by submillimeter sized inclusions in the raw material of the superconductor or at welds. The defects are normal conductors. In the case of a DC voltage, the conduction electrons would simply pass around the defects and no effect would occur. When an AC voltage is applied, however, the normally conducting electrons within the defect are also excited to move, so that a certain amount of the injected power is dissipated in the defects. As the field level increases, so does the temperature rise in the defects until they exceed the critical value T_C and the superconducting material surrounding the defects also becomes normally conducting (see figure 25). As a result, more power is now dissipated in a larger region and the temperature increase spreads until superconductivity in the entire structure can collapse [32].

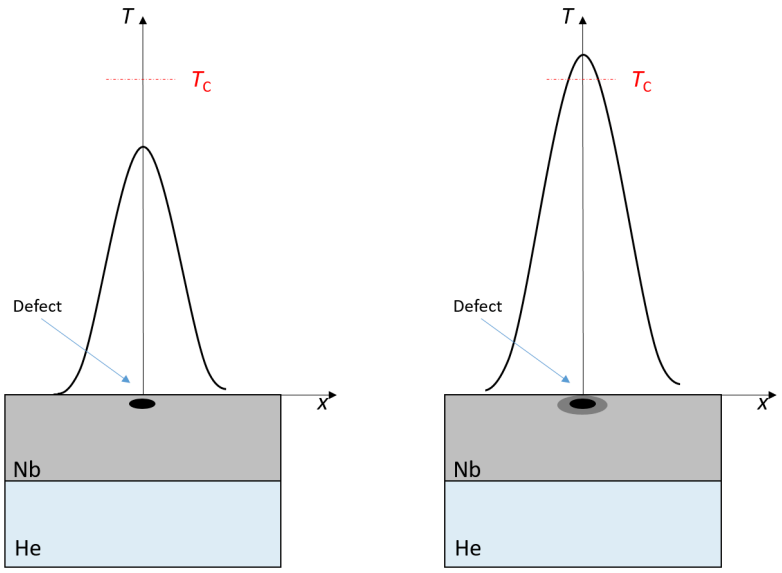

Fig. 25 Schematic representation of a thermal breakdown of superconductivity in Niobium. Left: If the strength of the field is not high enough to raise the temperature above T_C due to the power dissipated in the defect. Right: Now the field is sufficiently strong to raise the temperature by the dissipated power above T_C.

A thermal breakdown can be recognized by its characteristic course of the reflected and transmitted power P_r and P_f with an RF pulse switched on. When the power P_f is coupled into the cavity, after an initial maximum P_r decays with time as P_t increases. When the field level reaches a sufficiently large value to cause a quench, the superconductivity breaks down and the Q factor Q_0 of the resonator changes, and with it the coupling factor β_e, so that all power is now reflected. Thus

P_r increases again and P_t decreases. If the field level decreases and the cavity is cooled sufficiently again by the liquid Helium surrounding it, it re-enters the superconducting state so that Q_0 increases again. Thus, the resonator is properly coupled again and the P_r decreases while P_t increases again. After a sufficiently large field level is reached, the process starts again [32]. Figure 26 shows schematically the course of the three readings P_f, P_r and P_t for the occurrence of a quench.

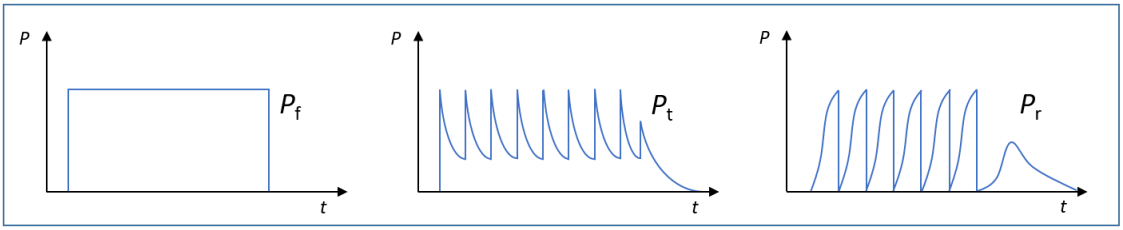

Fig. 26 Course of the powers in an RF pulse during a thermal breakdown

To counteract quenching, Nb of particularly high purity (RRR > 250) should be selected, and the surface should be chemically treated and rinsed with high-purity water. This prevents the formation of defects.

4.5 Field Electron Emission

Another effect that influences the performance of superconducting cavities is the so-called field emission. Electrons are released from the metal surface by the influence of an electric field. These emitted electrons are then accelerated in the field, analogous to multipacting (see section 4.3), and can strike the surface of the cavity and deposit heat there, which can lead to a quench under certain circumstances. The power required to accelerate the electrons is a part of P_f in this case, so the stored energy within the cavity does not increase with an increasing P_f. From (63) it can be seen that at high acceleration gradients E_a the quality Q_0 decreases as soon as field emission occurs (see figure 27).

In a metallic conductor, the electrons bound in the material are enclosed in a potential well, so that their energy is insufficient for them to leave the surface. However, if energy is supplied to the electrons in the form of heat (thermal emission) or radiation (photoelectric effect), they can overcome this potential barrier and be released. Another possibility of electron emission is the so-called Fowler-Nordheim tunneling [45], named after the two physicists Ralph Howard Fowler[61] and Lothar Nordheim[62]. Considering the electron inside the potential barrier as a quantum

[61] ⋆17 January 1889 in Fresden, United Kingdom; †28 July 1944 in Cambridge, United Kingdom
[62] ⋆7 November 1899 in Munich, Germany; †5 October 1985 in La Jolla, USA

mechanical picture, the wave function of the electron behind the potential barrier is exponentially attenuated to such an extent that the electron cannot overcome the barrier. If an external electric field E is applied to the metal surface, the electron sees the potential [32]

$$\phi_{\text{ext}}(x) = -eEx. \tag{101}$$

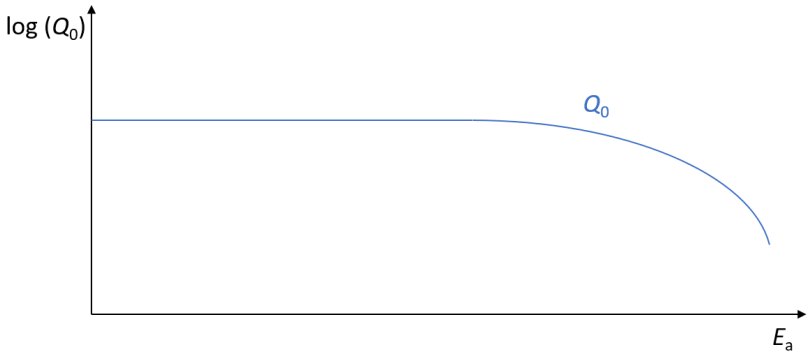

Fig. 27 Schematic curve of the quality factor Q_0 with field emission. When field emission occurs, the quality factor drops at high field levels.

This potential $\phi_{\text{ext}}(x)$ gives the potential barrier a triangular shape (see figure 28). The electron also experiences an attractive force due to the charge shift on the surface of the metal. This shift of charges can be considered as image charge and is located at position x when the electron is at position $-x$ and generates the potential [32]

$$\phi_{\text{im}}(x) = -\frac{e^2}{16\pi\epsilon_0 x}. \tag{102}$$

The additional potential $\phi_{\text{im}}(x)$ rounds off the triangular course of the potential barrier and lowers it further. From these two potentials $\phi_{\text{ext}}(x)$ and $\phi_{\text{im}}(x)$ as well as the potential barrier the total potential $\phi_{\text{eff}}(x)$ results to [32]

$$\phi_{\text{eff}}(x) = -\frac{e^2}{16\pi\epsilon_0 x} - eEx. \tag{103}$$

This resulting potential barrier is sufficient thin that the wave function of the electron behind it does not completely drop to 0. Thus, there is a certain probability that electrons can escape from the surface without an additional energy input (see figure 28). This process is called tunnelling.

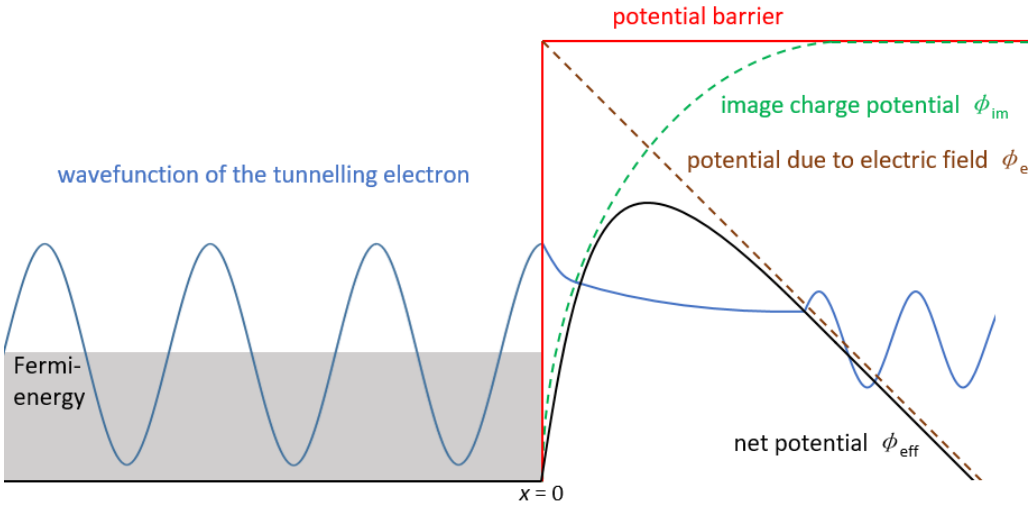

Fig. 28 Resultant potential barrier of a metallic surface due to the influence of an external electric field and an image charge, and the wave function of an electron tunnelling through the resulting barrier.

Fowler and Nordheim have established an expression for the tunnel current density within the framework of their theory [45]:

$$j = \frac{e^2}{8\pi h}\frac{E^2}{\phi t^2(y)} exp\left(-\frac{8\pi\sqrt{2m_e(e\phi)^3}v(y)}{3heE}\right) \tag{104}$$

Here e is the elementary charge, m_e the electron mass, h the Planck constant, ϕ the work function in eV and $t(y)$ and $v(y)$ the two so-called Fowler-Nordheim functions, by which the lowering of the potential barrier by the image charge is represented. In the case of the triangular course of the potential barrier considered here, (104) simplifies to the effect that $t(y) = 1$ and $v(y) = 1$, so that for $j(E)$ holds [32]:

$$j(E) = \frac{A_{FN}E^2}{\phi} exp\left(-\frac{B_{FN}\phi^{3/2}}{E}\right) \tag{105}$$

Here $A_{FN} = 1.54 \cdot 10^6$ and $B_{FN} = 6.83 \cdot 10^3$ are the so-called Fowler-Nordheim coefficients, E the electric field strength in MV/m and j the current density in A/m^2. According to the theory of Fowler and Nordheim, field emission is expected only from electric field strengths of the order of GV/m, but in practice field emission can be observed already from field strengths of the order of MV/m. This fact can be explained by so-called field emitters. These field emitters are μm large impurities on the surface of the resonator, at which locally very high field strengths can occur due to their surface structure. To take these field emitters into account, the so-called field enhancement factor β_{FN} is introduced. Usually values for β_{FN} are in the range of $\beta_{FN} = 100 - 1000$. Together with the emitter surface area A_E, the tunnelling current strength $I(E)$ results in [32]:

$$I(E) = \frac{A_{\mathrm{FN}} A_e (\beta_{\mathrm{FN}} E)^2}{\phi} exp\left(-\frac{B_{\mathrm{FN}} \phi^{3/2}}{\beta_{\mathrm{FN}} E}\right) \tag{106}$$

A good surface preparation can significantly reduce the occurrence of field emission and thus improve the performance by avoiding field emitters.

5 Quick Introduction in Structural Mechanics

Structural mechanics is a sub-discipline of engineering in which forces, stresses and deformations of solids are calculated. This is necessary for the design as well as for the recalculation of mechanical components. A wide variety of components made of different materials such as wood, rubber, plastics and also metals are being investigated. The aim is to gain a more precise overview of the strength of the material under investigation with regard to external forces before the material fails. In this context, a failure of the material means a deformation or fracture.
Since superconducting cavities are designed with a very thin wall thickness to ensure uniform cooling to cryogenic temperatures on the one hand and to save production costs on the other hand, they are particularly vulnerable to external mechanical stresses acting on them during operation. This can be stresses due to thermal contraction of the material at low temperatures, mechanical vibrations during operation due to the maintenance of the vacuum, or forces acting intentionally, as in the mechanical displacement of the dynamic bellow tuner to tune the frequency. To be confident that the cavity can withstand these mechanical stresses, it is of great interest to determine and calculate the strength of the cavity. For this purpose, the cavities designed and presented in this thesis were analysed for their mechanical properties and strength using the program CST Studio Suite [40]. In the following chapter, a brief overview of the underlying theory will be given and the basic concepts for the simulations will be briefly explained. A detailed insight into the subject of structural mechanics can be found in the technical literature [46] [47].

5.1 Stress Concept

In order to be able to examine a component unit for its mechanical characteristics and its strength, first of all some definitions for the description of the mechanical characteristics must be made. One of the most important is the definition of the mechanical stress $\vec{s}$. For an illustration of this mechanical stress, one can imagine a component placed between two points A and B. Different external loads act on this component, such as forces $\vec{F}$, moments $\vec{M}$ or area loads $\vec{q}$ (see figure 29 left).
These external loads inevitably cause forces to occur inside the component, which are unevenly distributed over its volume and are in equilibrium with the external loads. To define the mechanical stress, a section plane is cut through the component and a small partial area ΔA is considered (see figure 29 mid). The internal stress of this partial area is described by the effective force $\Delta\vec{F}$, whereby it must be added that $\Delta\vec{F}$ represents an averaged, resulting force, since the distribution of the internal stress over the partial area ΔA is non-uniform. To limit the mechanical stress as closely as possible to one point, ΔA must be chosen as small as possible ($\Delta A \rightarrow 0 = dA$). The ratio of $d\vec{F}$ to dA is defined as the mechanical stress [46].

$$\vec{s} = \lim_{\Delta A \to 0} \frac{\Delta \vec{F}}{\Delta A} = \frac{d\vec{F}}{dA} \tag{107}$$

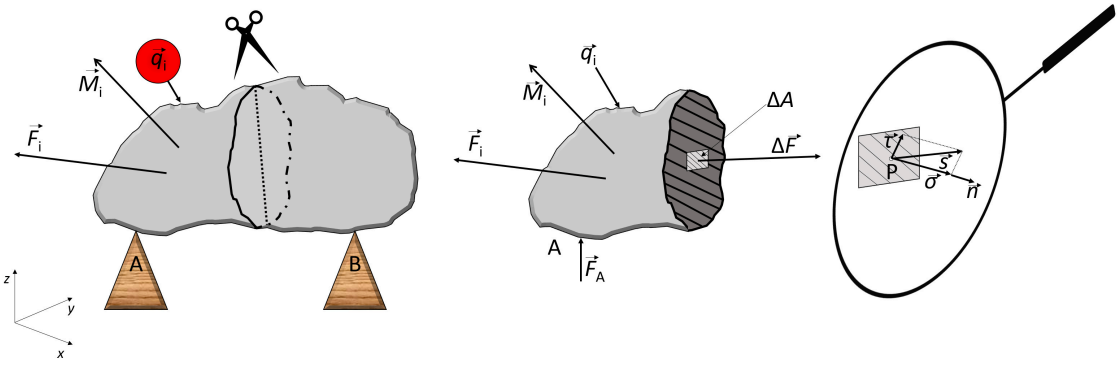

Fig. 29 Illustration of the definition of mechanical stress in a solid. The solid is viewed in a section and the stress in the interior is examined in more detail.

Since the mechanical stress $\vec{s}$ is a vector quantity, it can be divided into two components, the so-called normal stresses σ and the shear stresses τ (see figure 29 right). The normal stress σ represents the part of $\vec{s}$ orthogonal to dA and the shear stress τ the part parallel to dA. If $\vec{s}$ should be orthogonal to dA, the magnitude of the shear stress is equal to 0 [46].

To better distinguish the stress components from each other, indices are introduced. For the shear stresses τ, the first index stands for the direction of the normal vector, for example x, and the second index stands for the direction of the shear stress itself, for example y, resulting in a shear stress of τ_{xy}. For normal stresses σ, a double index is omitted and only the direction of the normal vector is given: σ_x (see figure 30).

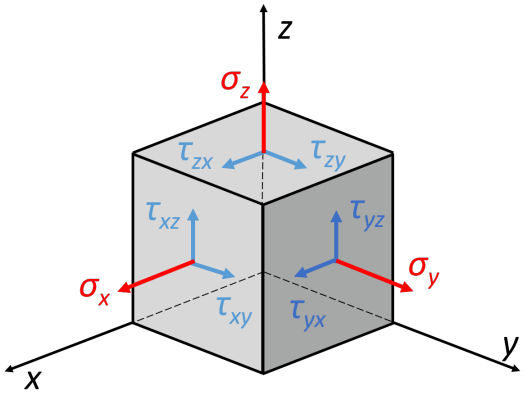

Fig. 30 Indexing of the normal stresses and the shear stresses using the example of a cuboid in cartesian coordinates.

If the stress state of any stressed component at a point P is to be determined (as indicated in figure 29 right), a small cube-shaped section whose edges are parallel to the axes of the coordinate system (see figure 30) must first be examined. There

are three independent normal stresses (σ_x, σ_y and σ_z) and six independent shear stresses (τ_{xy}, τ_{yx}, τ_{xz}, τ_{zx}, τ_{yz} and τ_{zy}) acting on this section. [46].

5.2 Cauchy Stress Tensor

The stress tensor was introduced by Augustin-Louis Cauchy[63] to determine the stress state at any point of a component. For this purpose, the cube-shaped element of the component is cut so that a tetrahedron is formed. On the four surfaces of this tetrahedron (ΔA, ΔA_1, ΔA_2 and ΔA_3) the stresses $\vec{s}$, $\vec{s}_1$, $\vec{s}_2$ and $\vec{s}_3$ appear. These stresses are composed of the normal stresses σ and the shear stresses τ as well as an angle α, β or γ (see figure 31). The stress $\vec{s}$ is given by [46]

$$\vec{s} \cdot \Delta A = \vec{s}_1 \cdot \Delta A_1 + \vec{s}_2 \cdot \Delta A_2 + \vec{s}_3 \cdot \Delta A_3. \tag{108}$$

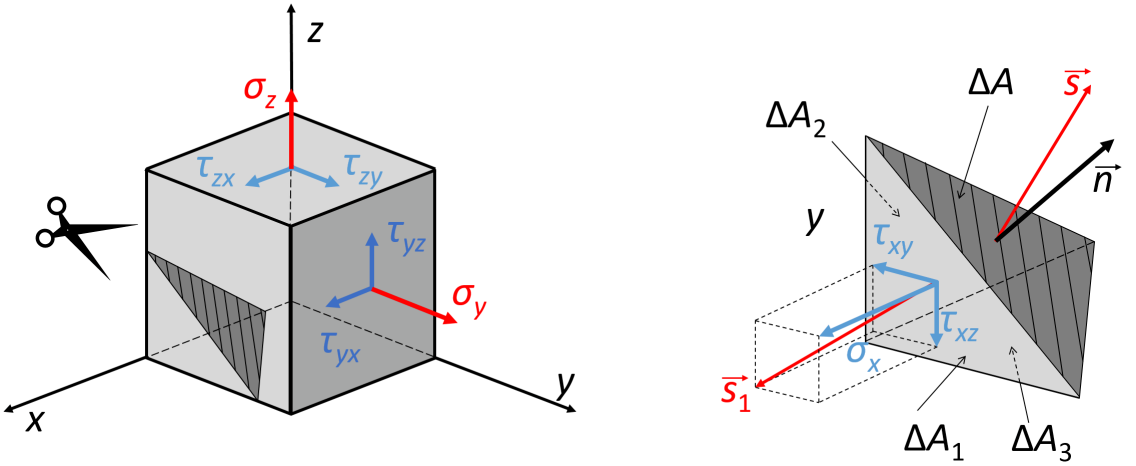

Fig. 31 Section on a cube-shaped element of a component (left) and examination of the stresses acting on the tetrahedron (right).

The determination of the surfaces ΔA_1, ΔA_2 and ΔA_3 is necessary for the further derivation of the stress tensor. For this purpose, different triangles are placed in the tetrahedron to determine the respective edge heights h_1, h_2 and h_3. With the resulting angles α, β and γ the areas can be calculated. Fig 32 shows exemplarily the trigonemtrical relations for the angle γ and the height h_3. The other determinations are made analogously [46].

[63] ⋆21 August 1789 in Paris, France; †23 May 1857 in Sceaux, France

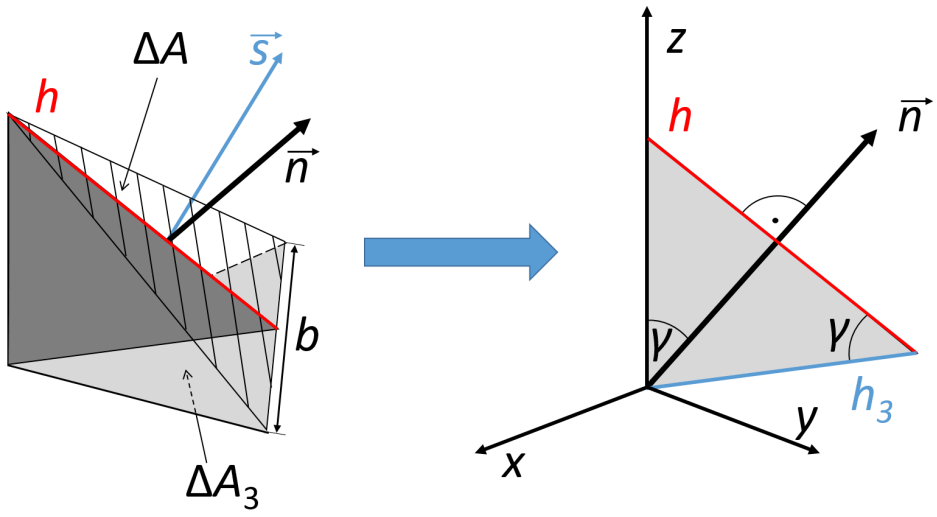

Fig. 32 Determination of h_3 and thus of ΔA_3 based on the trigonmetric analysis of the tetrahedron.

For the surfaces of the triangles applies with base b

$$\Delta A = \frac{1}{2} b \cdot h \quad \text{and} \quad \Delta A_i = \frac{1}{2} b \cdot h_i \quad \text{with } i = 1, 2, 3. \tag{109}$$

Using the trigonometric relationships

$$h_1 = h \cdot \cos(\alpha), \quad h_2 = h \cdot \cos(\beta) \quad \text{and} \quad h_3 = h \cdot \cos(\gamma), \tag{110}$$

the following equations are obtained for the areas

$$\Delta A_1 = \Delta A \cdot \cos(\alpha), \quad \Delta A_2 = \Delta A \cdot \cos(\beta), \quad \text{and} \quad \Delta A_3 = \Delta A \cdot \cos(\gamma). \tag{111}$$

If now the calculations of the areas are put into (108), it results in

$$\vec{s} \cdot \Delta A = \vec{s}_1 \cdot \Delta A \cdot \cos(\alpha) + \vec{s}_2 \cdot \Delta A \cdot \cos(\beta) + \vec{s}_3 \cdot \Delta A \cdot \cos(\gamma) \tag{112}$$

Further simplified to:

$$\vec{s} = \vec{s}_1 \cdot \cos(\alpha) + \vec{s}_2 \cdot \cos(\beta) + \vec{s}_3 \cdot \cos(\gamma). \tag{113}$$

The stresses $\vec{s}_1$, $\vec{s}_2$ and $\vec{s}_3$ acting on the surfaces can now be expressed in terms of the normal stresses and the shear stresses, and thus the stress vector $\vec{s}$ on the section plane ΔA can be determined (see figure 31).

$$\vec{s} = \begin{pmatrix} \sigma_x \\ \tau_{xy} \\ \tau_{xz} \end{pmatrix} \cdot \cos(\alpha) + \begin{pmatrix} \tau_{yx} \\ \sigma_y \\ \tau_{yz} \end{pmatrix} \cdot \cos(\beta) + \begin{pmatrix} \tau_{zx} \\ \tau_{zy} \\ \sigma_z \end{pmatrix} \cdot \cos(\gamma) \tag{114}$$

(114) can also be expressed in matrix notation:

$$\vec{s} = \begin{pmatrix} s_x \\ s_y \\ s_z \end{pmatrix} = \begin{pmatrix} \sigma_x & \tau_{yx} & \tau_{zx} \\ \tau_{xy} & \sigma_y & \tau_{zy} \\ \tau_{xz} & \tau_{yz} & \sigma_z \end{pmatrix} + \begin{pmatrix} \cos(\alpha) \\ \cos(\beta) \\ \cos(\gamma) \end{pmatrix} \tag{115}$$

Where here the 3x3 matrix in the center represents the stress tensor $\boldsymbol{S}$ [46]:

$$\boldsymbol{S} = \begin{pmatrix} \sigma_x & \tau_{yx} & \tau_{zx} \\ \tau_{xy} & \sigma_y & \tau_{zy} \\ \tau_{xz} & \tau_{yz} & \sigma_z \end{pmatrix} \tag{116}$$

It consists of the three normal stresses, which are located on the diagonal, and the shear stresses. However, since three pairs of shear stresses are equal, the number of shear stresses within the stress tensor is reduced from six to three. These equal shear stresses, acting in section planes orthogonal to each other and either leading toward or away from a common section edge, are called associated shear stresses [46]. In this way, the following applies

$$\tau_{xy} = \tau_{yx}, \quad \tau_{xz} = \tau_{zx}, \quad \text{and} \quad \tau_{yz} = \tau_{zy}. \tag{117}$$

The stress tensor can therefore also be written as:

$$\boldsymbol{S} = \begin{pmatrix} \sigma_x & \tau_{xy} & \tau_{xz} \\ \tau_{xy} & \sigma_y & \tau_{yz} \\ \tau_{xz} & \tau_{yz} & \sigma_z \end{pmatrix} \tag{118}$$

5.3 Principal Stress

In order to examine a component for its strength, the stress tensor must be adjusted so that it contains the so-called principal normal stresses (σ_{P1}, σ_{P2} and σ_{P3}). For this purpose, the previously considered cube element is rotated until the shear stresses disappear and the normal stresses reach an extreme value (see figure 33). This is the case when the principal normal vectors $\vec{n}_{\mathrm{P}i}$ and the stresses $\vec{s}_{\mathrm{P}i}$ are parallel to each other, which is not the case in the normal case. If they are parallel after the rotation of the cube element, the stresses are equal to the normal stresses ($\vec{s}_{\mathrm{P}i} \equiv \vec{\sigma}_{\mathrm{P}i}$) [46].

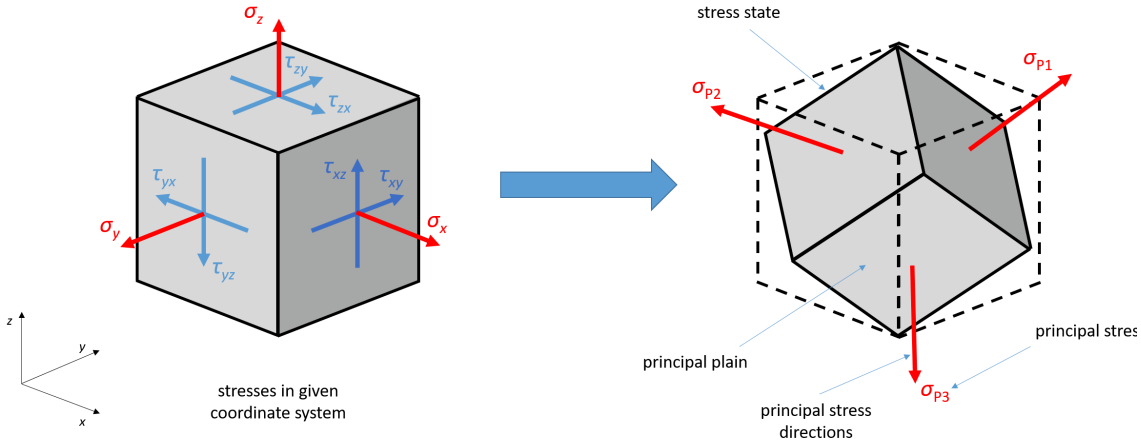

Fig. 33 Schematic representation to visualize the definition of the principal stresses. For this purpose, the general stress state is rotated so that the shear stresses disappear and the normal stresses $(\sigma_x, \sigma_y, \sigma_z)$ reach extreme values. These normal stresses then correspond to the principal stresses $(\sigma_{\mathrm{P1}}, \sigma_{\mathrm{P2}}, \sigma_{\mathrm{P3}})$.

Thereby, the principal normal stresses can be expressed as a multiple of the normal unit vectors by the magnitude of the principal stresses

.

$$\vec{\sigma}_{\mathrm{P}i} = \sigma_{\mathrm{P}i} \cdot \vec{n}_{\mathrm{P}i} \qquad \text{with } i = (1, 2, 3) \tag{119}$$

$$\begin{pmatrix} \sigma_{\mathrm{P}i\,x} \\ \sigma_{\mathrm{P}i\,y} \\ \sigma_{\mathrm{P}i\,z} \end{pmatrix} = \sigma_{\mathrm{P}i} \cdot \begin{pmatrix} \cos(\alpha_i) \\ \cos(\beta_i) \\ \cos(\gamma_i) \end{pmatrix} \qquad \text{with } i = (1, 2, 3). \tag{120}$$

The principal stress normal vectors $\vec{\sigma}_{\mathrm{P}i}$ can also be expressed in matrix notation by the stress tensor $\boldsymbol{S}$ and the normal unit vectors $\vec{n}_{\mathrm{P}i}$.

$$\begin{pmatrix} \sigma_{\mathrm{P}i\,x} \\ \sigma_{\mathrm{P}i\,y} \\ \sigma_{\mathrm{P}i\,z} \end{pmatrix} = \begin{pmatrix} \sigma_x & \tau_{xy} & \tau_{xz} \\ \tau_{xy} & \sigma_y & \tau_{yz} \\ \tau_{xz} & \tau_{yz} & \sigma_z \end{pmatrix} + \begin{pmatrix} \cos(\alpha_i) \\ \cos(\beta_i) \\ \cos(\gamma_i) \end{pmatrix}. \tag{121}$$

Equating and transforming (120) and (121) results in a homogeneous linear system of equations for the direction cosine of the normal vectors of the individual principal stresses and principal stress planes [46].

$$\begin{aligned} (\sigma_x - \sigma_{\mathrm{P}i}) \cdot \cos(\alpha_i) + \tau_{xy} \cdot \cos(\beta_i) + \tau_{xz} \cdot \cos(\gamma_i) &= 0 \\ \tau_{xy} \cdot \cos(\alpha_i) + (\sigma_y - \sigma_{\mathrm{P}i}) \cdot \cos(\beta_i) + \tau_{yz} \cdot \cos(\gamma_i) &= 0 \\ \tau_{xz} \cdot \cos(\alpha_i) + \tau_{yz} \cdot \cos(\beta_i) + (\sigma_z - \sigma_{\mathrm{P}i}) \cdot \cos(\gamma_i) &= 0 \end{aligned} \tag{122}$$

This system of equations has non-trivial solutions only if the determinant of the coefficient matrix is zero.

$$\det(\boldsymbol{S} - \sigma_{\mathrm{P}i}\boldsymbol{E}) \begin{vmatrix} \sigma_x - \sigma_{\mathrm{P}i} & \tau_{xy} & \tau_{xz} \\ \tau_{xy} & \sigma_y - \sigma_{\mathrm{P}i} & \tau_{yz} \\ \tau_{xy} & \tau_{yz} & \sigma_z - \sigma_{\mathrm{P}i} \end{vmatrix} = 0 \tag{123}$$

Here $\boldsymbol{E}$ is the unit matrix and (123) is also called the characteristic equation. The solution of this equation gives the eigenvalues σ_{H1}, σ_{H2} and σ_{H3} of the stress matrix $\boldsymbol{S}$ and thus the desired principal stresses. The calculation of the determinant leads to a third order equation, the so-called eigenvalue equation. The mathematical derivation of this equation will be omitted at this point, instead reference shall be made to the corresponding literature [48]. The eigenvalue equation is:

$$\vec{\sigma}^3_{\mathrm{P}i} - I_1\vec{\sigma}^2_{\mathrm{P}i} + I_2\vec{\sigma}_{\mathrm{P}i} - I_3 = 0 \tag{124}$$

Where here the coefficients I_1, I_2 and I_3 of the eigenvalue equation are the invariants of the stress tensor. These are derived from [46]

$$\begin{aligned} I_1 &= \sigma_x + \sigma_y + \sigma_z \\ I_2 &= \sigma_x \cdot \sigma_y + \sigma_y \cdot \sigma_z + \sigma_x \cdot \sigma_z - \tau^2_{xy} - \tau^2_{yz} - \tau^2_{xz} \\ I_3 &= \sigma_x \cdot \sigma_y \cdot \sigma_z + 2 \cdot \tau_{xy} \cdot \tau_{yz} \cdot \tau_{xz} - \sigma_x \cdot \tau^2_{yz} - \sigma_y \cdot \tau^2_{xz} - \sigma_z \cdot \tau^2_{xy}. \end{aligned} \tag{125}$$

By introducing principal normal stresses and transforming them into the principal stress axis system, the stress state in any point P of any body can now be described by the three principal normal stresses σ_{H1}, σ_{H2} and σ_{H3}. Thus, the stress state no longer depends on shear stresses, since for a three-dimensional stress state there are three mutually orthogonal, shear stress-free sectional planes at each point of a component. It is convention that the largest principal normal stress in magnitude is referred to as σ_{H1} and then numbers progressively from large to small [46].

$$\sigma_{\mathrm{H1}} > \sigma_{\mathrm{H2}} > \sigma_{\mathrm{H3}} \tag{126}$$

5.4 Strength Hypotheses

It is of great interest to consider a component in terms of its maximum mechanical load capacity. For this purpose, a distinction is made between yield stress (yielding) and tensile strength (breaking). However, since a large number of different loads are applied simultaneously to real component, they usually exhibit a multiaxial stress state, such as bending with superimposed torsion or multiaxial tensile loading. The question here is which stress and which combination of different stresses ultimately led to the failure of the component. This question cannot be answered experimentally, instead, so-called strength hypotheses have been developed to differentiate the various combinations of stresses. A strength hypothesis is a transfer function in which the multiaxial stress state is transformed into an equivalent, fictitious uniaxial stress state σ_{v}. This uniaxial stress state σ_{v} is also called equivalent tensile stress and represents the total stress state as uniaxial normal stress and thus allows a direct comparison with uniaxially determined characteristic values from tensile

tests. It should be noted that this way of considering the total stress state is only an approximation and some information may be lost in the transformation. The condition for the failure of a component is that [46]

$$\sigma_v \leq \sigma_y \tag{127}$$

must be valid. Where σ_y is the material-dependent maximum load limit before failure. Different strength hypotheses are distinguished, which involve different calculations of σ_v depending on the material behaviour (see figure 34 left). The three most frequently used strength hypotheses are:

- Maximum Normal Stress Failure Theory (maximum normal stess)
- Tresca[64] Yield Condition (maximum shear stress)
- von Mises[65] - Yield Criteria (maximum distortional energy)

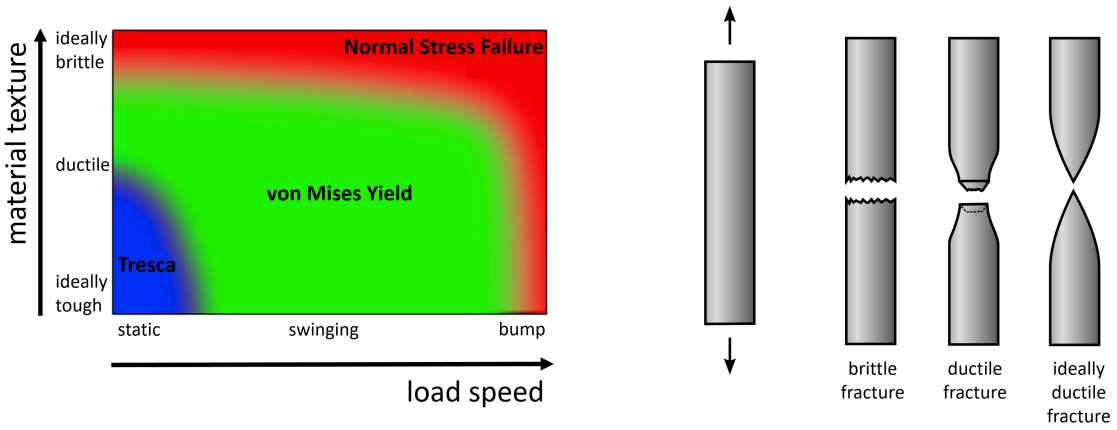

Fig. 34 Left: Exemplary distribution of the strength hypotheses used depending on material properties and load conditions [49]. Right: Schematic representation of different failures depending on material properties [50].

Apart from these three hypotheses, there are a large number of other hypotheses which, however, are used much less in practical applications. Since in this thesis the cavities to be investigated were analysed with the programs CST Studio Suite [40], and this program analyses the material for the von Mises yield criterion, only the von Mises yield criterion will be explained in more detail in the following. For

[64] named after Henri Tresca (⋆12 October 1814 in Dunkirk, France; †21 June 1885 in Paris, France)

[65] named after Richard Edler von Mises (⋆19 April 1883 in Lemberg, Austria; †14 July 1953 in Boston, USA)

a more detailed insight into the other strength hypothesis, reference shall be made to the literature [46] [47].

5.4.1 The von Mises Yield Criterion

As already mentioned, strength hypotheses are an approximation to describe a complex multidimensional loading of a body by a uniaxial stress σ_{v} to such an extent that a well-founded statement can be made about the behaviour of the body under consideration regarding its failure. The von Mises yield criterion is a common hypothesis to make statements about isotropic and ductile metals. If a force acts on such a material, it stretches by the strain ϵ and/or distorts by the distortion γ. These two quantities are thereby directly proportional to the normal stresses σ and the shear stresses τ [47]:

$$\sigma = E \cdot \epsilon \tag{128}$$
$$\tau = G \cdot \gamma \tag{129}$$

The two proportionality factors E and G are material constants and are called elastic modulus E and shear modulus G. Since an elastic material is considered here, it should be noted that a spatial expansion in one spatial direction results in an automatic compression ϵ_p in the other directions [47].

$$\epsilon_p = -\nu\epsilon \tag{130}$$

Here ν is also a material constant and is called Poisson's constant[66]. With this further material constant, E and G can also be correlated [47]

$$E = 2G(1+\nu). \tag{131}$$

For simplification, the stressed body is considered in the principal axis system introduced above, so that shear stresses τ_{ij} no longer occur. A stretching in the direction of one of the principal normals causes a compression in the other two directions.

$$\epsilon_{\mathrm{P1}} = \frac{\sigma_{\mathrm{P1}}}{E}; \qquad \epsilon_{\mathrm{P2}} = -\nu\frac{\sigma_{\mathrm{P1}}}{E}; \qquad \epsilon_{\mathrm{P3}} = -\nu\frac{\sigma_{\mathrm{P1}}}{E} \tag{132}$$

If a stress occurs in one of the other two main directions, the occurring strains are calculated analogously. If these strains of all three stress directions are combined, the result is simplified as follows [47]:

[66] named after Siméon Denis Poission (⋆21 June 1781 in Pithiviers, France; †25 April 1840 in Paris, France)

$$\epsilon_{\mathrm{P1}} = \frac{1}{E}[\sigma_{\mathrm{P1}} - \nu(\sigma_{\mathrm{P2}} + \sigma_{\mathrm{P3}})] \tag{133}$$

$$\epsilon_{\mathrm{P2}} = \frac{1}{E}[\sigma_{\mathrm{P2}} - \nu(\sigma_{\mathrm{P1}} + \sigma_{\mathrm{P3}})] \tag{134}$$

$$\epsilon_{\mathrm{P3}} = \frac{1}{E}[\sigma_{\mathrm{P3}} - \nu(\sigma_{\mathrm{P1}} + \sigma_{\mathrm{P2}})] \tag{135}$$

If an external load acts on a body and it is stretched, work is done on it and this is stored in it in the form of energy. This energy U is divided into a hydrostatic part U_{h} and a deviatoric part U_{d} [47].

$$U = U_{\mathrm{h}} + U_{\mathrm{d}}. \tag{136}$$

Hydrostatic means that the shape of the body does not change, so all stresses in all spatial directions are equal in magnitude, but the volume is variable, while deviatoric means that the volume is constant, but the shape of the body changes. This stored energy can be expressed by the strains and principal normal stresses

$$U = \frac{1}{2}(\sigma_{\mathrm{P1}}\epsilon_{\mathrm{P1}} + \sigma_{\mathrm{P2}}\epsilon_{\mathrm{P2}} + \sigma_{\mathrm{P3}}\epsilon_{\mathrm{P3}}) \tag{137}$$

Inserting (133) to (135) into (137) results in

$$U = \frac{1}{2E}(\sigma_{\mathrm{P1}}^2 + \sigma_{\mathrm{P2}}^2 + \sigma_{\mathrm{P3}}^2 - 2\nu(\sigma_{\mathrm{P1}}\sigma_{\mathrm{P2}} + \sigma_{\mathrm{P2}}\sigma_{\mathrm{P3}} + \sigma_{\mathrm{P1}}\sigma_{\mathrm{P3}})). \tag{138}$$

As mentioned above, the energy U_{h} is hydrostatic in nature, which means that all principal normal stresses are equal

$$\sigma_{\mathrm{P1}} = \sigma_{\mathrm{P2}} = \sigma_{\mathrm{P3}} = \frac{\sigma_{\mathrm{P1}} + \sigma_{\mathrm{P2}} + \sigma_{\mathrm{P3}}}{\sigma_{\mathrm{P2}}} = \sigma_{\mathrm{hyrd}} \tag{139}$$

Where here σ_{hyrd} corresponds to an averaged hydrostatic stress. From this follows from (137) [47]

$$U_{\mathrm{h}} = \frac{1-2\nu}{2E}3 \cdot \sigma_{\mathrm{hyrd}}^2 \quad \Rightarrow \quad U_{\mathrm{h}} = \frac{1-2\nu}{6E}(\sigma_{\mathrm{P1}} + \sigma_{\mathrm{P2}} + \sigma_{\mathrm{P3}})^2. \tag{140}$$

In the von Mises yield criterion considered here, however, it is assumed that only the deviatoric part of the energy U_{d} is responsible for the failure of the material. This is calculated with the use of (137) and (140) to be [47]

$$U_{\mathrm{d}} = U - U_{\mathrm{h}} = \frac{1-\nu}{3E}\left[(\sigma_{\mathrm{P1}} - \sigma_{\mathrm{P2}})^2 + (\sigma_{\mathrm{P2}} - \sigma_{\mathrm{P3}})^2 + (\sigma_{\mathrm{P1}} - \sigma_{\mathrm{P3}})^2\right]. \tag{141}$$

To obtain uniaxial equivalent stress state σ_{v} of the von Mises yield criterion necessary for a strength hypothesis, the equivalent stress must be chosen to correspond

to the multidimensional stress state. For this purpose

$$\sigma_{\mathrm{v}} = \begin{pmatrix} \sigma_{\mathrm{v}} \\ 0 \\ 0 \end{pmatrix} \tag{142}$$

must provide the same shape change energy. Substituting this into (141), it results in

$$U_{\mathrm{d}} = \frac{1-\nu}{3E}\left[(\sigma_{\mathrm{v}}-0)^2 + (0-0)^2 + (\sigma_{\mathrm{v}}-0)^2\right]. \tag{143}$$

If (141) and (143) are set equal, the equivalent stress state for the von Mises yield criterion is given by

$$\sigma_{\mathrm{v,\ von\ Mises}} = \frac{1}{\sqrt{2}} \cdot \sqrt{(\sigma_{\mathrm{P1}}-\sigma_{\mathrm{P2}})^2 + (\sigma_{\mathrm{P2}}-\sigma_{\mathrm{P3}})^2 + (\sigma_{\mathrm{P3}}-\sigma_{\mathrm{P1}})^2}. \tag{144}$$

Where (126) applies here. This uniaxial equivalent stress state can be compared with values determined experimentally from tensile tests to make statements about the properties of the component with regard to failure.

6 Goals of the Thesis

In the following three chapters, the results obtained in the course of this thesis will be explained in more detail.

In the first of these three sections, the measurement results of the cold test of cavity CH2 of the HELIAC project are presented and evaluated. These include the pressure sensitivity, the frequency response to temperature change and the RF properties of the cavity.

The next chapter contains the main part of this thesis. Here, the developed concept for a modular cavity design is explained. This method for the development of superconducting cavities is novel and allows to design superconducting CH cavities at low cost as well as to manufacture them later. This makes mass production of superconducting CH cavities possible for the first time. For this purpose, the method was not only developed but also tested for its actual suitability by various simulations. These simulation results are also explained and analysed in this chapter.

In the last of the next three chapters, the concept and operation of a test bench for investigating the mechanical properties of dynamic bellow tuner made of Niobium is explained, and the simulation results, which were necessary for determining the suitability of this test bench for subsequent operation, are presented and analysed.

7 Cold Measurement of the CH2 Cavity

As part of the HELIAC project of GSI, HIM and IAP, three superconducting CH cavities have been designed and built up to the date of this thesis. Cavity CH0, which was designed and built as a demonstrator cavity [27], has been successfully tested for its RF properties in the cold state in a vertical cryostat and has already successfully accelerated a beam of charged particles. The cavities CH1 and CH2, which have been designed structurally identical, were designed and built as part of Markus Basten's PhD thesis [1]. In the process, cavity CH1 was also successfully tested for its RF properties in the cold state [1]. The design of these two cavities is thereby based on the design of the CH structures of the injector design C by Dominik Mäder [51]. Special attention was paid to the manufacturability of the cavities, so that both production time and production costs were reduced. As shown in figure 35, CH1 and CH2 are based on a simple cylindrically symmetrical geometry in which a total of seven spokes were installed, which are completely flooded with liquid Helium so that the cavities each have eight accelerating gaps. The conical sunken lids of the cavities reduce the pressure sensitivity of the tank and eliminate the need to use beveled spokes, as was still done with CH0, so that only one type of spoke had to be manufactured, which reduced costs. A total of four tuners were installed per cavity, with two variable-height dynamic bellow tuner and two static tuner [1]. Tab. 2 lists the main design parameters of CH1 and CH2.

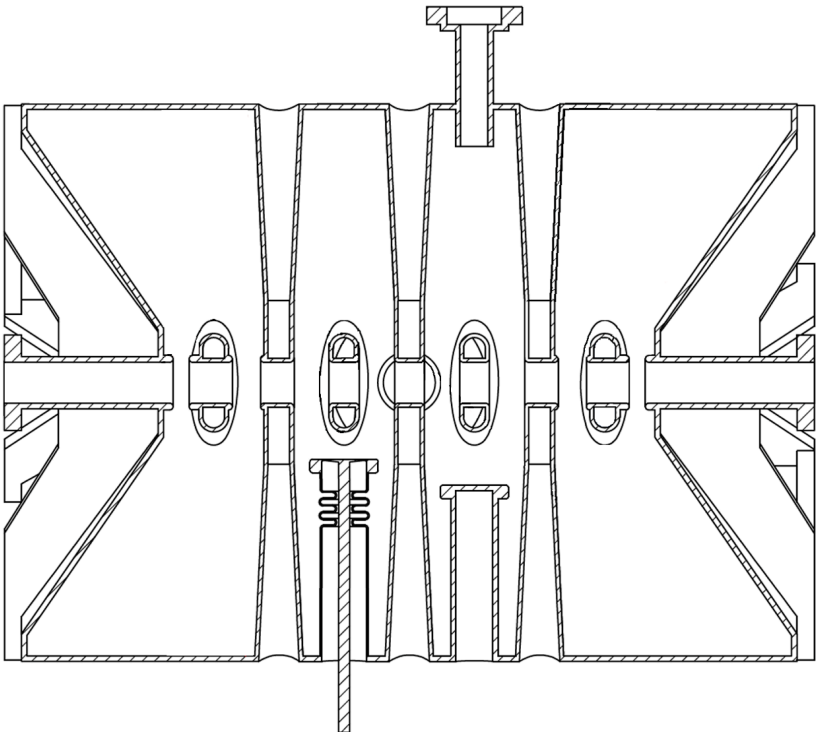

Fig. 35 Technical drawing of the superconducting cavities CH1/CH2 [1].

Tab. 2 Overview of the most important parameters of the superconducting cavities CH1/CH2 of HELIAC [1].

Parameter	Unit	
β		0.069
design frequency (f_{des})	MHz	216.816
effective length (L_{eff})	mm	381.6
total length (L_{tot})	mm	593
inner radius (r_{in})	mm	400
wall thickness of spokes / tank	mm	3 / 4
wall thickness dynamic tuner	mm	1
number of dynamic / static tuner		2 / 3
acceleration field ($E_{\mathrm{eff}}^{\mathrm{design}}$)	MV/m	5.5
acceleration voltage ($U_{\mathrm{eff}}^{\mathrm{design}}$)	MV	2.1
Q-factor (Q_0^{design})		$3 \cdot 10^8$
geometric shunt impedance (R_{a}/Q_0)	Ω	1050
geometry factor G	Ω	51
electric peak fields ($E_{\mathrm{peak}}/E_{\mathrm{a}}$)		6.5
magnetic peak fields ($B_{\mathrm{peak}}/E_{\mathrm{a}}$)	mT/(MV/m)	8.5

Following the design of these two structurally identical cavities, they were manufactured by Research Instruments (RI)[67]. Before the Helium vessel of cavity CH1 was attached by RI, it was successfully tested by Markus Basten for its RF properties in the cold state at IAP Frankfurt [1]. After these tests, the cavity was transported back to RI for attachment of the Helium vessel. In figure 36 is an exploded view of the CH1/CH2 as well as a three-quarter cross-section of the cavities including the Helium vessel. In the next section of this thesis, the follow-up superconducting cavity CH2 is investigated for its RF properties in the cold state at 4 K. A cold test for CH2 has already been started once, but it had to be stopped early due to the occurrence of a cold leak [1]. For this purpose, the behaviour during cooling and heating of the cavity, the pressure sensitivity, the behaviour during conditioning, as well as the maximum field gradient were investigated.

[67] RI Research Instruments GmbH, Bergisch Gladbach, Germany

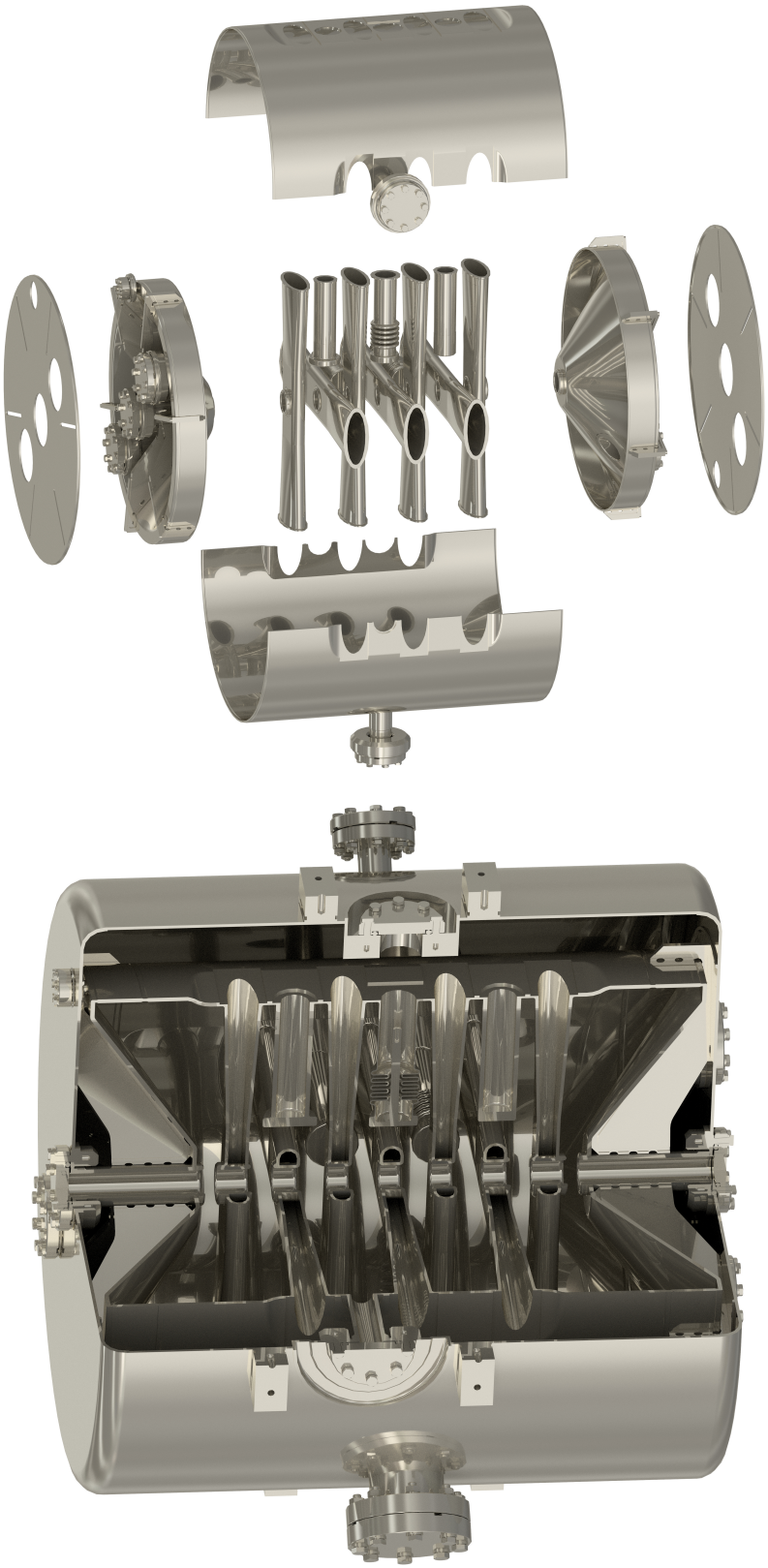

Fig. 36 Top: Exploded view of the CH1/CH2 superconducting cavity without Helium vessel as designed at IAP Frankfurt. Bottom: A three-quarter cross-section of the CH1/CH2 cavity with the Helium vessel attached [1].

7.1 Measurement Setup for RF-investigation

The complete investigation of a cavity for its RF properties requires a large number of different instruments and measuring devices. A direct comparison of the measurement setups for characterizing a normal conducting cavity and a superconducting cavity reveals some similarities as well as some serious differences. For instance, most of the measurement equipment and instruments are the same for both types of cavities. The most obvious of the differences is the cooling of the cavity. For normal conducting cavities, it is generally necessary only to cool the heat generated by the dissipated power, which can be done by installing cooling water channels, whereas for superconducting cavities it is mandatory to keep the entire cavity below the critical threshold temperature of the material used. This fact complicates the characterization of a superconducting cavity enormously compared to a normal conducting one. In the following sections, both the necessary cryostatic infrastructure and the electrical equipment required to control and monitor the cavity in the measurement setup used will be explained.

7.1.1 Cryogenic Infrastructure of the Measurement Setup

In order to be able to investigate the cavity for its RF properties, it must first be cooled to a temperature below the critical temperature of Niobium (9.2 K) so that it enters the superconducting state. For this purpose, liquid Helium is used as a coolant, since its temperature is around 4 K, which is below said transition temperature. To ensure that the cavity is completely surrounded by the liquid Helium, it is immersed in a vertical bath cryostat (see figure 37). The volume of the inner Helium reservoir of the cryostat comprises about $V_{\text{He-reservoir}} \approx 625\,\text{l}$ when completely empty. For better isolation from environmental temperature, the inner Helium reservoir is isolated by a Nitrogen shield, in which liquid Nitrogen is filled, whose temperature is about 77.2 K. The volume of the Nitrogen shield is approximately $V_{\text{N-shield}} \approx 470\,\text{l}$. Another isolation layer between the Helium reservoir and the environmental temperature is provided by an isolation vacuum created in the walls of the cryostat. This elaborate isolation is necessary to keep the resulting Helium losses as low as possible. The Helium evaporated during the cold test of the cavity is returned via a recirculation system to the in-house Helium supply facility of the Goethe University Frankfurt. Here, the Helium gas is collected in large gas balloons and then re-liquefied by two compressors and filled into cans as required. The amount of Helium flowing back from the cryostat was measured by two Helium gauges, which cover different measuring ranges. The first dial gauge from the company Höntzsch[68] with a measuring range of $0.04 - 740\,\text{m}^3\text{h}^{-1}$ is suitable for larger gas quantities and the second dial indicator of the company Vögtlin[69] with a measuring range of $0 - 0.036\,\text{m}^3\text{h}^{-1}$ for smaller gas quantities. Two valves can be used to switch back and

[68] Höntzsch GmbH & Co. KG, Wiblingen, Germany
[69] Vögtlin Instruments GmbH, Muttenz, Switzerland

forth between the two Helium gauges. To avoid freezing of the dial gauges and the return line, the out flowing Helium is warmed up in a water bath heated by an immersion heater. The inlet for the Nitrogen shield is located at the upper edge of the cryostat wall, while the inlet for the liquid Helium is located in the lid of the cryostat.

The lid of the cryostat is also shielded by several isolation layers of styrofoam and several radiation shields. On this lid, in addition to the Helium inlet and outlet, there are all the other cold-warm feedthroughs for the measuring instruments that are required for monitoring and measurements during the cold test. The cavity itself was mounted on the lid by an Aluminium holding frame, which is attached to the lid and thus sunk into the cryostat when it is closed. At the cavity directly, a total of 8 temperature sensors were installed, prior to being lowered into the cryostat. The temperature sensors are read out by a Model 218 temperature monitor from LakeShore[70] and associated software. This sensors were distributed over the entire cavity. Thus, there was one sensor on each of the two lids, one in a spoke in the spoke row containing three spokes, one in a spoke in the spoke row containing four spokes, one exactly in the center of the cavity, and three in a circle around the cavity at the level of the sensor in the spoke of the three-spoke row. This distribution of sensors over the entire cavity made it possible to calculate an average temperature of the cavity and also to determine a temperature gradient between the top and bottom, which can occur during cooling and heating or during measurements with increased power. In addition to temperature, an important operating variable to observe were the pressure both inside the cryostat (p_{cryostat}) and inside the cavity (p_{cavitiy}). For the measurement of p_{cavitiy}, the pressure gauge from Pfeiffer Vacuum[71] PKR 251 was used. p_{cryostat}, in turn, was measured by the CPT 200 pressure gauge, also from Pfeiffer Vacuum. Both pressure measurements were thereby taken at the lid of the cryostat, so that the measurement of p_{cavitiy} was taken about 2 m away from the actual cavity. Therefore, it can be assumed that the actual pressure inside the cavity differed from the measured p_{cavitiy}. The deviation can be estimated to an order of one magnitude. The cavity has already been accepted evacuated and a value of $p_{\mathrm{cavitiy}} \approx 1 \times 10^{-10}$mbar was maintained during operation by an ion getter pump, which was also placed on the lid of the cryostat. Finally, a heater was attached to the cavity so that the remaining Helium in the cryostat could be heated more quickly after the cold test was completed.

[70] LakeShore Cryotronics Westerville, OH, USA
[71] Pfeiffer Vacuum GmbH Asslar, Germany

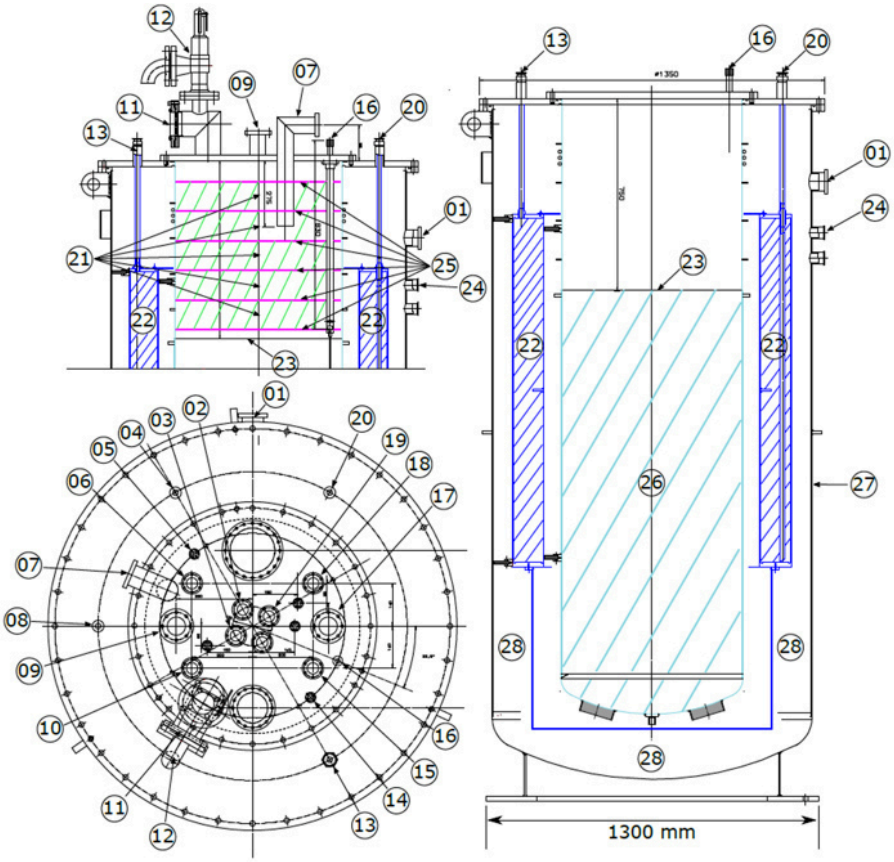

01 vacuum safety valve
02 He pressure relief valve 1
03 RF outcoupling signal
04 N_2 exhaust
05 fill level He (liquid)
06 piezo sensor 1
07 He exhaust
08 N_2 pressure relief valve
09 pressure gauge / vacuum pump Cavity
10 heater port
11 rupture disc
12 He pressure relief valve 2
13 fill level N_2 (liquid)
14 Dewar analog pressure gauge
15 Dewar digital pressure gauge
16 He (liquid) inlet
17 temperature sensor
18 Piezo sensor 2
19 RF coupling signal
20 N_2 (liquid) inlet
21 isolation layer
22 N_2 (liquid) isolation layer
23 Maximum filling level He (liquid)
24 pressure gauge isolation vacuum
25 radiation shields
26 He Dewar
27 cryostat outer wall with µ-metal shield
28 Isolation vacuum

Fig. 37 Schematic drawing of the cryostat used here with all necessary components. Top view of the lid (bottom left) and cross-sections of the lid (top left) and the cryostat (right) [1].

7.1.2 RF-Investigation Infrastructure of the Measurement Setup

The setup of the infrastructure for investigating the RF properties is similar to that of a normal-conducting cavity, as described earlier, and is shown schematically in figure 38. First, a high-frequency signal is generated by an RF signal generator. The amplitude of this signal is of a small value and does not exceed 10 mW. This signal is transmitted to the control system, where both the amplitude and the phase of the signal can be adjusted manually. However, the main purpose of the control system is to automatically readjust the frequency and phase of the generated RF signal from the RF signal generator. For this purpose, the generated RF signal is compared with the RF signal extracted from the cavity and a phase shift is calculated. A corresponding voltage is assigned to this phase shift and transmitted to the voltage-controlled oscillator (VCO) integrated in the RF signal generator. This incoming voltage is then used to readjust the generated RF signal. This type of automatic frequency control is called self-excited loop mode. By means of a pulse generator integrated into the control system, the output RF signal can be pulsed so that the continuous signal becomes a square wave pulse. This is necessary to be able to determine the coupler factor β from the on and off swing signal of the cavity (see section 3.2.6).

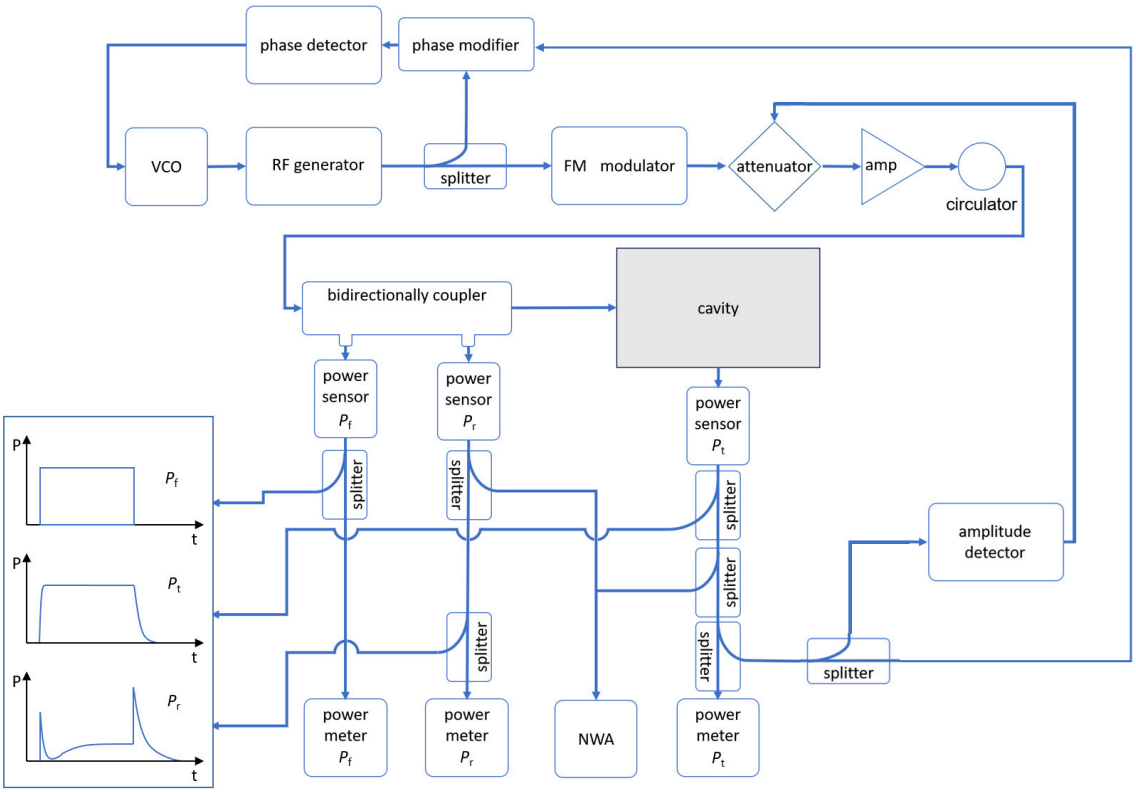

Fig. 38 Sketch of the experimental setup of the cold test of CH2 with liquid Helium at the IAP Frankfurt.

After the control system, the RF signal is injected through a circulator into a 50 W broadband amplifier where it is amplified. Before the cavity, the RF signal is split into two signal paths by a bidirectional coupler, where the diverted signal is used to measure P_f corresponds to only a fraction of the signal passed on to the cavity. A third output of the bidirectional coupler decouples the power P_r reflected from the cavity. Both powers are forwarded to an oscilloscope on the one hand and measured by a power sensor on the other, which has been appropriately calibrated to remove all cable paths and additional components from the measurement. At the pick-up, P_t is also passed to both an oscilloscope and a power sensor. The values read out by the power sensors can be viewed on powermeters on the one hand, and on the other hand were graphically displayed and stored directly by a software on a computer. In addition to the values of the power, also both the values of p_cavity and p_cryostat as well as both flows of the two Helium clocks were graphically displayed and stored by the software.

7.2 Cooling of the Cavity to 4 K

After closing the cryostat with the cavity inside (see figure 39), the inner Helium reservoir was flushed out with two cans of liquid Helium, each having a volume of $V_\mathrm{bottle\ He} \approx 250\,\mathrm{l}$. Then, the isolation shield was started to be filled with liquid Nitrogen. A can of liquid Nitrogen has a volume of $V_\mathrm{bottle\ N} \approx 200\,\mathrm{l}$ in this case. Once the isolation shield was about half full, the Helium reservoir was started to be filled at the same time. During the filling of the Helium reservoir a recording of the temperature, frequency and Q-factor could not be done due to a software bug. These measurements were repeated when the cavity was reheated (see section 7.7). Special care was taken to pass through the temperature range of 150 – 60 K as fast as possible and without delay to avoid the formation of Niobium hybrids (see section 7.2.1).

During the closing of the cryostat lid, the Helium level sensor wire was accidentally pinched between the lid and the cryostat and tore off, so that no direct electronic measurement of the liquid Helium level was possible. Nevertheless, in order to have a rough estimation of the current level of the Helium tank, an estimation was made based on the filled Helium cans and the returned Helium flow. For this purpose the equation

$$V_\mathrm{He,\,l} = N_\mathrm{bottle} \cdot 200\,\mathrm{l}_l - (V_\mathrm{clock\ now,\,g} - V_\mathrm{clock\ start,\,g}) \cdot 1.43\,{}^{\mathrm{l}}/_{\mathrm{m_g^3}} \tag{145}$$

was used. Because before the first Helium bottle was filled the state of the Helium clock of the experimental hall of the IAP Frankfurt was noted and this experiment was the only experiment using liquid Helium at that time, the total amount of consumed Helium could be calculated with the state of the Helium clock at the beginning ($V_\mathrm{clock\ start,\,g}$) and the current state ($V_\mathrm{clock\ now,\,g}$). The factor of volume increase between liquid Helium and gaseous Helium corresponds to about $1.43\,{}^{\mathrm{l}}/_{\mathrm{m^3}}$.

This factor must be used because the amount of Helium filled corresponds to liquid Helium, but the amount of Helium returned corresponds to gaseous Helium. The quantity to be estimated was now the amount of Helium filled to that point. A Helium bottle has a volume $V_{\text{bottle He}}$ of approximately $V_{\text{bottle He}} \approx 250\,\text{l}$. However, since some residual liquid is always left in the can to prevent the can from warming up and thus facilitate refilling and cause less evaporation of the liquid Helium, a volume $V_{\text{bottle He drained}}$ of approximately $V_{\text{bottle He drained}} \approx 200\,\text{l}$ was assumed to be filled per bottle. Thus, multiplying the estimated volume per can by the number of cans gives the completely filled volume of liquid Helium. Subtracting the completely refluxed volume and converted Helium from the estimated complete volume of liquid Helium gives the estimated level of liquid Helium inside the cryostat. A plot of the estimated level against the duration of the cold test is shown in figure 40.

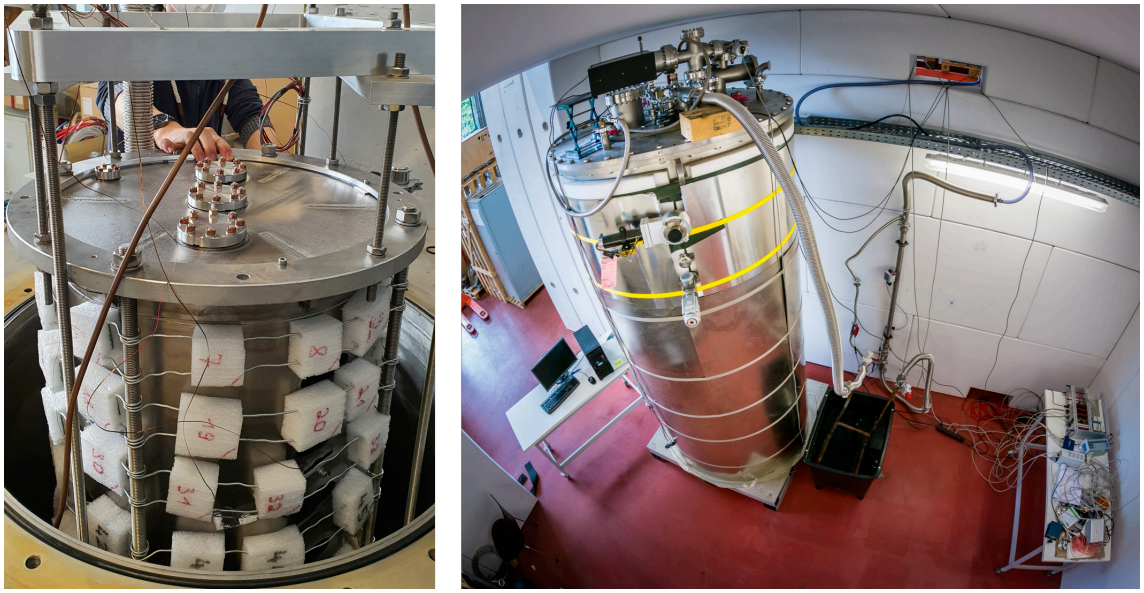

Fig. 39 Left: Image taken while closing the cryostat. Right: (archive image cold test CH1 [1]): the closed cryostat with finished assembly. To the right of the cryostat is the water basin used to warm up the Helium reflux.

The blue line in figure 40 indicates the point in time from which it was clear that the estimated level could no longer match the actual level. Previously, it was indeed possible to determine the amount of Helium needed to be refilled using the equation (145). However, when a full can of Helium was to be filled again at the time of the blue line, the cryostat overflowed at the pressure relief valve, so that only half a can could be filled (see figure 40) . From this point on, the Helium was refilled by the operator's intuition or, at the latest, when the top temperature sensor was uncovered.

After cooling the cavity to approximately 4 K, a frequency of about 216.904 MHz

was achieved. This corresponds to a deviation from the design resonant frequency $f_{\text{design}} = 216.816\,\text{MHz}$ of $\Delta f = 88\,\text{kHz}$, which is still within the tuning range of the dynamic bellow tuner.

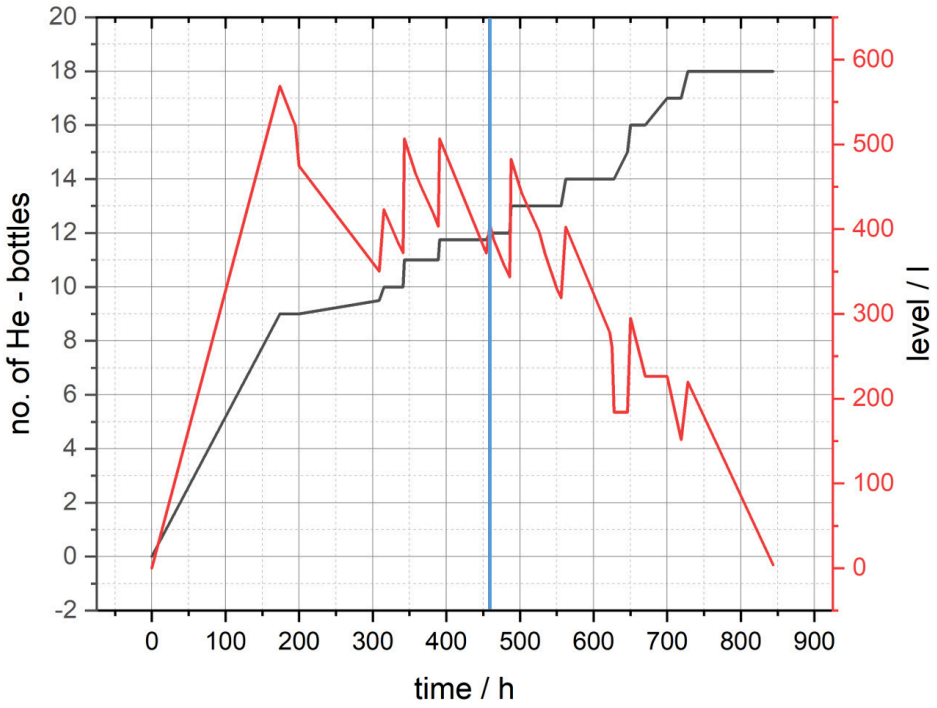

Fig. 40 Recorded level of liquid Helium estimated according to (145) versus time. The blue line marks the estimated time from which the deviation between the estimated level and the actual level differs strongly.

7.2.1 Formation of Niobium Hydrogen Hybrid

As already mentioned, when cooling the temperature of the cavity to 4 K, special care was taken to make the cooling as fast as possible or, more precisely, to pass through the temperature range of 150 – 60 K as quickly as possible. Therefore, the Nitrogen isolation shield and the Helium reservoir were filled at simultaneous times, because the temperature of liquid Nitrogen with 77 K is exactly in this temperature range. The reason for this procedure is the so-called Q-disease. This effect describes the incorporation of Hydrogen into the surface of the resonator and the formation of Niobium-Hydrogen hybrids (NbH), which lead to surface losses and strongly influence the material-dependent residual resistance R_{mat}. As a result, the intrinsic Q factor of the resonator can drop by orders of magnitude (see figure 41). The formation of these NbH depends on several factors. Besides the concentration of Hydrogen, both the time of cooling and the diffusion rate play an important role [32].

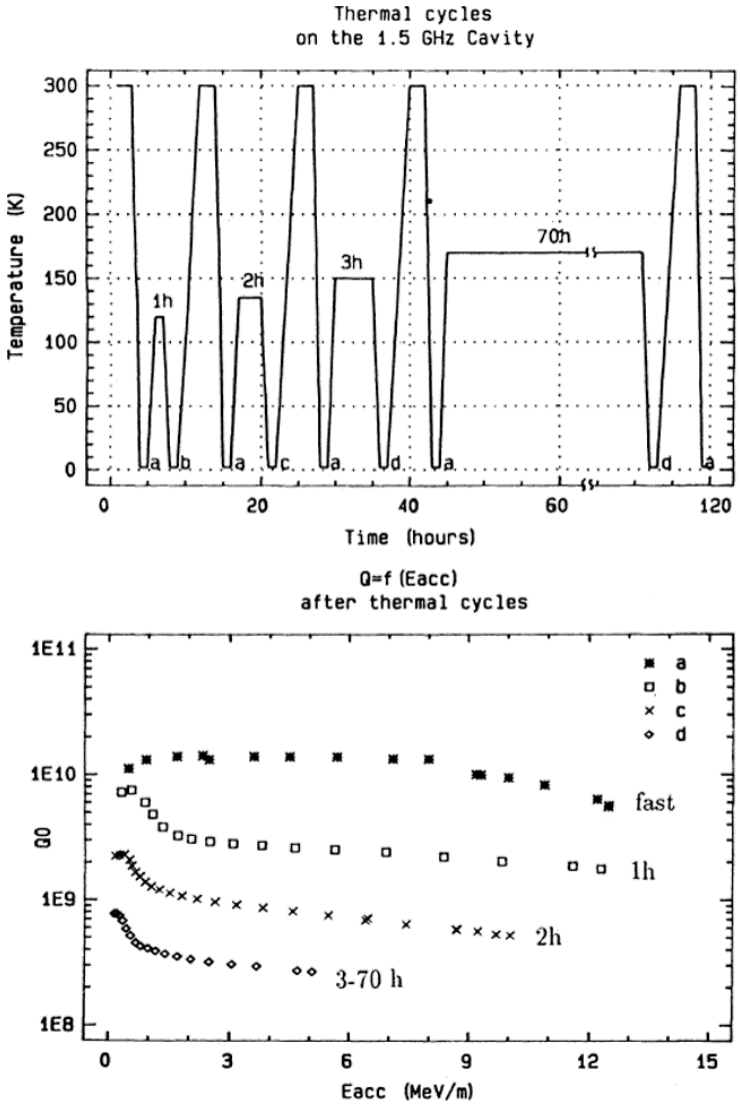

Fig. 41 Top: Thermal cooling of a 1.5 GHz Cavity with different durations at different temperatures. Bottom: A measurement of the intrinsic Q-factor Q_0 after the respective cooling [52].

Pure Niobium used for the construction of cavities usually has a high purity, which is also reflected in the concentration of Hydrogen. Thus, the concentration is approximately 1 wt ppm of dissolved Hydrogen. However, various processing steps or surface preparations can increase this concentration. However, this low concentration is not sufficient to form NbH at room temperature, which would require a concentration of about 4.6×10^3 wt ppm up to 7.5×10^3 wt ppm. If the cavity is now cooled down, this required concentration decreases. Starting at a temperature of about 150 K, the concentration needed to form hybrids has dropped to a value below 2 wt ppm. In addition, at these temperatures the diffusion rate increases, so

that overall the probability for the formation of NbH at the surface and an associated growing material-dependent residual resistance R_{mat} increases strongly from this temperature. After further cooling, the diffusion rate of Hydrogen decreases to the point where no Hydrogen can penetrate the Niobium from a temperature of approximately 60 K, so that no NbH can be formed [32].
It has been shown that the time a cavity of Niobium is in the critical temperature range of 150 – 60 K plays a major role in the formation of NbH. So, for cavities with a long cooling time in this range, a clear drop in the intrinsic quality Q_0 could be measured (see figure 41). In order to avoid an increase of the material dependent residual resistance R_{mat}, this temperature range has to be traversed as fast as possible. An alternative method to reduce the formation of NbH would be to bake the cavity under high vacuum for several hours at temperatures ranging from 700 °C to 1000 °C, as this will dissolve out the Hydrogen [32].

7.3 Pressure Sensitivity at 4 K

An interesting property of the cavity for later operation is the so-called pressure sensitivity. It indicates how the resonant frequency of the cavity changes during operation due to an increase or decrease of the pressure inside the cryostat p_{cryostat}. For this, when the cryostat is sufficiently filled with liquid Helium, the exhaust valve of the cryostat's Helium reservoir was closed causing p_{cryostat} to increased. As the pressure increases, at previously determined pressure values, the resonance frequency of the cavity was measured and the frequency change Δf was determined. Figure 42 shows the recorded measurement points as well as a linear fit through the measurement points to determine the gradient of the curve. At higher values, the increase in pressure increased rapidly, so fewer points could be measured manually. A pressure sensitivity of $\Delta f/\Delta p \approx (-9.64 \pm 0.14)\,\text{Hz/mbar}$ was therefore measured. In a previous cold test of CH2, which had to be terminated prematurely due to a cold leak, a pressure sensitivity of $\Delta f/\Delta p \approx -8.2\,\text{Hz/mbar}$ was measured at a temperature of about 4 K. This discrepancy between the two measurements could have resulted from processing at the manufacturer. There, the cavity was opened again to eliminate the cause of the cold leak and also another HPR[72] was performed to rinse the cavity. Despite the slightly increased value, the pressure sensitivity of CH2 is sufficiently low, so that no major influences on the resonance frequency and on the performance of the cavity due to pressure fluctuations occurring in the Helium bath during subsequent operation are to be expected.

[72] **H**high **P**ressure **R**insing

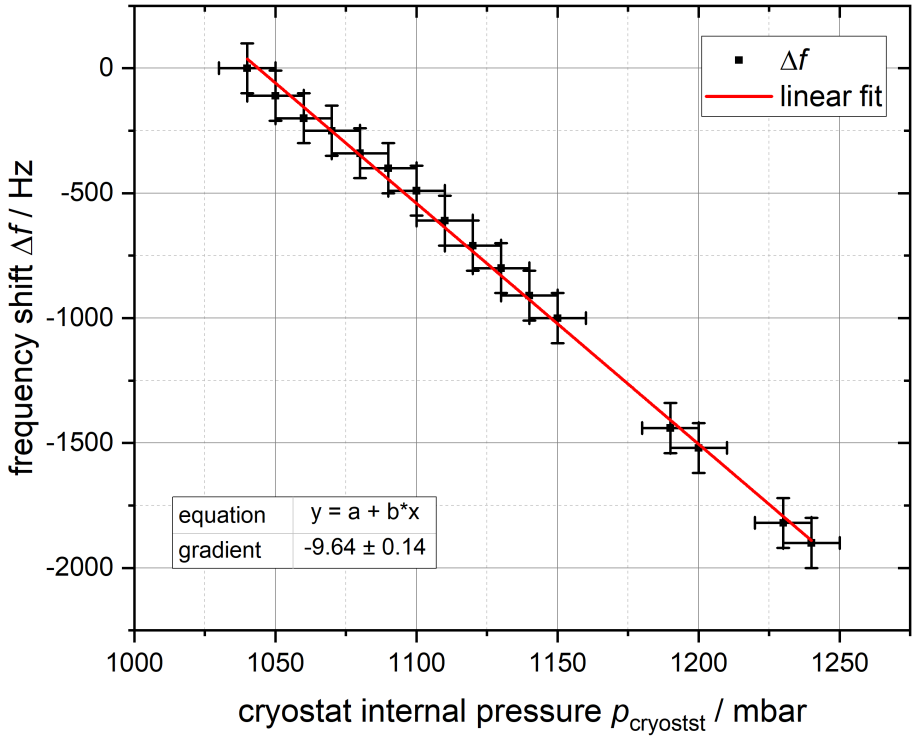

Fig. 42 The frequency change Δf versus the pressure p_{cryostat} prevailing inside the cryostat at a temperature of about 4 K. The linear fit yields a gradient of $\approx -9.64\,\mathrm{Hz/mbar}$.

7.4 Conditioning and Course of Measurement

Once the cavity is completely covered with liquid Helium and cooled to the operating temperature of approximately 4 K, the cavity still needs to be conditioned before actual operation. Conditioning involves using a network analyser at low field levels to clean the inner surface of the cavity. As described in section 4.3, the texture and purity of the inner surface plays a major role with respect to the occurrence of multipacting. Even if the surface of CH2 has been treated several times with BCP[73] and cleaned with HPR, isolated minor imperfections and impurities on the inner surface can still cause multipacting, especially after the cavity has been reopened and reprocessed by the manufacturer after the occurrence of the cold leak, even if a HPR was performed again after these processing steps.
During the conditioning of CH2, the network analyser was used to selectively process and successively condition the multipacting thresholds. In this process, the frequency bandwidth and repetition rate were varied several times during the 'passing' of the multipacting threshold, and the amount of forward power was gradually adjusted. Two different multipacting thresholds are shown in figure 43 on the network analyser. The shape of the curve is thereby formed as explained in section 4.3

[73] **B**ufferd **C**hemical **P**olishing

and figure 21.

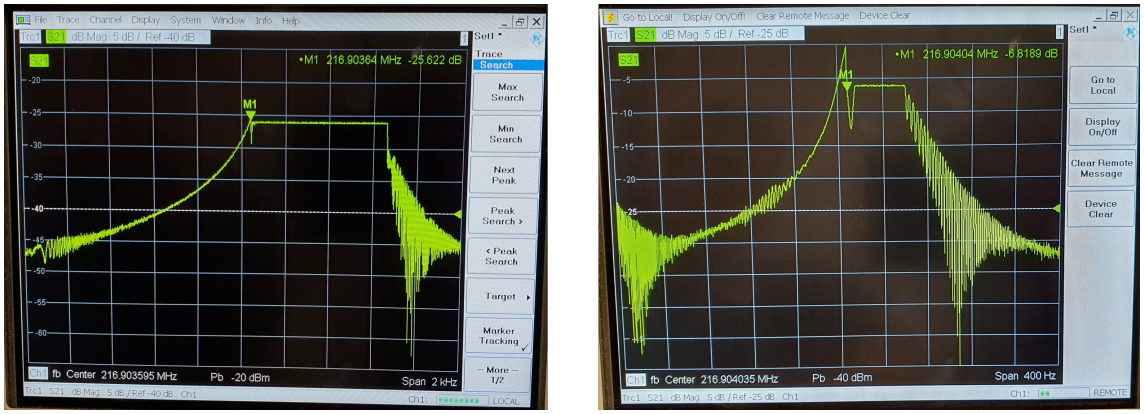

Fig. 43 Photography of two multipacting barriers. The signal is seen to slowly build up until it reaches the multipacting threshold.

Remarkable in the conditioning of CH2 was both the early appearance of multipacting thresholds at low powers of $P_\mathrm{f} \approx 2\,\mu\mathrm{W}$ and the frequency of thresholds at these low levels and the persistence. For this reason, conditioning at these minimal powers required an enormous amount of time of two weeks (see figure 44). Once these smaller thresholds could be conditioned, only a few thresholds occurred at higher powers that could be conditioned much quicker. This further progression of increased powers can be seen in figure 45. It can be observed clearly that in the beginning of this plot the forward power P_f could be increased successively and that after the thresholds in the low power region could be overcome the power could be increased much faster until the maximum output of the 50 W amplifier was reached and P_f amounted to $P_\mathrm{f} \approx 49\,\mathrm{W}$.

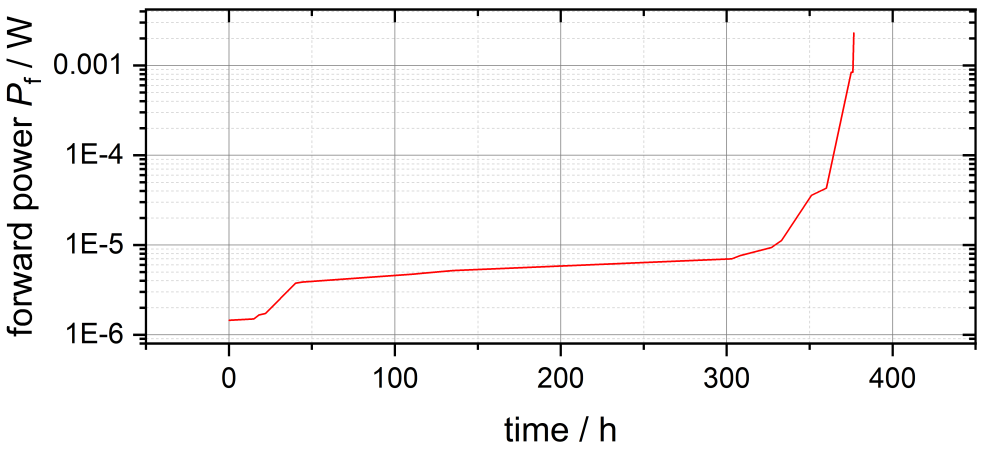

Fig. 44 Time evolution of the forward power line P_f during conditioning.

7.5 Further Measurements and Behaviour during the Test

After the cavity was conditioned and the desired field level inside the cavity was achieved, a so-called Q over E curve could be recorded to characterize the cavity, which is decisive for the performance of the cavity in later beam operation (see section 7.6). In addition to recording this curve, other parameters were observed and recorded alongside, such as further recording of the three powers P_f, P_r and P_t (see figure 45), observation of the temperature of the cavity (see figure 49) and the pressure inside the cavity.

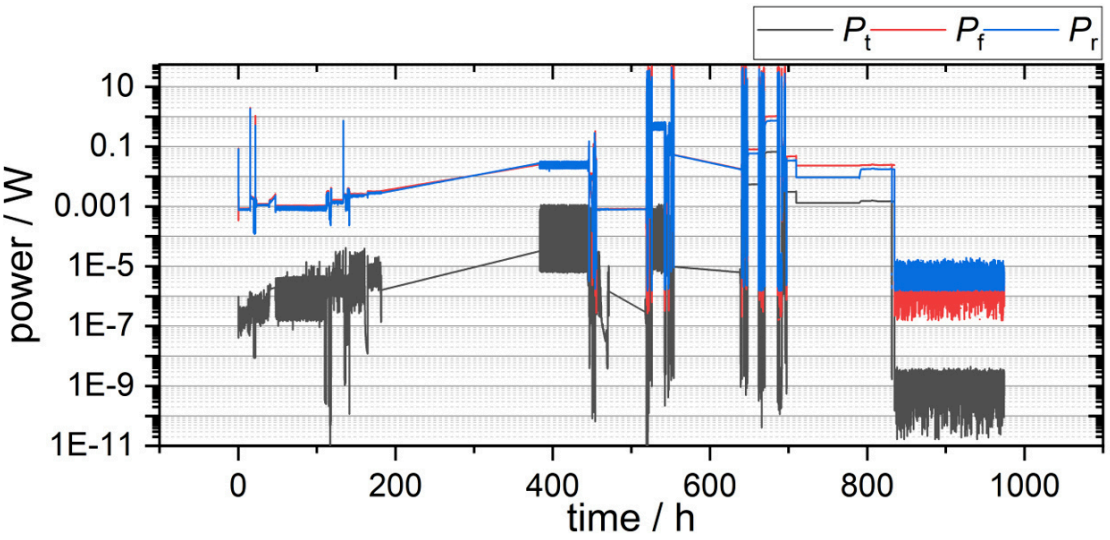

Fig. 45 Measured time course of the three powers P_t, P_f andP_r.

When measuring the three powers, it was observed that a noticeable behaviour occurred in the high field level region, which is probably reflected in the Q versus E curve recorded later. After the cavity was first conditioned, the power within the cavity was increased to the point where a transmitted power P_t of $P_\mathrm{t} = 2.67\,\mathrm{W}$ could be achieved. Thereby, a power $P_\mathrm{f} = 48.3\,\mathrm{W}$ was coupled into the cavity and a power of $P_\mathrm{r} = 5.55\,\mathrm{W}$ was reflected. These powers were held for a short period to plot a Q versus E curve (see section 7.6). This plot of the powers is shown on the left in figure 46. It can be seen that after reaching the maximum output power of the 50 W amplifier, some kind of conditioning process continued to take place over a period of about 3 min, and that at a slightly increasing P_f ($+1\,\%$) P_t also slightly increased ($+3\,\%$), while P_r slightly decreased($-6\,\%$).

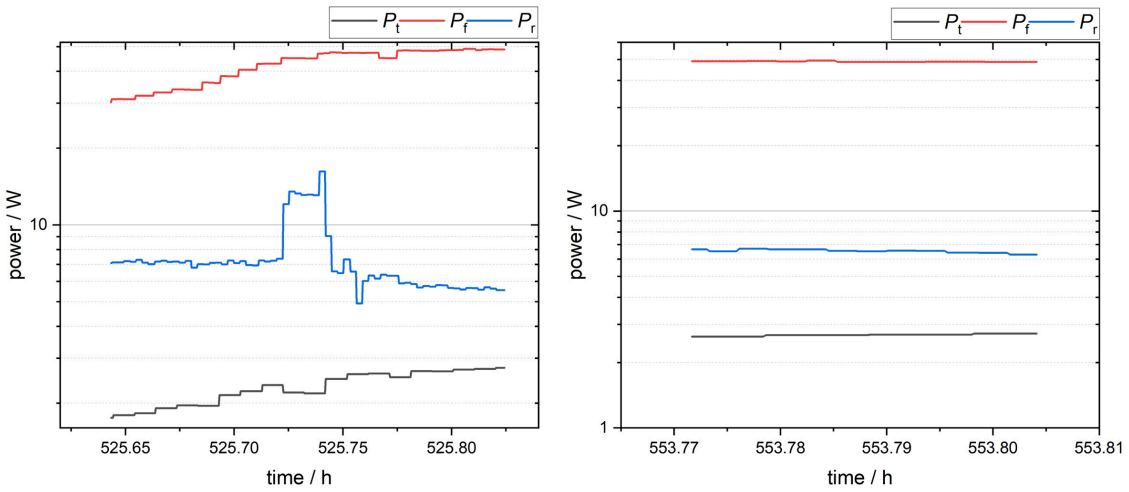

Fig. 46 Left: The first time the maximum output power of the 50 W amplifier was reached after conditioning. It can be seen that the power was increased slowly at the beginning and then stopped at $P_f \approx 48\,W$. Right: The second time the maximum output power of the 50 W amplifier was reached after conditioning.

The following day this procedure was repeated (see figure 46 right). Now the power could be directly increased to such an extent that at maximum output of the amplifier the forward power could be set to a value of $P_f = 49\,W$. Here, $P_t = 2.63\,W$ and $P_r = 6.65\,W$ were observed. A Q over E curve was again recorded. For this, the powers were held for a period of about 2 min. Also over this period, the powers P_t and P_r changed constantly, while P_f remained almost constant, only dropping to a value of $P_f = 48.8\,W\,(-0.5\,\%)$. P_t increased to a value of $P_t = 2.72\,W\,(+3.4\,\%)$ and P_r decreased to a value of $P_r = 6.3\,W\,(-5.5\,\%)$. It can be seen that the changes are of a similar magnitude to the changes in the previous measurement, but over a smaller period of time. These small changes, however, could be due to measurement errors.
However, another anomaly became apparent in the next measurements. During the third recording of a Q over E curve, it became noticeable that despite setting the maximum output of the 50 W amplifier, the previously achieved powers could no longer be reached (see figure 47). Thus, the forward power reached only a value of $P_f = 44.9\,W$ despite the unchanged measurement setup. Accordingly, the transmitted power P_t also showed a lower value than in the previous measurements of $P_t = 1.67\,W$. P_r, on the other hand, increased to a value of $P_r = 7.19\,W$.

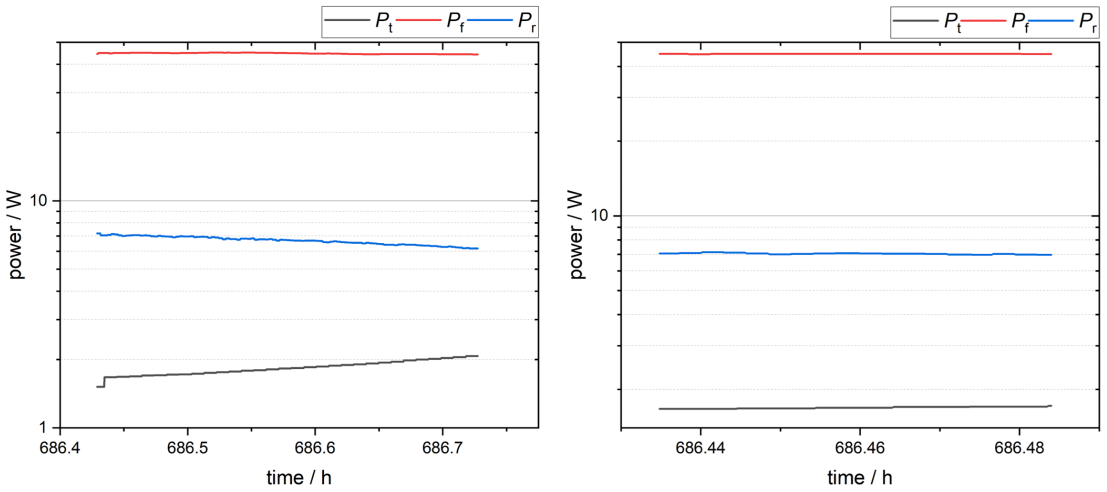

Fig. 47 Left: The plot of all three powers during the third recording of a Q over E curve over the entire period of the measurement. Right: A section of the measurement of the left graph over the same duration of time as the measurement in figure 46 right.

Thus, despite the unchanged measurement setup, the forward power dropped by nearly 9 % and the transmitted power decreased by approximately 37 %, while the reflected power increased by about 8 % compared to the previous measurement. Holding these powers for a longer time period of about 18 min, it became noticeable that P_t and P_r changed constantly. So, P_t continuously increased to a value of $P_t = 2.07\,\mathrm{W}\,(+2.4\,\%)$ and P_r steadily decreased to a value of $P_r = 6.18\,\mathrm{W}\,(-14\,\%)$, while P_f changed only slightly to a value of $P_f = 44.24\,\mathrm{W}\,(-1.5\,\%)$. Considering these temporal changes over a period of time equal to the time period of the measurement in figure 46 right (see figure 47 right), the changes amount to $\approx -0.1\,\%$ for the forward power, $\approx +2.4\,\%$ for the transmitted power, and $\approx -1.1\,\%$ for the reflected power. Thus, it can be seen that the change in the three powers, when considered on similar time scale, was significantly smaller than in the previous two measurements. However, the steady changes lasting over a longer period of time argue against measurement errors as the source of these changes. Similar behaviour has also been observed with a later recording of a Q over E curve. Again, P_t increased constantly over a longer period, while P_r decreased and P_f remained almost constant. Likewise, once again, despite maximum amplifier output, the outputs from measurements 1 and 2 could not be achieved (see figure 48). It is noticeable in measurement 4 that P_t dropped again after reaching a maximum. However, this behavior could not be observed again in a later measurement. After these four measurements, both the power meter and the power sensors were replaced, which is why the plot shown in figure 45 does not show any further maxima. However, this measurement showed very similar behaviour, so it will not be discussed further here.

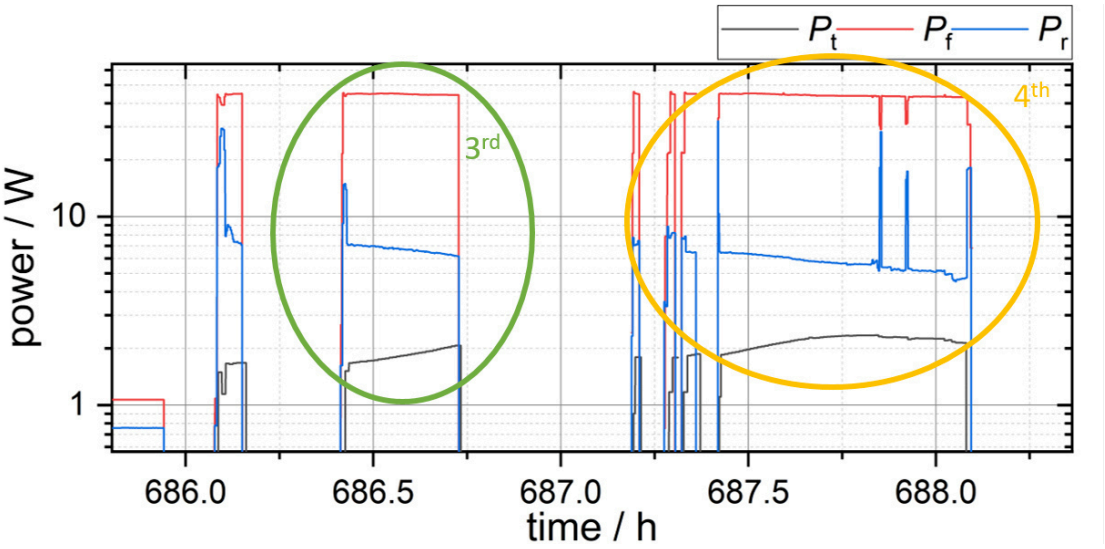

Fig. 48 Temporal recording of the three powers. The green circle shows the third measurement from figure 47 and in the orange circle the fourth measurement.

Due to the occurrence of this anomaly during the recording of the Q over E curves, the cold test unexpectedly extended by several days. Since this greatly delayed some experiments at the physics department of the Goethe University Frankfurt due to the additional liquid Helium necessary, it was decided to stop the cold test after these measurements and to send the cavity again to the manufacturer to have the Helium vessel attached. As a result, further investigation of the conspicuous behaviour was no longer possible within the scope of this thesis, since the attachment of the Helium vessel was also severely delayed and thus took place directly without re-examination of the cavity. In a future cold test, this possible re-occurring behaviour could be further investigated.

In addition to the power, the temperature was also recorded and monitored during the entire cold test to ensure that quenching and thus potential damage to the cavity could be prevented. For this purpose, as already described in section 7.1.1, a total of eight temperature sensors were placed at different locations on the cavity and were read out. The top of figure 49 shows all recorded temperatures during the entire cold test until the start of the reheating of the cavity. It can be seen that there was a permanent offset between each sensor. This offset is due to different settings of the resistors within the readout electronics and is only in the range of a few 0.1 K. Since this offset had only a minor influence on the monitoring of the temperature and had a positive effect on the clarity both during the measurement and in the evaluation, it was not taken into account in figure 49. The distribution of the sensors was as follows

- T_1: On the mantle to the right of T_6

- T_2: On the lower lid of the cavity
- T_3: In the second spoke from the top in a row with a total of 4 spokes
- T_4: On the mantle left of T_6
- T_5: In the center of the cavity between the two middle spokes in a row with a total of 4 spokes
- T_6: In the middle spoke in a row with a total of 3 spokes
- T_7: On the opposite side of the cavity from T_1, T_4 and T_6
- T_8: On the upper lid of the cavity.

It can be seen in the top of figure 49 clearly that despite repeated local heating of the cavity, either by dropping the level of liquid Helium or coupling higher power, no temperature could be reached that was greater than the transition temperature of Niobium ($T_{\mathrm{C,\,Nb}} = 9.2\,\mathrm{K}$). The highest temperature reached was measured during measurement 4 and was corrected to be $T_6 = 5.136\,\mathrm{K}$, because this temperature sensor was positioned inside a spoke and this location has the highest field level and thus dissipates the most power. Despite the high power coupled in, the distance between the temperatures and the critical temperature was sufficiently large.
The most interesting temperature sensor here is the sensor T_8, since this sensor was the highest sensor spatially and thus is the sensor that would be exposed first should the liquid Helium level drop too far. In the bottom of figure 49, the difference in temperatures of the two sensors T_8 and T_2 is shown, and thus the temperature gradient of the cavity between the two lids. Noticeable here are the two peaks in the course of the curve, the first peak being due to a heating of T_8 because there was too insufficient liquid Helium in the reservoir, and the second peak during the long measurement 4 shown in figure 48, occurred because the long in coupling of high power caused the cavity to heat up more and thus more Helium was evaporated until the sensor T_8 was also exposed here, which is why measurement 4 was also stopped. The last rise of the curve shows the beginning of the heating of the cavity. Here it can be seen that all sensors show an increase in temperature, apart from T_2, as this was the lowest sensor in terms of space and was still covered at this time. A complete record of the temperature as well as the Q factor and frequency during the heating of the cavity is given in section 7.7.

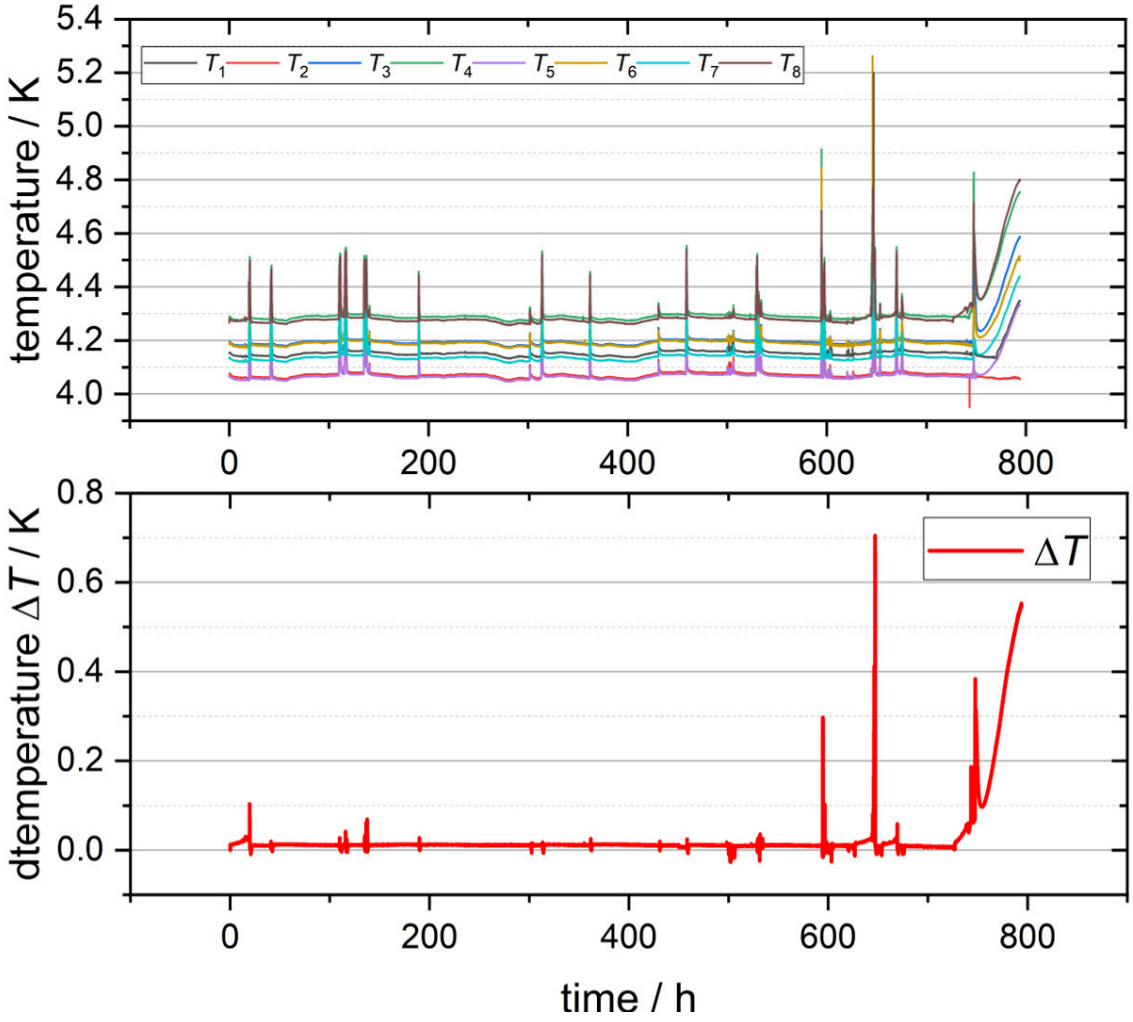

Fig. 49 Top: The time course of the temperature measured by all eight temperature sensors. Bottom: The temperature gradient between the spatially highest sensor T_8 and the spatially lowest sensor T_2. The offset between the sensors, as still seen above, has been corrected.

7.6 The Q over E Curve

After the conditioning of the cavity was completed, it could be started to determine the maximum achievable field level of the cavity by plotting the intrinsic quality factor Q_0 as a function of the accelerating field E_a. As the field level within the cavity increases, non-ohmic losses such as multipacting or field emission occurring above a certain field strength cause the intrinsic quality factor of the cavity Q_0 to decrease until these losses can lead to a breakdown of the superconductivity. The point at which the Q_0 drop occurs defines the performance of the cavity and how much energy can be stored within. First, for plotting the Q over E curve, the intrinsic quality of the cavity Q_0 must be determined for low and high field levels. For this purpose, a constant RF power was applied and coupled into the cavity. The coupler was designed to overcouple the cavity ($\beta_\mathrm{e} > 1$, see section 3.2.6), so equation (80) must be used to calculate the coupling parameter β_e.

$$\beta_\mathrm{e} = \frac{1 + \sqrt{\frac{P_\mathrm{r}}{P_\mathrm{f}}}}{1 - \sqrt{\frac{P_\mathrm{r}}{P_\mathrm{f}}}} \tag{146}$$

Since in equation (80) the coupling factor is calculated from the measured forward power P_f and the reflected power P_r and these two powers showed a conspicuous behaviour as described in section 7.5, these conspicuities also carry over to the plot of β_e. During the course of the measurement β_e should be nearly constant, but since the ratio of the two powers from which β_e is calculated changes continuously, β_e is not constant either. This fact is valid for all four measurements of the Q over E curve described in section 7.5. The shape of β_e for the individual measurements is shown in figure 50 as a function of injected power P_f.

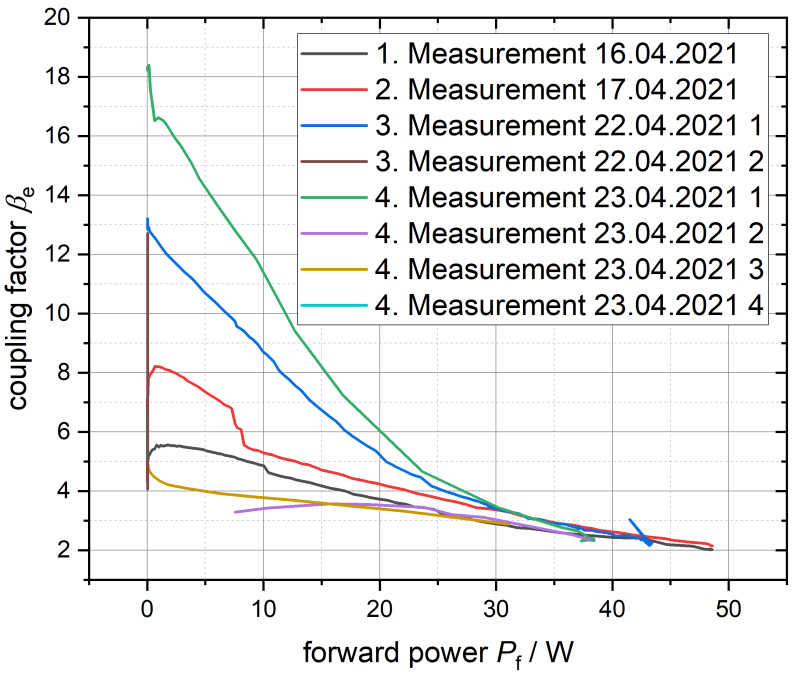

Fig. 50 Plot of β_e versus P_f.

It can be seen that despite identical settings for both, signal generator and 50 W amplifier, different β_e were calculated. This is due to the fluctuating powers as described in section 7.5. After reaching higher powers starting at about $P_f \approx 40\,W$, the different β_e converge to each other. The coloured brown curve in figure 50 represents a time history where no changes were made to either the signal generator or the 50 W amplifier settings. It can be seen that for this curve, β_e increases over some time course, while P_f is constant and therefore P_r increases. Using these β_e and the loaded quality Q_L ($Q_{L,\,mean} = 7.8 \cdot 10^7$) previously measured using the network analyser, the unloaded quality Q_0 for low field levels was determined according to equation (78). The values for Q_0 at low field levels and the associated β_e are given in Tab. 3.

$$Q_0 = Q_L \cdot (1 + \beta_e + \beta_t) \approx Q_L \cdot (1 + \beta_e) \text{ for } \beta_e >> \beta_t \tag{147}$$

Tab. 3 The calculated Q_0 for low field levels of the four measurements made.

	Q_L	β_e	Q_0
1^{st} measurement	$7.8 \cdot 10^7$	4.6	$4.49 \cdot 10^8$
2^{nd} measurement	$7.8 \cdot 10^7$	5.02	$5.33 \cdot 10^8$
3^{rd} measurement	$7.8 \cdot 10^7$	12.95	$1.15 \cdot 10^9$
4^{th} measurement:	$7.8 \cdot 10^7$	18.28	$1.48 \cdot 10^9$

For the determination of both Q_0 at high field levels and E_a, the effective acceleration voltage U_{eff} is required. To determine this, the power P_c stored in the cavity is first defined by

$$P_c = P_f - P_r - P_t. \tag{148}$$

From equation (60) U_{eff} can be calculated. However, in order to calculate U_{eff} directly from the measured values (here P_t was used), a calibration must first be performed at small fields using the shunt impedance R_A at low field levels:

$$U_{\text{eff}} = \sqrt{R_A \cdot P_c} = B \cdot \sqrt{P_t}. \tag{149}$$

In this context, B is a calibration constant which, at low field levels where no additional losses are yet to be expected and thus Q_0 depends directly on the stored energy and thus P_t, can be determined by

$$B = \sqrt{\frac{R_a \cdot P_{c,\,\text{low}}}{P_{t,\,\text{low}}}} = \sqrt{\left(\frac{R_a}{Q_0}\right) \cdot Q_{0,\,\text{low}} \left(\frac{P_{c,\,\text{low}}}{P_{t,\,\text{low}}}\right)} \tag{150}$$

The normalized shunt impedance R_A/Q_0 was taken from simulations of the structurally identical cavities CH1 and CH2, which were performed with CST Studio Suite. As a result, R_A/Q_0 for CH2 amounts to $R_A/Q_0 = 1050\,\Omega$ [1]. The values for B for the four different measurements were averaged over several measurements and are shown in Tab. 4.

Tab. 4 The calibration constant B averaged over several measurements for all four measurements.

	R_A	B
1^{st} measurement	$1050\,\Omega$	$2.01 \cdot 10^6 \sqrt{\Omega}$
2^{nd} measurement	$1050\,\Omega$	$1.96 \cdot 10^6 \sqrt{\Omega}$
3^{rd} measurement	$1050\,\Omega$	$1.92 \cdot 10^6 \sqrt{\Omega}$
4^{th} measurement:	$1050\,\Omega$	$1.69 \cdot 10^6 \sqrt{\Omega}$

Thus U_{eff} can be determined independently of the energy stored in the cavity. Using the calibration constant, measured powers at high field levels and the normalized shunt impedance known from the simulations, it is now possible to calculate the intrinsic Q-factor at high field levels $Q_{0,\,\text{high}}$

$$Q_{0,\,\text{high}} = \frac{U_{\text{eff}}^2}{P_{c,\,\text{high}} \cdot \left(\frac{R_a}{Q_0}\right)} = \frac{B^2 \cdot P_{t,\,\text{high}}}{P_{c,\,\text{high}} \cdot \left(\frac{R_a}{Q_0}\right)}. \tag{151}$$

The accelerating field E_a is thereby calculated from the consisting relation between the simulation results of CH1/CH2 with respect to $U_{\mathrm{eff,\ CST}}$ and $E_{\mathrm{a,\ CST}}$ and the now calculated U_eff

$$\frac{E_\mathrm{a}}{E_{\mathrm{a,\ CST}}} = \frac{U_\mathrm{eff}}{U_{\mathrm{eff,\ CST}}} \Rightarrow E_\mathrm{a} = \frac{U_\mathrm{eff}}{U_{\mathrm{eff,\ CST}}} \cdot E_{\mathrm{a,\ CST}}. \tag{152}$$

The values for $U_{\mathrm{eff,\ CST}}$ and $E_{\mathrm{a,\ CST}}$ are $U_{\mathrm{eff,\ CST}} = 1.25\,\mathrm{MV}$ and $E_{\mathrm{a,\ CST}} = 3.41\,\mathrm{MV/m}$. [1].

With the now calculated values for the intrinsic qualities at low and high field levels ($Q_{0,\ \mathrm{low}}$ and $Q_{0,\ \mathrm{high}}$) and the calculated acceleration field E_a, the four Q over E curves for the respective four measurements described in section 7.5 can be plotted. For the upcoming plots of the four Q over E curves, the y-axis was plotted with the same range of values to simplify the comparison of the four curves with each other. The curve of the first measurement is shown in figure 51.

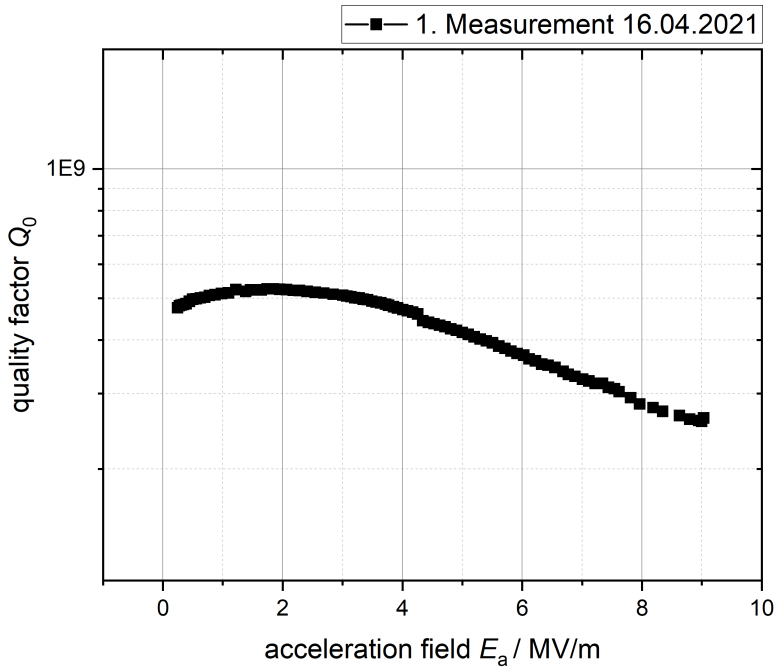

Fig. 51 Plot of the Q over E curve recorded for the first time in this cold test. To simplify the comparison of all recorded Q over E curves, the two axes here and in the following plots always represent the same area.

The shape of this curve is quite similar to the expected shape of a typical Q over E curve, but direct comparison with the same measurement for CH1 shows a clear difference (see figure 52) [1]. The most striking parts of the curve in figure 51 are the maximum in the low field level range of 1.5 – 2 MV/m, the dip at 4.2 MV/m and the slight increase in the high field level range at about 9 MV/m. These anomalies

are shown in the course of the coupling factor β_e in figure 50 (black) as well, so that the progression is due to the anomalous behaviour of the powers described in section 7.5, since both β_e and thus $Q_{0,\,\mathrm{low}}$ (see (147)) and $Q_{0,\,\mathrm{high}}$ (see (151)) are calculated directly from the powers. The direct comparison with the Q over E curve previously recorded for the structurally identical CH1 in figure 52 shows that no abnormalities occurred in this measurement and the curve follows the expected course. Moreover, the values of Q_0 at CH1 are significantly higher than the values for Q_0 at CH2 measured here.

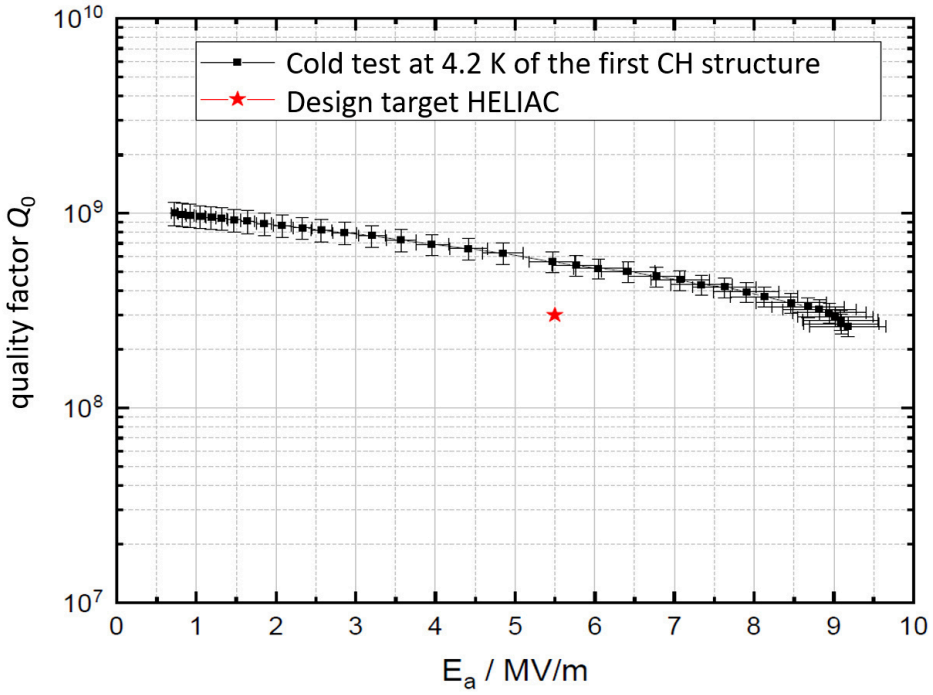

Fig. 52 Previously recorded Q over E curve of the identical CH1 cavity for comparison [1].

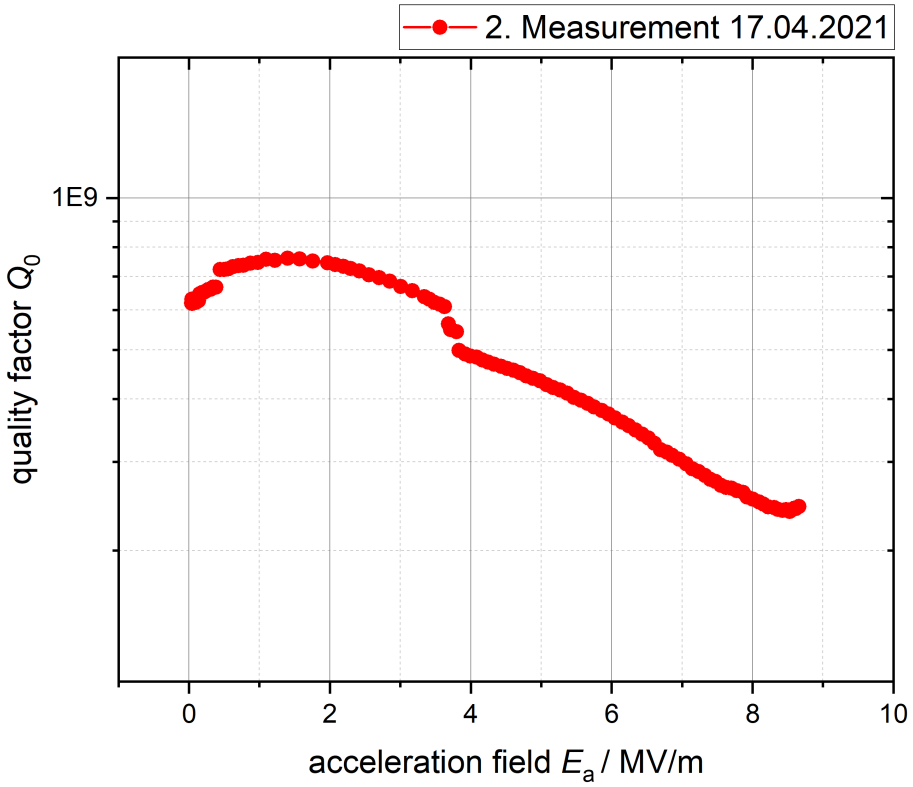

Fig. 53 Course of the second recorded Q over E curve.

Since it was already noticed during the recording of the first Q over E curve of CH2 that the values for Q_0 were significantly below the expected values from figure 52, a new curve was recorded the next day without changing the setup. This curve is shown in figure 53. As already described in section 7.5, a strange behaviour in the measured powers also occurred in this second measurement, which is also reflected in the course of the Q over E curve. Thus, also as in figure 51, there is a maximum in the low field level range, a discontinuity in the form of a dip at just under $\approx$ 3.8 MV/m as well as a rise of the quality Q_0 at high field levels. The shape of this curve is again similar to the shape of the coupling factor β_e in figure 50 (red). It can be clearly seen that the described conspicuous spots in this course, are clearly more prominent than in the first measurement, shown in figure 51, although the measurement was repeated with the same measuring instruments and the same settings. Thus, it can be clearly seen that the discontinuity is more pronounced in the middle of the curve and the maximum is much higher in the low field level region, even though the highest Q_0 reached is still below the expected value. Before recording the third Q over E curve, all power measurement sensors, the power meters, the circulator and he bidirectional coupler were checked for proper operation. No deficiencies were found.

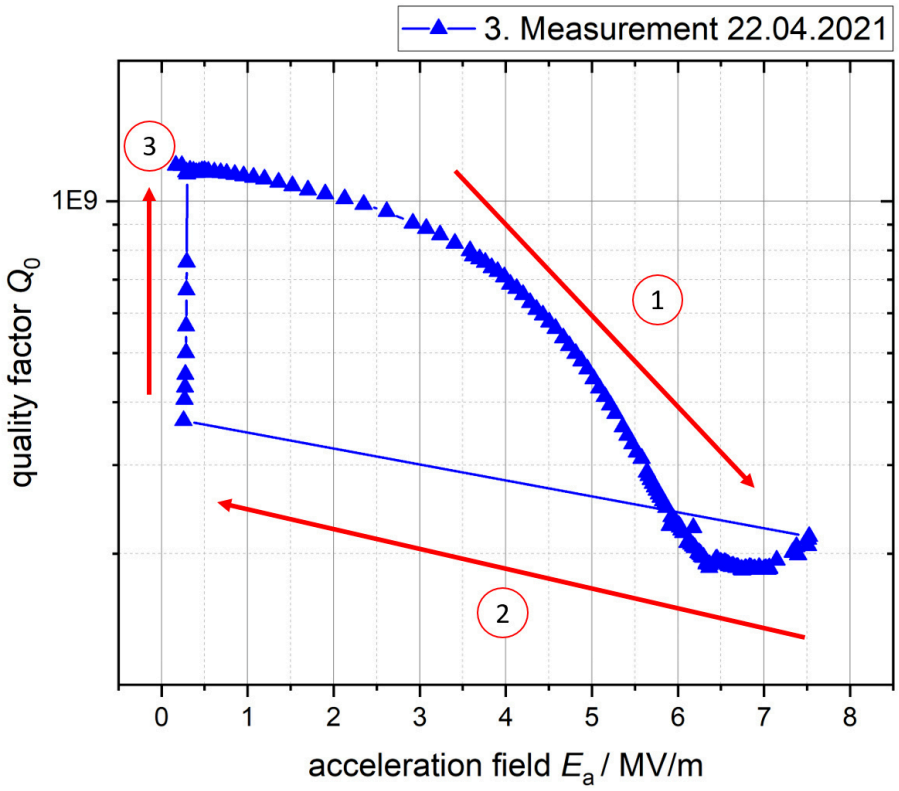

Fig. 54 Course of the third recorded Q over E curve.The red arrows indicate the time course of the measurement, where the measurement starts with 1 and ends with 3.

As shown after considering the curve of β_e in figure 50 (blue), the value of Q_0 at the beginning of the curve is far above the values of the first and second measurements. This high value is much closer to the expected value as shown in figure 52 of CH1. Similar to the blue curve for β_e in figure 50 (blue), no discontinuity is seen for the third Q over E curve in figure 54 However, the values of the Q-factor Q_0 for high field levels are below the values of the Q-factor of the first two measurements. Thus, the negative slope here is much steeper than before (1 in figure 54). The lower values at high field levels here occur because, despite the maximum output of the 50 W amplifier, the previously achieved powers could no longer be reached. In this measurement, a conditioning effect could be detected. After reaching the maximum output of the 50 W amplifier, the maximum power was maintained for a few minutes. During this process, as described in section 7.5, the power P_t increased while P_r dropped constantly, causing $Q_{0,\,\mathrm{high}}$ to also increase according to equation (151) and E_a to also increase according to equations (149) and (152). After this conditioning effect could be observed, the output of the 50 W amplifier was turned down to the initial value again. Here, a sort of hysteresis effect could be observed, so that the previously achieved high values for Q_0 at low field level, which were in the range of the expected values, could not be reached anymore (2 in figure 54). Now, it is further noticed that a sort of conditioning effect occurred again and the

initially low value for Q_0 approached the previously reached values with time (3 in figure 54).

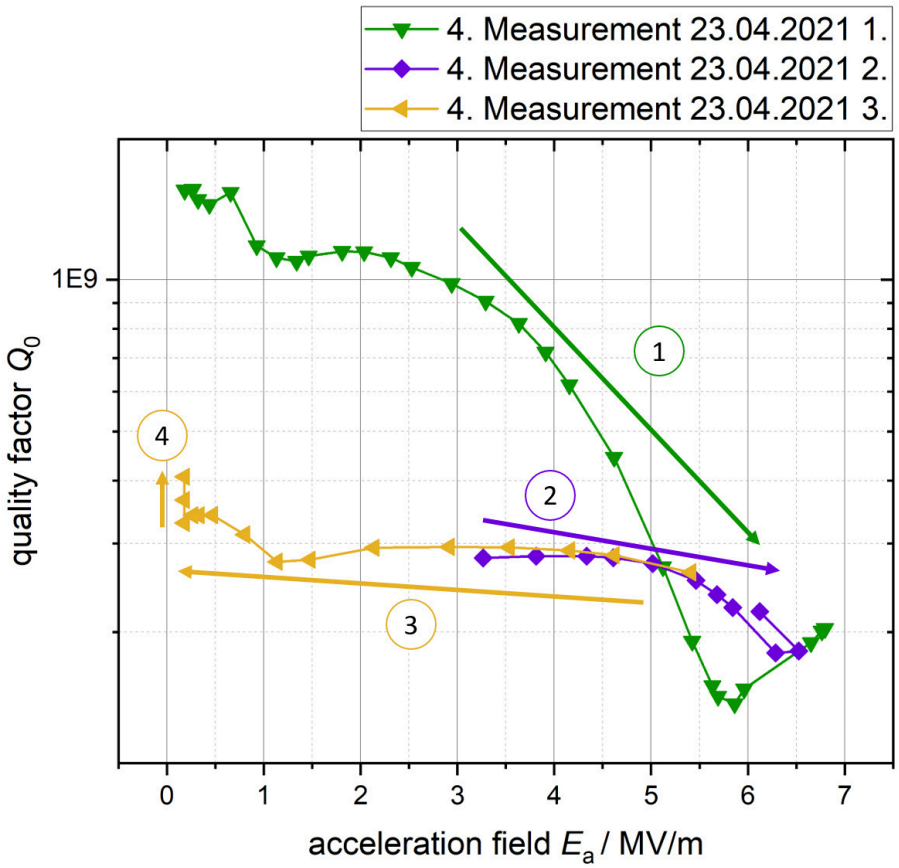

Fig. 55 Course of the fourth recorded Q over E curve. During the fourth measurement, a total of 3 measurements were taken. The colored arrows show the time course of the color-coded measurement, starting with measurement 1 and ending with measurement 4.

To confirm this behaviour, a fourth measurement was made the following day (see figure 55). Similar to the measurement before, it was possible to estimate the behaviour of the Q over E curve by looking at β_e in figure 50 (green). Again, the values for Q_0 are above those of the measurement before and then drop more significantly with increasing field level until they were below the values of the previous measurement (1 in figure 55). After reaching the maximum output of the 50 W amplifier, a conditioning effect was also observed here. In contrast to measurement 3, in this measurement the power was not turned back to the initial output of the amplifier, but an intermediate output was selected from where the power was increased again (2 in figure 55). Here, a similar hysteresis effect could be observed as before in measurement 3, so that the previously achieved values for Q_0 could no longer be reached at the same field levels. In this case, the course of the violet curve 2 in figure 55 resembles the expected course, as shown in figure 52. After

reaching the maximum output of the 50 W amplifier again, this output was successively reduced back to the initial value (3 in figure 55). Here, also as before at 2 in figure 55 the same hysteresis effect could be observed, so that these two curves lie on top of each other. When the initial value was reached again, the conditioning effect with time again set in, so that the values for Q_0 increased with time at same field level. Thus, the striking behaviour of the third measurement could be repeated.

7.6.1 Conclusion of the Measurement

A direct comparison of the four measurements shows the more and more prominent abnormalities in the course of the curve apart from the discontinuity at medium field levels, which was no longer reproducible after the second measurement. In figure 56 all four measurements are shown in one plot, where measurement 4 was again split as in figure 55 into three sub-curves. The gold star in the diagram of figure 56 shows the desired design target value of the maximum field gradient $E_a = 5.5\,\mathrm{MV/m}$ at a quality of at least $Q_0 = 3 \cdot 10^8$ for cavities of the HELIAC project.

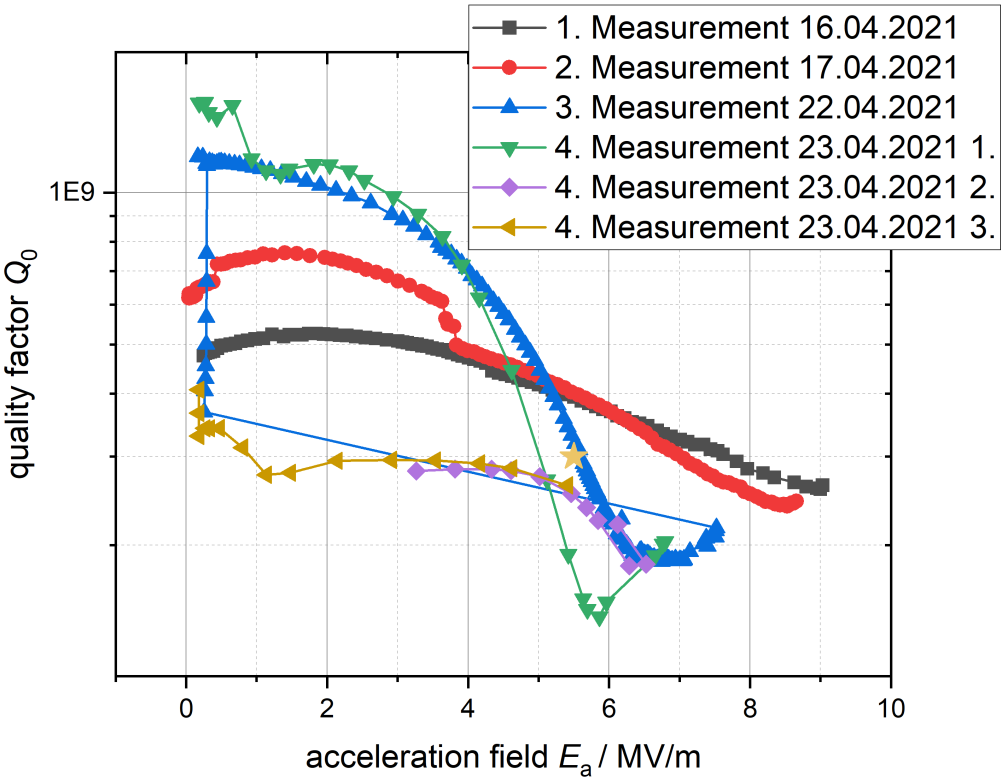

Fig. 56 Combined plot of all recorded Q over E curves of the different measurement days.

It can be seen that only the first two measurement are above this value. Measurement 3 is directly on it, while measurement 4 is clearly underneath it. However,

since the curves as such showed new values and a slightly different course with each new measurement, it can be assumed that the cold measurement as such was error-prone in this experiment. Several things can be considered as sources of error. The first possible source of the error could be some damage to the 50 W amplifier. Since, as described in section 7.5, with the same output setting of the amplifier after measurement 2, the same forward power P_f could not be achieved as in the previous measurements. For example, a single, peak of reflected power could have damaged the circulator during measurement 2 and thus damaged the amplifier. This would be supported by the fact that the forward power P_f is measured by the splitting by the bidirectional coupler before coupling into the cavity and thus would not be affected by it. However, this does not explain the already striking deviation of the curves of measurements 1 and 2 from the expected one, nor the hysteresis or conditioning effects in measurements 3 and 4.
Another theory concerning the sources of error relates to a damage to the coupler or the environment of the coupler. Since β_e already changes during the first measurement, it is currently assumed that there must have been a point of disturbance around the coupler. When more power was coupled in, this disturbance heated up and possibly expanded minimally, which could already have enormous effects on the performance with the extremely thin bandwidth of superconducting cavities. This would be supported by the fact that the curve of β_e in figure 50 for measurement 1, the curve starts at a realistic value of approximately 5 and up to a power of nearly 10 W varies in a rather small range and from higher powers, from the occurring dip, steadily decreases to a value of about 2. Thus, at increased power level, the impurity would continue to heat up until at a power of about 10 W it has sustained permanent damage, which is why the dip occurs. In the second measurement, this damage was extended and amplified, which is why a second now much more significant dip occurred. In the third measurement and fourth measurement, the damage was already so large that it no longer coupled in as expected and thus β_e took on very large values of approximately 13 and 18, respectively. The conditioning effects here could have been a slow expansion of the impurity by further heating of the impurity, and the observed hysteresis effect could have been the cooling of the impurity by the liquid Helium and the slow thermal re-contracting of the material to its initial condition.
It is to be noticed that due to the already much longer duration of the cold test, it had to be stopped without being able to record another Q over E curve. Likewise, it was not possible to visualize and examine the coupler, since the cavity had to be sent to the manufacturer again immediately after the cold test. There, without further testing, the Helium vessel was fused onto the cavity, the cavity was rinsed again with a HPR, and the coupler was replaced by the later high-performance coupler for later beam operation, so that in retrospect no more precise statements can be made about the causes of the anomalies described here, and the sources of error described above are pure speculations based on the measured values. In later cold tests at GSI in Darmstadt, it will be necessary to observe whether this conspicuous

behaviour is repeating itself. Therefore, the measurements made here are not conclusive enough about the characteristics or the performance of the cavity CH2 of the HELIAC project.

7.7 Reheating the Cavity

As mentioned in section 7.2, no measurement data regarding frequency and Q-factor could be recorded when cooling the cavity to 4 K due to a software bug. This measurement was then repeated when reheating after the cold test was completed using a network analyser and software routine. The temperature, quality and frequency were measured independently of each other and calibrated to a common time scale in the subsequent evaluation. During the measurement of the frequency, a temporal mismatch occurred in a small measurement section, so that the values recorded in this section were unusable for the evaluation. This mismatch is expressed in a small gap within the curves of the frequency measurement (see figure 58 and figure 59).
To accelerate the heating of the interior of the cryostat, the heater, which was attached to the bottom of the cavity hanging freely before closing the cryostat, was turned on. This was initially set to a fairly low value until the cavity was no longer surrounded by liquid Helium. Now that the cavity was surrounded only by gaseous Helium, the heater was set to a higher temperature value. Warming up to room temperature took several hours despite the heater. The progression of temperatures from the eight temperature sensors is shown in figure 57.

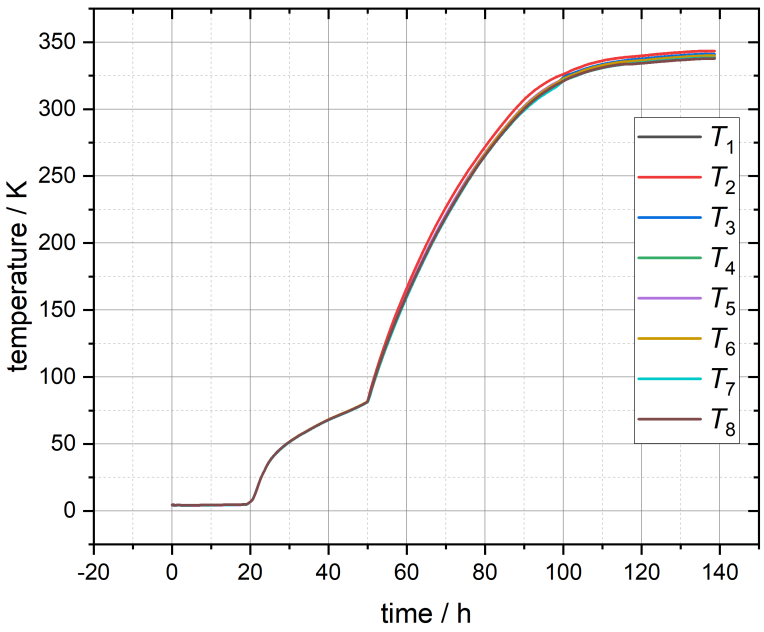

Fig. 57 Time course of the eight measured temperatures during cavity heating.

It can be seen that at the end of heating T_2 displayed the highest temperature value, as this sensor was located at the bottom lid of the cavity and was therefore closest to the heater. The discontinuities within the curve represent the times from which, on the one hand, the heater was turned on and, on the other hand, it was set to a higher temperature level. The temperature value of the heater was also increased for the reason that the temperature range described in section 7.2.1, which is critical for the formation of NbH, could be passed through more quickly, even if this effect plays a rather subordinate role in heating, since further surface preparation by means of a HPR was intended by the manufacturer anyway. In addition to the temperatures, the Q-factor Q_L and the resonant frequency f were also recorded. These measurements are shown in figure 58.

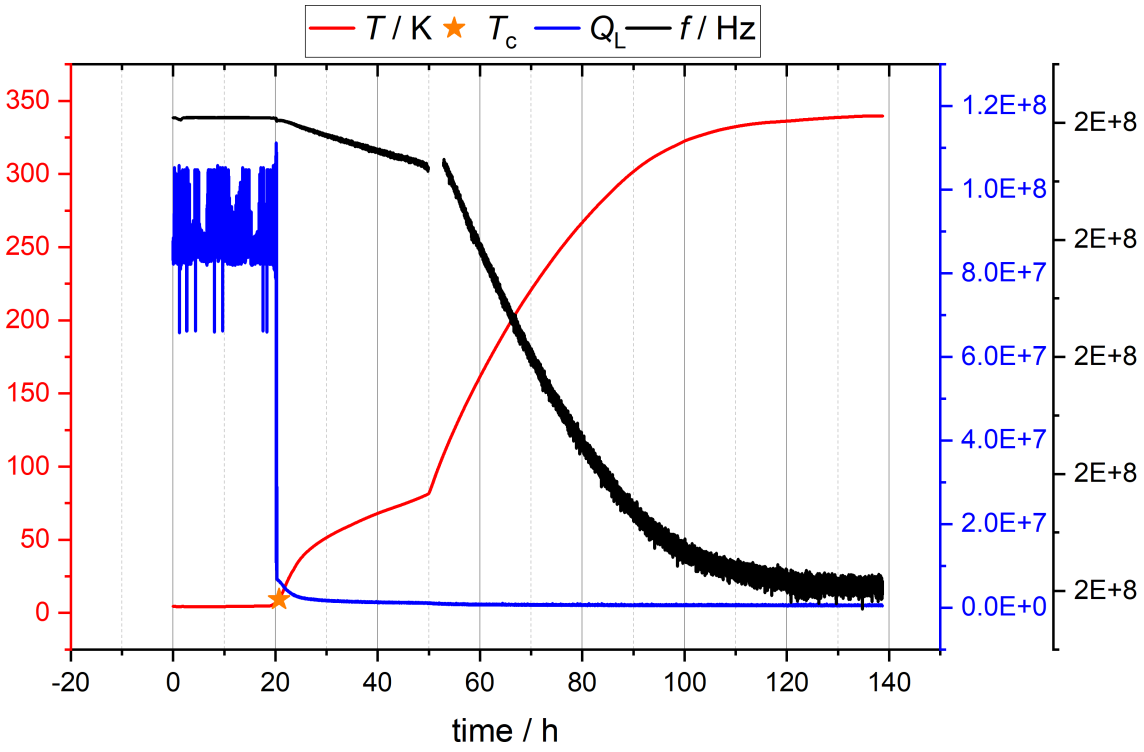

Fig. 58 Mean temperature T, frequency f and quality factor Q_L recorded during heating. The orange star indicates the transition temperature T_c of Niobium, above which the cavity is no longer in the superconducting state.

The orange star on the plot of temperature during heating indicates the threshold temperature T_c of Niobium, above which the cavity is no longer in the superconducting state. It can be clearly seen that once the cavity has exceeded the threshold temperature, the superconductivity has collapsed and thus the Q-factor Q_L abruptly drops by several orders of magnitude. This is because both the loaded Q-factor Q_L and the intrinsic Q-factor Q_0 depend strongly on the surface resistance R_S of the cavity. Once the superconductivity is collapsed, the surface resistance increases

rapidly, and therefore the loaded Q factor drops rapidly. In the superconducting phase, the loaded Q-factor was $Q_{\mathrm{L}} \approx 8.8 \times 10^7$. The frequency, which is independent of the conductive state of the cavity, drops constantly during heating. The gap in the course of the measurement of the frequency was caused by a temporal mismatch of the frequency measurement, as described above, and therefore no data could be collected here.
An interesting comparison is between the measurement of thermal frequency change and the theoretically expected thermal frequency change of the cavity during heating or cooling. Thus, the cavity had contracted equally in all three spatial directions during cooling, and thus the frequency increased during cooling and is now decreasing again during heating. The degree of thermal contraction is calculated from [53]

$$\frac{\Delta L}{L} = \frac{L_{293\,\mathrm{K}} - L_{4\,\mathrm{K}}}{L_{293\,\mathrm{K}}} = 0.143\,\%. \tag{153}$$

This proportional change is referred to as the expansion coefficient. In order to make a comparison between the theoretically expected and the actual frequency change, the theoretically expected frequency response must first be determined [53]. For this purpose, the literature values for the thermal contraction of Niobium at different temperatures were taken and the corresponding frequency changes were simulated using the CST Studio Suite software [40]. The comparison of these two frequency changes are shown in figure 59.

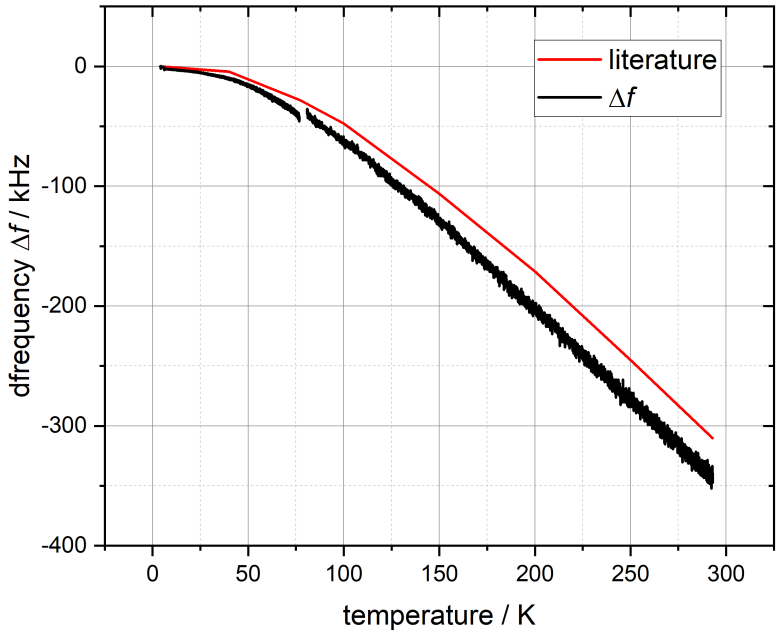

Fig. 59 Course of the measured frequency during heating of the cavity (black) including the theoretically assumed thermal contraction and the associated theoretical frequency change of the cavity during heating (red).

It is immediately apparent that there is a deviation between the measured frequency change and the theoretically determined frequency change. This deviation is due to the different thermal expansion coefficients of the materials used. For example, although the cavity is made entirely of Niobium, the welded-on Helium tank end caps are made of titanium, which has a similar coefficient of expansion of 0.151 % as Niobium, but the mounting frame in which the cavity is suspended and thus connected to the cryostat lid is made of Aluminium, which has a different coefficient of expansion than Niobium of 0.3 %. As a result, this frame contracts differently from the cavity and provides slight deformations, so that the actual frequency differs from the theoretically determined one. It is worth mentioning that for this reason, the cavity was not connected too tightly to the suspension frame to avoid internal stresses or damage to the cavity. In this case, the measured frequency change deviates from the theoretically expected by $\Delta f_{\text{theory}} \approx 0.095\,\text{MHz}$. Here, the frequency of the cavity at 4 K is $f_{4\,\text{K}} = 216.904\,\text{MHz}$ and at room temperature $f_{293\,\text{K}} = 216.499\,\text{MHz}$, resulting in a frequency change due to thermal contraction of $\Delta f_{\text{thermal}} = 0.405\,\text{MHz}$.

8 Modular Cavity Design and Optimization

The main focus of this thesis was to develop a way to design the nine cavities CH3 to CH11 of the HELIAC in such a way that both the production cost and the manufacturing time can be reduced as far as possible. After some considerations and discussions with both the future operators and possible manufacturers, it was decided to design the cavities in such a way that they could be mass produced. For this purpose, a modular cavity design was created and the suitability of the cavities designed in this way was confirmed by simulations (see section 8.1.1). The basic design is thereby based on the already successfully built and tested cavities CH1 and CH2 of the HELIAC project [1]. Special attention was paid to the optimization of the cavities with respect to high frequency performance and both the reduction of peak electric and peak magnetic fields (see section 8.3). The cavities were designed and analysed using CST Studio Suite [40]. A superconducting CH cavity conceptualized and designed for the HELIAC project has to meet the following requirements:

- Acceleration gradient from 5 to 6 MV/m
- Reduction of both production time and production costs
- Simplified cylinder geometry
- Reduced pressure sensitivity due to increased mechanical stability
- A frequency deviation of the dynamic bellow tuners of $\Delta f \approx 150\,\mathrm{kHz}$
- A minimum surface treatment of 200 μm BCP

8.1 General Design of the Cavities

The general design of the CH cavities CH3 to CH11 of the superconducting HELIAC at GSI introduced here is based on the two previous cavities CH1 and CH2 [1]. The distinguishing features of these cavities are the lids with a conical tapered deepening, straight spokes that widen outward and stabilizer ribs on the lids for better stability and reduced frequency variation due to cavity evacuation and pressure fluctuations within the Helium reservoir, two static tuners for frequency readjustment during manufacturing and two dynamic bellow tuner for frequency correction during operation, two flanges embedded in the cone of each lid for HPR of the cavity off the beam axis and two drain flanges for both the rinsing water of the HPR and

the chemical buffer solution for the BCP surface treatment. However, cavities CH3 to CH11 differ from their predecessors in that a new approach to mass production capability was applied to the design (see section 8.1.1). Thus, in order to simplify the production of these cavities, a modular cavity design was developed and these cavities created in this new approach were evaluated for their suitability for future operation through simulations using CST Studio Suite [40]. In addition, a new bellow tuner design was created that improves the electrical properties of the cavity (see section 8.2).

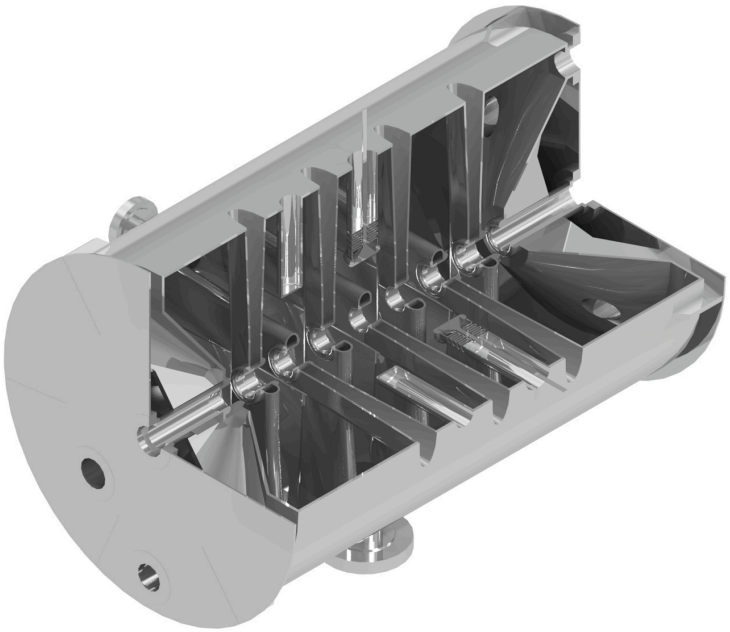

Fig. 60 Representative of all cavities CH4 of the HELIAC. The conical lids, the straight spokes and both the dynamic bellow tuner and the static tuner can be seen.

8.1.1 Elaboration of a Modular Cavity Design

The main focus of this thesis was to develop a possibility of significantly reducing both the production time and the production costs. This reduction in production costs is a challenge, since the material used, Niobium, is in itself a very expensive material and must be of very high purity, and the complex internal geometry of a CH cavity requires many processing steps. In addition, the wall thickness of the outer walls, the spokes, the lids and the tuner amount to only a few mm due to the required cooling by the liquid Helium to 4 K, so that handling during production is already a challenge. Thus, no major savings in terms of cost or time can happen either in the selection of the material or in the method of fabrication, so these cost reductions have to be realized already in the design of the cavities.
A discussion with the manufacturer RI, who had produced the cavities CH0 [27],

CH1 and CH2 [1], and an exchange of their experiences and their way of working, a possible methodology could be developed to significantly reduce both the production costs and the production time. A large and costly part of the production is the additional fabrication and adaptation of tools, mounts and machines to the individual geometries of the components of the cavities, such as spokes, lids, flanges or tuners. Thus, a separate mount or adaptation is normally manufactured for each new component, for example, for deep drawing or electron welding. This generates additional costs and an enormous amount of additional time. To avoid this additional effort, the concept of a modular CH cavity was developed. In this concept, some essential components are designed with the same geometry for all nine CH cavities of the HELIAC, so that only one set of mounts, tools and adaptations has to be manufactured. Figure 61 shows the modular lids and spokes. Here, similar to CH1 and CH2, the depth of the spokes was chosen to match the length of the drift tube in CH3 [1].

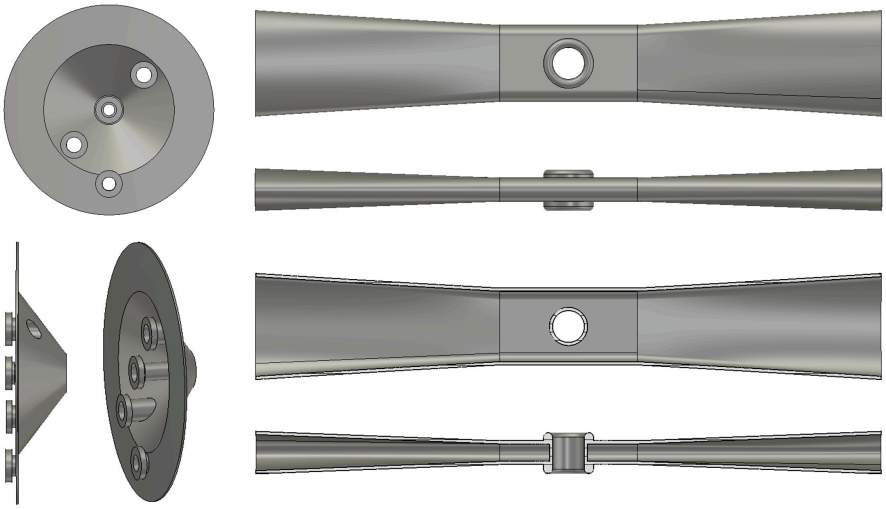

Fig. 61 Models of the modular parts of the cavities as they can be manufactured for all nine cavities. On the left, the lids with the required flanges are shown in various views, and on the right, the spokes are shown frontally, laterally and in each case in a cross-section.

Consequently, these individual modular components will be manufactured to a unit length, which will then be adapted to the appropriate boundary conditions of each cavity, such as the changing radius (see figure 62 and figure 63).

An initial estimate of the possible costs showed that, despite the additional material required, there would be a significant cost reduction. In figure 64, all nine cavities (from CH3 to CH11) are shown one above the other. They are aligned once at the right lid and once at the first spoke. It can be seen that apart from the length of the spoke or the radius of the lid, these are identical for all nine cavities.

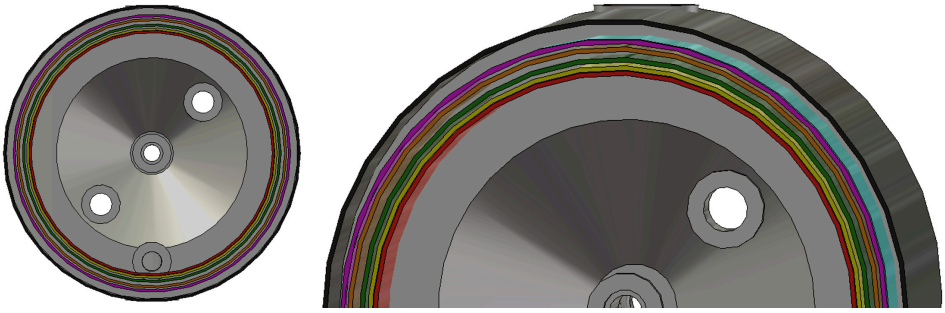

Fig. 62 The modular lid of the CH cavities with the radii of cavities CH3 (red), CH4 (yellow), CH5 (green), CH6 (orange), CH7 (purple), CH8 (turquoise), CH9 (blue), CH10 (dark turquoise) and CH11 (black) drawn in.

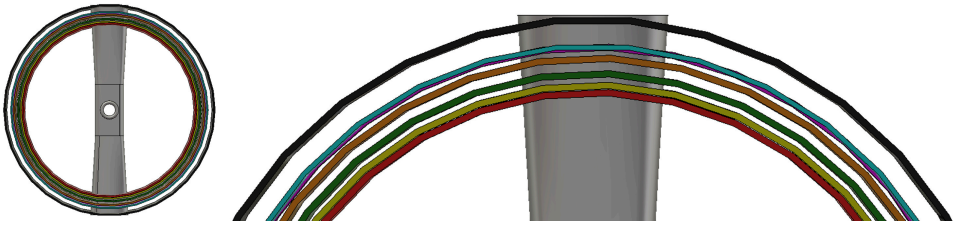

Fig. 63 The modular spoke of the CH cavities with the radii of cavities CH3 (red), CH4 (yellow), CH5 (green), CH6 (orange), CH7 (purple), CH8 (turquoise), CH9 (blue), CH10 (dark turquoise) and CH11 (black) drawn in.

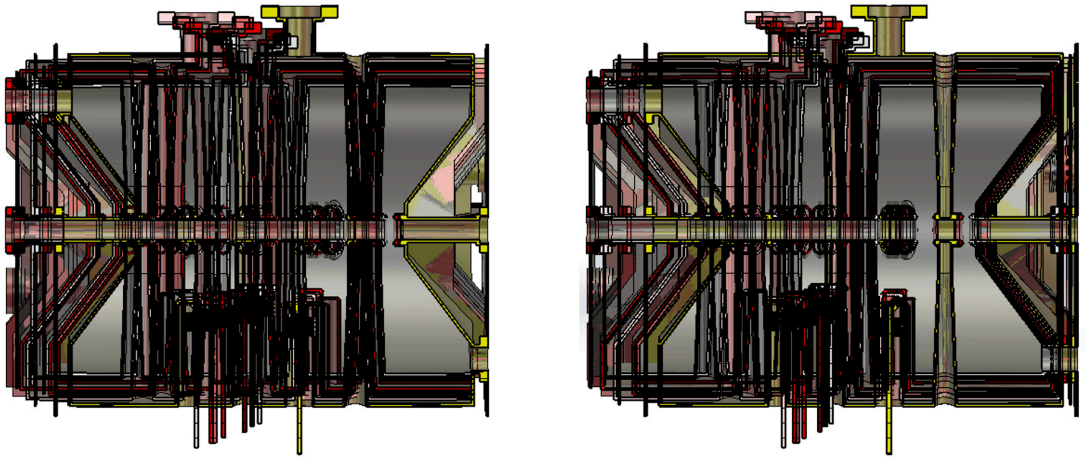

Fig. 64 All nine CH cavities of the HELIAC project designed in this thesis are shown overlaid on top of each other. Each cavity is marked with a different colour, from CH3 with yellow to CH11 with black. Left: The fixed point of this representation is the right lid. Right: Here the fixed point is the first spoke of all cavities.

8.2 Adjusting the Dynamic Bellow Tuner

In addition to the spokes and lids, another component that has been adapted as part of the modular cavity design compared to the CH1 and CH2 designs is the dynamic bellow tuner. The bellow tuner are used to adjust the resonant frequency of the cavity during operation by either moving them closer to or away from the beam axis, thus changing the capacity within the cavity, which also results in a change of the resonant frequency. These bellow tuner are also made of Niobium like the rest of the cavity and are fully welded to the cavity (see figure 60).

The dynamic bellow tuner consists of four parts, the outer tuner tube, the bellow, the tuner head and the inner tuner rod (see figure 65). The lower end of the outer tuner tube is welded to the cavity. The bellow is used to displace the tuner. Unlike normal conducting tuner, the welded superconducting bellow tuner cannot simply be pushed further into the cavity, but must expand spatially without creating an opening, otherwise the liquid Helium flowing through the cavity and therefore through the tuner would flow into the cavity. The principle of the dynamic bellow tuner was designed for this purpose. A force is applied to the inner tuner rod, which is connected to the tuner head, and this expands the bellow.

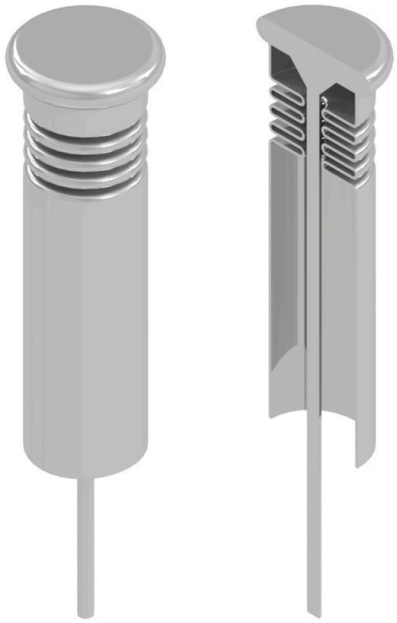

Fig. 65 Representation of the dynamic bellow tuner once as a whole and once in cross-section.

Since the wall thickness of the dynamic bellow tuner is only 1 mm, no large force is required for a sufficiently large displacement of ±1 mm. Compared to the dynamic bellow tuner design of both CH1 and CH2 cavities, the bellow tuner of the modular cavity design has been simplified. For the CH1/CH2 bellow tuner, the ribs of the bellow were extended outward (see figure 36). This was necessary because, due to the small gap center distance, there was not enough space between the spokes to fully fabricate the bellow tuner to one uniform radius, but larger ribs were needed to lower the force required for displacement [1]. With the modular bellow tuner design, this restriction is no longer necessary, so the bellow tuner now has a uniform radius. This simplification saves some additional welding and therefore production time and cost. In designing the modular bellow tuner, the first consideration was to conceptualize the bellow so that a displacement of ±1 mm could be achieved at

a force less than ±300 N without the von Mises internal stress exceeding a value of 0.25 GPa. This resulted in a bellow with three ribs and a rib length of 16.4 mm. Simulation results for both the deflection and the von Mises stress are shown in figure 66.

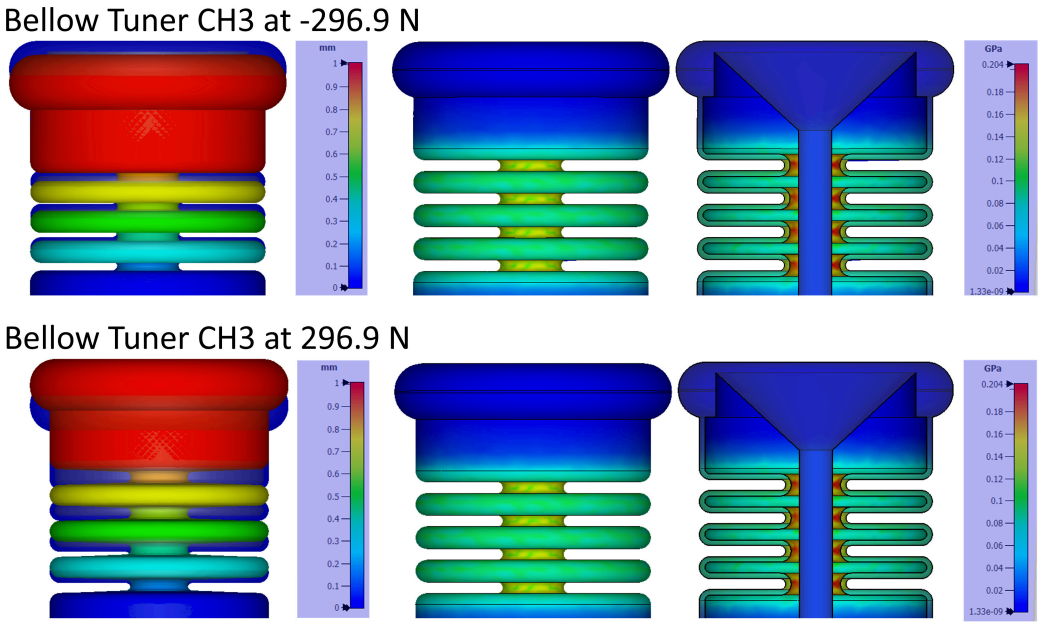

Fig. 66 Simulation results for the displacement (left) of the dynamic bellow tuner of cavity CH3 and for the internal stress of the bellow (middle and right). A force of ±296.9 N was applied to the tuner rod and the Helium vessel covers were defined as fixed points. When plotting the displacement, a factor of 3.96 was applied to the result for better illustration. The blue representation of the tuner indicates the shape and position of the tuner without the displacement force.

It can be seen that the tuner shown in figure 65 satisfies the above mentioned requirements. The simulation results shown in figure 66 were obtained by simulations on a tuner installed in cavity CH3. Here, the tuner head is displaced the most, and the displacement of the ribs increases from the bottom to the top. The internal von Mises stress within the material is thereby greatest in the inner curvature of the ribs. The simulation results for cavities CH4 to CH11 are shown in the appendix under figure 106 to figure 113. A graphical representation of the force required for deflection as well as the internal von Mises stress versus displacement of all nine cavities is shown in figure 67.

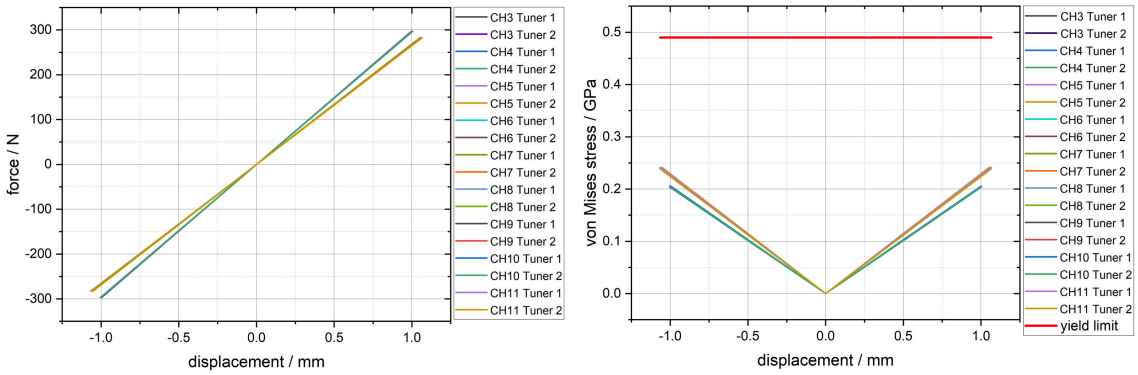

Fig. 67 Simulation results of the dynamic bellow tuner of cavities CH3 to CH11. Left: The maximum displacement versus the force required for the displacement. Right: The internal von Mises stress at a given displacement. In red is the maximum stress value for cold Niobium. If this value is exceeded, material failure and fracture will occur.

It can be seen that the modular bellow tuner installed in all nine cavities has very similar properties in terms of the force required or the internal stress. The slight differences between CH3/CH4 and the other cavities are due to the closer spokes, which stabilize the cavity and the tank wall and thus require more force. After the geometry of the bellow was determined, the tuner height was individually adjusted to the respective cavities in order to be able to achieve the desired frequency change by displacing the tuner. A total frequency change of approximately 150 kHz was specified as a goal for the design. In addition to achieving this goal, the height of the two bellow tuner within a cavity was set to be different from each other, in contrast to the dynamic tuner of CH1 and CH2. This condition has the benefit that both bellow tuner thus produce a different magnitude of frequency change. One bellow tuner was set to cause a frequency change of approximately 50 kHz in total (tuner 1) and the second one to cause a frequency change of about 100 kHz (tuner 2), so that when both are jointly displaced, a frequency change of approximately 150 kHz can be achieved. For this purpose, the outer tuner tube of tuner 1 is shortened until the tuner head is sufficiently far away from the beam axis and thus the influence on the capacity is sufficiently small to cause the small frequency change of circa 50 kHz. Conversely, for tuner 2, the outer tuner tube was extended until the effect on the capacity was sufficiently large for a frequency change of about 100 kHz. This adjustment of the modular bellow tuner was performed for all nine cavities until the desired frequency changes were achieved. These frequency changes versus the displacement of the bellow tuner for all nine cavities are shown graphically in figure 68.

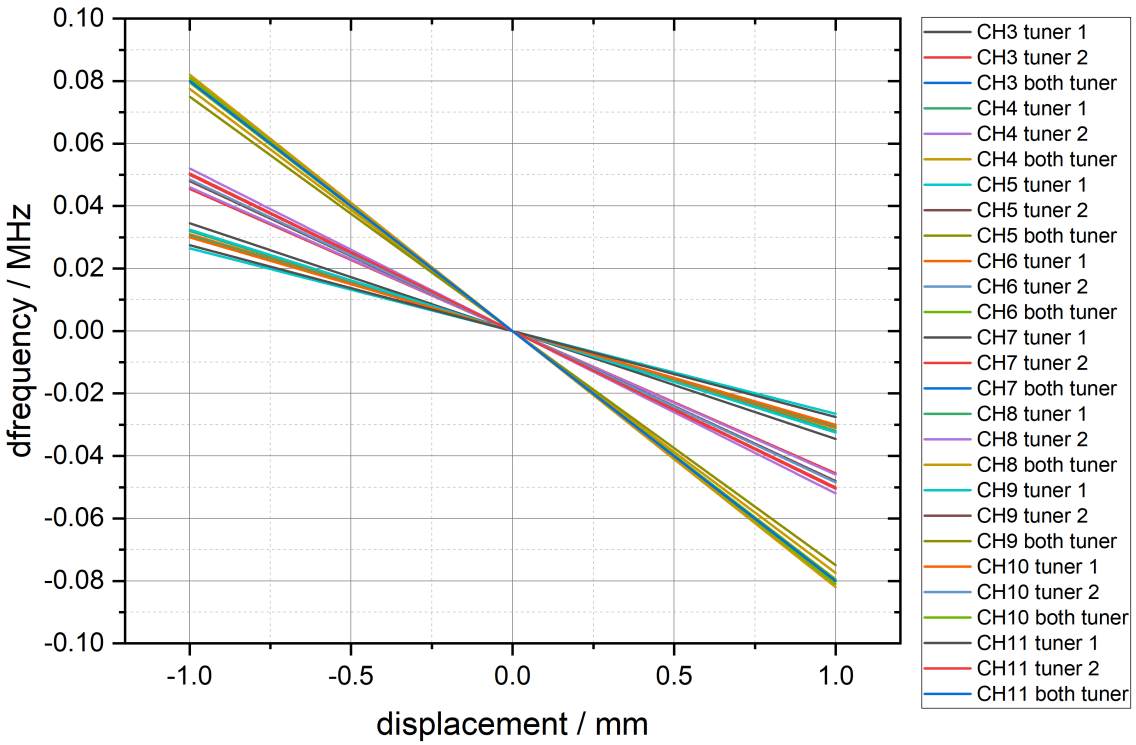

Fig. 68 Frequency change by displacement of the tuner. It can be seen that the individual tuner cause different frequency changes when they are displaced as well as when both are displaced at the same time and about the same amount.

In addition to defining the frequency change, the new design of the bellow tuner could be used to reduce peak electric fields within the cavity. Since the tuner heads are close to the beam axis for a sufficiently large frequency change, these are often sites of increased field levels. To counteract these peak fields, tuner 1 and not tuner 2 was initially placed in the gaps with the highest field levels. This already had the effect of reducing the peak fields at the edges of the tuner head. Next, the rounding around the edges of the tuner head was significantly increased compared to the CH1/CH2 bellow tuner, since corners and edges are a potential source of peak fields. In figure 69, the electric field is shown for different rounding radii of the tuner head.

It can be seen that the magnitude of the peak fields decreases with increasing rounding radius from $E_{\mathrm{peak,\,0\,mm}} = 1.61 \times 10^7\,\mathrm{V/m}$ to $E_{\mathrm{peak,\,5\,mm}} = 1.57 \times 10^7\,\mathrm{V/m}$. This decrease in the peak fields simultaneously indicates an increase in the performance of the cavity, since for the same acceleration field E_a (see figure 70), the magnitude of the peak fields E_peak decreases.

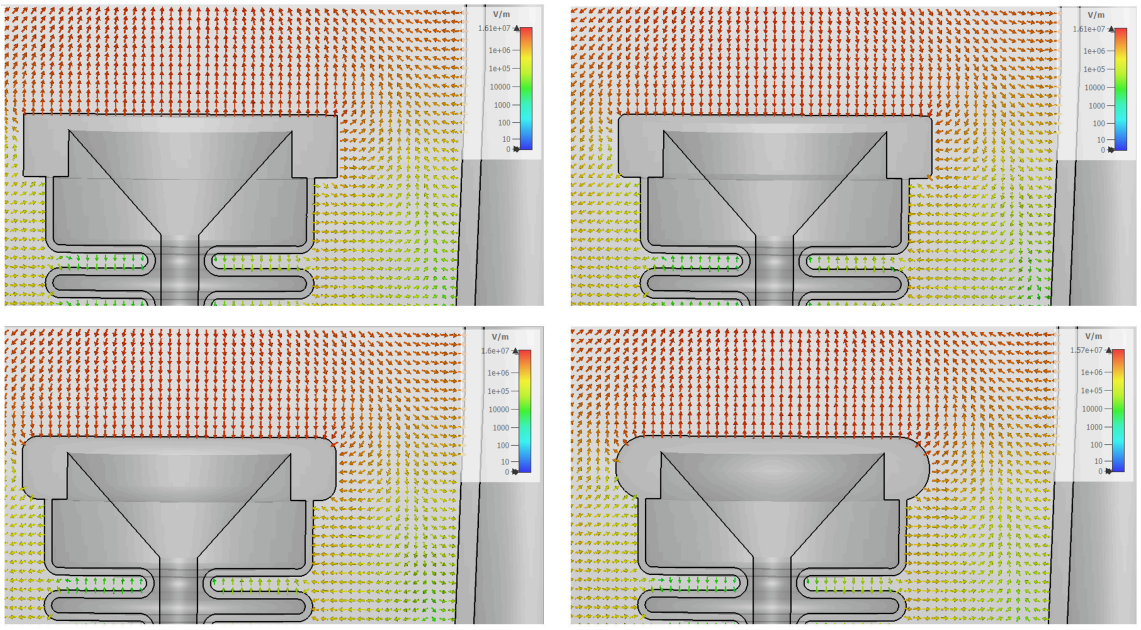

Fig. 69 Field distribution around the tuner head at different curvature radii of the head. Top left: No rounding. Top right: A radius of 0.1 mm. Bottom left: A radius of 2.5 mm. Bottom right: A radius of 4.9 mm.

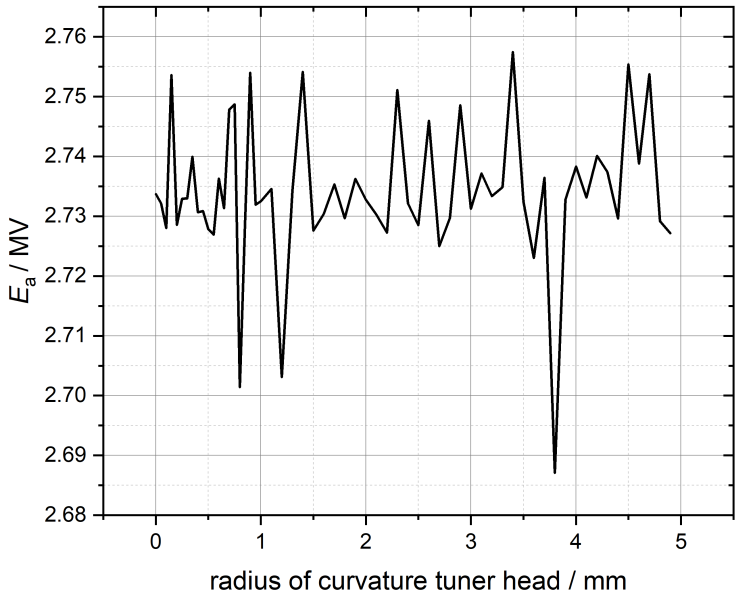

Fig. 70 Simulation results of tuner head design optimization. The influence of the rounding radius of the tuner head on the acceleration field E_a is shown.

Considering now the two ratios E_{peak}/E_a and B_{peak}/E_a (see section 4.1) at constant acceleration field E_a, it is noticeable that although the electrical peak fields could be reduced significantly by adjusting the rounding of the tuner head, the

magnetic peak fields remain unaffected. This is consistent with the field distribution within the cavity. Figure 71 shows the course of the two ratios against the rounding of the tuner head.

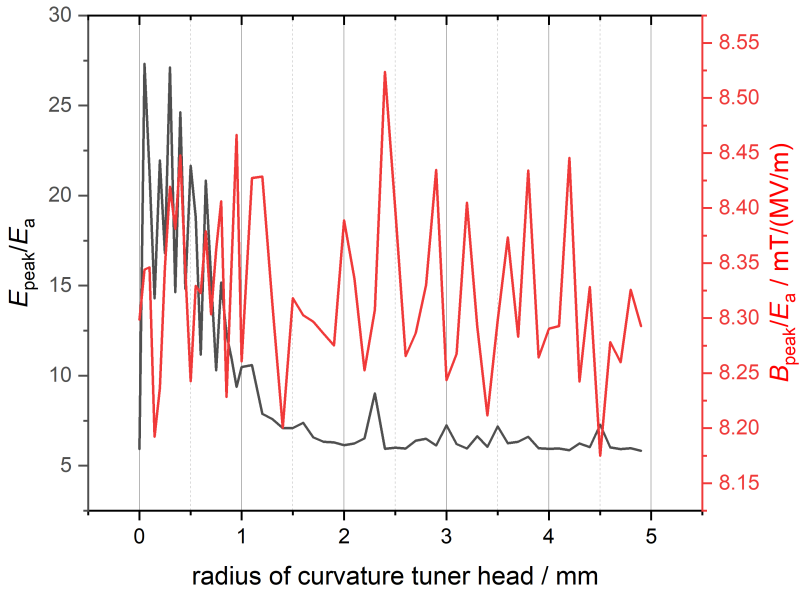

Fig. 71 Simulation results of tuner head design optimization. The influence of the radius of curvature of the tuner head on $E_{\mathrm{peak}}/E_{\mathrm{a}}$ (black) but not on $B_{\mathrm{peak}}/E_{\mathrm{a}}$ (red) can be seen.

In addition to the RF properties, the mechanical properties of the bellow tuner were also examined. Since the bellow tuner has a wall thickness of only 1 mm, as already mentioned, it is very vulnerable to mechanical vibrations. Mechanical vibrations of the tuner can influence the resonant frequency of the cavity via additional deformations. Thereby, the tuner can be excited to vibrate by external mechanical vibrations, which can be caused by pumps, the Helium flow or similar. Therefore, the bellow tuner was analysed for its intrinsic mechanical modes using the software Ansys Workbench [54]. The end of the inner tuner rod was assumed to be the fixed point. In figure 72 is a graphical representation of the modes and their corresponding frequencies.

After considering the simulation results, it can be concluded that the modular bellow tuner is sufficiently insensitive to external interference. Thus, with a total of 10 modes up to 1 kHz, it has significantly more mechanicals modes than the CH1/CH2 bellow tuner [1], but the fundamental mode is at 101 Hz. Most interference sources, such as pumps or the equivalent, are in a frequency range of $f \leq 100\,\mathrm{Hz}$, so the modular bellow tuner is unaffected by these interference sources. In figure 73, 5 of the 10 mechanical eigenmodes of the tuner are shown.

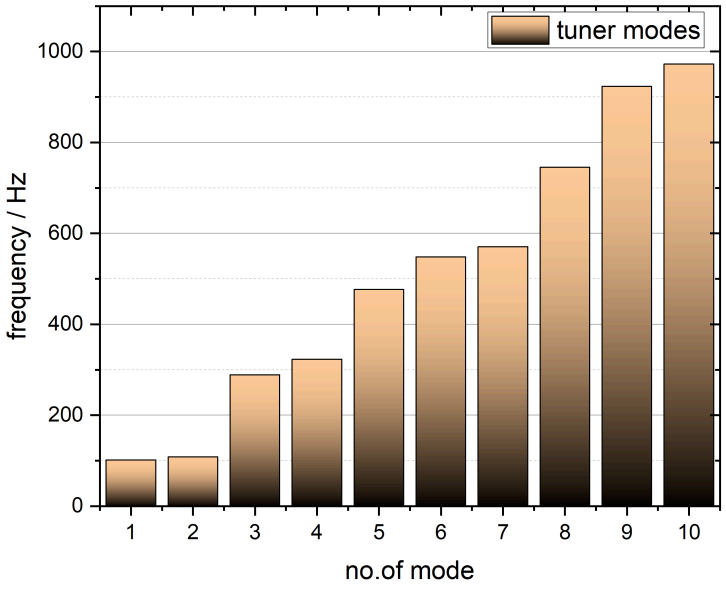

Fig. 72 Graph of the mechanical vibration modes of the bellow tuner against the frequency at which they are excited.

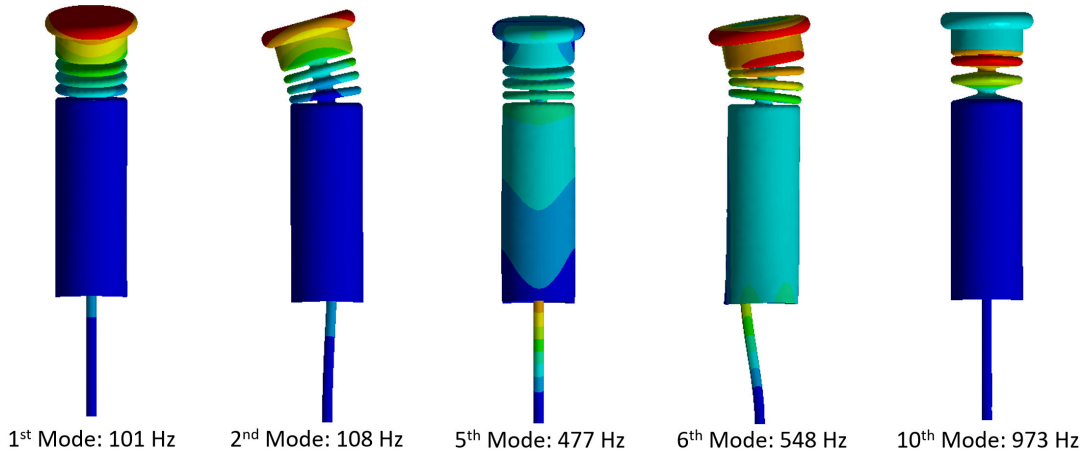

Fig. 73 5 Simulation result of the mechanical modes with Ansys Workbench [54] with the corresponding frequencies in Hz.

The first and second modes, which are close to each other, are transverse oscillation modes of the tuner head relative to the rest of the tuner. The following modes 3 to 9 are transverse vibrations of the entire tuner and mode 10 is a longitudinal vibration of the bellow. Since the modular dynamic bellow tuner is sufficiently insensitive to external mechanical vibrations, the desired tuning range could be realized, the tuner head could be adapted to reduce the peak electric fields and the mechanical requirement and limitations due to displacement and internal von Mises stress could be met, the modular dynamic bellow tuner is suitable to be incorporated as part of the modular cavity design in cavities CH3 to CH11 of the HELIAC.

8.3 Field Distribution Optimization

After the modular cavity design and the adapted design of the modular bellow tuner had been completed the individual cavities CH3 to CH11 of the HELIAC could be assembled from these components. For this purpose, the number of gaps of the individual cavities as well as the gap center distances were taken from the previously determined beam dynamics of the HELIAC [25] and the cavities were then assembled individually in a modular manner. It is noticeable that the gap center distances increase from cavity to cavity, but at the same time the number of gaps decreases, so that the total length of the cavities varies (see section 8.6). As shown in section 3.1, the TE_{211}-mode generated in the CH cavity has no electric field component in z-direction ($E_z = 0$ in (42)), however, the insertion of the spokes into the resonator generates a potential distribution in z-direction between neighboring spokes which has its maximum in the center and decreases to zero towards the outside of the cavity (see figure 74).

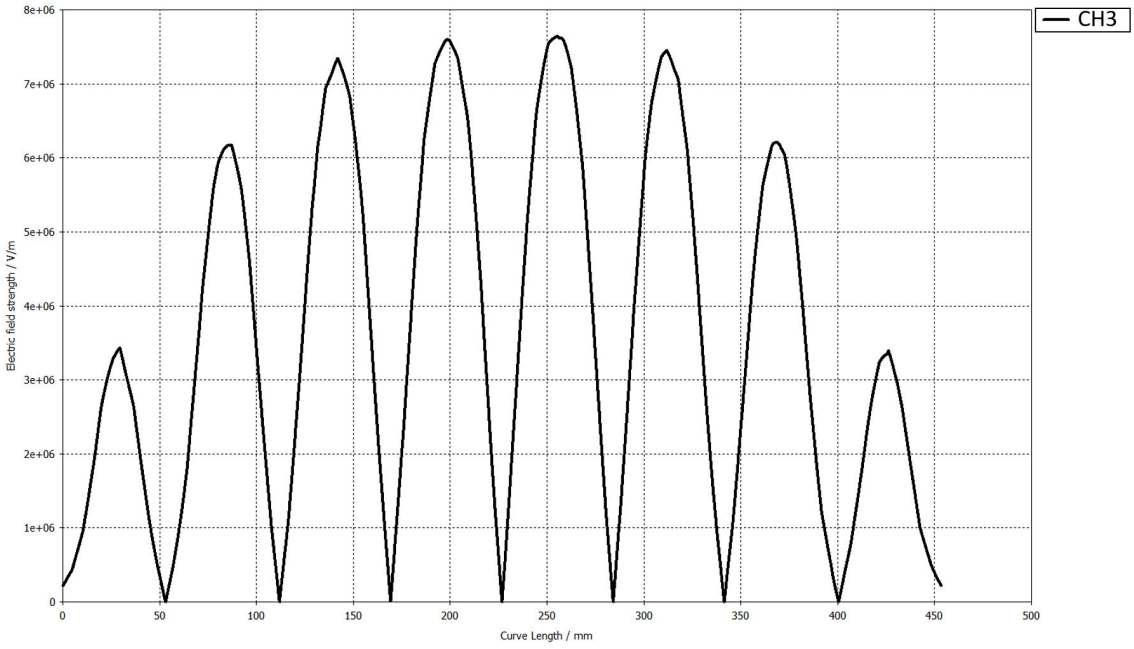

Fig. 74 Electric field distribution inside cavity CH3. On the x-axis represents the length of the accelerating field inside the cavity and the y-axis represents the electric field strength in V/m determined by CST Studio Suite [40] when coupling a power of 1 J electric power.

The field distribution shown in figure 74 corresponds to the simulated field distribution within CH3 should a electric power P_f of $P_\mathrm{f} = 1\,\mathrm{J}$ be injected into the cavity. The field distributions of the other eight cavities are shown in the appendix under figure 114 to figure 121. The outward decrease of the electric field and therefore of

the voltage between the spokes can be counteracted by adjusting the responded drift tube length. It should be noted, however, that while lengthening the drift tubes increases the voltage in the respective gap, insufficient spacing between neighbouring drift tubes can lead to electrical arcs. This limitation of the length of the drift tubes has a particularly large influence in the case of cavities with a smaller gap center distance, such as CH3 and CH4. Here, the comparatively short drift tubes at the outer gaps lead to a small voltage between the spokes and thus to a large drop in voltage towards the outside of the cavity compared to the maximum. For the cavities with a large gap center distance, such as CH10 and CH11, the drift tubes can be lengthened to such an extent that the voltage in all gaps remains very similar. Besides the potential electrical arcs, an insufficient distance between the drift tubes can increase the acceleration field on the beam axis E_a, but also increase the potential local peak fields located at the drift tubes, so that the length of the drift tubes has a great influence on the ratio $E_\mathrm{peak}/E_\mathrm{a}$ and thus on the performance of the cavity. For this reason, in the case of cavities CH3 to CH11 which are based on the modular cavity design, the different drift tube lengths were crucial parameters for the performance-oriented optimization of the cavities. The parameters $D_\mathrm{thickness}$, $D_\mathrm{length,\,1}$, $D_\mathrm{length,\,2}$ and $D_\mathrm{length,\,3}$ used for the optimization are defined in figure 75.

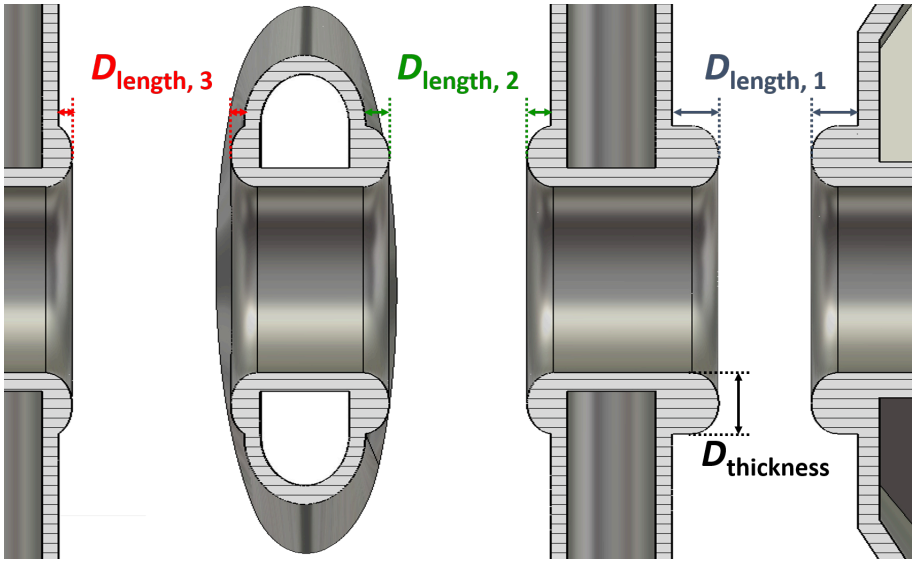

Fig. 75 Cavity CH3 shown in cross section with the four optimizations parameters $D_\mathrm{thickness}$ (black), $D_\mathrm{length,\,1}$ (blue), $D_\mathrm{length,\,2}$ (green) and $D_\mathrm{length,\,3}$ (red) marked.

In order to determine the length of the individual drift tubes, the optimizer integrated in CST Studio Suite [40] was used. For this, the parameters $D_\mathrm{thickness}$, $D_\mathrm{length,\,1}$, $D_\mathrm{length,\,2}$ and $D_\mathrm{length,\,3}$ as well as the inner radius of the cavity were set as variable parameters and both the desired resonant frequency of the cavities and the lowest possible values for the ratios $E_\mathrm{peak}/E_\mathrm{a}$ ($E_\mathrm{peak}/E_\mathrm{a} < 4$) and $B_\mathrm{peak}/E_\mathrm{a}$ ($B_\mathrm{peak}/E_\mathrm{a} < 7$) were set as targets, where the weighting of the objectives decreased

from reaching the resonant frequency to the ratio $E_{\mathrm{peak}}/E_{\mathrm{a}}$ and finally to the ratio $B_{\mathrm{peak}}/E_{\mathrm{a}}$. The algorithm chosen for the optimization was the Nealder-Mean method (see section 8.7.1). After the optimizer had determined a first configuration, it was possible to manually adjust the individual parameters. For this purpose, a much smaller range was defined for the sweep of the individual parameters than for the optimizer. First the drift tube thickness was used and then the lengths. The inner radius of the individual cavities was varied as the last optimization parameter, since this exerts a direct influence on the frequency without affecting the acceleration field E_{a} too much. The process was then repeated with an even smaller parameter optimization range until almost no improvements were noticeable. With this method of manual optimization, it should be noted that not every newly found optimal parameter configuration with regard to performance of a single parameter directly results in a new ideal overall parameter optimization. Thus every change of the parameters listed above also causes a frequency change. The readjustment of the changed frequency to the target resonance frequency by readjusting the cavity inner radius changes the acceleration field E_{a}, even if relatively small. Therefore, constant readjustment and re-optimization of each parameter is required. By multiple iterations of the individual optimization parameters and constant readjustment of the resonance frequency by the radius, an optimum can thus be found with respect to the performance. In figure 76 the last optimization steps for cavity CH3 are shown by variations of the optimization parameters. Figure 122 to figure 129, which can be found in the appendix, show the last optimization steps for CH4 to CH11.

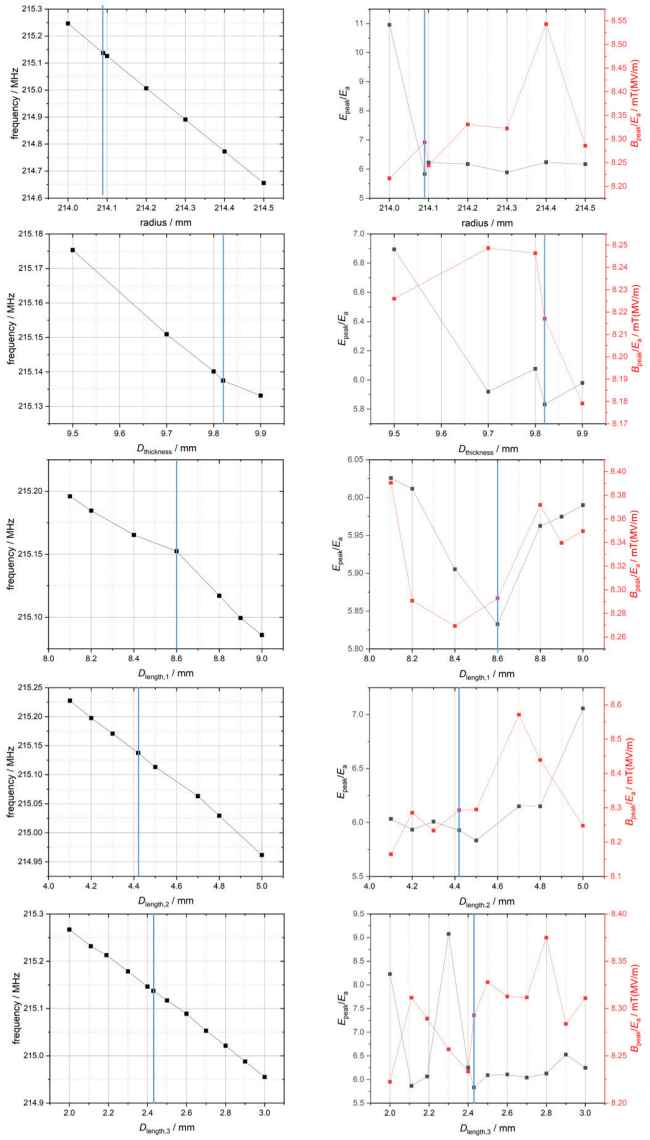

Fig. 76 Simulation results for the optimization of cavity CH3. The blue line indicates the final value of the respective parameter. Left: Course of the frequency against the corresponding optimization parameter. Right: Course of $E_{\mathrm{peak}}/E_{\mathrm{a}}$ (black) and $B_{\mathrm{peak}}/E_{\mathrm{a}}$ (red) against the corresponding optimization parameter.

The blue lines drawn in the graphs of figure 76 mark the final values for the parameters. It is noticeable that the optimal value of the respective parameter for the final geometry of the cavity was not always chosen, since, as described above, readjustment of the resonance frequency with this parameter configuration would ultimately result in poorer performance. In figure 77, the values for the ratios $E_{\mathrm{peak}}/E_{\mathrm{a}}$ and $B_{\mathrm{peak}}/E_{\mathrm{a}}$ are plotted as indicators for the performance of the cavities for the cavities CH3 to CH11 as well as for the two predecessor cavities CH1 and CH2 as a comparison.

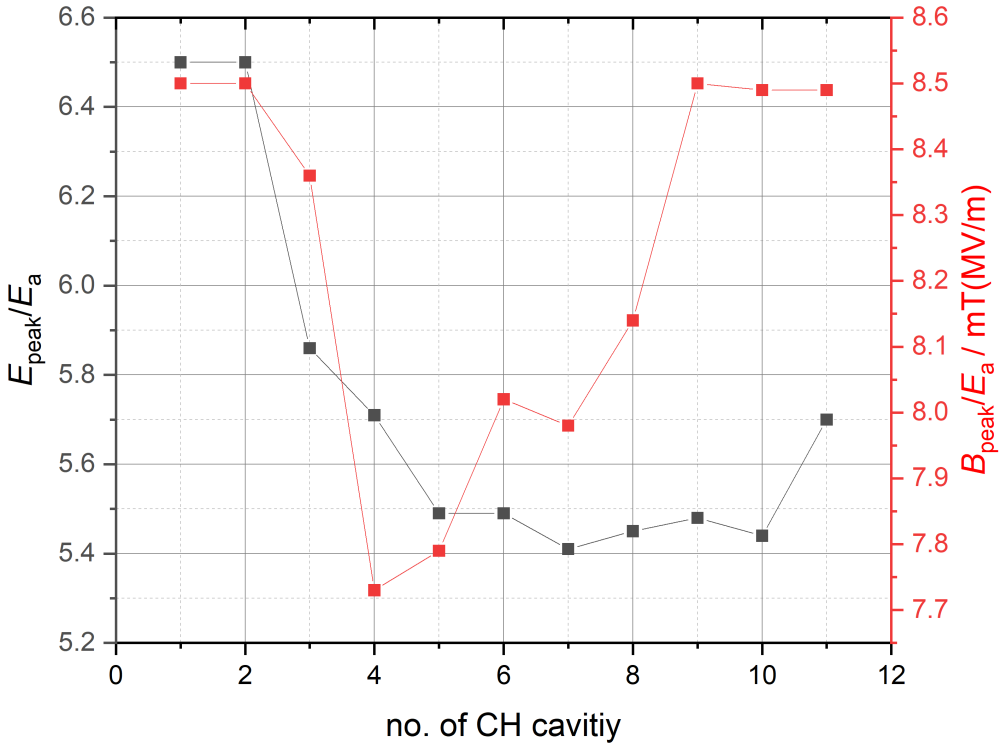

Fig. 77 The results of the optimization of the cavities CH3 to CH11 in the form of the ratios $E_{\mathrm{peak}}/E_{\mathrm{a}}$ (black) and $B_{\mathrm{peak}}/E_{\mathrm{a}}$ (red).

It can be seen that for all nine cavities based on the modulare cavity design better values for $E_{\mathrm{peak}}/E_{\mathrm{a}}$ and for CH3 to CH8 also better values for $B_{\mathrm{peak}}/E_{\mathrm{a}}$ could be achieved compared to the two predecessor cavities CH1 and CH2. This demonstrates that despite the modular cavity design reducing production costs and production time, the nine superconducting CH cavities perform better in the simulations than the individually designed CH1 and CH2 cavities.

8.4 Frequency Tuning

In designing the cavities, they were intentionally designed so that their resonant frequencies deviate from the HELIAC project's actual desired target frequency of 216.816 MHz. As the designed cavities continue to undergo a wide variety of manufacturing steps and mechanical deformation during commissioning, the resonant frequencies of the cavities increase with each of these steps until they are close to the desired target frequency. A necessary treatment step, which has an enormous influence on the resonant frequency during the construction of the cavities, is the so-called BCP (see section 8.4.1). During commissioning both the evacuation of the cavities (see section 8.4.2) and the cool down to the operating temperature of about 4 K (see section 8.4.3) further influence the resonant frequency. In order to achieve the desired target frequency for the later cavities in operation, simulations were performed to determine the frequency change of the individual and combined structural as well as operational measures and thus determine a required preliminary design resonant frequency of the cavity. These are shown in figure 78.

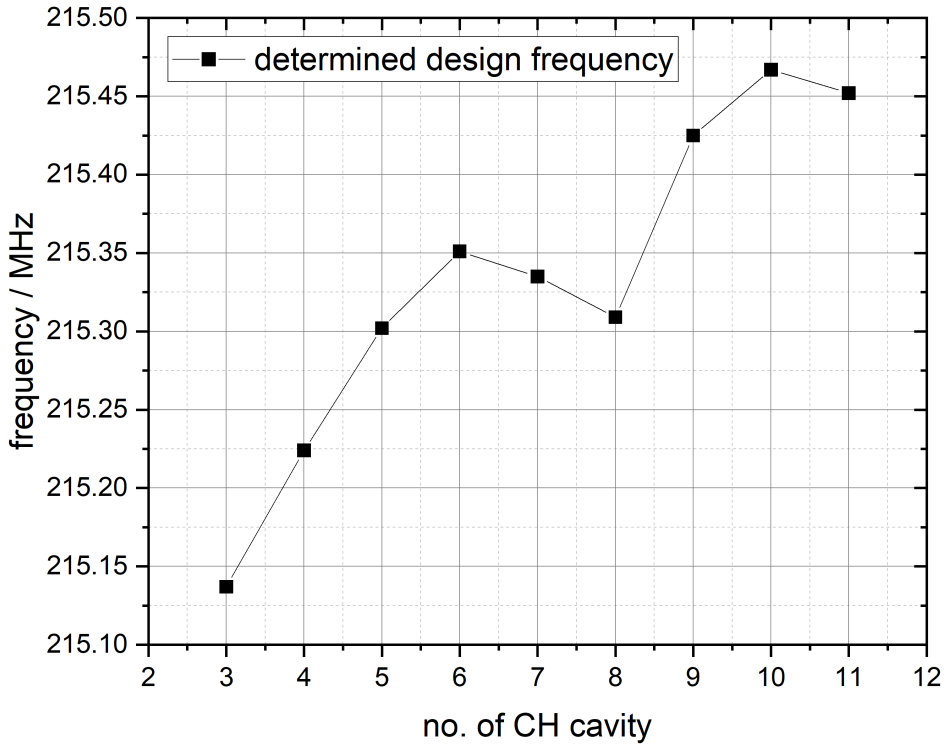

Fig. 78 Determined design frequency without adjustments of the frequency by BCP, evacuation or thermal contraction.

The deviation of the resonant frequencies of the individual cavities from each other is due to the fact that they react differently to the influence of the individual frequency changing steps, since the geometric differences of the cavities, such as

increasing radius and increasing gap length, can compensate for these influences to a different extent due to the modular cavity design. In the following, the individual frequency changing steps will be explained in more detail and their influence on the resonant frequency will be shown.

8.4.1 Buffered Chemical Polishing

As already described in chapter 4, the surface quality of a superconducting cavity has a direct influence on its performance. For example, impurities or microscopic imperfections on the surface of the resonator can lead to local peak fields, which can ultimately lead to multipacting, field emissions, or an increase in surface resistance. To minimize the number of these impurities or imperfections, a superconducting cavity is prepared with a 1:1:2 mixture of hydrofluoric acid (HF), nitric acid (HNO_3), and phosphoric acid (H_3PO_4) after its construction is completed. This acid mixture removes the imperfections and thus increases the performance of the cavity. For this purpose, the acid mixture is pumped into the vertically positioned cavity via the lower of the two additional rinsing flanges on the lids and collected on the upper rinsing flange. While the cavity is flushed with the acid mixture, material is constantly removed from the inner cavity walls. The amount of material removed depends on the saturation of the acid mixture. With the time of the surface treatment the amount of removed Niobium within the acid mixture increases steadily, so that the effect of the acid decreases with increasing treatment time. In order to be able to make a statement about how long the treatment must last for the desired removal, the removal rate is first determined with a Niobium sample before each BCP surface treatment. However, since the superconducting CH cavities considered here have a very complex internal structure, it is extremely difficult to make an accurate statement even with the method of previously estimated removal. The BCP treatments for the CH1 and CH2 cavities have shown that the spokes and the tuner have a significantly higher removal rate than, for example, the tank wall [1]. However, in the simulation considered here to determine the frequency change after an removal of 200 μm, a uniform removal in the entire cavity was assumed (see figure 79).

It can be seen that the resonant frequencies of the cavities are affected differently by the BCP treatment. This is because the first cavities have more spokes, which are also closer to each other, so increasing the distance between neighbouring spokes due to the removal of Niobium from the spoke walls has a greater effect on the capacities within the cavities, resulting in a greater change in frequency. After each BCP treatment, a HPR is provided so that the cavities are flushed with high purity water for several hours to remove acid residues from the cavity. In addition, the treatment time is first set so that only half the desired removal of BCP is achieved. The cavity is then rotated and the process repeated for the second half of the ablation to ensure the most uniform removal possible. The frequencies to be expected after complete removal of 200 μm can be seen in figure 80.

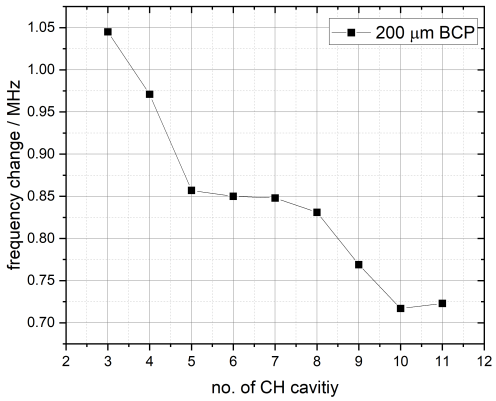

Fig. 79 Simulation results for the frequency change after surface treatment with BCP assuming a surface removal of 200 μm.

no. of CH cavity	Δf after BCP/ Hz/μm
CH3	5225
CH4	4855
CH5	4285
CH6	4250
CH7	4240
CH8	4155
CH9	3845
CH10	3585
CH11	3615

Tab. 5 Change in frequency after BCP per μm BCP.

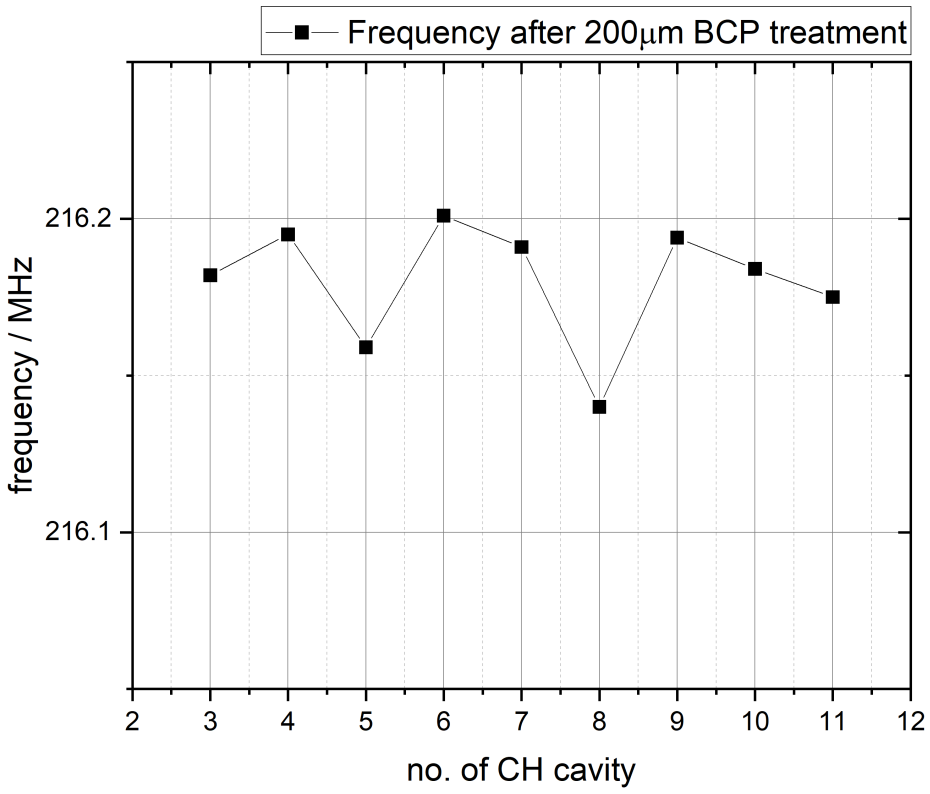

Fig. 80 Simulated resonant frequency of the cavities after uniform 200 μm surface treatment with BCP.

Comparing the resonant frequencies of the individual cavities from figure 78 with those from figure 80, it can be seen that the greater influence of the BCP treatment

on the resonant frequencies of cavities CH3 and CH4 compensates for the large deviation of the preliminary design frequencies, and thus the resonant frequencies after BCP treatment show a significantly smaller deviation from each other. As mentioned above, since experience has shown that the tuner are among the most affected by the removal, the two dynamic bellow tuner of each cavity have already been designed with an additional wall thickness of 200 μm, so that the desired wall thickness of 1 mm is reached only after the BCP treatment, in order to prevent this wall thickness from becoming even thinner, since especially strong stress is placed on the material there during the displacement of the tuner, which could lead to damage if the wall thickness is too thin.

8.4.2 Pressure Sensitivity

Superconducting accelerator structures are particularly vulnerable to frequency changes that occur during evacuation of the interior. The entire beam line of a particle accelerator is usually evacuated by a variety of different pumps and cavities are operated at internal pressures of $10^{-6} - 10^{-8}$ mbar to avoid collisions between the particles being accelerated and the residual gas, and consequently beam loss. As a result, there is usually a pressure difference between the environment and the inside of the cavity of about 1 atm $\hat{=}$ 1.013 25 bar. For normal-conducting cavities, this is usually no problem, since the walls of these are made of tens of mm of steel or similar material. For superconducting cavities, however, the situation is completely different, since the wall thickness of the components are only a few mm to ensure sufficient cooling by the liquid Helium to 4 K. For superconducting CH cavities, this is a particularly big problem, since too much displacement due to evacuation could distort the complex internal spoke structure to such an extent that the field distribution within the cavity is disturbed, resulting in a resonant frequency very different from the desired value. To counteract this, special attention was paid to pressure sensitivity in the design of CH1 and CH2 [1]. The measures taken in the design of these two identical cavities were also adopted for cavities CH3 to CH11. This includes both the tapered lid deepening with attached stabilizers and the straight, outward-widening spokes. However, in the designs from CH3 to CH11, these measures are only optimally effective for CH3, because of the modular cavity design, the modular lids and spokes, which are identical in construction for all nine cavities, were designed for CH3 as the cavity with the smallest gap center distance (see section 8.1.1). A direct comparison of the cavity with the smallest gap center distance CH3 with the cavity with the largest gap center distance CH11 shows that the deformation of the cavity increases in magnitude (see figure 81).

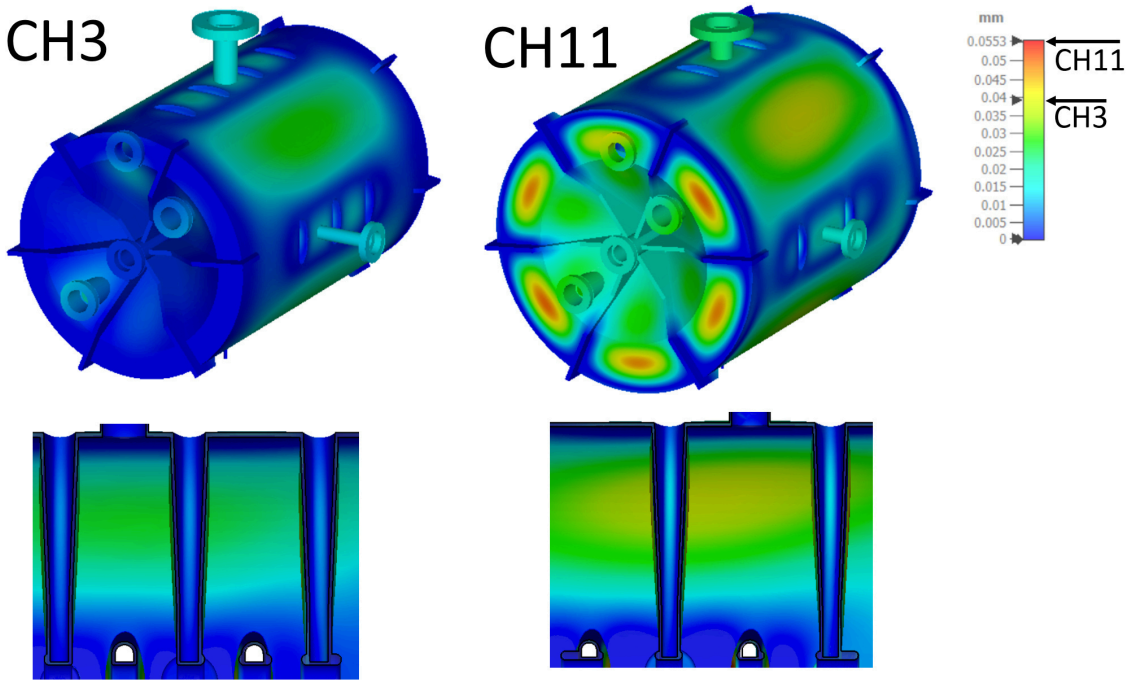

Fig. 81 Simulation of the expected mechanical deformation of cavity CH3 (left) and CH11 (right) due to evacuation of the cavity after the 200 μm BCP treatment. An internal pressure with force direction inwards of 1 atm was assumed. The scales of both result plots were set to the same range for better comparability.

In these simulations, the areas of the stabilizers welded to the Helium vessel lid and the end of the bellow tuner tubes were taken as displacement boundries, and the same pressure of 1 atm was applied to each inner surface of the cavity. In figure 81, the areas most affected by the deformation can be clearly seen in addition to the significantly increasing deformation of the cavity. Due to the modular cavity design, both the spokes and the lids are no longer ideally adapted to the larger radius of cavity CH11. Thus, the outward expansion of the spokes does not sufficiently compensate for the growing radius of the cavity, resulting in greater inward deformation of the tank, as well as a greater deformation of the spokes due to the growing length of the spokes. The ring located on the lid, surrounding the deepening of the lid, also grows with the radius of the cavity and is thus a site for severe deformation. A comparison of all nine cavities shows that this additional lid deformation does not occur only at CH11, but the first signs of it already appear at CH5, even if they only become significant from CH9 onwards (see figure 82).

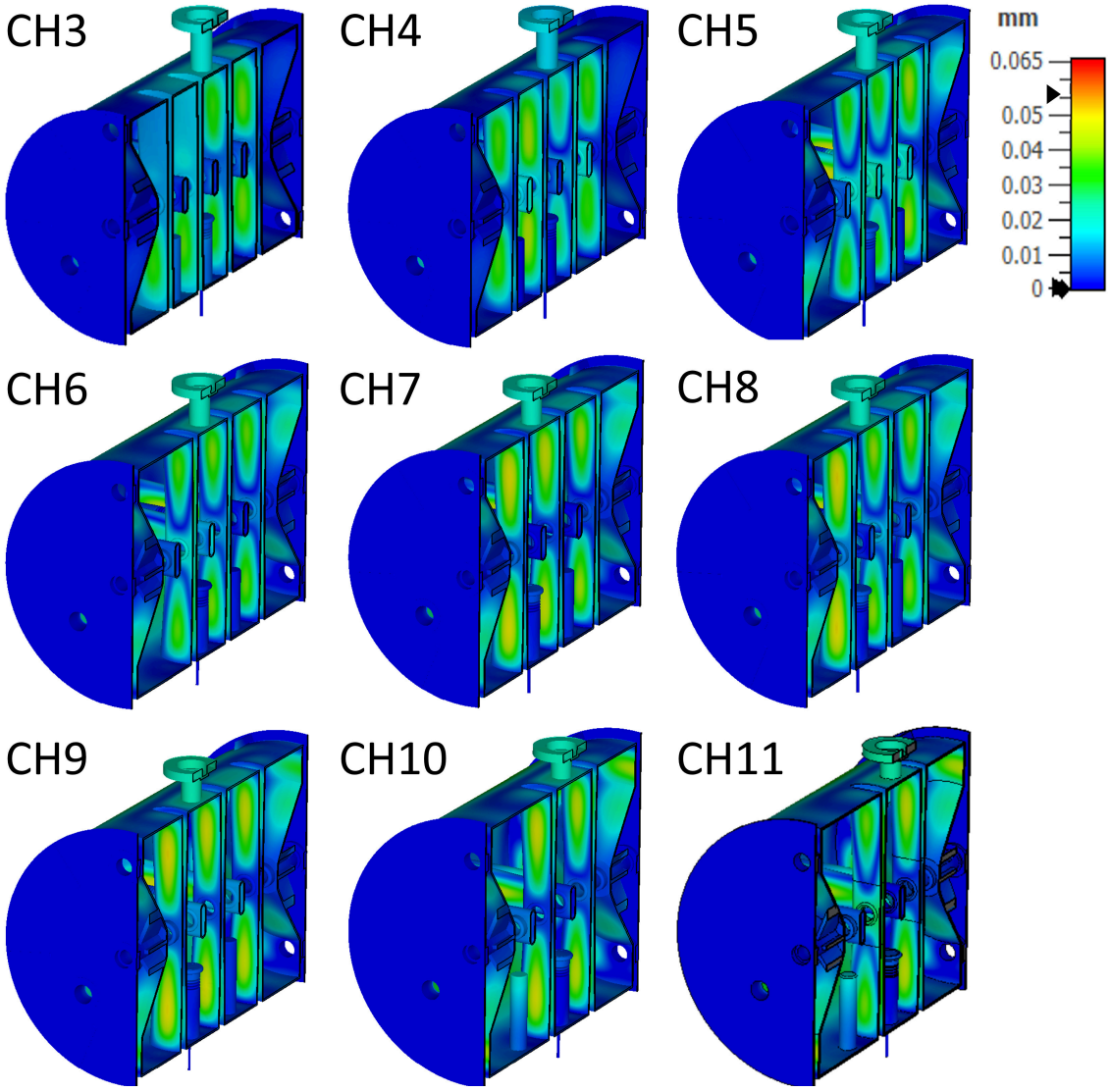

Fig. 82 Displacement of all cavities after evacuation. All scales are set to the same range to better the comparison. The upper black arrow indicates the maximum value of displacement of cavity CH11 of all nine cavities.

After determining the mechanical displacement of all nine cavities, these simulation results could be used to determine the frequency change due to the mechanical displacement. In figure 83 the maximum values of the mechanical displacement for all nine cavities are shown on the left and the calculated values for the pressure sensitivity of the nine cavities in Hz/mbar are shown on the right.

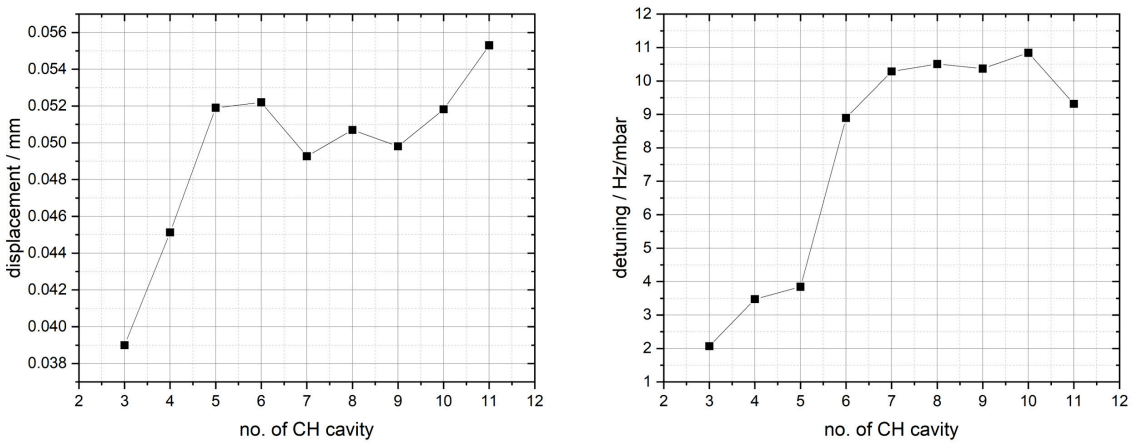

Fig. 83 Simulation results regarding the pressure sensitivity of cavities CH3 to CH11. Left: Displacement of the cavity in mm at a pressure difference from the interior to the environment of 1 atm. Right: The frequency change resulting from the deformation in Hz/mbar.

It can be seen that cavities CH3 and CH4 exhibit the lowest mechanical deformation. This can be explained by the fact that, on the one hand, the geometry for the modular lids and spokes were optimized for CH3 and CH4 is most similar to CH3 with the same number of gaps, but also by the fact that these two cavities have the most spokes, and thus the tank is better supported. Comparing the theoretical values of the pressure sensitivity of cavities CH3 to CH11 now determined by simulations with the experimentally determined values of the pressure sensitivity of CH1 ($\Delta f/\Delta p = -12.7\,\mathrm{Hz/mbar}$) [1] and CH2 ($\Delta f/\Delta p = -9.64\,\mathrm{Hz/mbar}$ see section 7.3), it is noticeable that although these values are of the same order of magnitude, they have an opposite sign. This arises from the fact that for CH1 and CH2, due to the small gap mean distance, the contraction of the lids and the spokes by evacuation additionally reduces the drift tube distances, which increases the capacity and thus decreases the frequency. This is counteracted by the decrease in volume due to contraction, which would increase the frequency, but for CH1 and CH2 the increase in capacity and so the decrease in frequency outweighs the decrease in volume and so the increase in frequency due to the small gap mean distance, which results in the negative sign. Looking now at CH3 to CH11, it is noticeable that the pressure sensitivity at CH3 is closest to 0, since in this cavity the two effects of volume reduction and capacity increase almost balance each other out. For the later cavities with an even larger gap mean distance, the volume reduction outweighs the capacity increase. This can be seen particularly well between CH5 and CH6. Even though these two cavities have the same number of gap, there is the largest increase in gap mean distance of approximately 8 mm between them. Therefore, it can be assumed that the increase in capacity due to closer moving spokes is no longer significant compared to the decrease in volume of the interior of the cavities from CH6 onwards, which is why all subsequent cavities show a similar pressure

sensitivity. This is further enhanced by the additional deformation occurring at the lid. The largest value of $\Delta f/\Delta p = 10.8\,\mathrm{Hz/mbar}$ at CH10, however, is of such a magnitude that possibly frequency changes due to occurring pressure fluctuations could be compensated by the dynamic bellow tuner. It can thus be said that the cavities and therefore the modular cavity design are suitable for later operation in terms of the expected pressure sensitivity.

The total resonance frequency of the cavities after evacuation is not only influenced by the mechanical displacement, but also by the fact that initially there is air in the cavities and after evacuation almost a vacuum. Since air now has a different electrical permittivity $\epsilon_{\mathrm{r,\,air}} = 1.0059$ than vacuum $\epsilon_{\mathrm{r,\,vacuum}} = 1$, the resonant frequency also changes. In figure 84 the absolute resonant frequencies of the cavities CH3 to CH11 are shown after BCP treatment and after evacuation, that is with a vacuum inside with $\epsilon_{\mathrm{r,\,vacuum}} = 1$ and mechanical displacement.

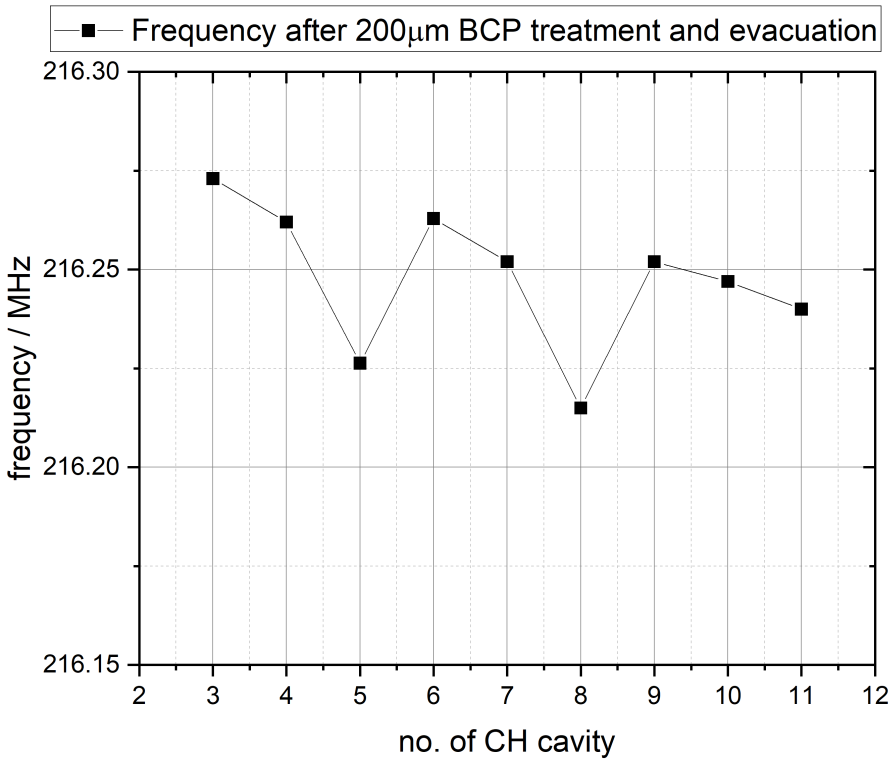

Fig. 84 Simulated resonant frequency of the cavities after uniform 200 μm surface treatment with BCP and evacuation.

The comparison between the resonance frequencies in figure 80 and those in figure 84 shows that the deviation of resonant frequencies from each other has been further reduced.

8.4.3 Thermal Contraction

The last frequency changing effect to be considered, is the thermal contraction of the cavities during cooling from room temperature to 4.2 K. During cooling, the cavities contract uniformly in all three spatial directions. The degree of this long contraction can be calculated by using equation (153) [53]. Accordingly, Niobium contracts by 0.143 %. Following Slater's theorem (see section 3.1.2) the frequency increases due to the volume reduction of the interior. The simulated frequency change resulting from cooling after 200 μm BCP treatment and evacuation of the cavities is graphically plotted in figure 85.

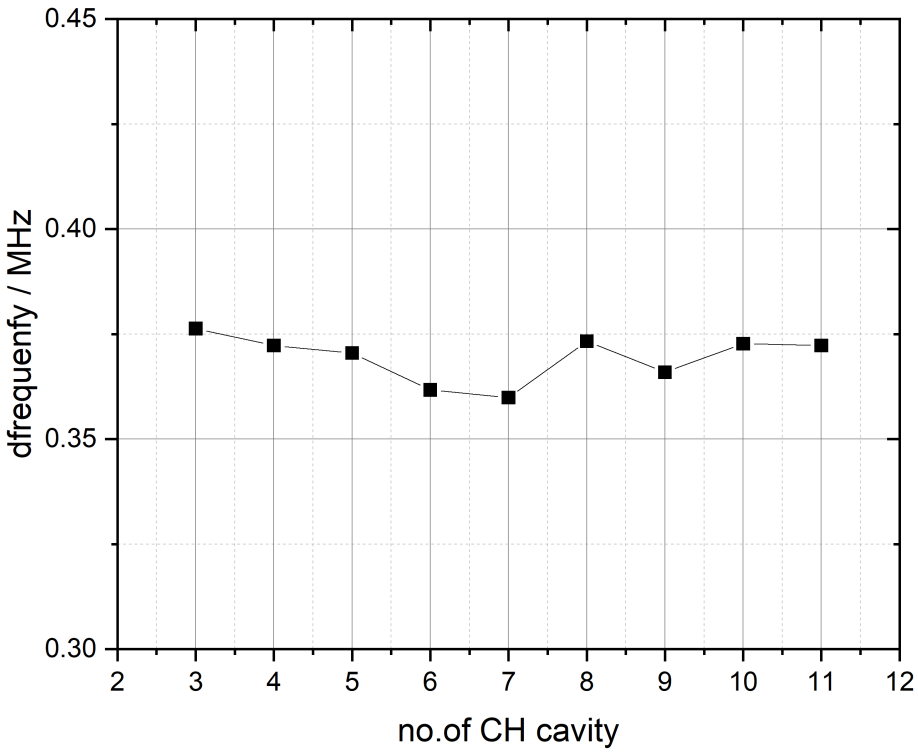

Fig. 85 Simulated frequency change of all nine cavities due to thermal contraction resulting of the cooling to 4.2 K.

It can be seen that the effect of thermal contraction on the resonant frequency is quite similar for all nine cavities. As a result, the average frequency change after cooling is $\Delta f_{\text{thermal contraction, mean}} \approx 369\,\text{kHz}$. Larger deviations, such as for CH3 or CH8, can be attributed to the mesh of the simulation.

8.4.4 Final Frequency

With the effects explained above and thus also with the simulations to be made, it is important to ensure that the simulations of the involvement of the individual effects from section 8.4.1 to section 8.4.3 are made in the same order as they occur in the later construction or during commissioning, since they may have an impact on each other. Thus, the surface treatment of the BCP is the first effect in time, since it is already made during the construction. The surface treatment of the BCP strongly affects the pressure sensitivity of the cavity, since it significantly reduces the wall thicknesses of the cavity, for which reason a larger displacement occurs at the same pressure, and thus the frequency is more affected. Thermal contraction, on the other hand, is almost unaffected by either effect. For this reason, the above simulations were performed gradually progressing from BCP treatment to evacuation and finally to cooling. Including these three frequency-changing steps and effects, the original design frequencies from figure 78 result in the final frequencies shown in figure 86.

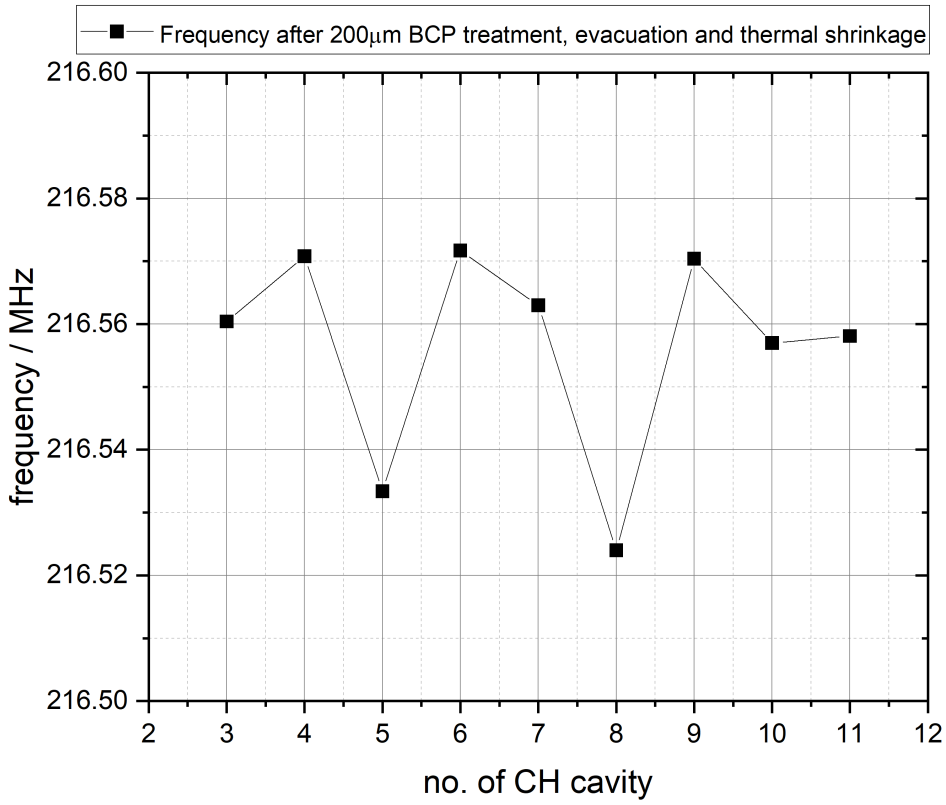

Fig. 86 Simulated resonant frequency of the cavities after uniform 200 μm surface treatment with BCP, evacuation and thermal contraction.

Looking at the resonant frequencies of the cavities, there are two things directly noticeable. First, the resonance frequencies have converged compared to those shown in figure 78, so that the deviations are only a few tens of kHz and thus the initial

strong deviations of several hundred kHz have been compensated. This is shown in figure 87, in which all resonant frequencies of the individual stages are again graphically displayed as a comparison.

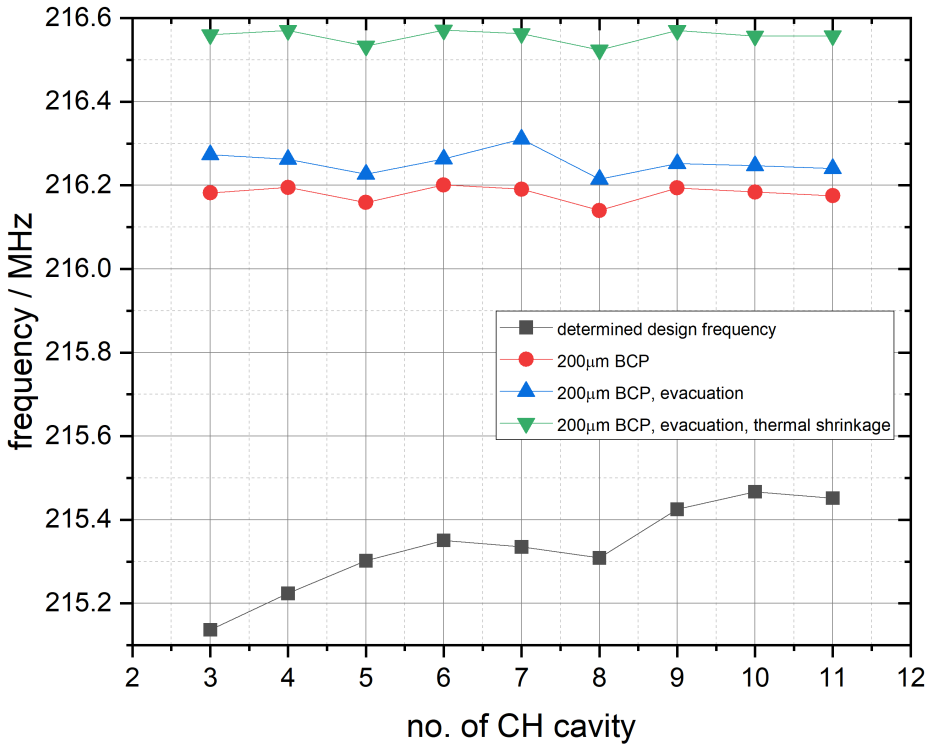

Fig. 87 The resonant frequencies of all nine cavities for each frequency changing step in one plot.

Second, it can be seen that no cavity reaches the target HELIAC frequency of 216.816 MHz even after including the frequency changing effects (see left in figure 88). However, this is because after consultation with the operators and the manufacturer a safety buffer of about 250 kHz is to be left initially (see right in figure 88). On the one hand, this serves to ensure that the target frequency is not directly surpassed should a manufacturing error occur, and on the other hand, should an removal of 200 μm not be sufficient after the surface treatment of the BCP, further treatments could still be performed.

All nine cavities based on the modular cavity design thus achieve the desired target frequency with the intended safety buffer. The small deviations can be compensated either by the dynamic tuner during operation or by the static tuner during construction. The deviations occur due to the optimization of the cavities in terms of perfomance and the reduction of the electrical and magnetic peak fields.

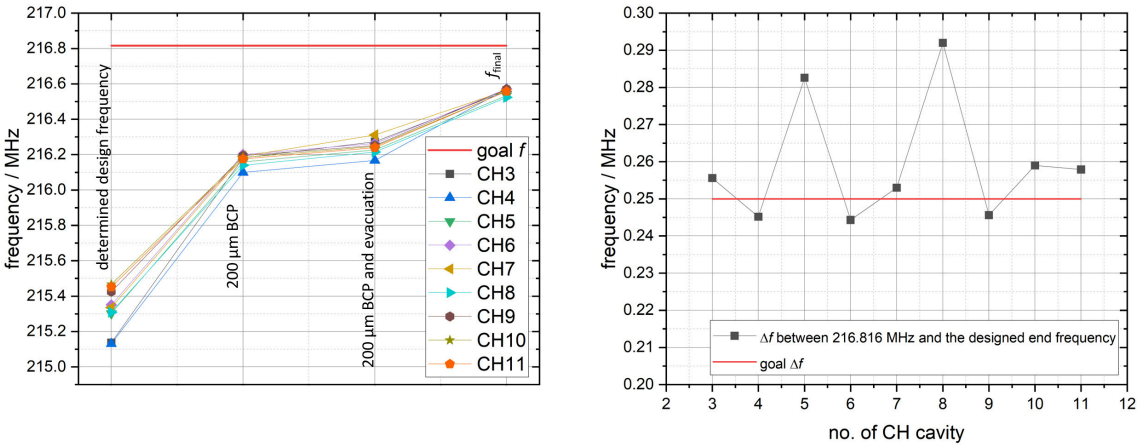

Fig. 88 Left: the convergence of the resonance frequency to the target frequency of the HELIAC with steps plotted. Right: safety frequency buffer Δf to the target frequency of the HELIAC of all nine cavities.

8.5 Adjustment of the Helium Vessel

Since the superconducting CH cavities must be kept constantly at their operating temperature of approximately 4 K throughout operation, they are permanently surrounded by liquid Helium. To ensure a sufficiently large supply of Helium, each individual cavity has its own Helium reservoir in which the cavity itself is tightly welded. The cavity together with the Helium reservoir is then installed in a cryostat and connected to a Helium supply system, which on the one hand feeds the liquid Helium into the reservoir and on the other returns the warmed Helium to the closed circuit of the in-house Helium recycling system. Unlike the cavities themselves, however, the Helium vessel is not made of pure Niobium but of Titanium. On the one hand, this element has a high mechanical stability and, on the other hand, it is cheaper than Niobium. The real advantage, however, is that Titanium has a very similar thermal expansion coefficient to Niobium [53]:

$$\frac{\Delta L}{L} = \frac{L_{293\,\mathrm{K}} - L_{4\,\mathrm{K}}}{L_{293\,\mathrm{K}}} = 0.151\,\%. \tag{154}$$

This allows the Niobium cavity to be welded to the Titanium vessel without stress caused in the material by different contraction during cooling, which could damage the cavity. In figure 89 CH3 with attached Helium shell is shown, once as a whole and once in cross-section.

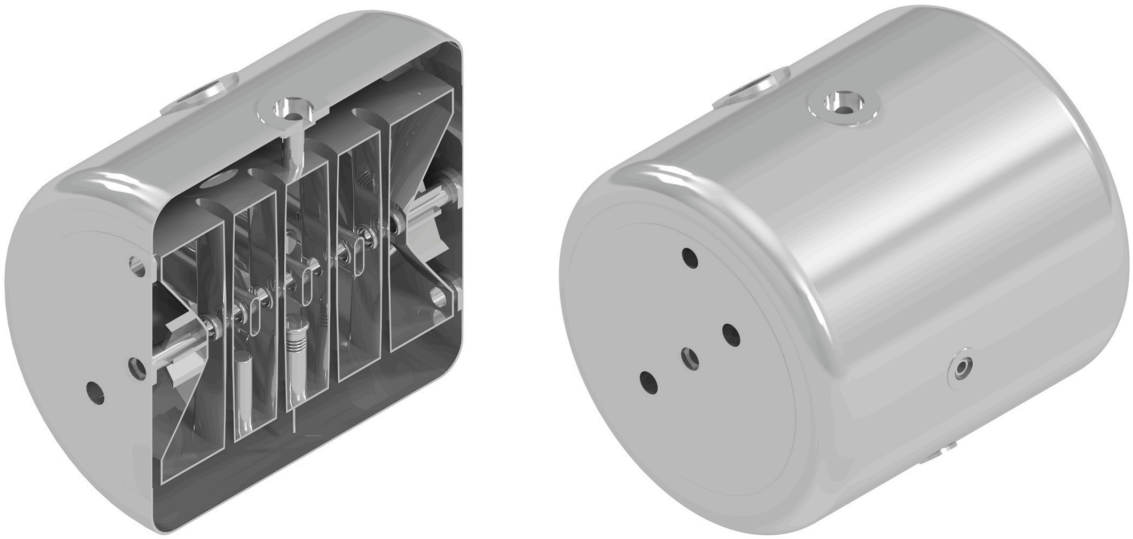

Fig. 89 CH3 with attached Helium vessel left in cross-section and right complete. It can be seen that the flanges have not been placed on the outer wall of the tank, but these have been lowered into the wall.

During the development of the cavity designs, a variety of different approaches were considered to include the Helium tank as part of the modular cavity design. After talking with the future operators and sharing their experiences, a value of 100 l liquid Helium as a reservoir was preliminarily determined to be the ideal. Another boundary condition for the design of the Helium tanks was the already ordered cryostat CM2 (see figure 5) for the cavities CH3, CH4 and CH5. CM2 is identical in construction to CM1, so that the connections of the cryostat are designed to the dimensions of cavities CH1 and CH2, which means a limitation of the radius of the Helium tanks. Different possibilities for meeting the boundary conditions were considered and the amount of liquid Helium of the Helium reservoir of each cavity was calculated. The considered possibilities were to equip all cavities with a Helium tank having the same radius as the Helium tank of CH1 and CH2, one having the same radius as the first version of the Helium tank of CH3, to fix the length of the coupling tube and to adapt the Helium tanks to it, which, however, is not compatible with the current cryostat design for the later cavities, or the maximum possible radius of the Helium tank is calculated according to the connections in CM1 and CM2 (diameter of 640 mm). The quantities of liquid Helium for these options are shown in figure 90.

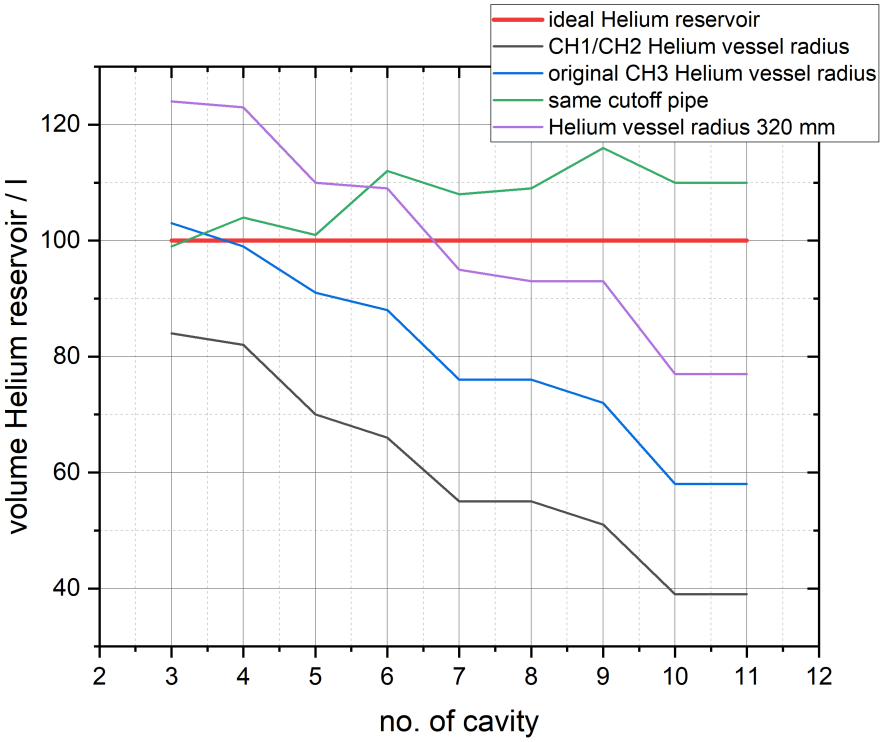

Fig. 90 Volume of the Helium reservoir of the individual Helium vessels of the cavities for different design scenarios in liters.

It is evident that not all boundary conditions can be completely fulfilled at the same time for all cavities. If the ideal amount of Helium was to be maintained for the later cavities, either a new cryostat design would have to be created or the tank would have to be designed outside the modular cavity design. After further consultation with the operators, it was decided to design the Helium tanks to all have the maximum radius of 320 mm for the cryostats (purple line in figure 90) for cost reasons, as an amount of nearly 80 l liquid Helium should also be sufficient for cavities CH10 and CH11. For this purpose, all flanges on the outer wall of the Helium tank are embedded in the outer wall (see figure 90). The decreasing amount of Helium from CH3 to CH11 is due to the fact that even if the outer radius of all tanks is the same, the inner radii of the cavities inside the tanks grow. This is shown in figure 91.

With the selection of this option, the Helium tank can also be considered part of the modular cavity design, as all nine tanks can now be produced in the same way and only the resulting tube needs to be cut to the appropriate length of the cavity.

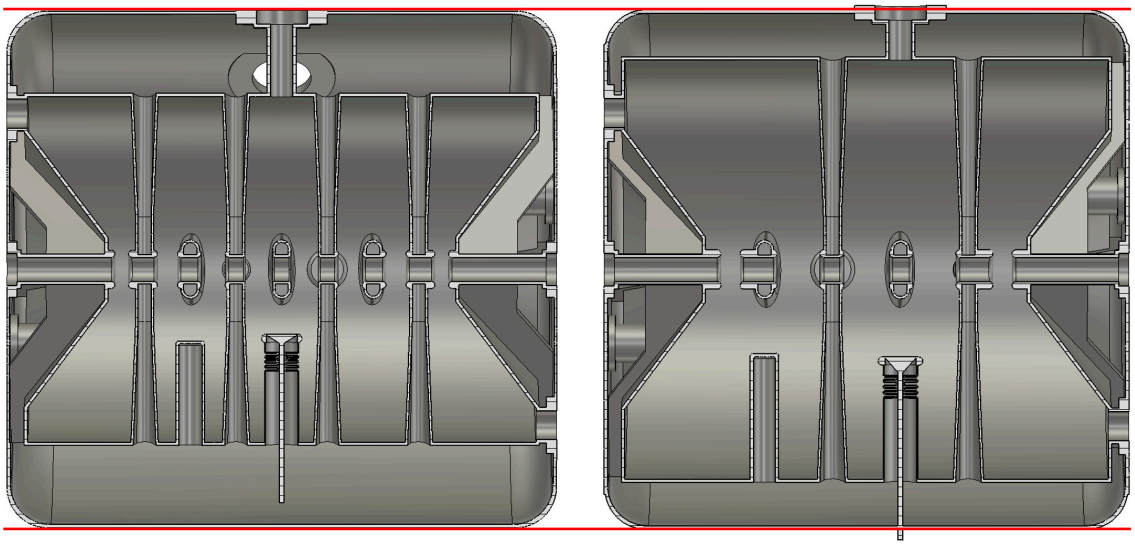

Fig. 91 Cross-section of the cavity with the smallest inner radius CH3 and the one with the largest inner radius CH11 with attached Helium vessels. The red lines mark the outer walls of the Helium vessels.

8.6 Final Design of all nine Cavities

After the frequency to be achieved, including the planned safety buffer, could be reached with all cavities after all frequency-changing effects, the design phase of cavities CH3 to CH11 based on the newly developed modular cavity design has been completed. For this purpose, the basic design of the two previous cavities CH1 and CH2 was first adapted in such a way that modular components were designed from them, which were then adapted to the respective boundary conditions of the individual cavities given by the beam dynamics. In addition, the dynamic bellow tuner, which is also part of the modular cavity design, was adapted to the new and larger cavities in such a way that the electrical peak fields, which previously occurred at the head of the bellow tuner, could be reduced. In addition, the height of the second dynamic bellow tuner was adjusted to cover a more precise tuner range. The cavities CH3 to CH11 were further optimized in terms of reducing the peak electric and magnetic fields compared to CH1 and CH2. This was achieved mainly by a detailed consideration of the drift tube distances and thickness. The simulations of the pressure sensitivity and the achievement of the desired resonant frequency confirmed the suitability of the cavities and thus the modular cavity design. In conclusion to this chapter, the most basic parameters of all nine cavities are shown in Tab. 6.

Tab. 6 Basic parameters of all nine superconducting cavities CH3 to CH11 of the HELIAC.

	CH3	CH4	CH5	CH6	CH7	CH8	CH9	CH10	CH11
β	0.076	0.083	0.09	0.096	0.102	0.107	0.112	0.116	0.120
f / MHz	216.8	216.8	216.8	216.8	216.8	216.8	216.8	216.8	216.8
no. gap	8	8	7	7	6	6	6	5	5
L / mm	681.2	704.4	674.4	719.7	669.2	673.0	710.0	645.6	647.1
r_{in} / mm	214.1	218.7	225.9	235.6	242.5	243.6	249.3	258.1	258.1
r_{tot} / mm	325	325	325	325	325	325	325	325	325
n. stat. tuner	2	2	2	2	2	2	2	2	2
no. dyn. tuner	2	2	2	2	2	2	2	2	2
$E_{\text{a}}^{\text{des.}}$ / MV/m	5.5	5.5	5.5	5.5	5.5	5.5	5.5	5.5	5.5
$U_{\text{a}}^{\text{des.}}$ / MV/m	2.1	2.1	2.1	2.1	2.1	2.1	2.1	2.1	2.1
$Q_0^{\text{des.}}$	$3 \cdot 10^8$	$3 \cdot 10^8$	$3 \cdot 10^8$	$3 \cdot 10^8$	$3 \cdot 10^8$	$3 \cdot 10^8$	$3 \cdot 10^8$	$3 \cdot 10^8$	$3 \cdot 10^8$
$E_{\text{peak}}/E_{\text{a}}$	5.83	5.57	5.49	5.49	5.34	5.45	5.48	5.44	5.7
$B_{\text{peak}}/E_{\text{a}}$ / mT/(MV/m)	8.29	7.98	7.79	8.02	8.09	8.14	8.5	8.49	8.49

8.7 Comparison Cost Efficiency and Optimal Performance

After the cavities CH3 to CH11 have been designed using the modular cavity design and optimized with respect to their RF properties by the method described in section 8.3, a comparison to cavities designed using the conventional individual design process is logical. This comparison will be made in the following section. For this purpose, cavity CH11 was optimized several times using the CST Studio Suites Optimizer [40]. In addition to the optimization parameters described in section 8.3, the spoke geometry was also optimized in this optimization process. Both the optimization parameters used in section 8.3 (blue) and those now added (red) are shown

in figure 92.

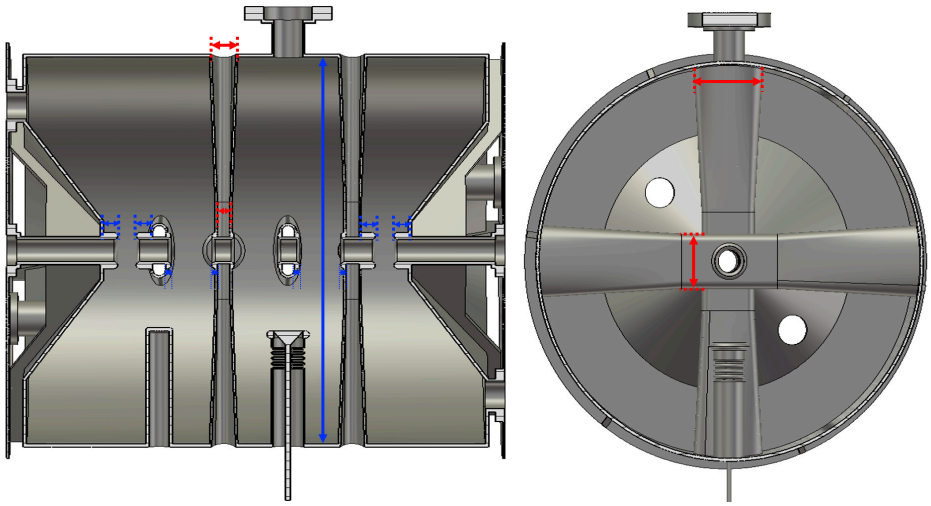

Fig. 92 Cross-sections of cavity CH11 with optimization parameters marked. In blue the parameters already used in section 8.3 and in red the parameters now added.

Again, the Nelder-Mead method (see section 8.7.1) was used as the optimization algorithm and the same optimization objectives as in section 8.3 were set. In total, the optimizer integrated in CST Studio Suite was applied three times to cavity CH11. Figure 93 shows the optimization process for the resonant frequency and figure 94 shows the optimization process for the ratios $E_{\mathrm{peak}}/E_{\mathrm{a}}$ (red) and $B_{\mathrm{peak}}/E_{\mathrm{a}}$ (blue).

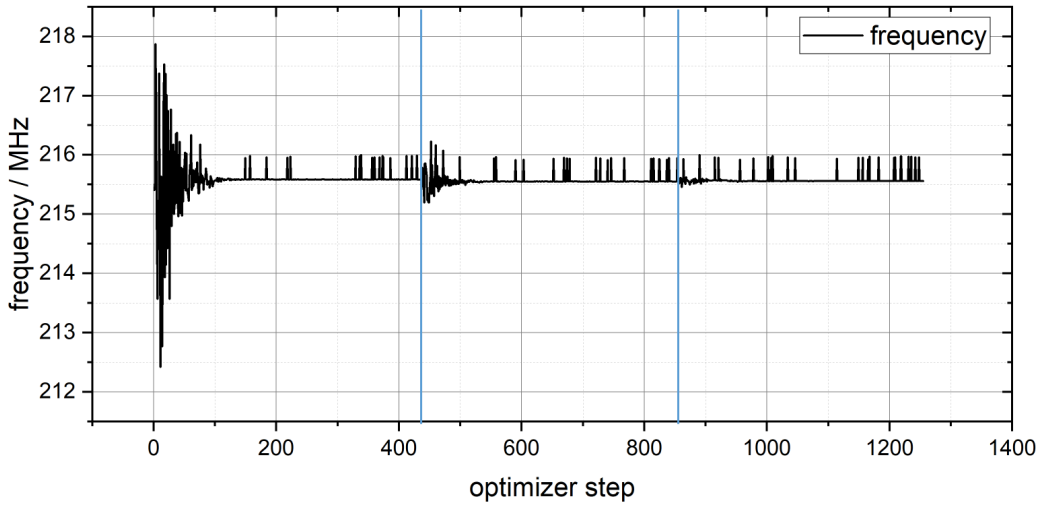

Fig. 93 Course of the resonance frequency of CH11 during the optimization process. The blue lines indicate the starting points of the respective optimizations.

The blue lines drawn in the graphs show the new start of each optimization process. Each optimization process consisted of about 400 steps. The noticeable peaks in the graphs of figure 93 and figure 94 arise from inaccuracies in the mesh generation during the simulation. It can be seen that with each start of a new optimization process the variations become larger, this is related to the downhill simplex method of the Nelder-Mead method.

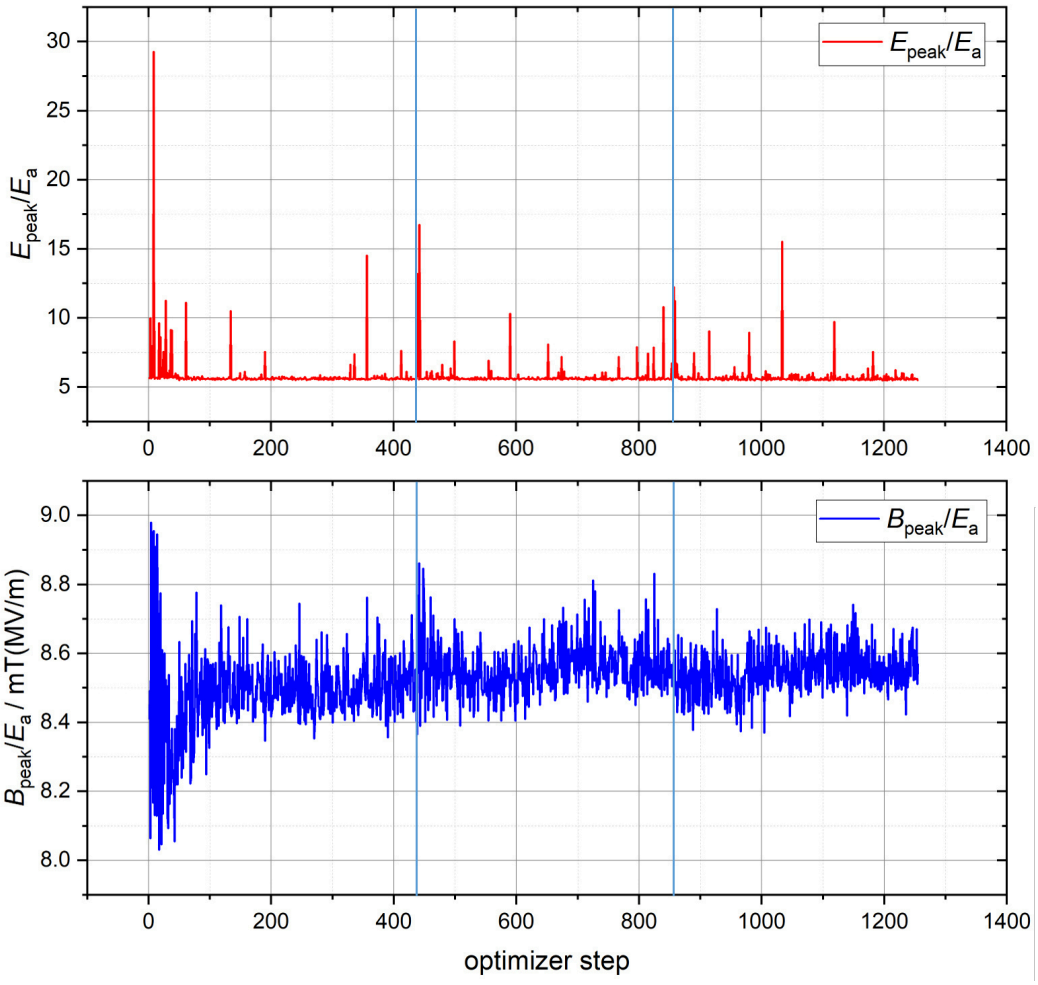

Fig. 94 Course of the ratios $E_{\mathrm{peak}}/E_{\mathrm{a}}$ (red) and $B_{\mathrm{peak}}/E_{\mathrm{a}}$ (blue) of CH11 during the optimization process. The blue lines indicate the starting points of the respective optimizations.

The CH11 cavity optimized in the classical way achieves the values shown in Tab. 7.

Tab. 7 Comparison of the ratios $E_{\mathrm{peak}}/E_{\mathrm{a}}$ and $B_{\mathrm{peak}}/E_{\mathrm{a}}$ for the classically designed CH11 cavity and the CH11 cavity based on the modular cavity design.

	classically designed CH11	modular cavity design CH11
$E_{\mathrm{peak}}/E_{\mathrm{a}}$	5.49	5.7
$B_{\mathrm{peak}}/E_{\mathrm{a}}$/ mT/(MV/m)	8.43	8.49

It can be seen that for the CH11 cavity designed in the classical way, both the peak electric and magnetic fields were further reduced compared to the CH11 based on the modular cavity design. Thereby, $E_{\mathrm{peak}}/E_{\mathrm{a}}$ decreased by 3.7 % and $B_{\mathrm{peak}}/E_{\mathrm{a}}$ decreased by 0.7 %. These small improvements do not offset the huge price advantage of the modular cavity design, so in the case of HELIAC it is still advisable to trade off the small improvements in performance for better and cheaper manufacturing.

8.7.1 Short excursus on the Nelder-Mead Method

The Nelder-Mead method is a method for optimizing non-linear functions with multiple parameters, which was first introduced in 1965 by John Nelder[74] and Roger Mead[75]. Thereby, this method belongs to the downhill search methods. The special characteristic of this optimization method is that it does not require derivation of the function under consideration according to the parameters. Instead, a simplex is used (see figure 95), at whose points the function values are calculated and then meaningfully compared to approximate the tendency of the values and the direction of the gradient.

When comparing the function values at the points of the simplex, the point whose function values contradict the set targets the most is replaced by another one at the next iteration step. The point whose function values are closest to the set targets is always retained. The selection of the new point for the next iteration can be done by mirroring the replaced point or by stretching or compressing the simplex. The method ends, if no further better points can be found. This optimization method is time consuming compared to other optimization methods, but it is also very robust. However, the same problems apply as with similar methods, so for example occurring secondary minima can be found incorrectly as optimum.

[74] ⋆8 October 1924 in Brushford, England; †7 August 2010 in Luton, England
[75] ⋆1938; †10 August 2015

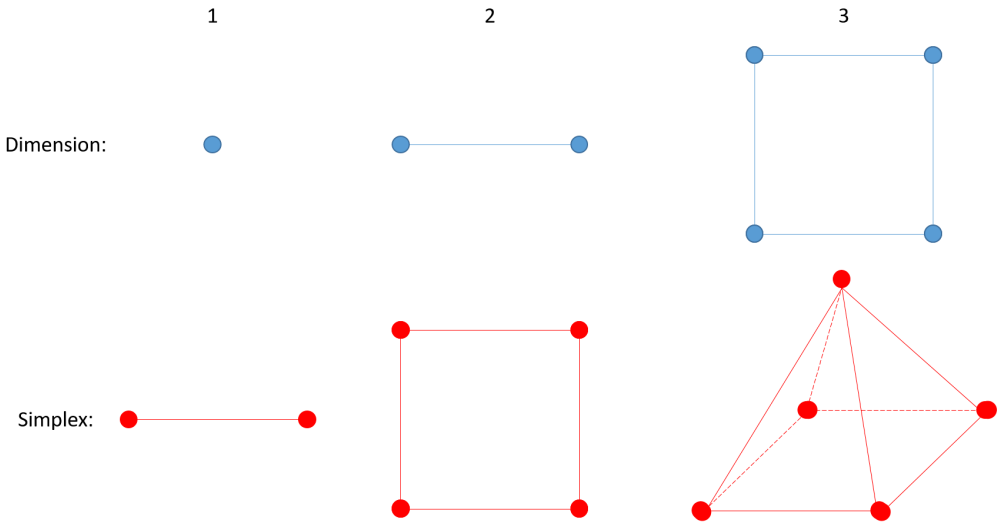

Fig. 95 Graphical illustration of the principle of the mathematical simplex. The simplex always has $n + 1$ corners in n-dimensional space.

9 Elaboration of a Tuner Test Bench

The tuner hub of the dynamic bellow tuner was also investigated during the production and testing of cavity CH1. The tuner rod of the dynamic bellow tuner was loaded with weights to such an extent that the bellow inside the tuner expanded and thus the desired extension was achieved [1]. During a measurement, the weight loading of the tuner was unintentionally increased once to such an extent that the bellow tuner then showed a slight, permanent deformation. For this reason, it was decided to develop a new method within the scope of this thesis that would allow the mechanical properties of dynamic bellow tuner to be investigated in greater detail. In later operation, unlike dynamic tuner in normal conducting cavities, a simple replacement of the damaged or the deformed tuner would not be possible, since as can be seen in section 8, the dynamic bellow tuner in the superconducting CH cavities designed here are firmly welded to the cavity. Damage to the bellow tuner thus also results in damage to the cavity, leading to long accelerator downtime and costly repairs.
The tuner test bench will be used to investigate the dynamic bellow tuner used in cavities CH3 to CH11. The properties to be investigated are the maximum load limit, above which the internal deformation stress $\sigma_{\mathrm{v,\ von\ Mises}}$ within the material becomes so large that the material fails (see section 5.4.1), and the maximum lifetime, which is the number of times the dynamic bellow tuner can be deflected to its maximum before material fatigue causes such deformation that the tuner no longer allows an appropriate, controlled frequency change. Accurate knowledge of these two properties of the tuner could prevent damage in later operation and thus extend the lifetime of the individual cavities.
The realization of this tuner test bench has several difficulties in this regard. First of all, the mechanical deformation that could occur due to material fatigue might initially be so small that it would not be noticeable by just measuring the length of the tuner or by just observing the component visually. However, for later preventive actions it could be interesting to determine at which point a deformation could be expected. For this reason, the approach taken in this thesis is to measure the deformation of the bellow tuner by a change in the resonant frequency within a pillbox cavity. For this purpose, an unused pillbox cavity already available at the IAP Frankfurt of the Goethe University Frankfurt is planned to be converted into the tuner test bench. This pillbox cavity has to be extended by some components in order to serve as a later tuner test bench (see section 9.1).
The second challenge is the material used for the dynamic bellow tuner itself. Like the entire cavity, the tuner is composed of pure Niobium. However, Niobium has significantly different mechanical properties at different temperatures, such as a different yield point or different strength. Since in later operation the bellow tuner is cooled down to about 4 K, it would be advisable to also operate the tuner test bench at low temperatures. However, since cooling to 4 K requires the use of liquid Helium as a coolant, and working with liquid Helium would involve an enormous amount

of work both in operating the test bench and in modifying the pillbox cavity, since additional isolation from ambient temperature and a complete cooling loop system would have to be installed, the initial realization of the tuner test bench will be designed to use liquid Nitrogen as a coolant, thus allowing the Niobium to cool to 77 K.
The following section will present the necessary steps to realize the tuner test bench as well as some simulation results to investigate the suitability and feasibility of the test bench.

9.1 Available Pillbox Cavity at IAP

The pillbox cavity at the IAP Frankfurt is currently located on the roof of the cryobunker and is not used for any experiment (see figure 96). The resonant frequency of this pillbox is 326.825 MHz without any internal installations like tuner, stems or spokes. For the operation of the pillbox as a tuner test bench some modifications have to be done. For example, in addition to installing input and output couplers for coupling the RF power, an operating vacuum inside the pillbox of a few 10^{-5}–10^{-7} mbar must be established and maintained to prevent condensation from forming on the surface of the cooled tuner. For this purpose, a fore-vacuum pump, a turbomolecular pump and two pressure gauges are required.

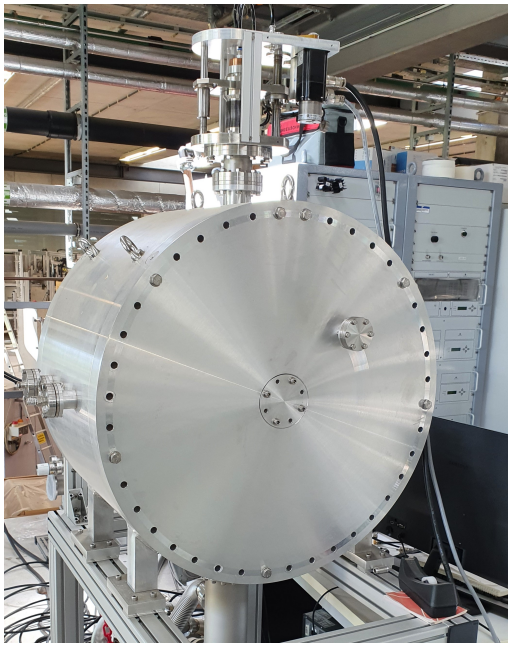

Fig. 96 Photograph of the pillbox cavity already present at the IAP on the roof of the cryobunker.

Additionally, maintaining the vacuum also acts as a detector for any minimal fracture within the tuner. For the detection of the maximum load limit, the bellow tuner shall be loaded with a force $\vec{F}_{\text{load}}$ until this force is so high that the material of the tuner breaks (see section 5.4.1). A very small fracture within the material causes an immediate increase in pressure due to evaporating Nitrogen, so that this can be detected immediately and the maximum load capacity of the bellow tuner can be determined. The determination of the maximum load capacity of the bellow tuner should first be carried out with a previously unused tuner and later repeated with a tuner that has already been used, in order to be able to determine any differences

that may occur due to possible material fatigue through use.

The most complex modification is the extension of the pillbox by the possibility of cooling the inserted tuner to be investigated with liquid Nitrogen to 77 K. On the one hand, safe working during the measurements should be ensured and, at the same time, a system as simple and modular as possible should be implemented, which should later be suitable for other types of tuners or other tests. For this reason, a Nitrogen cup including a filling lance was designed. The cup is attached to the top flange of the pillbox and the tuner to be tested is inserted through it (see figure 97), the filling lance is then inserted into the tuner (see figure 98).

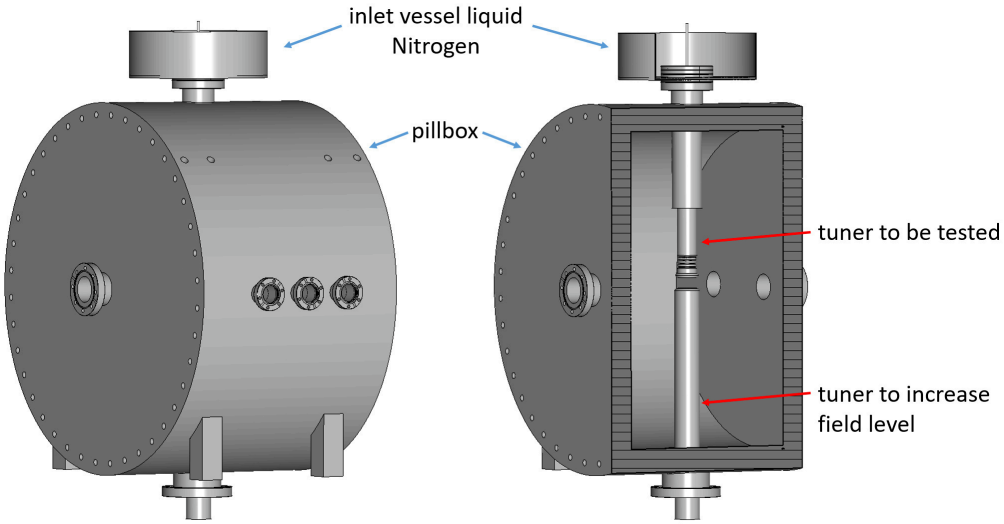

Fig. 97 Left: 3D model of the pillbox cavity already available at IAP with liquid Nitrogen inflow cup on top. Right: Cross-section through the pillbox. The dynamic bellow tuner adapted for the test and the additional opposite tuner for increasing the field level can be seen.

Both components are made of Aluminium. The liquid Nitrogen can be filled directly into the tuner for cooling with the help of the lance, so that the level of liquid Nitrogen rises from below. The cup surrounding the flange of the tuner prevents uncontrolled splashing of the liquid Nitrogen onto the environment and provides sufficient space to build up a possibly required reservoir of liquid Nitrogen. Furthermore, this system allows the tuner to be additionally filled with liquid Nitrogen during operation. Since the Nitrogen evaporating in the process is not returned to a closed circuit, the measurements on the tuner test bench must take place in the cryobunker of the IAP Frankfurt, since a residual Oxygen control device is installed there, thus avoiding a possible hazard to the experimenter due to insufficient ambient Oxygen.

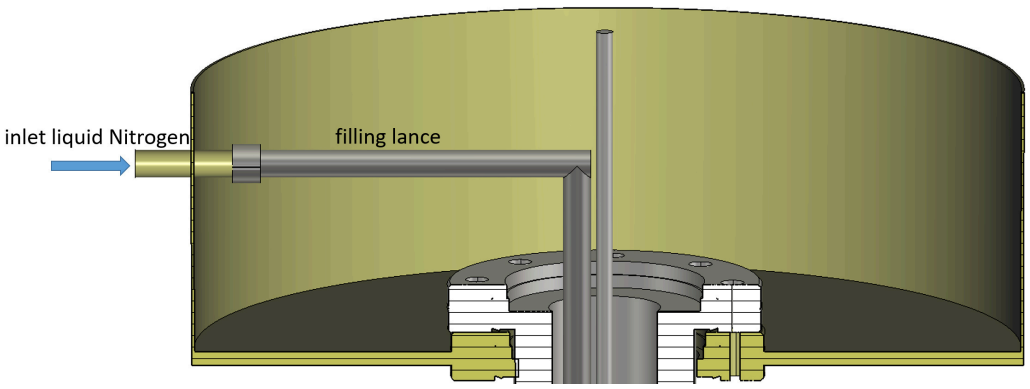

Fig. 98 Illustration of the Nitrogen filling cup and the filling lance inserted into the tuner.

When the dynamic bellow tuner under investigation is inserted into the pillbox cavity, the resonant frequency changes to 210.773 MHz. The previously excited TM_{010}-mode, also called pillbox mode, has been replaced by a mode in which the electric field lines lead toward the head of the tuner (see figure 99). In addition, the maximum achievable field strength within the pillbox cavity increases. This increase of the maximum field strength around the tuner head is of great importance for the later measurement of the displacement. The tuner, which is now installed in the pillbox, is now expanded under realistic conditions. This means that the same step motor is attached to the tuner rod extending out of the cup and the tuner is expanded several times over the maximum tuner displacement. According to the slater theorem, the spatial expansion of the tuner also changes the resonant frequency (see section 3.1.2). The frequency is constantly measured by a network analyser and the frequency at zero crossing is analysed. If the measured frequency at zero crossing deviates constantly from the initial value, the tuner has deformed. This deviation of the frequency at the zero state can be matched with previously made simulations and thus a statement about the deformation of the tuner can be made. If, in addition or instead, the frequency change changes, the material could have become softer or harder due to the stress and thus either expanded more or less at the same load. This can also be compared with previously made simulations.

The greater the field strength at the tuner head, the greater the effect of a deformation on the change in frequency at zero crossing. To additionally increase the field strength at the tuner head, a dynamic tuner is moved into the cavity on the opposite side of the dynamic bellow tuner (see figure 100).

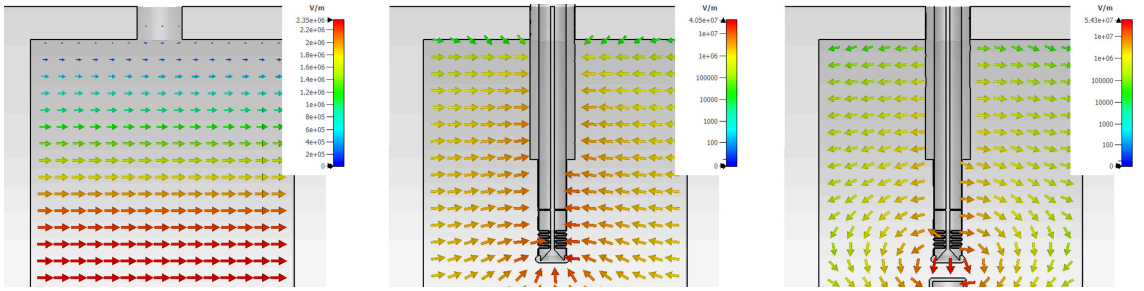

Fig. 99 Simulation of the electric field inside the pillbox cavity. Left: The empty pillbox cavity. Center: The pillbox cavity with dynamic bellow tuner. Right: The pillbox cavity with dynamic bellow tuner and static tuner.

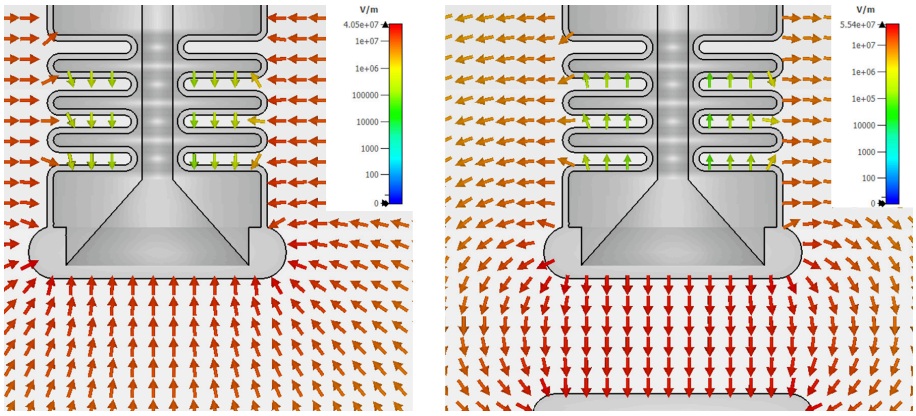

Fig. 100 Simulation of the electric field near the head of the dynamic bellows tuner. Left: Without additional static tuner. Right: With additional static tuner.

Between the two tuner heads the field level increases again and the resonant frequency of the pillbox drops further to 155.060 MHz. This increase in field level between the two tuner heads increases the resolution of the frequency change (see figure 101).

However, the degree of resolution gain is manageable. Since the production of an additional dynamic normal-conducting tuner is associated with additional costs, the tuner test bench should initially be set up without an additional dynamic tuner. The differences in the resolution of the frequency change Δf when the length of the dynamic bellow tuner Δh is changed by a deformation of the tuner are shown in Tab. 8.

It can be seen that a resolution of 1 μm can be achieved even without an additional dynamic tuner and the expected frequency change Δf with a value of $\Delta f \approx 1$ kHz is still within the well measurable range of the network analyser, so that for the first time an additional static tuner can be avoided. Should an even more precise resolution of the tuner deformation be desired for later measurements, this additional static tuner can be upgraded at any time.

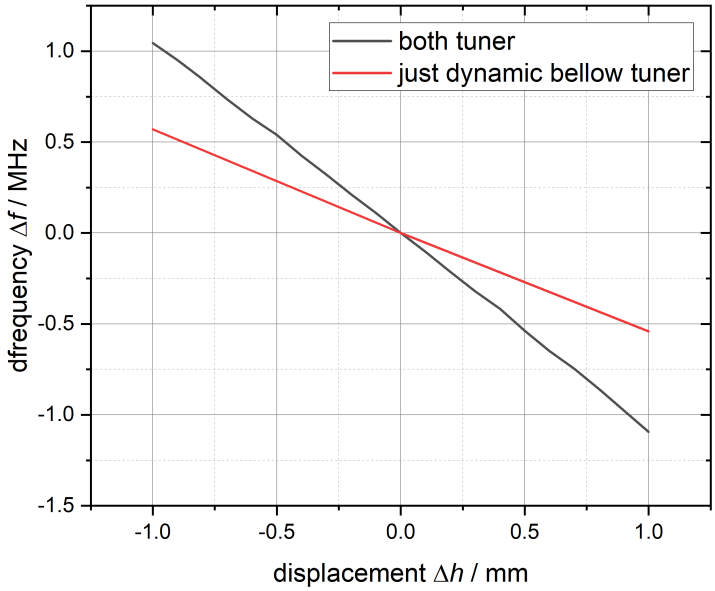

Fig. 101 Frequency change due to deflection of the dynamic bellow tuner within the cavity by ±1 mm.

Tab. 8 Frequency change over the entire tuning range from maximum displacement to minimum displacement.

Δh	one tuner Δf	both tuner Δf
± 1 mm	1.11 MHz	2.14 MHz
± 0.1 mm	120 kHz	212 kHz
± 0.01 mm	12 kHz	21 kHz
± 0.001 mm	1 kHz	2 kHz

9.2 Adapting the Bellow Tuner to the Pillbox Cavity

When designing the pillbox cavity upgrades to the tuner test bench, it was noticed that the tuner to be investigated had to be adapted compared to the tuner actually used. Since the pillbox has a radius of $r_{\text{pillbox}} = 351$ mm and the greatest possible field strength is achieved in the center of the cavity and a greater field strength means a greater influence on the frequency change Δf, the tuner to be investigated with the tuner test bench must be significantly enlarged. For instance, the dynamic bellow tuner actually used in cavities CH3 to CH11 is significantly shorter with

an average length $L_{\text{mean, bellow tuner}} \approx 154.13\,\text{mm}$ than the tuner used here with a length of $L_{\text{tt}} = 455.5\,\text{mm}$. The outer wall thickness of the tuner is thereby only $w_{\text{tuner}} = 1\,\text{mm}$. However, since forces of up to 600 N act on the tuner during mechanical testing and additional degrees of freedom in the x and z directions could distort the measurements, the extended tuner tube is reinforced by an additional wall thickness so that the wall thickness there is 12.4 mm.

In order to reduce the production costs of this adapted tuner, it is not made exclusively of pure Niobium, unlike the tuner used later, but of Niobium and Titanium, since these two elements have a similar coefficient of thermal expansion. Titanium is a more stable and at the same time more economical material than pure Niobium. For example, the flange, the tuner threaded rod and the extended tube can be made of Titanium to save material costs, while the tuner head and the bellow continue to be made of pure Niobium (see figure 102). The geometrical dimensions of the bellow and the tuner head are identical to the dynamic bellow tuner used in CH3 to CH11 in order to be able to transfer the conclusions from the measurements of the mechanical properties to the tuners used later. The tuner head, which is made of Niobium, can be welded to the Titanium tube and the tuner threaded rod can be screwed into a thread milled into the tuner head for this purpose.

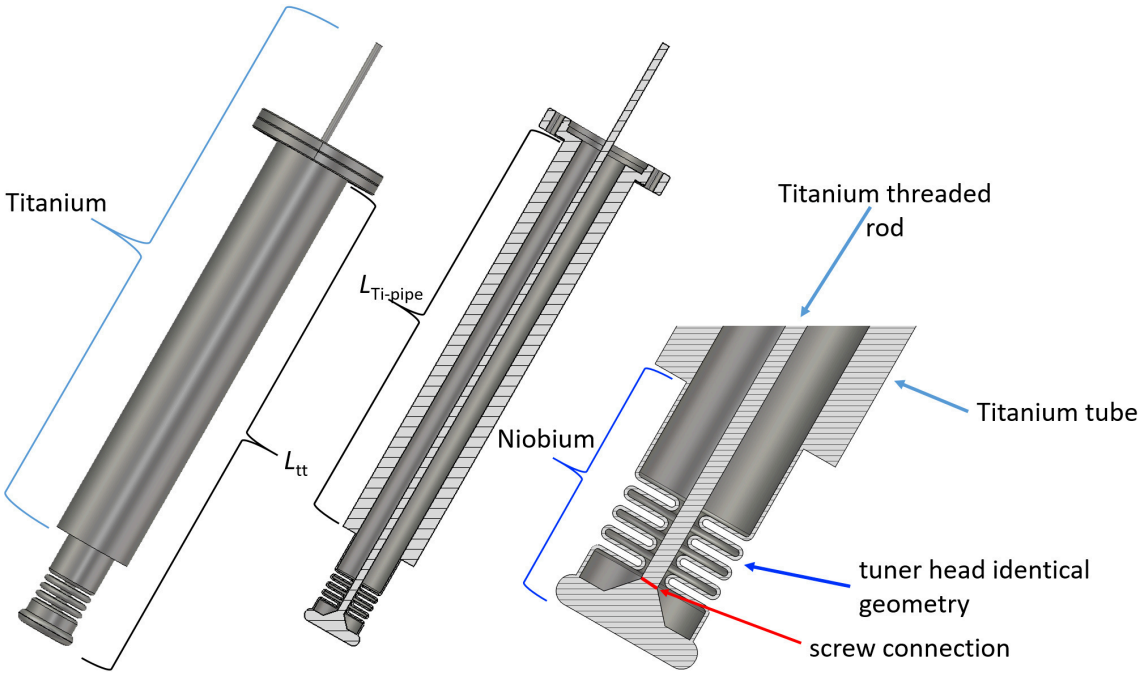

Fig. 102 Schematic of the dynamic bellow test tuner adapted for the tuner test bench complete, as a cross-section and as a close-up of the head in cross-section.

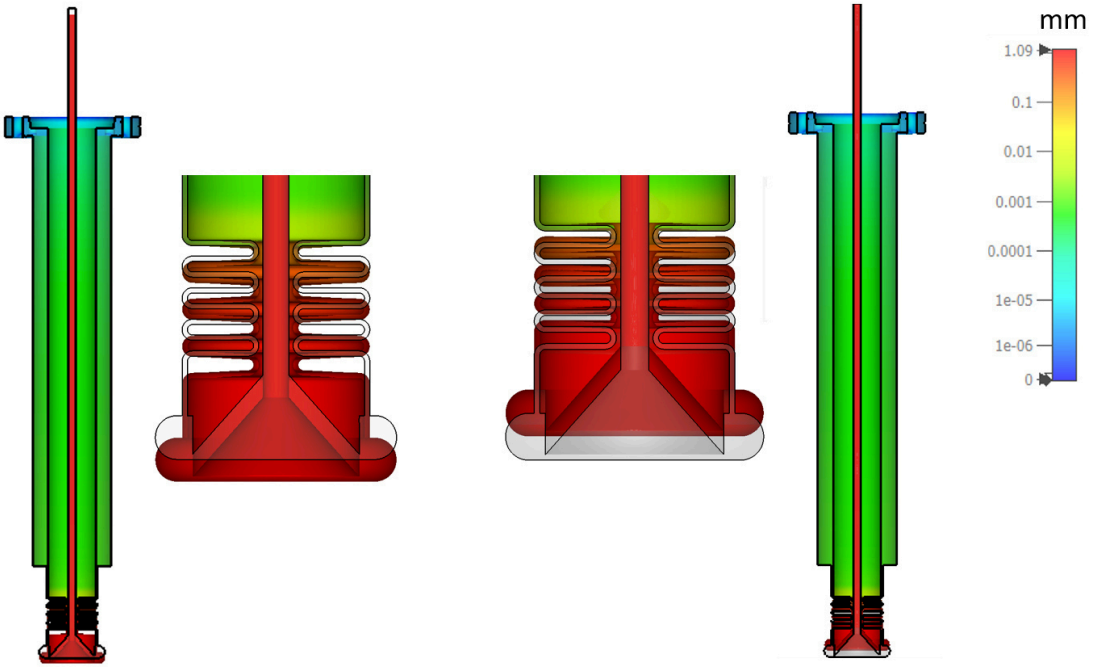

Fig. 103 Simulation of mechanical displacement of the test tuner. On the left, under the load of the tuner rod with 296.9 N and on the right under tension with a force of 296.9 N. For better illustration, the deflection was shifted by a factor of 5 in the representation. The outlines show the tuner in normal condition.

Since due to the additionally attached Titanium pipe and the significantly longer length L_{tt} of the test tuner large changes compared to the actually used design of the bellow tuner were applied, simulations were made to verify that the later measurements with this test tuner are still sufficiently representative for the later real bellow tuner. During the simulations, it was investigated whether the length of the additionally used Titanium pipe has an effect on the deflection or the internal deformation stress $\sigma_{\mathrm{v,\ von\ Mises}}$ under load of the tuner. For this purpose, a load of 282.74 N was applied at the end of the tuner threaded rod, while the flange was defined as fixed end. In the simulations of the bellow tuner used later this force of 282.74 N applied causes a deflection of approximately ± 1 mm in the y direction with an internal deformation stress of $\sigma_{\mathrm{v,\ von\ Mises}} \approx 0.24$ GPa (see figure 67). The simulation results in figure 103 show that the length of the Titanium pipe does not affect the mechanical properties of the bellow tuner, since the deformation of the tuner mainly takes place in the bellow designed for it. In addition, the simulation results in figure 104 show that the length of the Titanium pipe has only a very small effect on the displacement or the internal stress. The fluctuations in figure 104 can be attributed to different numbers of tetrahedral mesh cells in the simulations with CST Studio Suite [40].

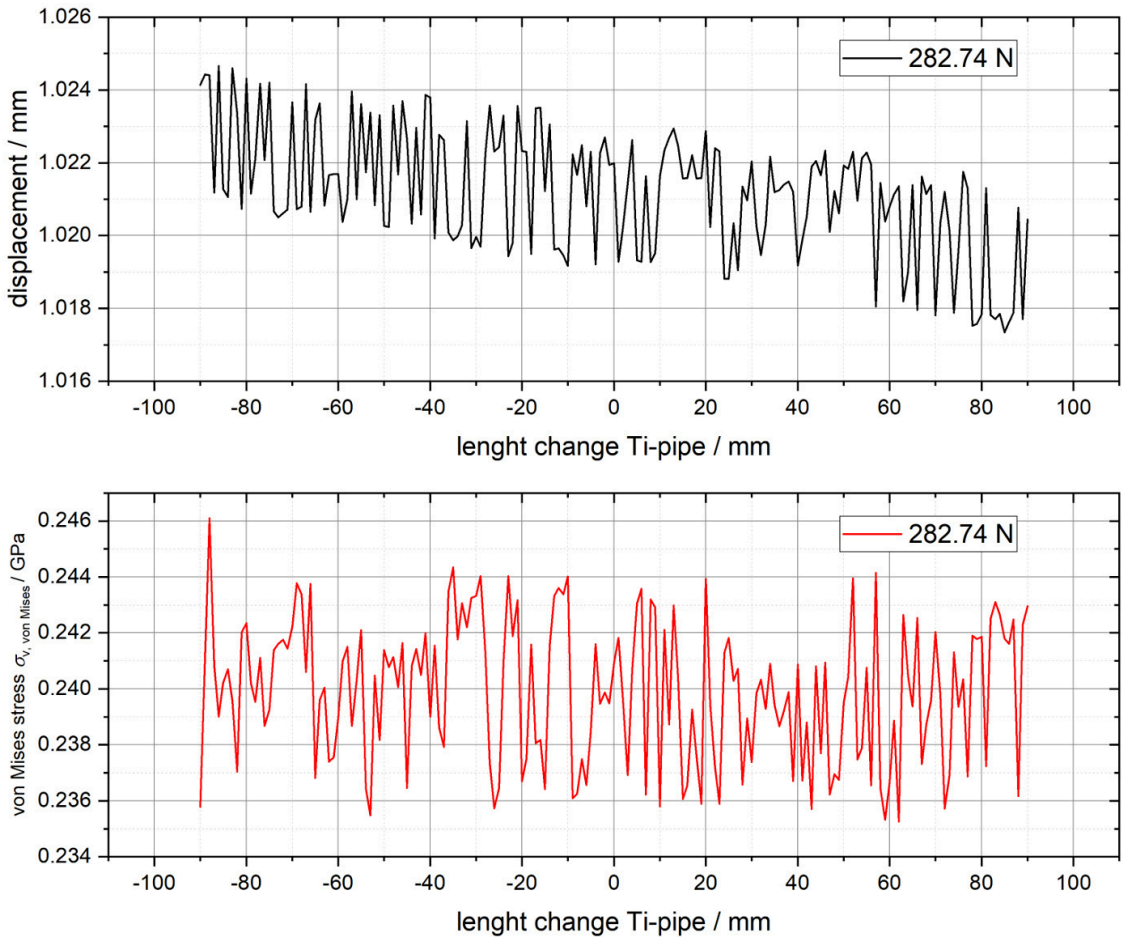

Fig. 104 Up: Simulation results to verify whether the length of the Titanium pipe influences the displacement of the dynamic bellow tuner at a constant force of 282.74 N. Bottom: Simulation results to verify if the length of the Titanium pipe has an influence on the von Mises stress $\sigma_{v,\ von\ Mises}$ generated within the dynamic bellow tuner at a constant force of 282.74 N.

It can be seen that the length of the additionally attached Titanium tuner pipe has only a very small influence on the displacement and the internal stress of the material. Since it could be confirmed by this simulation that the adapted tuner has sufficient informative value for the later real tuner, the maximum possible stress of the tuner, before the internal von Mises stress $\sigma_{v,\ von\ Mises}$ reaches the yield limit of cold Niobium of $\sigma_{v,\ yield\ limit} \approx 0.49\,GPa$, was additionally determined by simulations. For this, a variable force was applied to the end of the tuner rod and the flange was chosen as fixed point. The results of this simulation are shown in figure 105.

According to the calculations shown in figure 105, the dynamic bellow tuner of the modular cavity design should break at a maximum load of about 575 N. This maximum load value is sufficiently far from the 282.74 N to be used for the deflection of ± 1 mm so that safe operation is possible without the risk of accidentally breaking

the tuner directly. This simulated value has to be confirmed by an experimental investigation with the help of the tuner test bench.

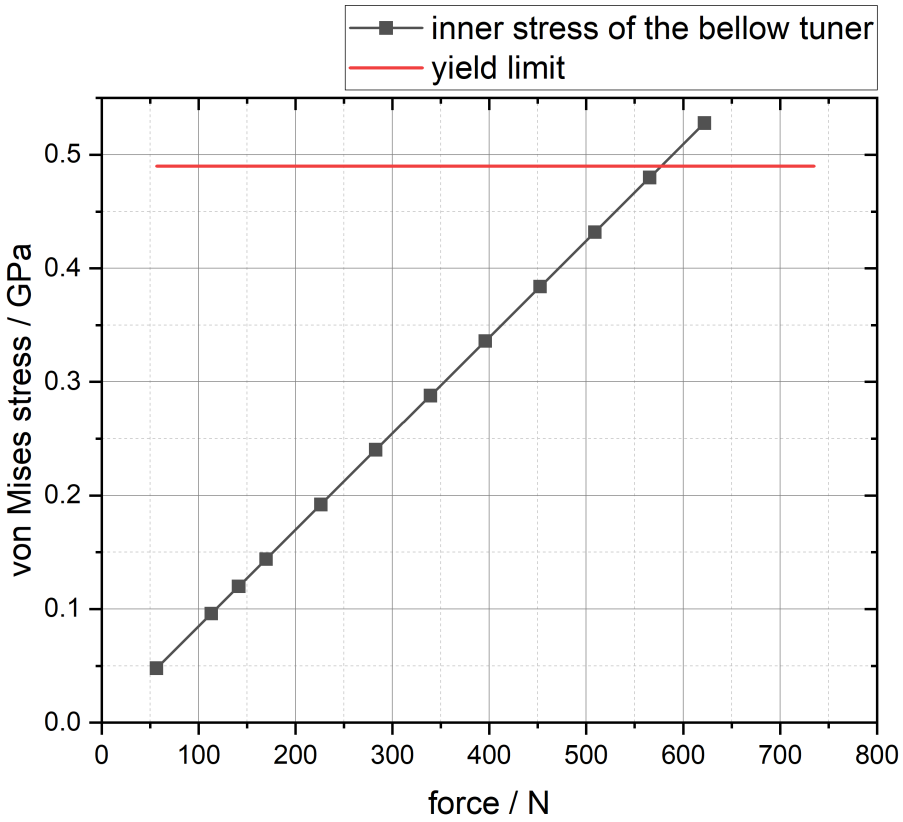

Fig. 105 Simulation results for determining the maximum possible displacement force of the dynamic bellow tuner. The critical yield limit of Niobium in the cold state is shown in red.

The methodology of the tuner test bench presented here is thus extremely suitable for experimentally determining the mechanical limit in terms of lifetime and the maximum load limit of the dynamic bellow tuner. The cooling system is suitable to safely cool the adapted test tuner, which is inserted into the pillbox, to 77 K with liquid Nitrogen during the measurements. By coupling an RF wave into the pillbox cavity, the possible deformation of the tuner due to material fatigue can be determined to an accuracy of approximately 0.001 mm by measuring the resonant frequency using a network analyser, and the adaptation of the tuner design to the conditions of the pillbox cavity not only have nearly no influence on the measurements, but also reduce the manufacturing costs of the tuner by using the less expensive material Titanium for parts of the tuner.

10 Summary and Outlook

10.1 Outlook

After the CH2 cavity behaved abnormally during the cold test at the IAP and both the acceleration gradient E_a and the required quality Q_0 required by the HELIAC project could only be achieved in the first measurement, the cold test was aborted for time and infrastructural reasons and the cavity was sent back to RI. There it was rinsed again and the Helium vessel was welded on. The cavity was then shipped to GSI Darmstadt, where it will be installed in the demonstrator cryostat together with cavities CH0 and CH1, along with a superconducting buncher and a superconducting solenoid, where it will be tested with beam after a new conditioning. The successful beam test of the complete cryomodule CM1 would represent a further milestone in the realization of HELIAC at GSI.

Since it could be shown that the modular cavity design developed in this thesis is suitable for the mass production of the nine subsequent superconducting CH cavities of the HELIAC project, the tender for the production of the first cavities was started and first offers were obtained. At present, it is planned to complete the production of the cavities cryomodule wise, starting with the three cavities CH3, CH4 and CH5 of CM2 and the three cavities CH6, CH7 and CH8 of CM3, so that by the end of the year in which this thesis is being written, a total of six cavities could enter the construction process. The current tender foresees that the production of these cavities will be completed one month apart from each other. The total production time of a single cavity is set at three years after the required Niobium is delivered. Once the contract has been assigned to a potential manufacturer, construction of the cavities' blueprints can begin. The cavities resulting from the blueprints will then be re-examined for their RF characteristics using CST Studio Suite. If the cavities resulting from the blueprints achieve the desired performance as well as the required resonant frequency, the required Niobium is ordered and construction is started upon its arrival. During the fabrication of each cavity, various intermediate measurements are to be taken to verify that the desired target frequency can also be achieved after fabrication. Once the cavity construction is complete, a cold test of the cavities is required to examine them for their RF characteristics in cold state. After the cavities have been successfully tested in cold state and the Helium vessels have been attached, the cavities can be installed in the cryomodules and tested with beam.
In addition, it is planned to integrate the modular cavity design for superconducting CH cavities into an autonomously working software for the development of normal conducting CH cavities, which is currently under development at the IAP Frankfurt. Thus, it would only be necessary to manually design the modular components such as spokes, tuner, lids, and flanges, while the adaptation of the individual cavities to the beam dynamics as well as the optimization with respect to the RF performance

of the cavity would be performed autonomously by the software. This would significantly reduce the amount of work required for longer linear accelerators, and thus reduce production costs.

The necessary components for the tuner test bench as well as for the required adapted tuner to be investigated can be manufactured according to the designs presented in this thesis as soon as sufficient funding for all components is available. The modifications of the pillbox cavity already located at the IAP Frankfurt can be manufactured by the in-house metalworking shop of the Goethe University Frankfurt. The bellow tuner to be investigated, however, must be manufactured by an external company and thus represent a significantly greater financial outlay than the modifications. After the first offers for the bellow tuner were obtained, it was determined that immediate implementation was not possible with the funds currently available for the tuner test bench.

10.2 Summary

The development of the designs of the superconducting CH cavities of the HELIAC project from CH0 [27] to CH1 and CH2 [1] has undergone permanent improvements and adaptations based on the learned experiences of each previous cavity. For example, the design of CH1 and CH2 focused on mechanical stabilization and optimization of performance by minimizing peak electric and magnetic fields. As a result, the changes made there were already able to increase stability and performance compared to CH0 by simplifying the design in different ways. The process of designing both cavities was time reasonable, since they are identical in construction and thus only one design had to be developed. However, for both the development and manufacturing of an entire accelerator of individual CH cavities, this type of design would become too time consuming and costly. In order to reduce this time-consuming design process and accelerate the fabrication of superconducting CH cavities, and also reduce costs, a modular cavity design for mass production of superconducting CH cavities was developed as presented in this thesis. In the following section, the conclusions gained in this work and the results already presented will be summarized once again.
So in the first chapters of this thesis the theoretical foundations were laid, which are necessary for the description of superconducting cavities and for their development process, like a theoretical description of superconductivity itself (see chapter 2), the physical basics of RF-acceleration and of the CH cavity (see chapter 3), but also the effects that limit the superconducting cavities in terms of acceleration (see chapter 4) or the properties and laws from structural mechanics needed in later measurements and simulation (see chapter 5). Based on the theoretical foundations given in these sections, all measurements, evaluations and simulations made in the following sections were made.

In the following section, the measurement results of the cold test of CH2, which was initially postponed due to a cold leak, were presented and explained, with particular emphasis on the conspicuity in the Q over E curve (see chapter 7). Similar to the cold test of CH1 [1], CH2 was also tested in the vertical cryostat of the IAP Frankfurt. For this purpose, the cavity was first attached to the lid of the cryostat, which was then lowered into the cryostat together with the cavity. After the Nitrogen shield was filled with liquid Nitrogen, the cavity was cooled down with liquid Helium as fast as possible to prevent the formation of Niobium hybrids. Due to a software error, the frequency change due to thermal contraction could not be measured during cooling. Once the cavity reached the operating temperature of $\approx 4\,\mathrm{K}$, the pressure sensitivity of the cavity in the cold state was determined to be $\Delta f/\Delta p \approx -9.6\,\mathrm{HZ/mbar}$. This value is close to the value of $\Delta f/\Delta p \approx -8.2\,\mathrm{Hz/mbar}$ measured in the cold test previously aborted due to the cold leak. The deviation may have been caused by the subsequent treatment of the cavity at the manufacturer. Initially, the cavity could be fully conditioned, but showed a large number of soft multipacting barriers in the very low energy range, which, however, could be fully conditioned after a total period of about two weeks. After conditioning, the Q over E curve could be measured. A strange behaviour was observed, where at high field levels the forward power P_f remained constant, but the reflected power P_r decreased and the transmitted power P_t increased. This effect thereby increased with each subsequent measurement of the Q versus E curve. This behaviour was also reflected in the Q over E curve, so that only for the first two curves recorded could both the desired acceleration gradient E_a and the desired Q-factor Q_0 of the HELIAC project be achieved. In later measurements, the Q-factor dropped off rapidly at higher gradients. It is suspected that the coupling of the RF signal into the cavity by the coupler was subject to error due to damage either to the coupler itself or to the environment surrounding the coupler. Due to time and infrastructural reasons, the cold test had to be aborted without being able to complete a detailed analysis of the phenomenon. During the cavity reheating, the measurement of the frequency change due to thermal contraction was repeated and resulted in a value of $\Delta f_\mathrm{thermal} \approx 0.405\,\mathrm{MHz}$

The main focus of this thesis is the design and the development of the modular cavity design of the cavities CH3 to CH11 of the HELIAC of GSI. Not only was the principle of this modular method of designing cavities explained, but also the suitability of these cavities for later operation confirmed by simulations (see chapter 8). For this purpose, based on the already successfully realized designs of the cavities CH1 and CH2, components were selected which are to be manufactured identically as a basis for the following cavities. After discussions with the company RI, which had manufactured the cavities CH1 and CH2, it was decided to manufacture the spokes, the lids, the Helium vessels, the dynamic bellow tuner, the static tuner and the flanges for all nine cavities identically and to cut only the length on the re-

spective geometry of the respective cavity. This approach of modular cavity design saves an enormous amount of time during the design phase of the cavity on the one hand, and on the other hand it also greatly reduces both the production costs and the production time. For the production of the individual parts, a wide variety of mounting devices and tools are manufactured, each of which is specifically adapted to the geometry of the particular part to be produced. Now that a large number of the parts for all nine cavities are manufactured in the same way, only one set of mountings and tools needs to be produced in each case. In addition to this modular design, the dynamic bellow tuner has also been adapted compared to the tuner used in CH1 and CH2. For example, the rounding of the head of the bellow tuner has been adjusted, greatly reducing the electrical peak field at the edges of the head, and the outwardly drawn lamellae of the tuner have also been made void by increasing the radius of the tuner. The new design of the bellow tuner was then examined for its mechanical properties. For this purpose, the internal stress of the tuner occurring in the material during displacement of the tuner was simulated. A comparison with the maximum load capacity of Niobium showed that a buffer to the critical limit of Niobium of almost a factor of two is given. In addition, the bellow tuner was examined for its mechanical modes, which are all outside the range for mechanical vibrations from interference sources such as pumps or equivalent, making the new design of the bellow tuner suitable for later operation. Once all the modular components for the cavities were designed, they were assembled and examined for their suitability for later operation. First, the pressure sensitivity of the individual cavities was determined by simulations. It was shown that the frequency change due to pressure change has a different sign than for the CH1 and CH2 cavities. This arises from the larger gap center distances of the cavities and the effect that the frequency increase due to the volume reduction has a greater effect than the frequency decrease due to an increase in capacity caused by a reduced spoke distance due to contraction. It was further shown that with all subsequent processing steps such as a BCP surface treatment and effects such as thermal contraction, the cavities reach the desired target frequency, with the current designs having a buffer of about 250 kHz to desired target frequency of the HELIAC of 216.816 MHz after consultation with the operators. By optimizing the drift tube geometries of the individual drift tubes once by CST Studio Suite's own optimizer as well as by hand-made adjustments, the cavities based on the modular cavity design were able to achieve significantly improved performance with respect to the peak fields E_{peak} and B_{peak}. Currently, the cavities based on the modular cavity design achieve a performance increase of electrically 15 % and magnetically 4 % at a cost reduction of about 5 % per cavity compared to CH1 and CH2. In addition, the amount of liquid Helium available to cool the cavity in the modular Helium vessels was determined. After consultation with future operators, it was determined that the amount of Helium was sufficient for operation despite decreasing to cavities CH10 and CH11. Finally, a comparison was made between CH11 based on the modular cavity design and a CH11 cavity designed in the classical way.

Furthermore, the concept for a tuner test bench developed in the course of this thesis for the experimental investigation of the mechanical properties of dynamic bellow tuner was explained and the simulation results on the suitability of this test bench were presented (see chapter 9). For this purpose, it is planned to modify a pillbox cavity already located at the IAP Frankfurt to such an extent that it can function as a tuner test bench. The bellow tuner to be tested will be inserted into the cavity and the resonant frequency of the cavity will be measured. The bellow tuner is then displaced several times over the entire tuner sweep range of ± 1 mm and the resonant frequency is measured. By comparing the resonant frequencies at the zero crossing of the tuner and any deviations from each other, the deformation of the tuner due to material fatigue can be determined and thus a statement made about the maximum lifetime of the tuner. In addition, a load test is planned in which the tuner is deflected until it is fractured. The expected value for the maximum loading force of the tuner was estimated to be approximately 575 N through simulations using CST Studio Suite. One challenge in modifying the pillbox cavity is safe operation. Since Niobium has different mechanical material properties in the cold state compared to the normal state, the bellow tuner under investigation must be cooled down during the stress test. Currently, it is planned to cool the bellow tuner down to 77 K with liquid Nitrogen. In order to ensure safe operation, a filling lance was designed to fill the bellow tuner safely from the inside and from the bottom up. In addition, a Nitrogen cup was designed to surround the bellow tuner, including the flange and filling lance, in order to avoid possible hazards from splashing liquid Nitrogen. In addition to the modifications to the pillbox cavity, the bellow tuner under investigation must also be adapted to the existing conditions. For example, the pillbox has a larger radius than the later cavities, so the bellow tuner to be examined must be extended. To avoid possible additional mechanical modes due to the extension, the wall thickness of the tuner up to the bellow was reinforced by a factor of twelve. After talking to a possible manufacturer, it was decided to make this reinforced tube, as well as the tuner rod and flange, out of Titanium, while only the tuner head and bellow would be made of Niobium to reduce production costs. Simulations confirmed that the adaptations of the tuner to the conditions of the pillbox do not have any effect on the validity of the tuner testing and thus the concept elaborated in this thesis can be realized.

11 Acknowledgments/ Danksagung

In diesem Abschnitt dieser Arbeit möchte ich mich zuletzt bei all denjenigen herzlichst bedanken, ohne die ich diese Arbeit nicht hätte vollenden können.

Mein erster Dank geht dabei an Prof. Dr. Holger Podlech für die Aufnahme in seine Arbeitsgruppe, das in mich und meine Fähigkeiten gesteckte Vertrauen, die investierte Arbeit und die viele Zeit, die für Gespräche, Anmerkungen und Gedanken geopfert wurden. Ebenso für die vielen ermöglichten Reisen seien es zu Konferenzen oder Schulen gewesen, aus denen ich nicht immer nur als besserer Wissenschaftler zurückgekommen bin, sondern auch als ein erfahrenerer Mensch.

Auch möchte ich mich bei ihm und auch Prof. Dr. Ulrich Ratzinger für das Begutachten dieser Arbeit bedanken, sowie Prof. Dr. Oliver Kester für die Betreuung während meiner Zeit bei HGS-HIRe.

Zudem möchte ich dem technischen Team des IAP Frankfurt, Daniel Bänsch und Thomas Metz, für die Unterstützung während des Kalttests der CH2 danken.

Ein besonderes Dankeschön geht dabei an meinen Vorgänger Dr. Markus Basten, ohne dessen Hilfe, Anleitung und Weisheit ich niemals so weit gekommen wäre. Aber auch den restlichen Arbeitskollegen am IAP, der GSI und dem HIM möchte ich danken. Spezielles Danke geht an meine Bürokollegen Dr. Klaus Kümpel, Nils Petry, Sarah Lamprecht und Stephan Wagner, sowie Jan Dominik Kaiser, welche mich immer unterstützt, motiviert und auch unterhalten haben. An euch gehen ganz besonders viele Fische raus. Lang lebe Haus Harkness.

Meinen Freunden Denis, Daniel, Daniel, Fabi, Fabi, Jan, Mareike, Marvin, Nils, Salif und meinem Bruder Timo möchte ich ebenfalls von ganzem Herzen danken. Dank euch konnte ich ausreichend Abschalten, um mich wieder auf die Arbeit fokussieren zu können. Auch danke ich euch, dass ihr mich trotz allem die letzten Jahre über so ertragen habt.

Ebenso auch meiner Familie und meinen Eltern möchte ich danken, die mich stets mit allen nötigen Mitteln unterstützt haben.

Zum Schluss möchte ich mich bei meiner Verlobten Jana bedanken. Durch Dich ist das eine ganz besondere Zeit geworden, die ich nie vergessen werde. Du warst immer eine ganz besonders wichtige Motivation, egal wie anstrengend und auch nervenaufreibend das Ganze wurde, das hier zu Ende zu bringen.

Danke euch allen.

List of References

[1] Basten, M. "Entwicklung und Inbetriebnahme zweier supraleitenden 217 MHz CH-Kavität für das HELIAC-Projekt". In: *PHD Thesis, Goethe Universität Frankfurt am Main* (2019).

[2] Scerri, E. *The periodic Table: Its Story and Its Significance*. 1st ed. Vol. 1. Oxford University Press, 2006. ISBN: 0978-0195305739.

[3] Hofmann, S. and Münzenberg, G. "The discovery of the heaviest elements". In: *Rev. Mod. Phys.* 72 (2000), pp. 733–767. DOI: 10.1103/RevModPhys.72.733.

[4] Fermi, E. "Radioactivity induced by neutron bombardment". In: *Nature* 133 (1934), p. 757. DOI: 10.1038/133757a0.

[5] Garrett, A. B. "The chemistry of elements 93, 94, 95 and 96 (Neptunium, Plutonium, Americium and Curium". In: *The Ohio Journal of Science* 47 (1947), pp. 103–106.

[6] Thompson, S. G. et al. "The New Element Berkelium (Atomic Number 97)". In: *Phys. Rev.* 80 (1950), pp. 781–789. DOI: 10.1103/PhysRev.80.781.

[7] Thompson, S. G. et al. "The New Element Californium (Atomic Number 98)". In: *Phys. Rev.* 80 (1950), pp. 790–796. DOI: 10.1103/PhysRev.80.790.

[8] Bethge, K. et al. *Kernphysik - Eine Einführung*. 3rd ed. Vol. 1. Springer Fachmedien, 2008, pp. 84–90. ISBN: 978-3-662-08062-7.

[9] Burkhard, F. *Superheavy elements a prediction of their chemical and physical properties*. Springer Berlin Heidelberg, 1975, pp. 89–144. ISBN: 978-3-540-37395-7.

[10] *de.wikipedia.org/wiki/Magische Zahl (Physik)*.

[11] Münzenberg, G. et al. "Identification of Element 107 by α Correlation Chains". In: *Z. Ohys. A - Atoms and Nuclei* 300 (1981), pp. 107–108.

[12] Oganessian, Y. T. et al. "Synthesis of nuclei of the superheavy element 114 in reactions induced by 48Ca". In: *Nature* 400 (6741 1999), pp. 242–245. DOI: 10.1038/22281.

[13] Schmelzer, C. "Study of a variable energy heaven ion linear accelerator". In: *Proceedings of the 1968 Proton Linear Accelerator Conference* (1968).

[14] Angert, N et al. "UNILAC Modifications for an Improved Synchrotron Injector Performance". In: *2nd European Particle Accelerator Conference* (1990), p. 503. URL: https://cds.cern.ch/record/963825.

[15] Dahl, L. "The GSI UNILAC upgrade programme to meet FAIR requirements". In: *Proceedings of Heacy Ion Accelerator Conference HIAT09* (2009), p. 193.

[16] Gerhard, P. et al. "Status of the UNILAC-Upgrade Programme for the Heavy Element Research at GSI-SHIP". In: *Proceedings of European Particle Accelerator Conference* (2008), p. 3416.

[17] Groening, L. et al. “Upgrade of the UNILAC for FAIR”. In: Sept. 2015. DOI: 10.18429/JACoW-HIAT2015-TUA1I02.

[18] Henning, W. “FAIR - An International Accelerator Facility for Research with Ions and Antiprotons”. In: *9th European Particle Accelerator Conference* (2004), p. 50. URL: https://cds.cern.ch/record/822761.

[19] Spiller, P. and Franchetti, G. “The FAIR accelerator project at GSI”. In: *http://web-docs.gsi.de* ().

[20] *gsi.de/en*.

[21] Mickat, S. et al. “The superconducting cw-LINAC-Demonstrator at GSI”. In: *Proceedings of Linear Accelerator Conference LINAC2021* (2010), p. 145.

[22] Barth, W. et al. “UNILAC-Upgrade Programme for the Heavy Element Research at GSI-SHIP”. In: *Proceedings of European Particle Accelerator Conference* (2006), pp. 1565–1567.

[23] Mickat, S. et al. “The sc cw-LINAC-Demonstrator - SRF Technology finds the Way to GSI”. In: *Proceedings of Superconducting Radiofrequency Conference* (2011), p. 646.

[24] Schwarz, M. et al. “Reference beam dynamics layout for the SC CW heavy ion HELIAC at GSI”. In: *Nuclear Instruments and Methods in Physics Research Section A: Accelerators, Spectrometers, Detectors and Associated Equipment* 951 (2020), p. 163044. ISSN: 0168-9002. DOI: https://doi.org/10.1016/j.nima.2019.163044. URL: https://www.sciencedirect.com/science/article/pii/S0168900219314019.

[25] Schwarz, M. “Beam Dynamics Design of an Energy-Variable CW-Operated Superconducting Heavy Ion Accelerator”. In: *PhD Thesis, Goethe Universität Frankfurt am Main* (2021). DOI: 10.21248/gups.64448.

[26] Podlech, H. et al. “Superconducting CH structure”. In: *Phys. Rev. ST Accel. Beams* 10 (8 2007), p. 080101. DOI: 10.1103/PhysRevSTAB.10.080101. URL: https://link.aps.org/doi/10.1103/PhysRevSTAB.10.080101.

[27] Dziuba, F. “Entwicklung und Test einer supraleitenden 217 MHz CH-Kavität für das Demonstrator-Projekt an der GSI”. In: *PHD Thesis, Goethe Universität Frankfurt am Main* (2016).

[28] Barth, W. et al. “First heavy ion beam tests with a superconducting multigap CH cavity”. In: *Physical Review Accelerators and Beams* 21:020102 (2018). DOI: 10.1103/PhysRevAccelBeams.21.020102.

[29] Buckel, W. and Kleiner, R. *Supraleitung*. 7th ed. WILEY-VCH Verlag G,bH und Co. KGaA, 2013, pp. 1–9. ISBN: 978-3-527-41139-9.

[30] *en.wikipedia.org/wiki/Heike_Kamerlingh_Onnes*.

[31] Delft, P. K. Dirk van. “The discovery of superconductivity”. In: *IEEE/CSC & ESAS European Superconductivity News Forum (ESNF)* 15 (2010).

[32] Padamsee, H. et al. *RF Superconductivity for Accelerators*. 2nd ed. A Wiley-Interscience Publication, JOHN WILEY and SONS, INC., 2008. ISBN: 978-3527408429.

[33] Kittel, C. *Introduction to Solid State Physics*. John Wiley and Sons, Inc., 2004. ISBN: 978-0471415268.

[34] Meissner, W. and Ochsenfeld, R. "Ein neuer Effekt bei Eintritt der Supraleitfähigkeit". In: *Naturwissenschaften* 21 (1933), p. 787.

[35] London, H. and London, F. "The electromagnetic equations of the supraconductor". In: *Proceedings of the Royal Society of London A: Mathematical, Physical and Engineering Sciences* 149.866 (1935), pp. 71–88. ISSN: 0080-4630. DOI: 10.1098/rspa.1935.0048.

[36] Schulze, K. "Niobium, Proceedings of the International Symposium". In: *The Metallurgical Society of AIME* (1981), p. 163.

[37] Ginzburg, V. L. and Landau, L. D. "On the Theory of Superconductivity". In: *ZH. EKSP. TEOR. FIZ* 20 (1950), p. 1064.

[38] Bardeen, J. et al. "Theory of Superconductivity". In: *Phys. Rev.* 108 (1957), pp. 1175–1204. DOI: 10.1103/PhysRev.108.1175. URL: https://link.aps.org/doi/10.1103/PhysRev.108.1175.

[39] Ratzinger, U and Tiede, R. "Status of the HIIF RF linac study based on H-mode cavities". In: *Nuclear Instruments and Methods in Physics Research Section A: Accelerators, Spectrometers, Detectors and Associated Equipment* 415.1 (1998), pp. 229–235. ISSN: 0168-9002. DOI: https://doi.org/10.1016/S0168-9002(98)00389-1. URL: https://www.sciencedirect.com/science/article/pii/S0168900298003891.

[40] Software, CST Microwave Studio. "Computer Simulation Technology GmbH; CST Studio Suite; CST Microwave Studio". In: *www.cst.com* (2014 - 2021).

[41] Wangler, T. P. *RF Linear Accelerators*. 2nd ed. Wiley-VCH Verlag GmbH und Co.KGaA, 2008. ISBN: 978-3-527-40680-7.

[42] Maier, L. C. and Slater, J. C. "Field Strength Measurements in Resonant Cavities". In: *Jornal of Applied Physics* 23.1 (1952). DOI: http://doi.org/10.1063/1.1707980.

[43] Wille, K. *Physik der Teilchenbeschleuniger und Synchrotronstrahlungsquellen*. 2nd ed. B.G. Teubner Stuttgart, 1996. ISBN: 3-519-13087-4.

[44] Podlech, H. J. "Entwicklung von normal- und supraleitenden CH-Strukturen zur effizienten Beschleunigung von Protonen und Ionen". In: *Habilitation, Goethe Universität Frankfurt am Main* (2008).

[45] Fowler, R. and Nordheim, L. "Electron Emission in Intense Electric Fields". In: *Proceedings of the Royal Society of London Series A: Containing Papers of a Mathematical and Physical Character* 119.781 (1928), pp. 173–181. ISSN: 0168-9002. DOI: https://doi.org/10.1098/rspa.1928.0091.

[46] Läpple, H. *Einführung in die Festigkeitslehre*. Fried. Vieweg und Sohn Verlag, 2006. ISBN: 978-3-528-03205-0.

[47] Balke, H. "Einführung in die Technische Mechanik - Festigkeitslehre". In: *Springer Verlag* (2008). ISSN: 978-3-540-37890-7. DOI: 10.1007/978-3-540-37892-1.

[48] Papula, L. *Mathematik für Ingenieure, Band 2.* Vieweg und Teuber Verlag 13. Auflage, 2012. ISBN: 978-3-8348-1589-7.

[49] *de.wikipedia.org/wiki/Vergleichsspannung.*

[50] *de.wikipedia.org/wiki/Duktilität.*

[51] Mäder, D. "Die CH-Sektion des 17 MeV Injektors für MYRRHA". In: *PHD Thesis, Goethe Universität Frankfurt am Main* (2014).

[52] Bonin, B. and Röth, R. "Q degradation of niobium cavities due to hydrogen contamination". In: *Proceedongs of the 5th Workshop on RF supercondauctivity* (1991), p. 210.

[53] Ekin, J. W. *Experimental Techniques for Low-Temperature Measurments*. Oxford University Press Inc., 2006. ISBN: 978-0198570547.

[54] Ansys. "Multiphysics Workbench, ANSYS, Inc." In: *www.ansys.com* (2015-217).

List of Figures

List of Tables

Appendix

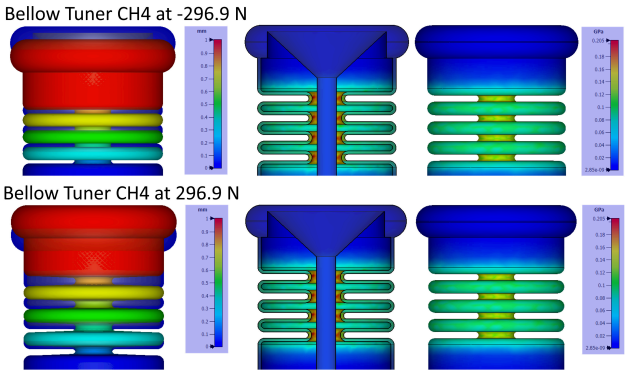

Fig. 106 Simulation results for the displacement of the dynamic bellow tuner of cavity CH4 and for the internal stress of the bellow. A force of ±296.9 N was applied to the tuner rod and the Helium vessel covers were defined as fixed points. When plotting the displacement, a factor of 3.96 was applied to the result for better illustration. The blue representation of the tuner indicates the shape and position of the tuner without the displacement force.

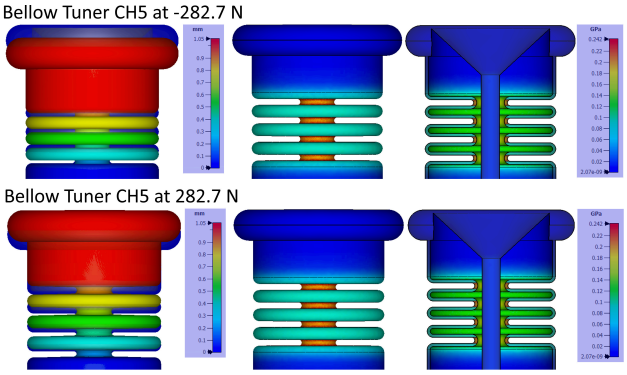

Fig. 107 Simulation results for the displacement of the dynamic bellow tuner of cavity CH5 and for the internal stress of the bellow. A force of ±282.7 N was applied to the tuner rod and the Helium vessel covers were defined as fixed points. When plotting the displacement, a factor of 3.96 was applied to the result for better illustration. The blue representation of the tuner indicates the shape and position of the tuner without the displacement force.

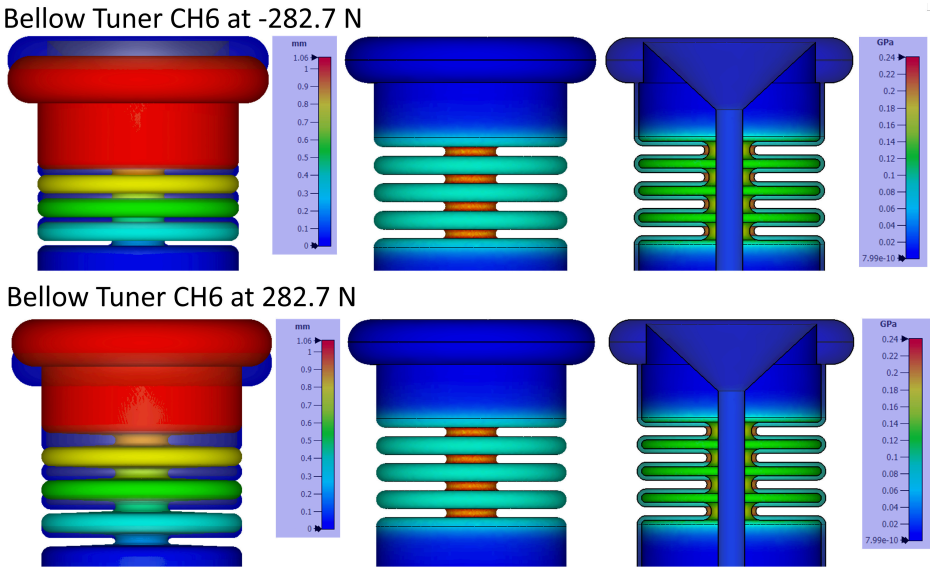

Fig. 108 Simulation results for the displacement of the dynamic bellow tuner of cavity CH6 and for the internal stress of the bellow. A force of ±282.7 N was applied to the tuner rod and the Helium vessel covers were defined as fixed points. When plotting the displacement, a factor of 3.96 was applied to the result for better illustration. The blue representation of the tuner indicates the shape and position of the tuner without the displacement force.

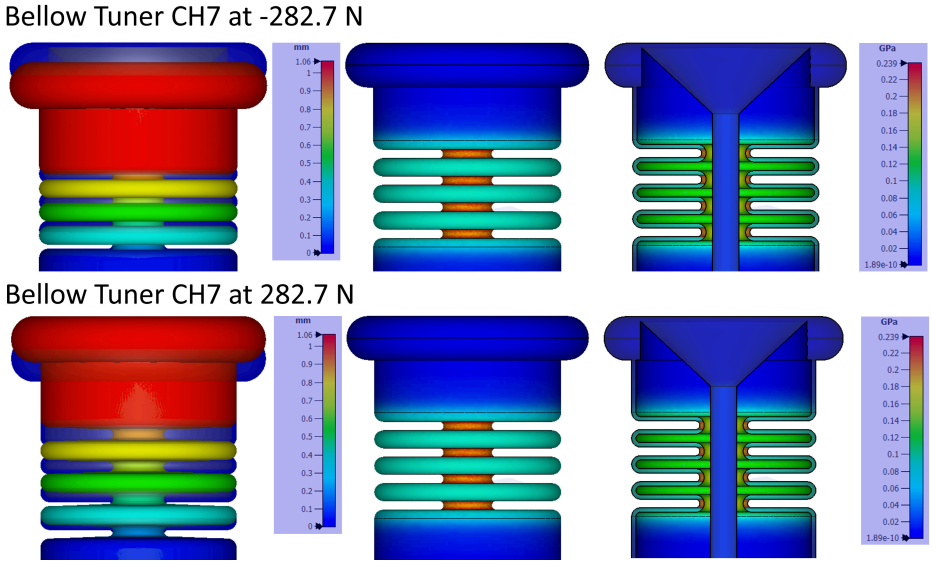

Fig. 109 Simulation results for the displacement of the dynamic bellow tuner of cavity CH7 and for the internal stress of the bellow. A force of ±282.7 N was applied to the tuner rod and the Helium vessel covers were defined as fixed points. When plotting the displacement, a factor of 3.96 was applied to the result for better illustration. The blue representation of the tuner indicates the shape and position of the tuner without the displacement force.

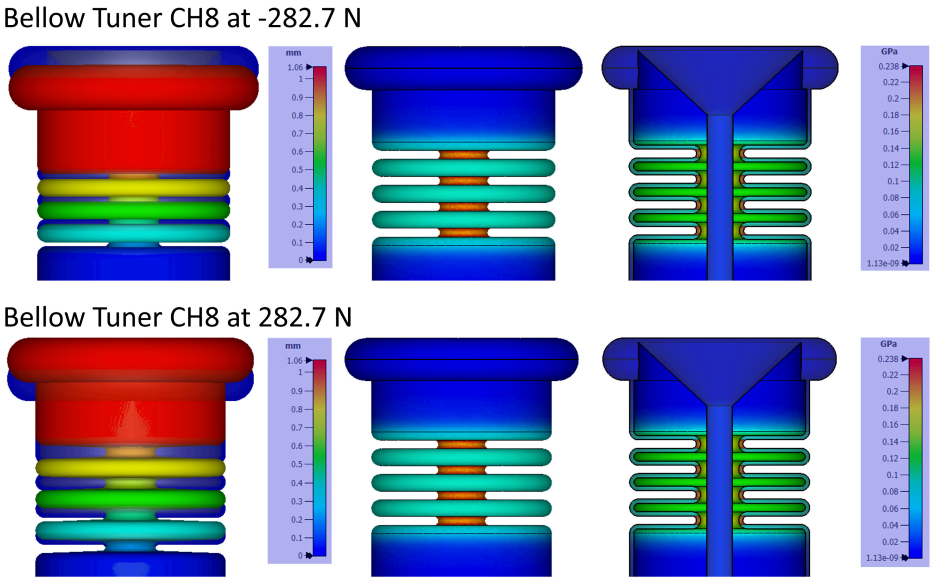

Fig. 110 Simulation results for the displacement of the dynamic bellow tuner of cavity CH8 and for the internal stress of the bellow. A force of ±282.7 N was applied to the tuner rod and the Helium vessel covers were defined as fixed points. When plotting the displacement, a factor of 3.96 was applied to the result for better illustration. The blue representation of the tuner indicates the shape and position of the tuner without the displacement force.

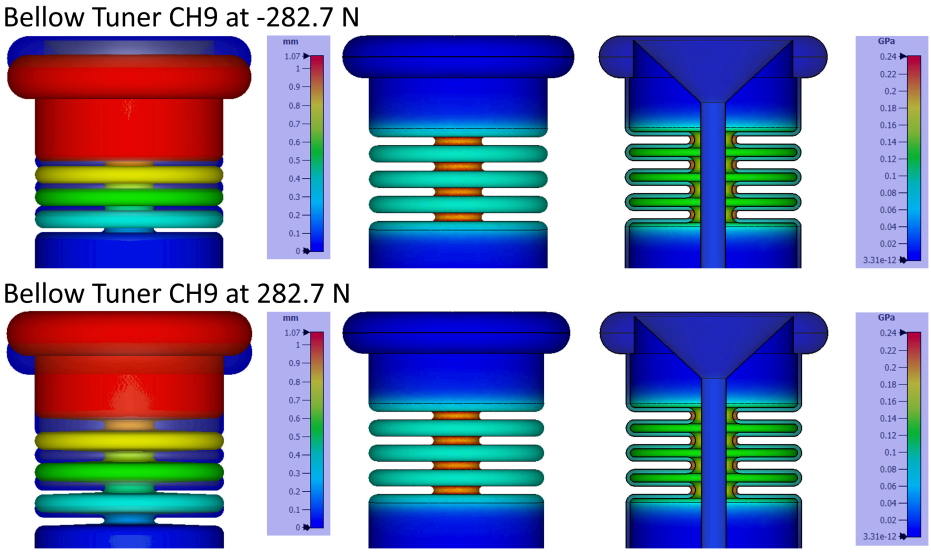

Fig. 111 Simulation results for the displacement of the dynamic bellow tuner of cavity CH9 and for the internal stress of the bellow. A force of ±282.7 N was applied to the tuner rod and the Helium vessel covers were defined as fixed points. When plotting the displacement, a factor of 3.96 was applied to the result for better illustration. The blue representation of the tuner indicates the shape and position of the tuner without the displacement force.

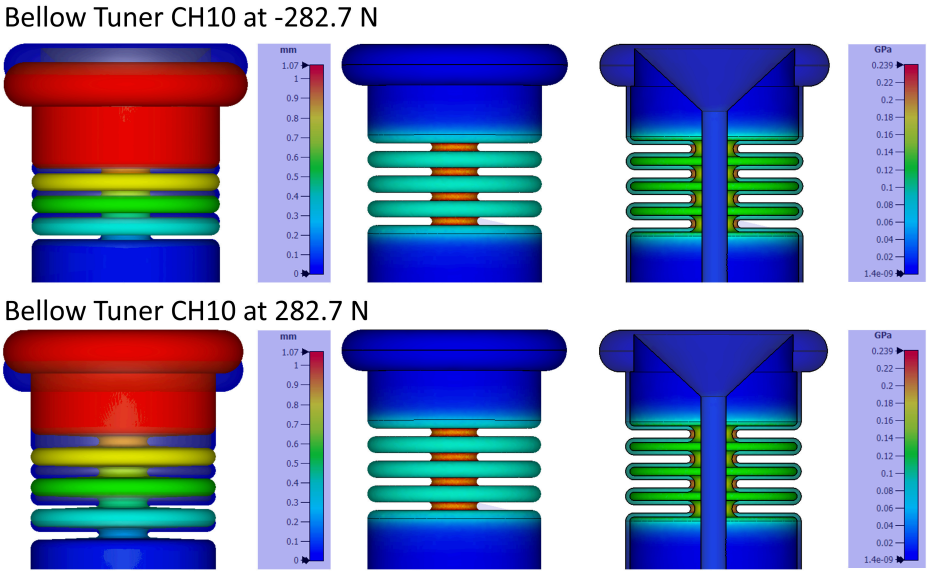

Fig. 112 Simulation results for the displacement of the dynamic bellow tuner of cavity CH10 and for the internal stress of the bellow. A force of ±282.7 N was applied to the tuner rod and the Helium vessel covers were defined as fixed points. When plotting the displacement, a factor of 3.96 was applied to the result for better illustration. The blue representation of the tuner indicates the shape and position of the tuner without the displacement force.

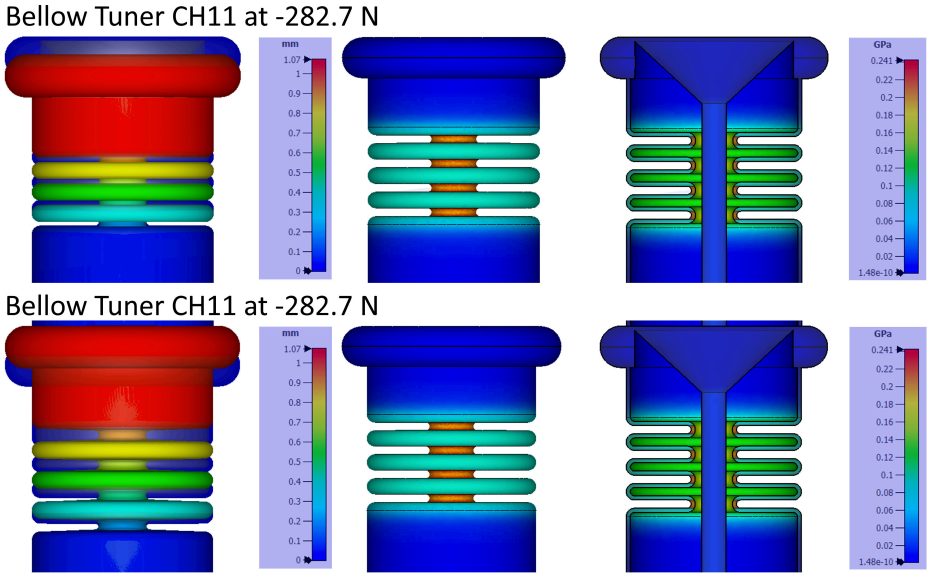

Fig. 113 Simulation results for the displacement of the dynamic bellow tuner of cavity CH11 and for the internal stress of the bellow. A force of ±282.7 N was applied to the tuner rod and the Helium vessel covers were defined as fixed points. When plotting the displacement, a factor of 3.96 was applied to the result for better illustration. The blue representation of the tuner indicates the shape and position of the tuner without the displacement force.

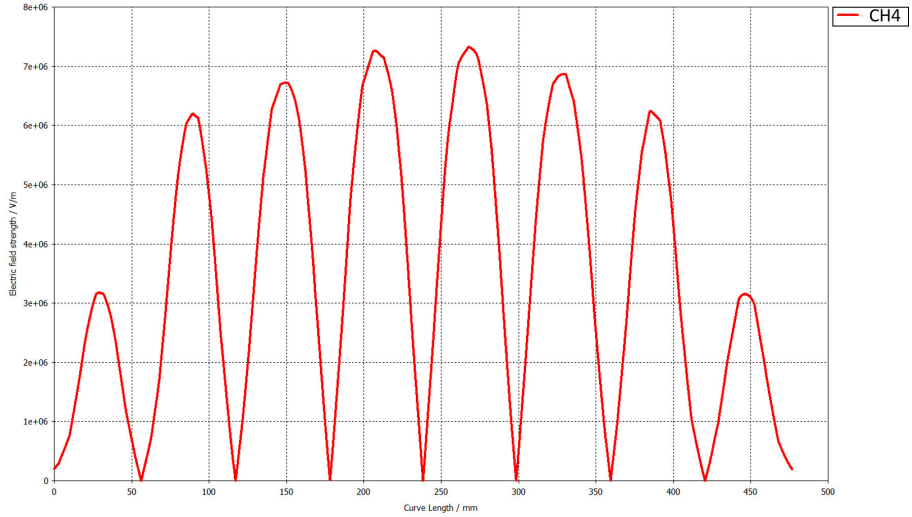

Fig. 114 Electric field distribution inside cavity CH4. On the x-axis represents the length of the accelerating field inside the cavity and the y-axis represents the electric field strength in V/m determined by CST Studio Suite [40] when coupling a power of 1 J electric power.

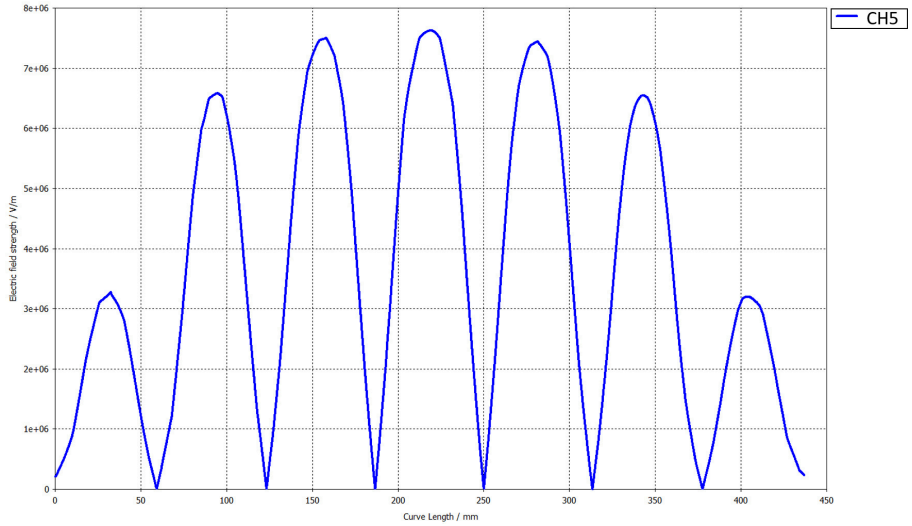

Fig. 115 Electric field distribution inside cavity CH5. On the horizontal axis represents the length of the accelerating field inside the cavity and the vertical axis represents the electric field strength in V/m simulated by CST Studio Suite [40] when a power of 1 J electric power is coupled into the cavity.

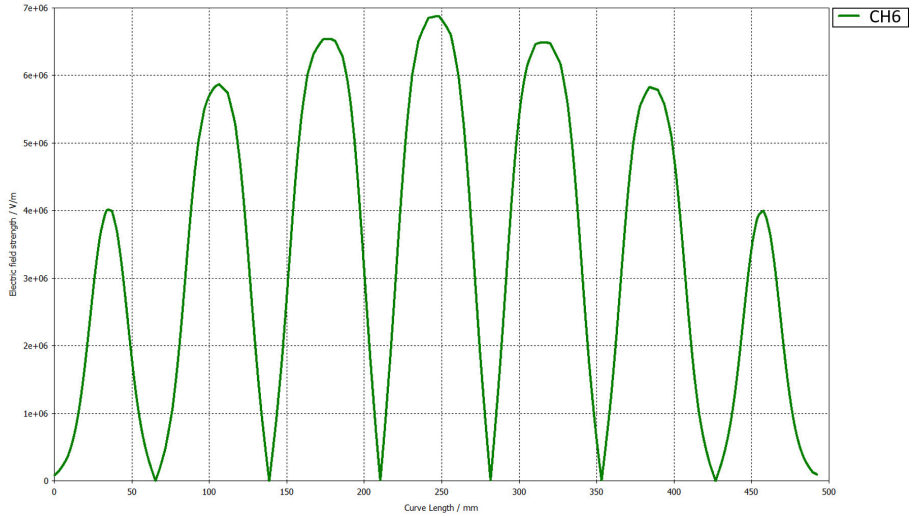

Fig. 116 Electric field distribution inside cavity CH6. On the horizontal axis represents the length of the accelerating field inside the cavity and the vertical axis represents the electric field strength in V/m simulated by CST Studio Suite [40] when a power of 1 J electric power is coupled into the cavity.

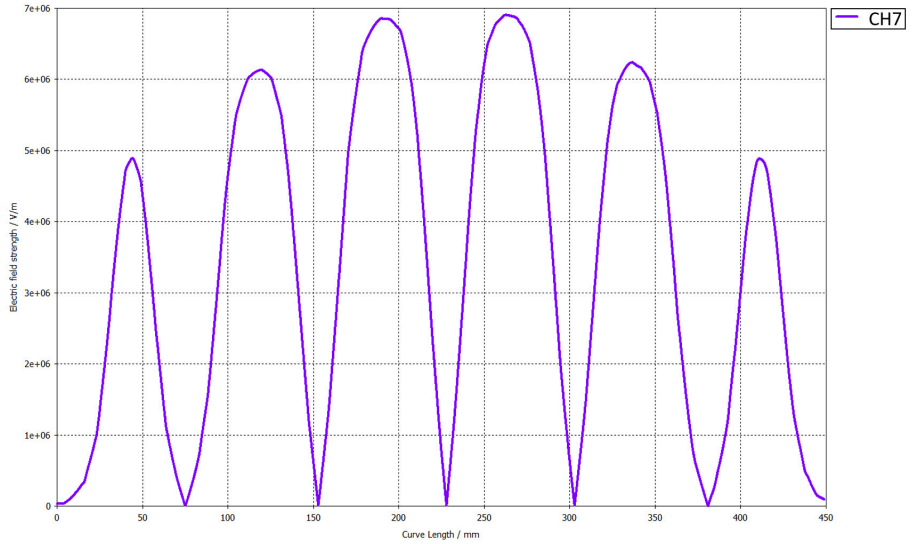

Fig. 117 Electric field distribution inside cavity CH7. On the horizontal axis represents the length of the accelerating field inside the cavity and the vertical axis represents the electric field strength in V/m simulated by CST Studio Suite [40] when a power of 1 J electric power is coupled into the cavity.

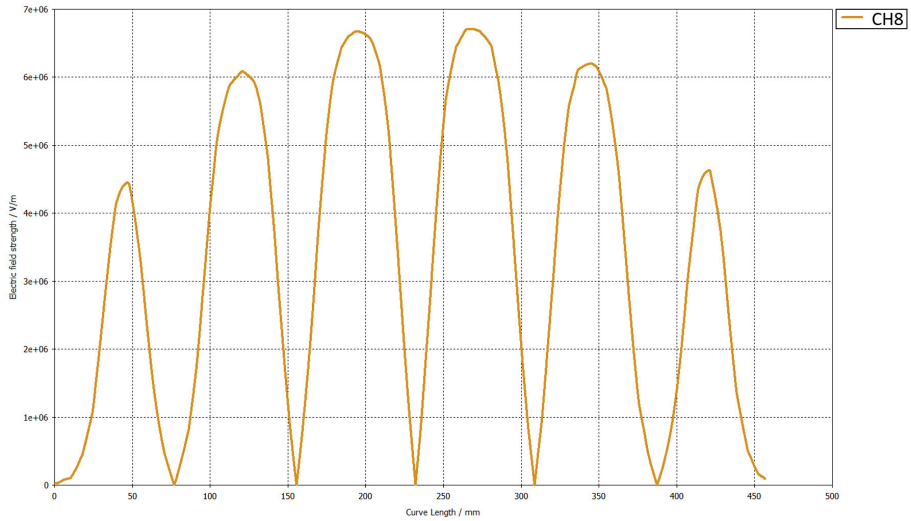

Fig. 118 Electric field distribution inside cavity CH8. On the horizontal axis represents the length of the accelerating field inside the cavity and the vertical axis represents the electric field strength in V/m simulated by CST Studio Suite [40] when a power of 1 J electric power is coupled into the cavity.

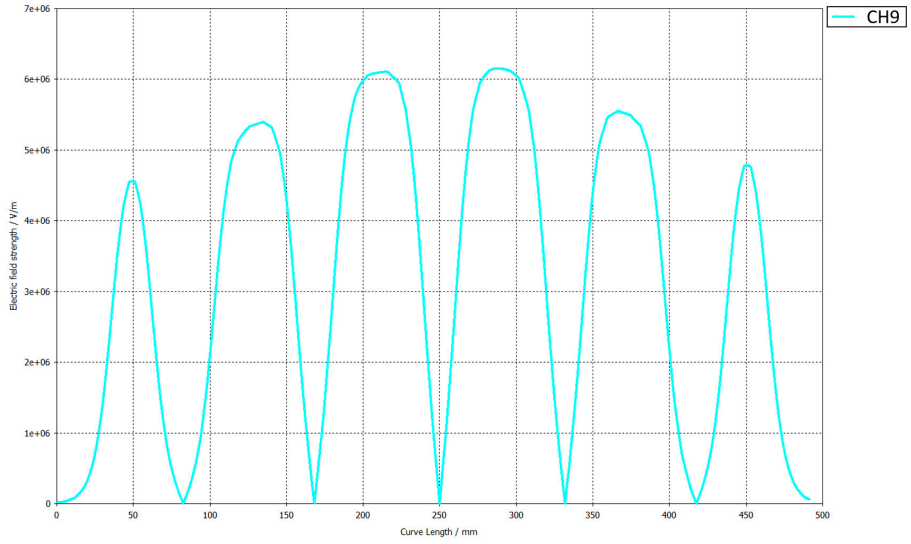

Fig. 119 Electric field distribution inside cavity CH9. On the horizontal axis represents the length of the accelerating field inside the cavity and the vertical axis represents the electric field strength in V/m simulated by CST Studio Suite [40] when a power of 1 J electric power is coupled into the cavity.

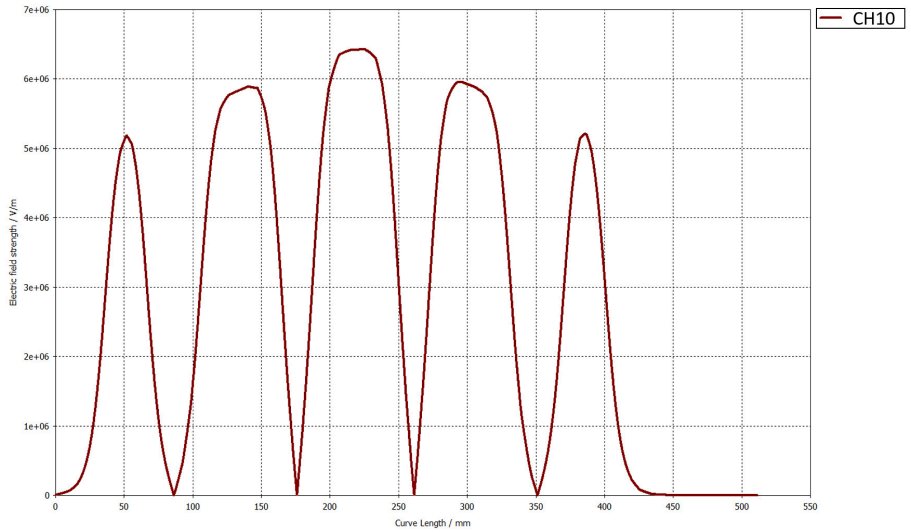

Fig. 120 Electric field distribution inside cavity CH10. On the horizontal axis represents the length of the accelerating field inside the cavity and the vertical axis represents the electric field strength in V/m simulated by CST Studio Suite [40] when a power of 1 J electric power is coupled into the cavity.

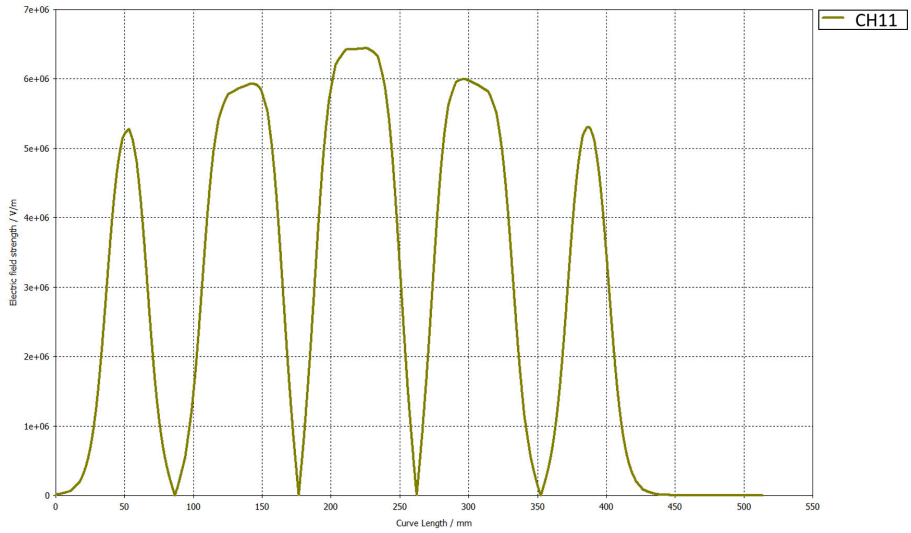

Fig. 121 Electric field distribution inside cavity CH11. On the horizontal axis represents the length of the accelerating field inside the cavity and the vertical axis represents the electric field strength in V/m simulated by CST Studio Suite [40] when a power of 1 J electric power is coupled into the cavity.

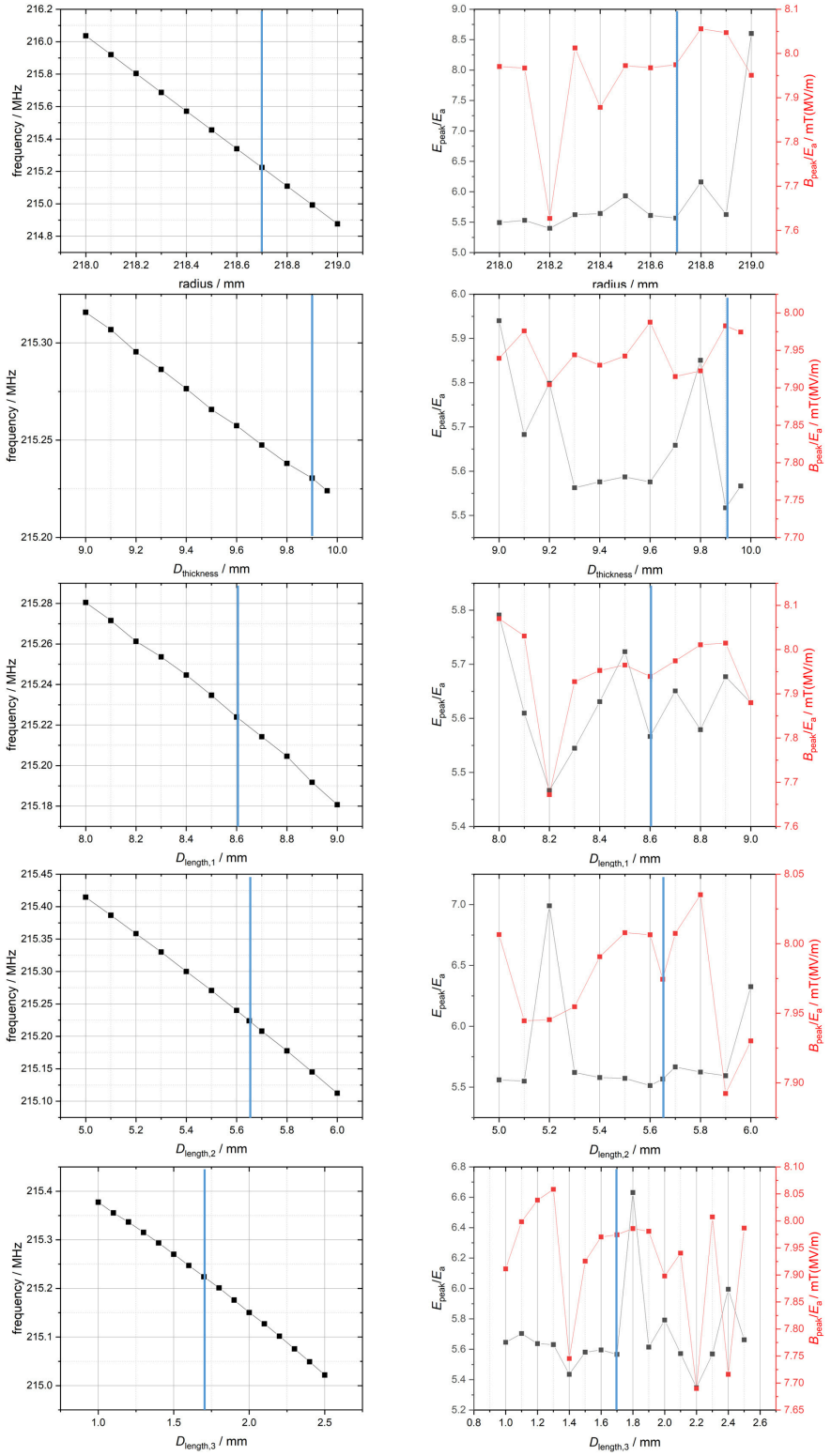

Fig. 122 Simulation results for the optimization of cavity CH4. The blue line indicates the final value of the respective parameter. Left: Course of the frequency against the corresponding optimization parameter. Right: Course of $E_{\mathrm{peak}}/E_{\mathrm{a}}$ (black) and $B_{\mathrm{peak}}/E_{\mathrm{a}}$ (red) against the corresponding optimization parameter.

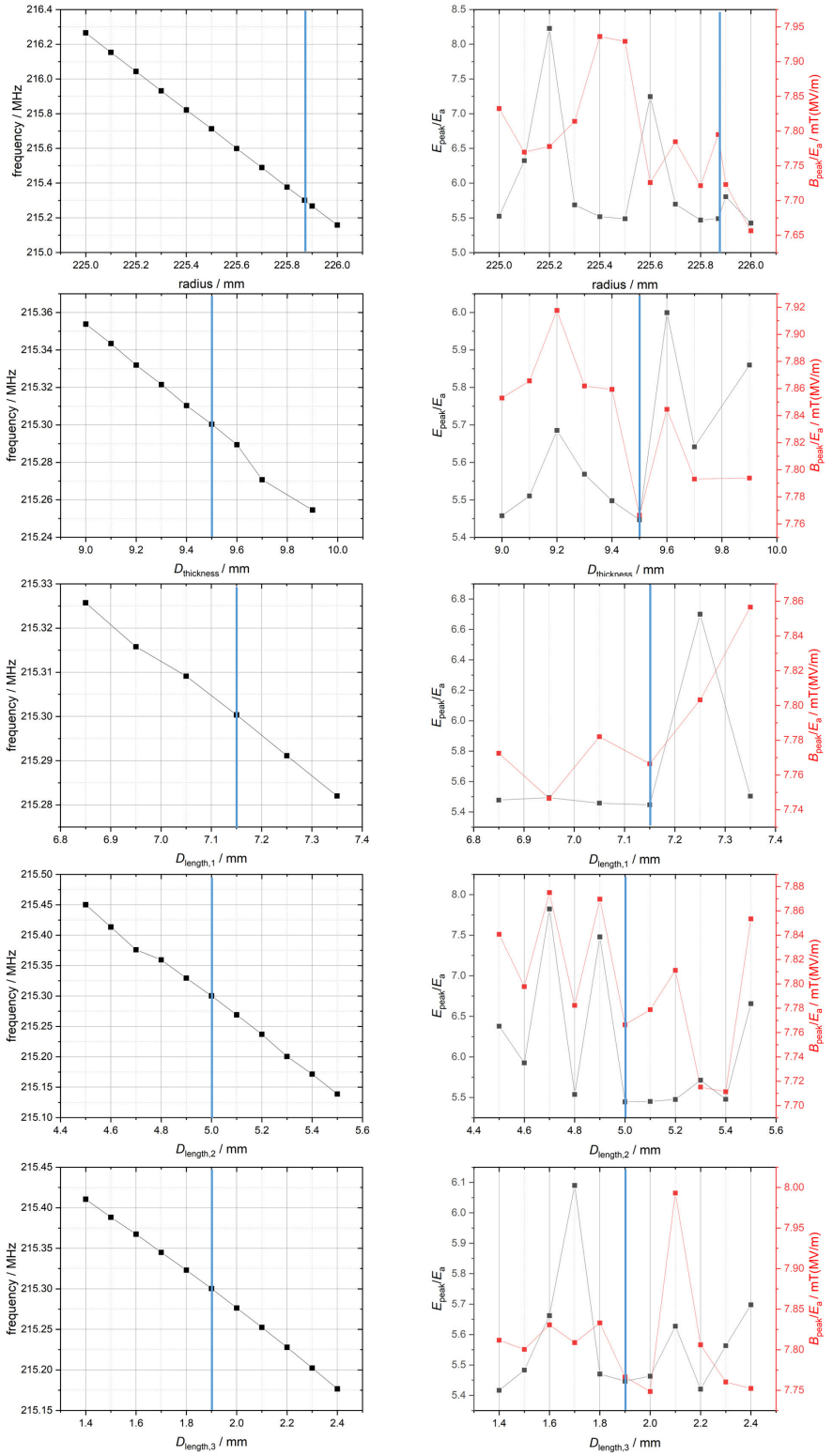

Fig. 123 Simulation results for the optimization of cavity CH5. The blue line indicates the final value of the respective parameter. Left: Course of the frequency against the corresponding optimization parameter. Right: Course of $E_{\mathrm{peak}}/E_{\mathrm{a}}$ (black) and $B_{\mathrm{peak}}/E_{\mathrm{a}}$ (red) against the corresponding optimization parameter.

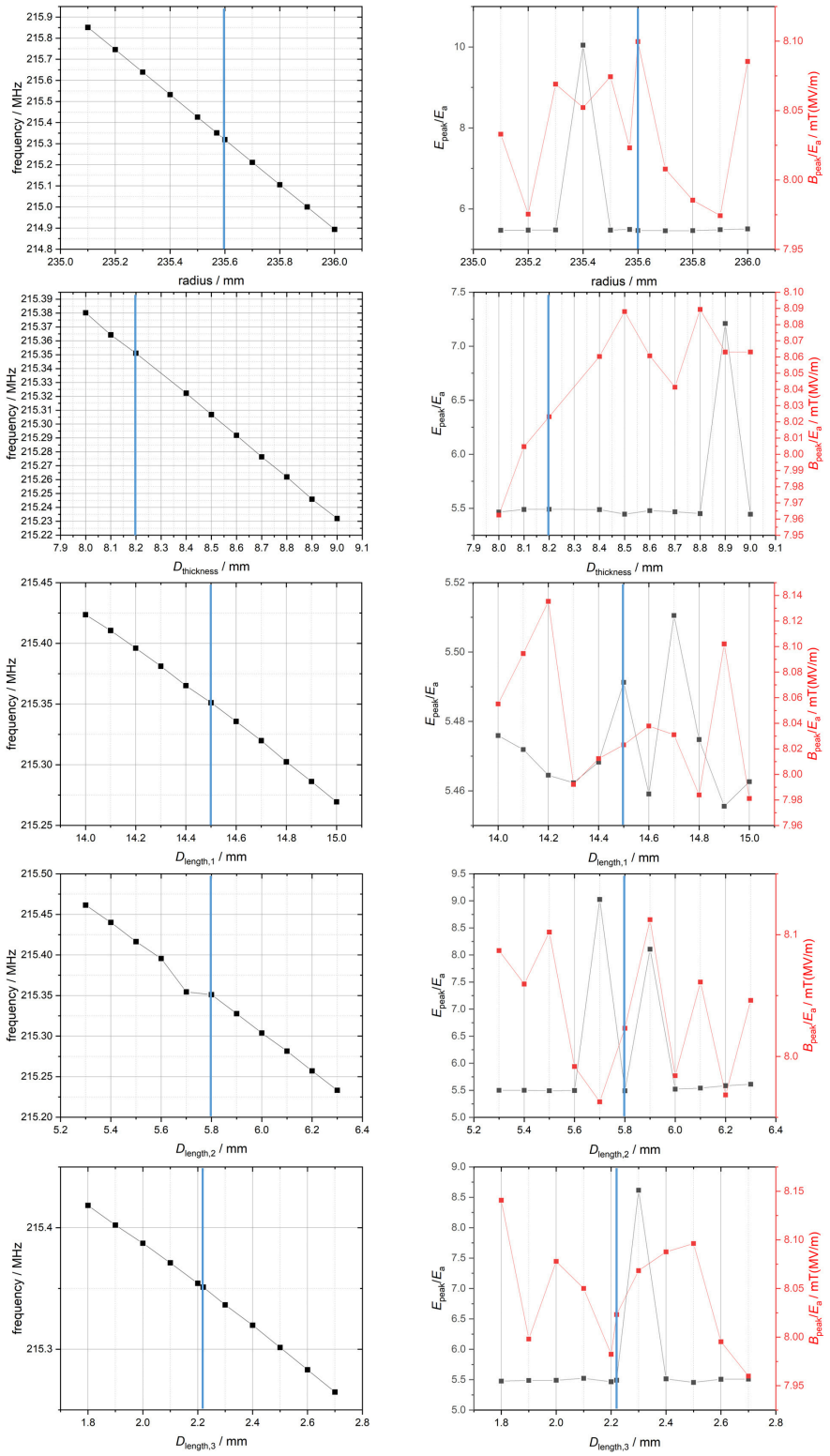

Fig. 124 Simulation results for the optimization of cavity CH6. The blue line indicates the final value of the respective parameter. Left: Course of the frequency against the corresponding optimization parameter. Right: Course of $E_{\mathrm{peak}}/E_{\mathrm{a}}$ (black) and $B_{\mathrm{peak}}/E_{\mathrm{a}}$ (red) against the corresponding optimization parameter.

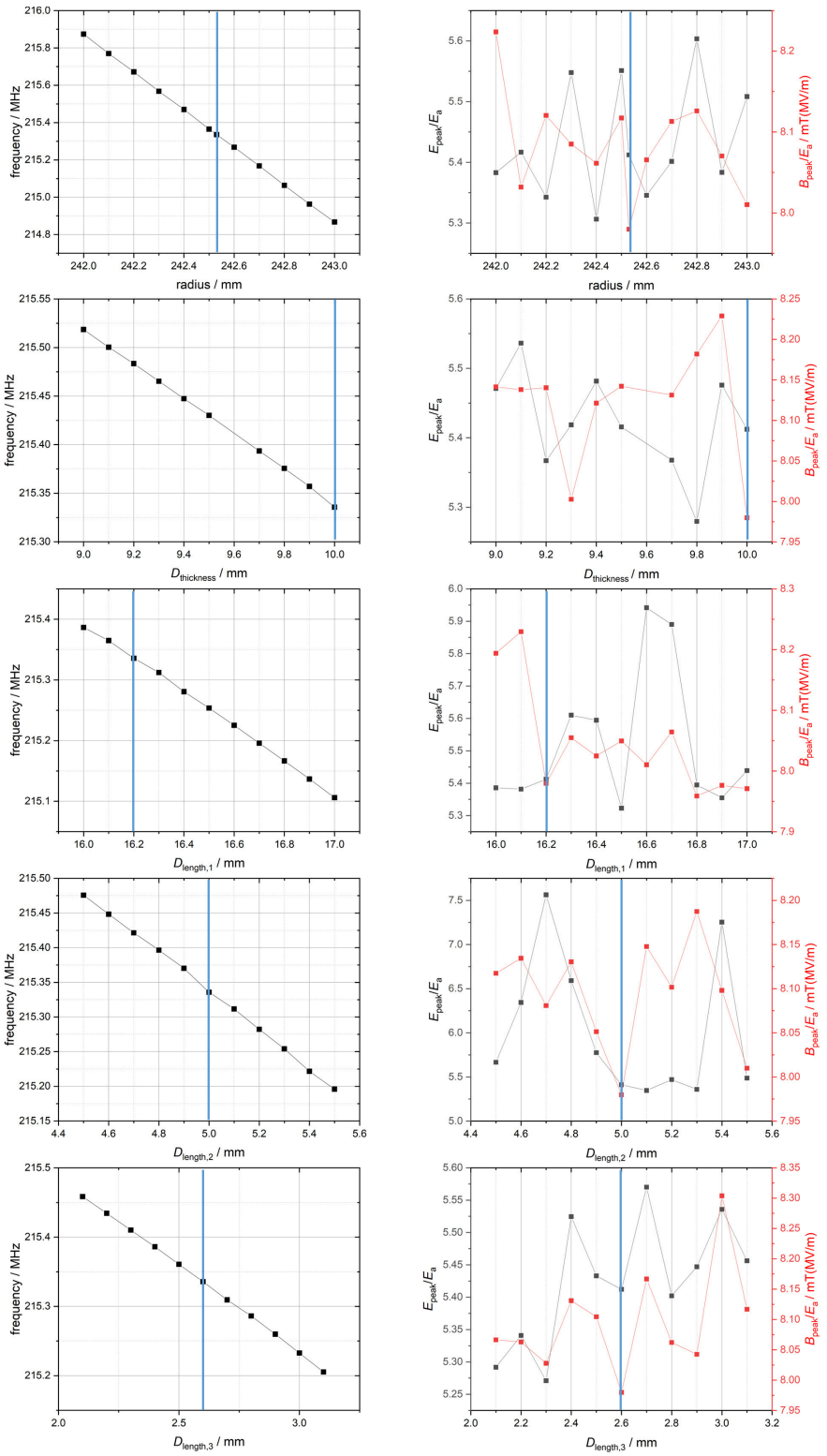

Fig. 125 Simulation results for the optimization of cavity CH7. The blue line indicates the final value of the respective parameter. Left: Course of the frequency against the corresponding optimization parameter. Right: Course of $E_{\mathrm{peak}}/E_{\mathrm{a}}$ (black) and $B_{\mathrm{peak}}/E_{\mathrm{a}}$ (red) against the corresponding optimization parameter.

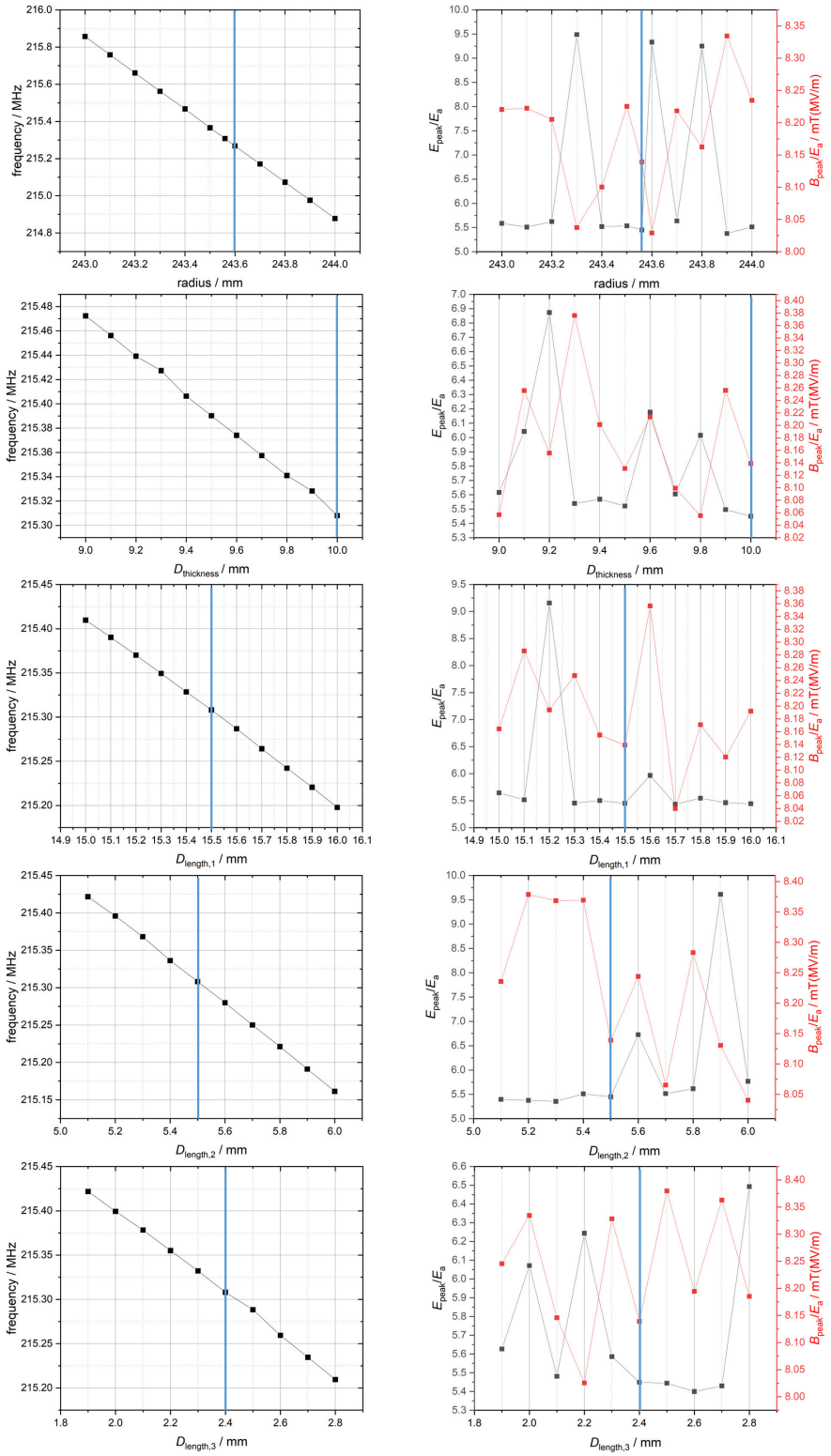

Fig. 126 Simulation results for the optimization of cavity CH8. The blue line indicates the final value of the respective parameter. Left: Course of the frequency against the corresponding optimization parameter. Right: Course of $E_{\mathrm{peak}}/E_{\mathrm{a}}$ (black) and $B_{\mathrm{peak}}/E_{\mathrm{a}}$ (red) against the corresponding optimization parameter.

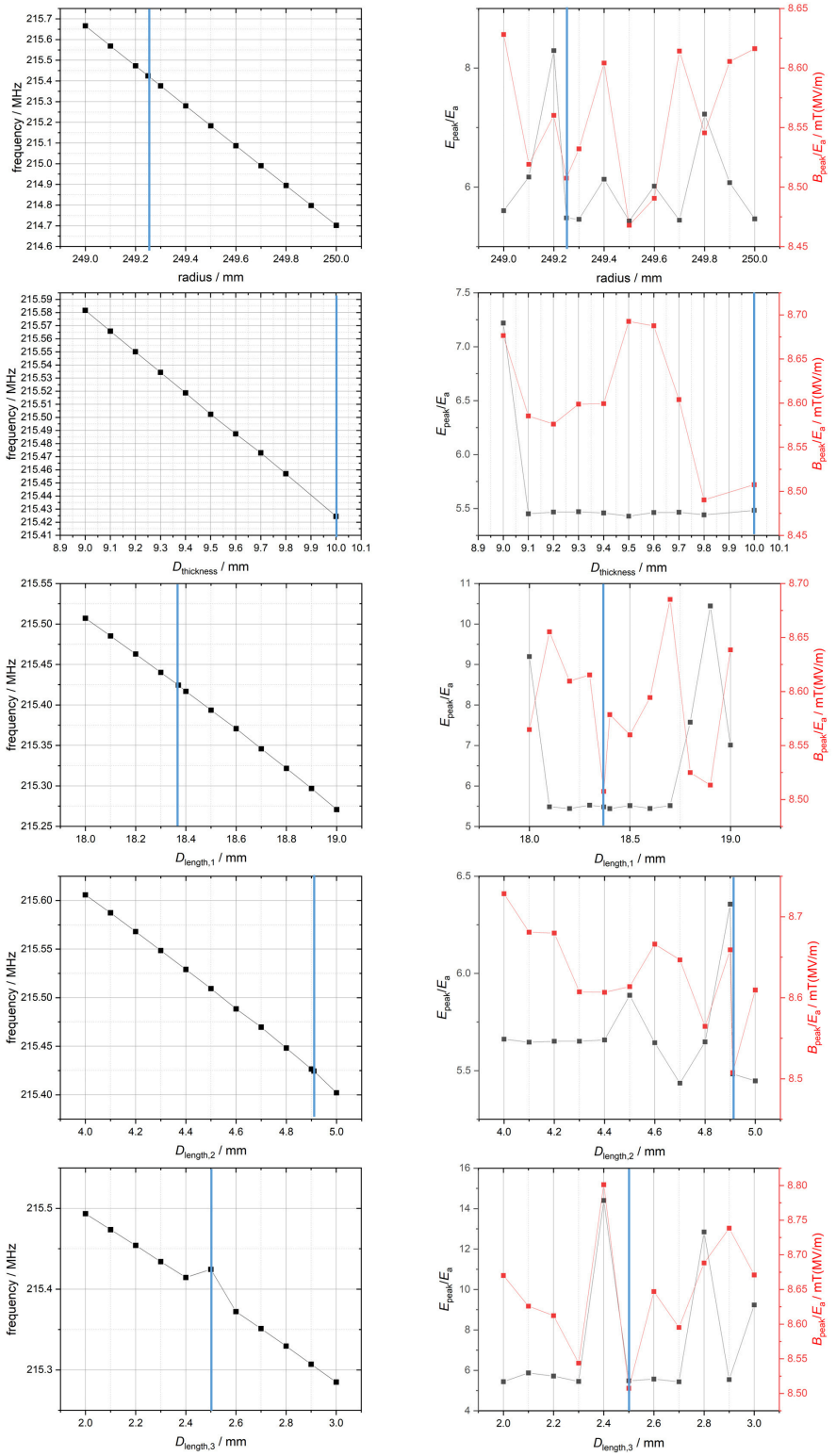

Fig. 127 Simulation results for the optimization of cavity CH9. The blue line indicates the final value of the respective parameter. Left: Course of the frequency against the corresponding optimization parameter. Right: Course of $E_{\mathrm{peak}}/E_{\mathrm{a}}$ (black) and $B_{\mathrm{peak}}/E_{\mathrm{a}}$ (red) against the corresponding optimization parameter.

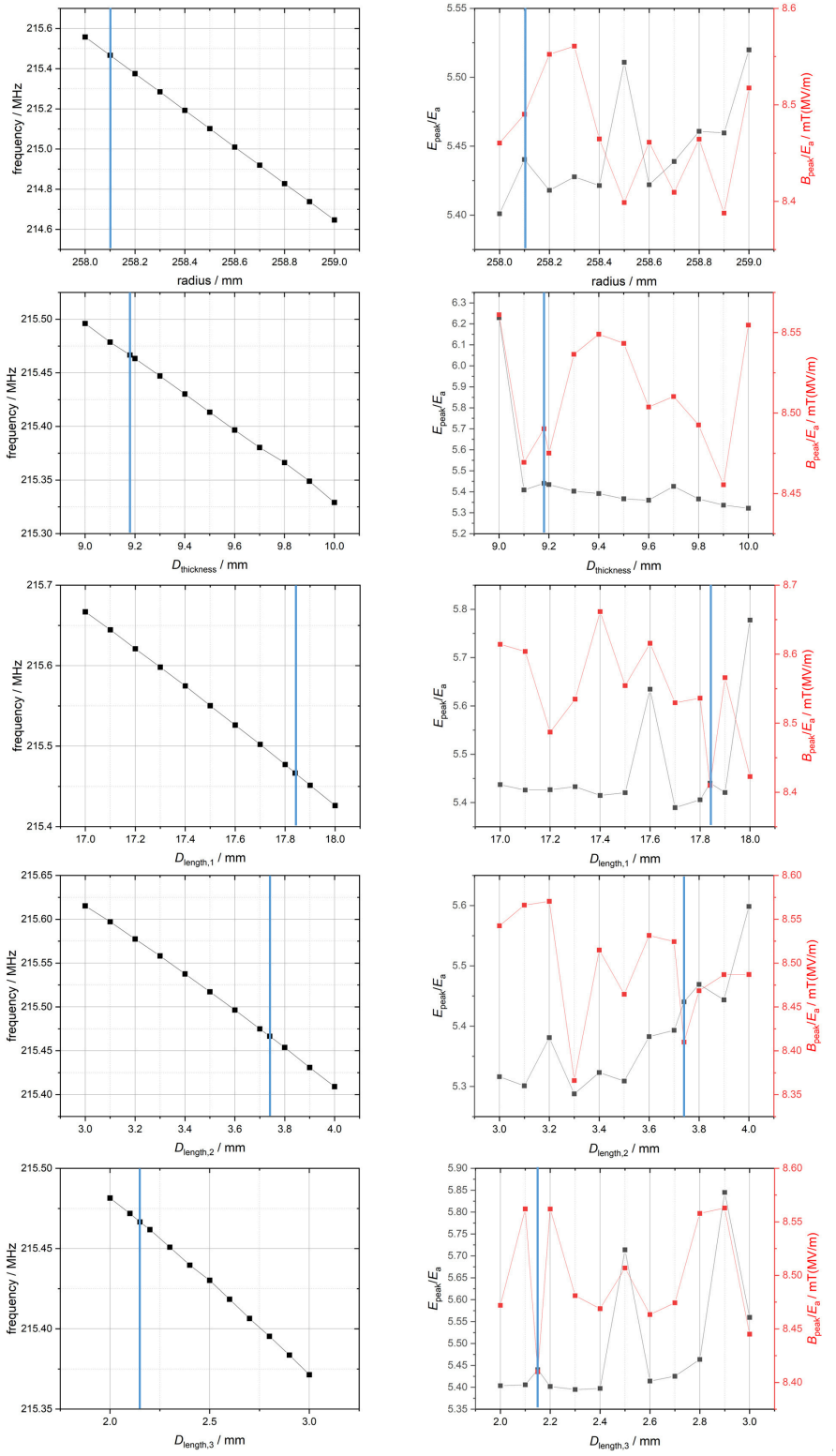

Fig. 128 Simulation results for the optimization of cavity CH10. The blue line indicates the final value of the respective parameter. Left: Course of the frequency against the corresponding optimization parameter. Right: Course of $E_{\mathrm{peak}}/E_{\mathrm{a}}$ (black) and $B_{\mathrm{peak}}/E_{\mathrm{a}}$ (red) against the corresponding optimization parameter.

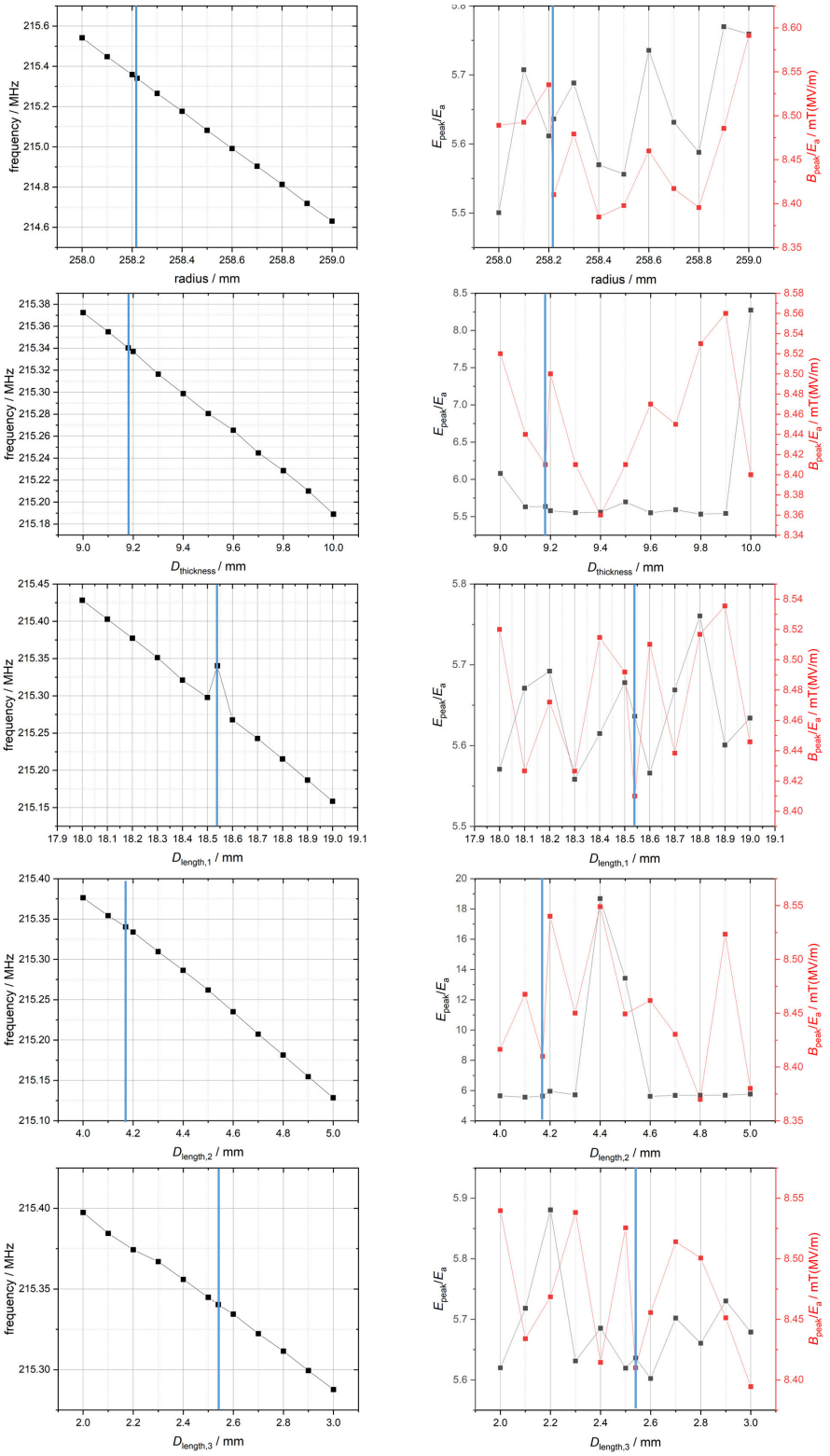

Fig. 129 Simulation results for the optimization of cavity CH11. The blue line indicates the final value of the respective parameter. Left: Course of the frequency against the corresponding optimization parameter. Right: Course of $E_{\mathrm{peak}}/E_{\mathrm{a}}$ (black) and $B_{\mathrm{peak}}/E_{\mathrm{a}}$ (red) against the corresponding optimization parameter.